REPORT DOCUMENTATION PAGE

1. REPORT DATE *(28 January 2003)*	2. REPORT TYPE Final Technical	3. DATES COVERED *(From - To)* 01/01/99 – 10/31/03

4. TITLE AND SUBTITLE
Modeling Dense Sprays in Liquid Rocket Engines

5a. CONTRACT NUMBER
F49620-99-1-0092

5b. GRANT NUMBER

5c. PROGRAM ELEMENT NUMBER

6. AUTHOR(S)
Stephen D. Heister

5d. PROJECT NUMBER

5e. TASK NUMBER

5f. WORK UNIT NUMBER

7. PERFORMING ORGANIZATION NAME(S) AND ADDRESS(ES)

School of Aeronautics & Astronautics
Purdue University
Grissom Hall
315 N. Grant Street
West Lafayette, IN 47907-2023

8. PERFORMING ORGANIZATION REPORT NUMBER

9. SPONSORING / MONITORING AGENCY NAME(S) AND ADDRESS(ES)
Dr. Mitat Birkan
AFOSR/NA
801 N. Randolph Road, Room 732
Arlington, VA 22203-1977

10. SPONSOR/MONITOR'S ACRONYM(S)

11. SPONSOR/MONITOR'S REPORT NUMBER(S)

12. DISTRIBUTION / AVAILABILITY STATEMENT

Approved for public release; distribution is unlimited.

20030205 253

13. SUPPLEMENTARY NOTES

14. ABSTRACT

Models have been developed to address instabilities inside coaxial injectors and for basic description of primary atomization processes. The coaxial injector simulations have provided a database to quantify the amplitude and frequency of hydrodynamic instabilities within the submerged region of the injector for a variety of design conditions. Results compare favorably with experimental data showing that plume "flickering" frequencies are correctly predicted by the model. A new nonlinear primary atomization simulation has been developed in a boundary element framework. Here, the influence of the boundary layer at the orifice exit (and hence the orifice geometry) is properly accounted for such that changes in orifice design are shown to affect the subsequent spray. Droplet size distributions have been predicted from first principles with no calibration constants; data agree very well with limited experimental observations.

15. SUBJECT TERMS

16. SECURITY CLASSIFICATION OF:			17. LIMITATION OF ABSTRACT	18. NUMBER OF PAGES	19a. NAME OF RESPONSIBLE PERSON Stephen D. Heister
a. REPORT unclassified	**b. ABSTRACT** unclassified	**c. THIS PAGE** unclassified	UL	168	19b. TELEPHONE NUMBER *(include area code)* (765) 494-5126

Standard Form 298 (Rev. 8-98)
Prescribed by ANSI Std. Z39.18

AQU03-04-0953

MODELING DENSE SPRAYS IN LIQUID ROCKET ENGINES

Stephen D. Heister, Professor
School of Aeronautics and Astronautics
Purdue University
1282 Grissom Hall
West Lafayette, IN 47907

7 January 2003

Final Technical Report for Period 1 July 1999 - 30 December 2002

r

Contents

1 Summary

This report summarizes findings from a three-year research effort aimed at enhancing the understanding of primary atomization processes and their role in liquid rocket engine combustion instabilities. A new fully nonlinear primary atomization model has been developed to provide fundamental information for droplet sizes for arbitrary injection conditions. This model makes use of no empirical parameters thereby providing a general tool capable of addressing the influence of various design changes on the primary atomization process. The model shows good agreement with limited experimental data as the experiments required to confirm the results are very challenging.

We have also developed a homogeneous model for addressing two-phase flow inside submerged regions of coaxial injectors. This unsteady, 3-D, Navier-Stokes calculation has been used to simulate flows in the Space Shuttle Main Engine injector successfully; although limited data are available results show a good correlation with fundamental flame flickering frequencies in recent experiments at DLR. The model has been used to characterize the amplitude and frequency of the instability over a wide range of operating conditions.

2 Research Objectives

Liquid rocket engine combustion chambers represent the most intense energy release (on a per unit volume basis) of any man-made device. Unfortunately, this situation makes the combustors particularly sensitive to instabilities - a problem that has plagued the industry virtually since its inception. The objectives of this research program are to assess the role of the atomization process in contributing to instabilities, to assess the potential frequencies of the instabilities and thereby to provide mechanisms to control the onset of these damaging phenomenon. The following section details the status of the research in achieving these goals.

3 Status of the Research

3.1 A Fully Nonlinear Model for Atomization of High-Speed Jets

A nonlinear model has been developed to assess the time evolution of an axisymmetric liquid jet using a boundary-element method. Vorticity transported from the boundary layer in the orifice passage to the free surface is modeled using a potential ring vortex placed at the orifice exit plane. The vortex strength is uniquely determined from the Kutta condition and information regarding the boundary layer thickness at the orifice exit plane. It is shown that primary breakup can occur even in the absence of the gas phase. Using a secondary stability analysis after Ponstein [1], the size of the droplets is estimated based on the size of the ring-type structures shed from the periphery of the jet. Computed droplet sizes are in reasonable agreement with experimental data, although turbulence effects obscure some comparisons.

The complete simulation of the Hoyt and Taylor's jet [2] is shown in Fig. 1. The jet structure is initially assumed to be a simple cylinder with a hemispherical tip. and its evolution is simulated via time integration. The simulation is completed at $t = 5.0$. A slight 'swelling' is observed at $t = 1.0$ and the fluctuation of the jet surface is seen at $t > 2.0$. The velocities induced by the bound vortex are large enough to penetrate the jet surface and it results in the primary atomization. It should be noted that most liquid ligaments, pinching from the jet surface, are in the 'rollup' motion in counterclockwise direction while the mean velocity of the ligament is in the streamwise direction. The counterclockwise rollup motion is a strong evidence that the boundary layer instability is the fundamental cause of the primary atomization. The mean velocity of most droplets are in streamwise direction as the droplets motion propagates along with the main jet stream, the most dominant convective source.

It is well known that the droplet size varies significantly within the atomization regime. Wu et al [3] reported the droplet size variation with U for the turbulent water jet into air. Hoyt and Taylor's experiment had been carried out for the Bernoulli pressure $\Delta P < 60$ psi; no result with higher ΔP is reported [2, 4, 5]. However, we hypothesized the increase in ΔP for the Hoyt and Taylor jet. The result is taken the jet speed up to $U = 40$ m/s which corresponds to $\Delta P \approx 116$ psi or slightly higher in order to account for some pressure loss within the nozzle. The final result for the Hoyt and Taylor's case [2] is shown in Fig. 2. Using the methodology employed in the previous section with no calibration constants, the model predicts the

Sauter Mean Diameter, SMD, with reasonable accuracy. As shown in Fig. 2, there is a steep gradient at a jet speed around $U \approx 20 \ m/s$ for the Wu et al. [3] turbulent jet experiment. Our model result overlaps with that obtained by Hoyt and Taylor. It is interesting to observe that Wu et al.'s data is also similar to our result and that of Hoyt and Taylor at about $U \approx 20 \ m/s$. While Wu et al. noted this as the region of 'uncertainty', it is possible that the rollup motion was competing with the turbulence and thus the perceptible effect of the rollup motion appears as shown in Fig. 2.

For $U \gtrsim 20 \ m/s$, differences between the calculations and the experiments emerge. It is known that linear analysis [6] overpredicts the droplet size (by less than 20%) because it neglects the satellite droplet mass due to the nonlinear effect [7, 8] which yields the multiple crests per wavelength. Ponstein's equation [1] is a linear analysis and thus it also tends to overpredict the droplet size. However, a 20% or smaller SMD difference does not explain the difference we see in Fig. 2 at a higher jet speed. This is due to the fundamental difference between the boundary layer instability jet and the turbulent jet: the boundary layer instability jet is scaled by the momentum thickness [9] and the turbulent jet is scaled by the Kolmogrov length scale, l_k or/and turbulence eddy characteristics length of kinetic energy, l_i [3]. Wu et al. derived the empirical formula using the 'surface kinetic energy' argument which gives SMD scaled by $\sim 1/U^{1.48}$. Thus the governing length scale (i.e. l_k and l_i) decrease significantly at about $U \sim 20 \ m/s$. On the other hand, the SMD of the boundary layer instability jet is scaled by δ_2: $SMD \sim 1/U^{0.5}$ and thus its change with respect to U is relatively moderate as shown in Fig. 2. In Fig. 3, the jet becomes more stable (or less atomization) as U increases. This is consistent with Rupe's observation [10]. As U increases, the nozzle exit velocity profile becomes flatter which contains less circulation. One may imagine the limiting case of such condition: $U \to \infty$ ($Re_d \to \infty$) and thus inviscid flow with the perfectly flat velocity profile which contains no circulation at the nozzle exit. In this limiting case, the jet is unconditionally stable unless it is perturbed by other instability mechanisms. If the circulation at the nozzle exit increases, the jet is more unstable.

3.2 Hydrodynamic Instability of Shear Coaxial Jet in a Recessed Region

In many coaxial injectors, liquid flowing down a central post is atomized by a high-velocity gas passing around the outer annulus. In many applications, the liquid post is submerged somewhat from the orifice exit plane to provide flame holding in combustion systems such as liquid rocket engines. The submergence provides for oscillations of the liquid jet within the confines of the submerged region. These disturbances could couple to the dynamics of the jet breakup process and potentially provide amplification of oscillations within the combustion chamber. Combustion instabilities of this nature can have severe impact on the performance of the engine and can in some cases lead to catastrophic failures.

In general, the combustion instability with high frequency is categorized into acoustic instability and hybrid instability. The acoustic instability shows dominant wave-type oscillation in the main chamber, but is independent of the feed system. With the hybrid form of instability, the wave character of the oscillation is strongly coupled between the feed system and the combustion chamber. Hutt and Rocker [11] also investigated the high frequency combustion instability associated with coaxial injectors. They classified the instability phenomena in the chamber as injection-coupled and intrinsic mechanism. The injection coupling implies chamber pressure/temperature variation as a key contributor in the change of flow dynamics through the injector. In the other hand, the intrinsic mechanism occurs in the flowfield due to its own flow dynamics with negligible feed system effect. It should be noted that injection coupling is never independent of the intrinsic subprocesses, such as atomization, propellant heatup, vaporization, and mixing because these processes determine the relationship between the injector response and the chamber response.

However, in hydrodynamics point of view, for the flow at high velocity, most of researchers agree that the principal source introducing instability to the jet is from aerodynamic forces arising from the interaction of the liquid jet with the surrounding gas flow. Reynolds and Weber numbers are generally very high in these atomizers and aerodynamic forces are several orders of magnitude larger than capillary forces. The interaction between the liquid and gas phases mainly comes from different velocities of each phase. The velocity discontinuity in a homogeneous fluid results wave growth on the interface, which is a common *Kelvin-Helmholtz* instability.

Mayer and his research group [12, 13, 14] have done a significant amount of work on the coaxial injector in terms of the combustion instability. They claimed the initiation of the jet surface deformation was due to internal liquid turbulence transforming energy between phases in forms of eddy structures, approximately
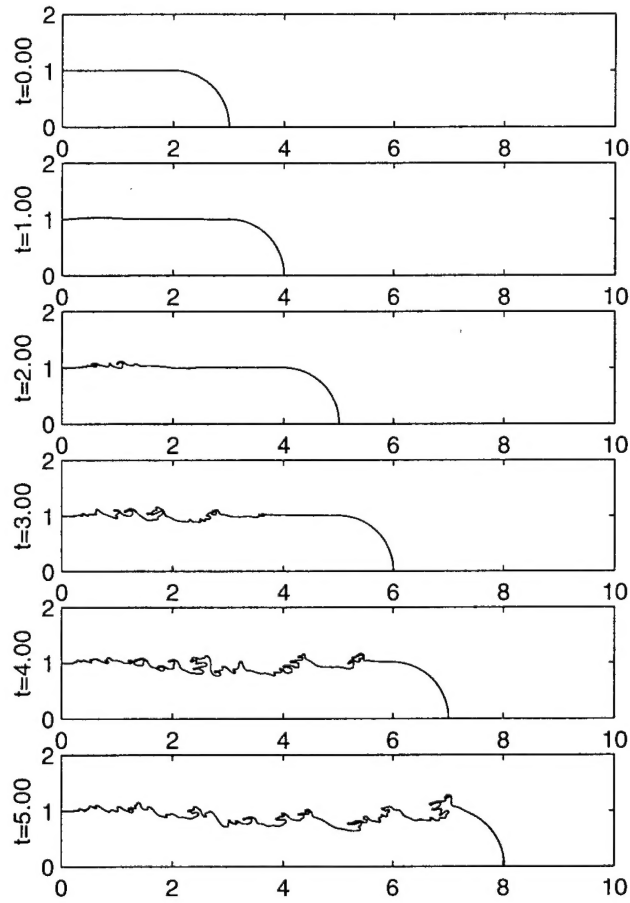
3

Figure 1: Jet evolution for conditions consistent with Hoyt and Taylors experiment [2]. Annular ligaments which have pinched off from the domain are not shown to improve clarity.

a size of 10-30% of the LOX post diameter. Instability mechanisms in coaxial injectors were investigated experimentally by Glogowski et al. [15, 16] under noncombusting conditions. Their experiment results showed that for the coaxial injector with the liquid oxygen (LOX) post recessed into the fuel annulus, the injector transitioned into a condition of resonance characterized by a whistling noise and significant modification to the overall structure of the spray due to the strong acoustic coupling between injector hydrodynamics and spray formation.

Bazarov [17, 18, 19] studied the self-oscillation phenomena along with the self-pulsation mode of jet instability in coaxial injector. He postulated that the self-oscillation occurs when the gas-liquid interaction forms a cavity inside nozzle, leading to jet swirling around the nozzle exit. The self-pulsation of the liquid jet mixed with the gas flow depends on the pressure drop at liquid and gas phase, correlating with the time of liquid propagation through the injector nozzle [19].

In this report, the hydrodynamic instability of the coaxial jet in the recessed region is presented using the three dimensional direct numerical simulation. The results indicate that the recess length to injector orifice diameter has a significant effect on spray structure over the velocity and gas ratio changes. Unfortunately, none of experimental data for exact comparison exists due to very small spartial and temporal scales involved in the area. However, some of recent experimental data provide good measure in a macroscopic point of view for the instability frequency as explained later in this section.

A fully unsteady, three dimensional, two-phase simulation has been developed utilizing a finite volume implementation of the Marker and Cell discretization method. The current model is based on locally ho-
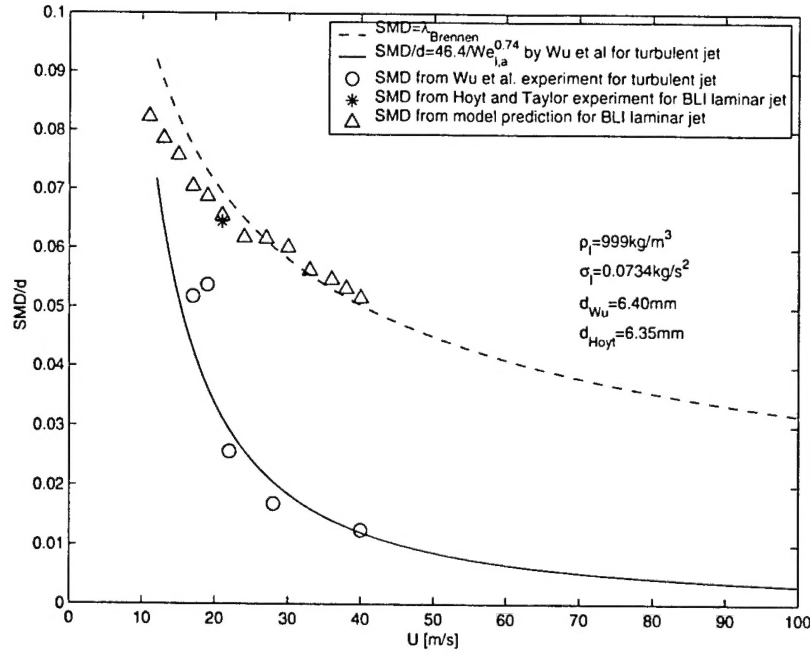
Figure 2: Sauter mean diameter comparison for various jet speed U in $[m/s]$.

mogeneous flow (LHF) assumption in which the relative velocity and temperature between two-phases are small enough in comparison to variation of the overall flow field that is predicted. Additional constituitive relation for desity field has been implemented in order to provide a mechanism of solving two-phase flow with a single phase Navier-Stokes equations set. This fictious "pseudo" density varies in amplitude between the liquid and gas extream. The LHF assumption and the pseudo-density implementation allow the current model to handle the two-phase flow field with one governing equations set rather than to compute separate governing equation sets for each flow phase, liquid and gas in this case.

The code runs on a state-of-art Beowulf Linux cluster that is equipped with 104 processors and fast ethernet network. One run usually requires 12 to 24 processors depending on mesh discretization. Since the cluster is dedicated to the modeling, each run makes use of nearly 100% of CPU power and network bandwidth. Even with this superb environment, one run up to 150,000 time steps takes about three weeks.

Parallel processing using MPI (Message Passing Interface) has been implemented in order to run the 3-D model in a timely manner. For the present 3-D atomization modeling, the computational domain is split up in axial direction for the desired number of processors, n. While each processor solves a flow field of subdivided domain, the boundary conditions of each subdomain are transfered to neighboring domain through message passing. All the processors involved in this procedure perform the same calculation in each step by copying the original task to other processors but solving different subdomains and boundary conditions.

The Space Shuttle Main Engine's (SSME) coaxial injector has been chosen for baseline modeling case. The injector of the SSME main combustion chamber (MCC) uses liquid oxygen (LOX) and gaseous hydrogen (GH_2) as an oxidizer and fuel respectively in fuel-rich injection environment entering the main combustion chamber.

The results exhibit characteristics termed "self-pulsation" and "self-oscillation" as theorized by Bazarov [17, 18, 19]. Pulsations are evident in changes in the flowrate with time, while oscillations are evidenced by azimuthal motion of the central liquid core about the annulus. Prior 2-D simulations [20, 21] have shown similar behavior, although the azimuthal motion cannot be resolved with decreased degree of freedom.

The overall density field behavior of the liquid jet for conditions roughly equivalent to the SSME MCC injector is illustrated in Figure 4. The left column in the figure depicts density contours in a cutaway view interpretation of the motion of the jet. The right column shows the density contours at the exit plane.
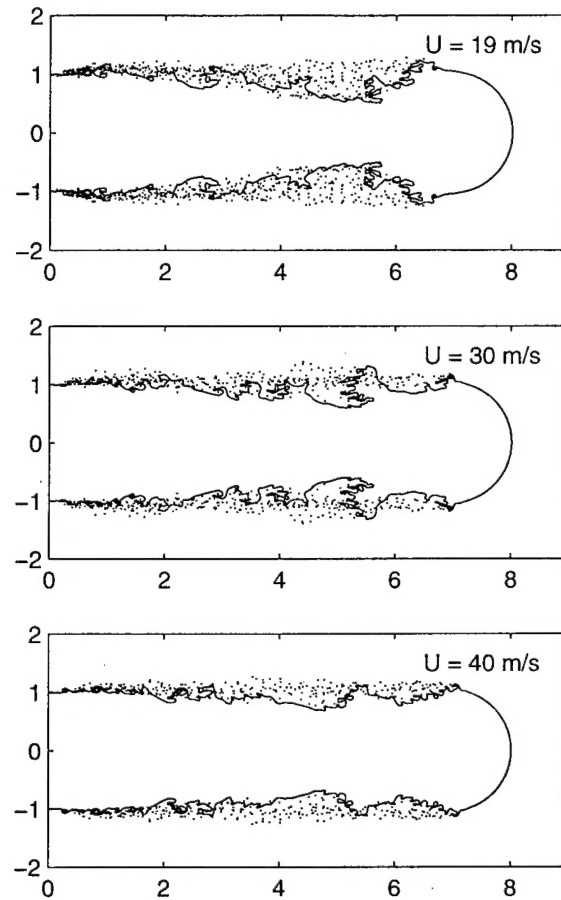
Figure 3: Effect of jet speed on jet surface structure of Hoyt-Taylor's jet. Due to larger circulation contained in the velocity profile, more unstable jet structure appears in the lower speed case.

The resultant highly nonlinear, quasi-periodic oscillation occurs naturally as a result of the Kelvin-Helmholtz instability mechanism. There is no oscillation in the inflow, yet strong oscillations/pulsations develop as a result of the large relative dynamic pressure between the gas and liquid streams. The development of self-pulsation mode of the liquid jet is apparent in the figure.

One interesting bulk measure of orifice performance is the massflow delivered at the orifice exit plane as a function of time. This quantity can be computed by quadrature of the density-axial velocity product over the exit plane area. eigure 5 shows the time history of mass flow for the density field computed in Fig. 4 and the attendant velocity field. The unsteadiness (self-pulsations) of the jet are quite evident in this figure; massflow variations of 39% about the mean flow are apparent.

The spectral content of the mass fluctuation signal provides information regarding the frequency spectrum present. Using a Fast Fourier Transform, the spectral content is shown in Figure 6. There is a significant energy content over a range of dimensionless frequencies with a maximum at $f = 2.2074$, which represent around 73,000 Hz in dimensional units. This frequency is about triple the frequency at which liquid is replaced in the submergence region.

In a recent study of Smith and Mayer [22], the liquid core jet oscillation in a coaxial injector was observed, and the frequency of flame flickering in a combustion chamber was reported as near 7000 Hz, which falls within the same frequency band of the SSME main burner coaxial injector's case. The same velocity and density ratios were used with similar geometry. Even though their coaxial injector was not exactly the same one used in this study, their experimental study provides some evidence that the liquid jet oscillation/pulsation

plays a significant role in combustion response within the chamber. This is an important finding requiring further experimental verification.

The three-dimensional simulation has shown a good predictive capability in terms of coaxial jet behavior. This allows conducting a series of parametric study before actual injector design and testing.

3.3 Simulating Droplet/Wall and Droplet/Film Collisions Using a Level Set Method

A numerical method, a coupled level set and Marker and Cell, is developed for computing axisymmetric, incompressible, and immiscible two-phase flows. In stead of using marker particles to track the free surface, the level set function is employed to "capture" the complex interfacial structure. An iterative process is devised in order to maintain the level set function as the signed distance from the interface.

As a base line case, the two-phase fluid code is implemented for simulating zero gravity capillary oscillations of liquid droplet in order to validate its capability to handle the surface tension effect. Initially deformed shapes of the second spherical harmonics are to oscillate and the simulation results are compared with linearized analytic solutions as well as other numerical calculations. We investigated the viscous effect on oscillatory damping and examined the role of surface tension on oscillatory period. The error analyses relative to the linearized analytic solutions were performed by the successive grid refinement. The code's numerical accuracy was found to be within a few percent.

An impact of a liquid droplet onto solid surface and/or shallow liquid layer results in three regimes: bouncing, spreading, and splashing depending on the relative importance of inertial, viscous, and surface tension effects. Three good examples among various experimental works on a single droplet impact are chosen to be simulated numerically. The direct comparisons are carried out between the experimental and numerical results. Navier slip condition is to be assigned as a velocity boundary condition at the contact surface. It is found that there exists a criterion to distinguish between the splashing and the deposition events in terms of a single impact parameter. A simple dimensional analysis on the fluid motion during the impact and the deformation process is performed and discussed.

4 Professional Activities

The efforts outlined in the previous section of this report were made possible by two grants from AFOSR. A single student, Mr. James H. Hilbing, was supported under the base grant (F49620-94-1-0151). In addition, an AASERT grant (F49620-93-1-0363) was utilized to support Chris A. Spangler, Mark W. Rutz, Michael P. Moses, Ian F. Murray, and Kurt Rump (all U.S. citizens). The following theses were written as a result of these two grants:

Ph.D. Dissertations

Yoon, S. S., "A Fully Nonlinear Model for Atomization of High-Speed Jets", December, 2002.

Kim, B., "Study of Hydrodynamic Instability of Shear Coaxial Injector Flow in a Recessed Region", December, 2002.

A list of journal publications (and submissions) associated with these efforts are provided in the following list. Highlighted items (*) have been attached in the Appendices of this report.

Refereed Journal Publications and Submissions

- Yoon*, S. S. and Heister, S. D., "A Fully Nonlinear Model for Atomization of High-Speed Jets", *Engineering Analysis with Boundary Element*, 2002, to appear.

- Yoon, S. S. and Heister, S. D., "Analytic Solutions for Computing Velocities Induced from Potential Vortex Ring", *AIAA Journal*, 2002, submitted.

- Yoon*, S. S. and Heister, S. D., "Categorizing Linear Theories for Atomizing Jets", *Atomization and Sprays*, 2002, submitted.

- Yoon*, S. S. and Heister, S. D., "Modeling Atomizing Jet due to Boundary Layer Instabilities", *Physics of Fluids*, 2002, submitted.

- Kim*, B and Heister, S. D., "Two-phase Modeling of Hydrodynamic Instabilities in Coaxial Injectors" *Journal of Propulsion and Power*, 2002, submitted.

- Kim*, B. and Heister, S. D., "Three-dimensional Simulations of Flow within the Recessed Region in a Coaxial Injector", In Review, *J. of Propulsion and Power*

A list of the conference papers presented in association with work under these grants is provided in the list below.

Conference Papers and Presentations

- Yoon, S. S. and Heister, S. D., "A Fully Nonlinear Primary Atomization", *15th Annual Conference on Liquid Atomization and Spray Systems*, pp. 36–40, 2002, held in Madison, Wisconsin.

- Yoon, S. S. and Heister, S. D., "A Fully Nonlinear Primary Atomization", *38th AIAA/ASME/SAE/ASEE Joint Propulsion Conference and Exhibit*, AIAA 2002-4179, held in Indianapolis, Indiana.

- Kim, B and Heister, S. D., "Two-phase Modeling and Hydrodynamic Instability Study of Shear Coaxial Injector Flow", *38th AIAA/ASME/SAE/ASEE Joint Propulsion Conference and Exhibit*, AIAA 2002-3696, held in Indianapolis, Indiana.

4.1   Technology Transfer/Coupling Activities

Numerous technology transfers have occurred during the period associated with these grants. At present, Professor Heister is consulting with AFRL officials (Dr. Tom Hawkins and Dr. Ron Spores) on alternate ignition schemes for high-performance monopropellants which have been developed at AFRL. Our laboratories have served as testing facilities for Aerojet, TRW, Lockheed Martin, Pratt & Whitney, and Boeing thereby producing useful interactions with engineers from each of these firms. We have also designed engines/injectors for NASA Dryden Flight Research Center and a small company (KB Sciences) which was run by the late Dr. Ron Humble.
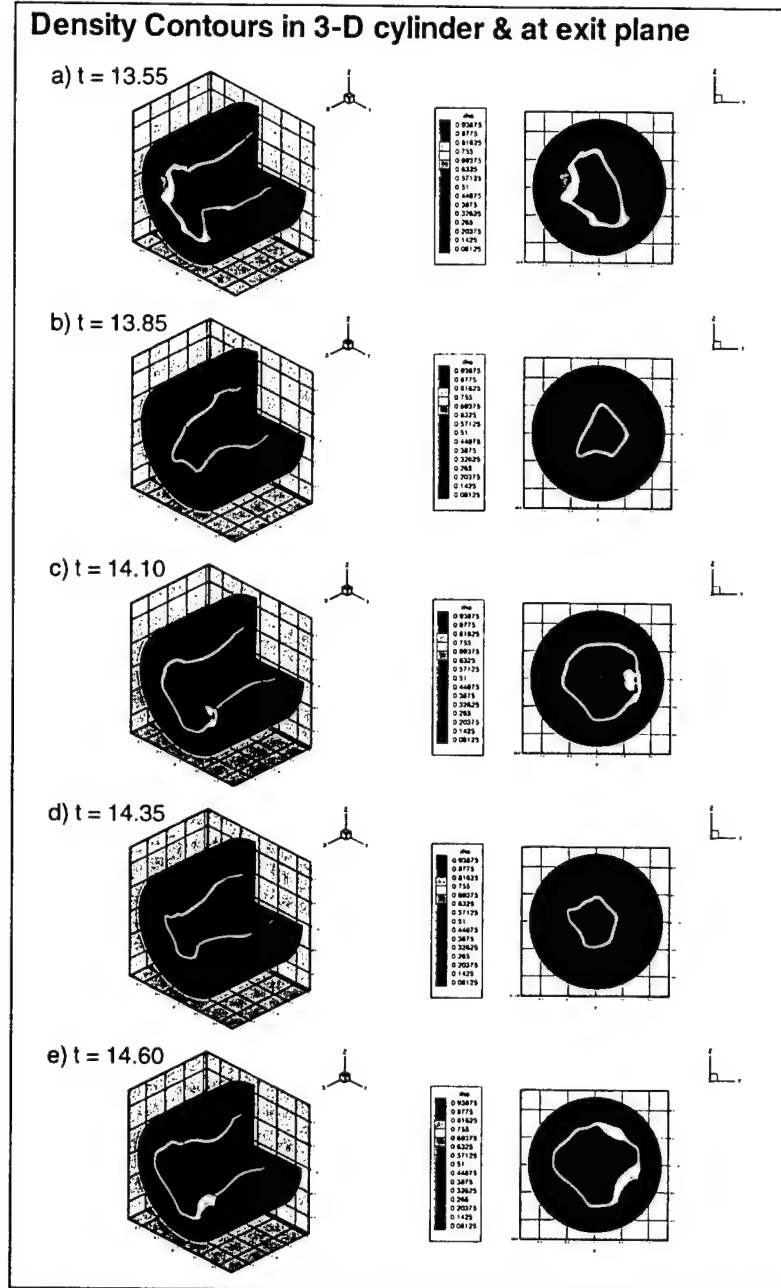
Figure 4: Cutaway view (left column) and orifice exit plane (right column) of density contours showing typical Self-Pulsation: SSME Mainburner injector, $\epsilon = 0.02$, $U_g/U_l = 12$, $L/D = 0.75$, $Re_l = 1.1 \times 10^6$, $Re_g = 9.0 \times 10^5$
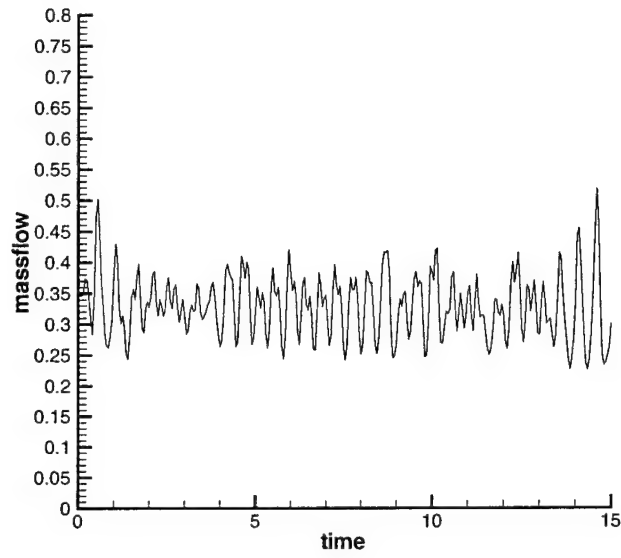
Figure 5: Time history of mass flow at exit plane: $\epsilon = 0.02$, $U_g/U_l = 12$, $L/D = 0.75$, $Re_l = 1.1 \times 10^6$, $Re_g = 9.0 \times 10^5$
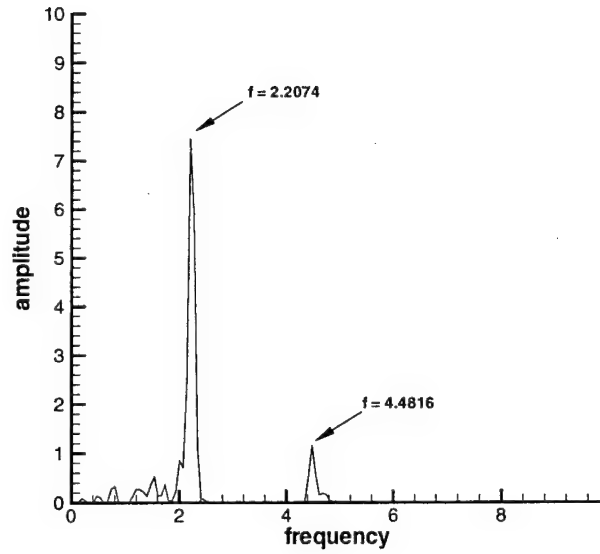
Figure 6: Spectral analysis of mass flow fluctuation: $\epsilon = 0.02$, $U_g/U_l = 12$, $L/D = 0.75$, $Re_l = 1.1 \times 10^6$, $Re_g = 9.0 \times 10^5$

10
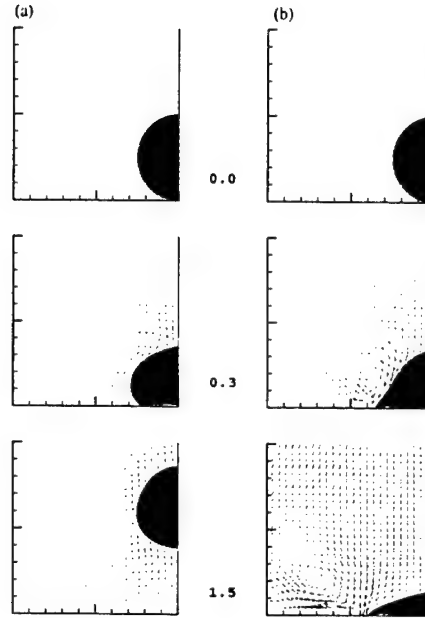
Figure 7: Droplet impact — deposition: Droplet impingement with low impact momentum experiences either (a)rebound or (b)spreading depending on the combination of Reynolds and Weber numbers. The impact conditions are Re=100, 200×200 grids in dimensions 4×4 (a) We=1,Δt=.0005; (b) We=100,Δt=.0001. Gas/liquid ratios are $\rho' = 10^{-3}$; $\mu' = 10^{-2}$. Gravitational effect is ignored.
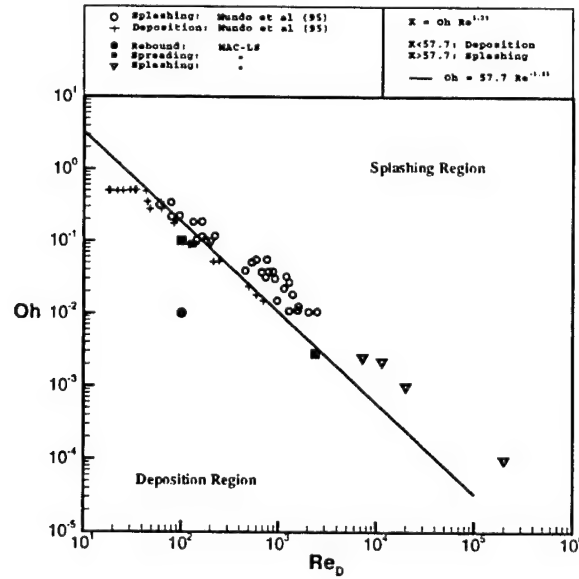
Figure 8: Limits for deposition/splashing of droplet
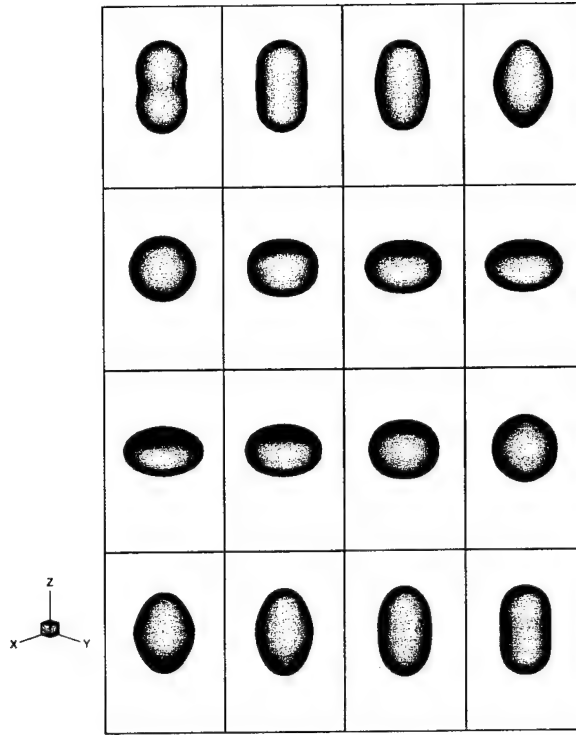
Figure 9: Capillary oscillation of liquid droplet: Released from a static deformation of second (oblate)-spherical harmonic with $\eta = 0.5$, a zero gravity liquid drop is oscillating due to the surface tension. This picture spans one period of oscillation. Re $= 100$; We $= 1$; 200×100 grids; $\rho_g/\rho_\ell = \mu_g/\mu_\ell = 10^{-3}$.

References

[1] J. Ponstein. Instability of rotating cylindrical jets. *Applied Scientific Research*, 8(6):425–456, 1959.

[2] J. W. Hoyt and J. J. Taylor. Waves on water jets. *Journal of Fluid Mechanics*, 83:119–127, 1977.

[3] P. K. Wu, L. K. Tseng, and G. M. Faeth. Primary breakup in gas/liquid mixing layers for turbulent liquids. *Atomization and Sprays*, 2:295–317, 1992.

[4] J. W. Hoyt and J. J. Taylor. Turbulence structure in a water jet discharging in air. *Physics of Fluids*, 20(10):S253–s257, 1977.

[5] J. W. Hoyt and J. J. Taylor. Effect of nozzle boundary layer on water jets discharging in air. In *Jets and Cavities–International Symposium*, pages 93–100. ASME, 1985. held in Miami Beach, Florida, Nov. 17–22.

[6] W. S. Rayleigh. On the instability of jets. *Proc. London Math. Soc.*, 10(4), 1878.

[7] M. C. Yuen. Non-linear capillary instability of a liquid jet. *Journal of Fluid Mechanics*, 33(1):151–163, 1968.

[8] E. F. Goedde and M. C. Yuen. Experiments on liquid jet instability. *Journal of Fluid Mechanics*, 40(3):495–514, 1970.

[9] C. Brennen. Cavity surface wave patterns and general appearance. *Journal of Fluid Mechanics*, 44(1):33–49, 1970.

[10] J. H. Rupe. On the dynamic characteristics of free liquid jets and a partial correlation with orifice geometry. *NASA JPL Technical Report*, 32-207, 1962.

[11] J. J. Hutt and M. Rocker. High-frequency injector-coupled combustion. *Liquid Rocket Engine Combustion Instability*, 169:345–356, 1995.

[12] W. Mayer and G. Krulle. Rocket engine coaxial injector liquid/gas interface flow phenomena. *Journal of Propulsion and Power*, 11(3):513–518, 1995.

[13] W. Mayer and H. Tamura. Flow visualization of supercritical propellant injection in a firing lox/gh2 rocket engines. *AIAA 95-2433*, 1995.

[14] W. Mayer, A. Schik, and M. Schaffler. Injection and mixing processing in high-pressure liquid oxygen/gaseous hydrogen rocket combustors. *Journal of Propulsion and Power*, 16(5):82300828, 2000.

[15] T. Kaltz, M. Milicic, and M. Glogowski. Shear coaxial injector spray characterization. *AIAA 93-2190*, 1993.

[16] M. Glogowski and M. M. Micci. Shear coaxial injector spray characterization near the lox post tip region. *AIAA 95-2552*, 1995.

[17] V. G. Bazarov and Vigor Yang. Liquid-propellant rocket engine injectors dynamics. *Journal of Propulsion and Power*, 14(5):797–806, 1998.

[18] V. G. Bazarov and L.A. Lyulka. Nonlinear interactions in liquid propellant rocket engine injectors. *AIAA 98-4039*, 1998.

[19] V. G. Bazarov. Self-pulsations in coaxial injectors with central swirl stage. *AIAA 95-2358*, 1995.

[20] B. Kim. *Study of Hydrodynamic Instability of Shear Coaxial Injector Flow in a Recessed Region*. PhD thesis, Purdue University, 2002.

[21] B. Kim and S. D. Heister. Two-phase modeling of hydrodynamic instabilities in coaxial injectors. *Journal of Propulsion and Power*. submitted.

[22] J. Smith, D. Klimenko, W. Claus, and W. Mayer. Supercritical lox/hydrogen rocket combustion investigations using optical diagnostics. *AIAA 2002-4033*, 2002.

5 Appendix A - Boundary Element Modeling

Yoon*, S. S. and Heister, S. D., "A Fully Nonlinear Model for Atomization of High-Speed Jets".

A Fully Nonlinear Model for Atomization of High-Speed Jets

Sam S. Yoon * and Stephen D. Heister[†]

* Graduate Research Assistant, [†] Professor, School of Aeronautics and Astronautics, Purdue University, W. Lafayette, IN

ABSTRACT

A nonlinear model has been developed to assess the time evolution of an axisymmetric liquid jet using a boundary-element method. Vorticity transported from the boundary layer in the orifice passage to the free surface is modeled using a potential ring vortex placed at the orifice exit plane. The vortex strength is uniquely determined from the Kutta condition and information regarding the boundary layer thickness at the orifice exit plane. It is shown that primary breakup can occur even in the absence of the gas phase. Using a secondary stability analysis after Ponstein [1], the size of the droplets is estimated based on the size of the ring-type structures shed from the periphery of the jet. Computed droplet sizes are in reasonable agreement with experimental data, although turbulence effects obscure some comparisons.

INTRODUCTION

The atomization of a liquid jet is one of the most fundamental problems of two-phase flow and has received much attention due to the large number of practical applications. Since the formation of droplets is ultimately dictated by a balance of capillary and inertial forces, numerical methods that provide high resolution of these forces perform best in simulating these flows. The capillary force depends on local surface curvature, which is a function of surface shape with dependence on second derivatives of local surface coordinates. Resolving the curvature accurately is of paramount importance in these problems. For these reasons, the Boundary-Element Method (BEM) is uniquely suited for atomization modeling in that the optimal placement of nodes on the gas/liquid interface provides a mean for maximizing accuracy of surface curvature calculations.

BEM techniques have been applied to a wide variety of free surface/atomization problems including liquid jets [2, 3, 4, 5, 6, 7, 8, 9, 10], droplets [11, 12] and electrostatic atomization [13, 14]. Along with the difficulty in computing surface curvature, the inherent nonlinearity of the free-surface condition has been addressed by many researchers. Several proven techniques available at the present time. In the liquid jets field, high-resolution and high fidelity BEM solutions for low-speed flows are now available and applicable to problems in chemical engineering and inkjet printing.

Despite these advances, the atomization process increases in complexity with increasing jet speed. For this reason, the modeling of high-speed jets which produce small droplets of interest in many application, are still an area requiring significant efforts. Prior research [3, 15, 16] has indicated the importance of the boundary layer structure at the orifice exit plane in mapping instabilities just downstream of the injection point, as shown in Fig. 1. The present study focuses on this issue via an axisymmetric simulation that properly accounts for the presence of, and vorticity within, this boundary layer. The following section provides a description of the model, followed by convergence studies and comparisons with experimental data.

MODELING

The model is based on unsteady axisymmetric potential flow of a liquid exiting a round orifice in the absence of a gas-phase medium. A ring vortex is employed to simulate viscous effects associated with vorticity in the boundary layer formed in the orifice passage. Carefully controlled experiments have shown a nearly axisymmetric structure during the early stages of the free-surface instability. Fig. 2 provides a schematic representation of the geometry and nomenclature. The size of the Rankine vortex [17] is defined as R_c, as will be discussed in detail in a later section. A vortex ring of strength Γ_v and overall radius $\bar{r}$ is assumed to lie at the orifice exit plane. A computational domain is represented by a simple cylindrical column of length z_l, and a hemispherical cap is selected to initialize the calculation. Constant nodal spacing, Δs, is employed

along this domain, and nodes are added as the jet issues forward from the orifice. Fig. 3 compares the actual flow condition with the current superposition modeling. Because the concentrated vortices at the filament vortex-ring are transported to the free-surface, the jet surface is unstable. We choose the liquid density, ρ, jet average exit velocity, U, and orifice radius, a as characteristic dimensions in the problem.

The formulation of the BEM starts with the integral representation of the solution of Laplace's equation, $\nabla^2 \phi = 0$, with ϕ being the velocity potential. Following Liggett and Liu [18], the integral form for this relation is given by:

$$\alpha\phi(\vec{r}_i) + \int_\Omega \left[\phi\frac{\partial G}{\partial\hat{n}} - qG\right] d\Omega = 0 \tag{1}$$

where $\phi(\vec{r}_i)$ is the value of the potential at a point $\vec{r}_i$, Ω is the boundary of the 3D domain, and G is the free space Green's function of Laplace's equation. If $d\Omega$ is a 3D surface element, ds is a 2D surface with $d\Omega = rd\theta ds$. Then the governing Eqn. (1) can be written as:

$$\alpha\phi(\vec{r}_i) + \int_s \left[\phi D_{kern} - qS_{kern}\right] ds = 0 \tag{2}$$

where the source and doublet kernels are:

$$S_{kern} = \frac{4rK(m)}{\sqrt{\hat{a}}} \qquad D_{kern} = -\frac{1}{2\sqrt{\hat{a}}}\left[\hat{n}_r K(m) + \frac{E(m)}{c}[d\hat{n}_r + 2r\hat{n}_z(z - z_i)]\right] \tag{3}$$

and the auxilliary quantities, $\hat{a}, c, d$ are defined:

$$\hat{a} = (r_i + r)^2 + (z - z_i)^2 \qquad c = (r - r_i)(z - z_i)^2 \qquad d = r^2 - r_i^2 - (z - z_i)^2 \tag{4}$$

where $m = 4rr_i/\hat{a}$. Here, $K(m)$ and $E(m)$ are the elliptical integral [19] of the first and second kind respectively, and $\hat{n}_{z,r}$ is the component of the normal vector in z and r direction. We utilize linear elements for the velocity potential,

$$\phi = \phi_j\left(\frac{s_{j+1} - s}{s_{j+1} - s_j}\right) + \phi_{j+1}\left(\frac{s - s_j}{s_{j+1} - s_j}\right) \tag{5}$$

with an analogous form for the normal velocity, $\partial\phi/\partial n = q$. Substitution of Eqn. (5) into Eqn. (2) yields the following $N_{node} \times N_{node}$ matrix:

$$[\alpha I + D][\phi] = [S][q] \tag{6}$$

where α arises from singular contributions to the doublet terms as the integral passes through the base point z_j, r_j.

Because the matrix system can be quite large (i.e. $N_{node} > 1000$), the matrix inversion step is parallelized to incorporate multiple processors. Since a 4th-order Runge-Kutta time integration scheme is employed, the calculation requires solving the large matrix system four times at every time step. In addition, the size of the computational domain increases in time, which yields a larger matrix system at every time step [20, 21]. The Scalable Linear Algebra Package [22] (SCALAPACK) is implemented into the current code as a parallel solver. Under this parallelization, the code can utilize up to N_p number of processor. We have used $N_p = 6$ because little variation is observed for the computational efficiency after $N_p = 6$ with the current 104 node LINUX-Cluster networking system. Here, a tradeoff exists between individual node speed (we use 1.2 GHz Athalon chips) and nodal communication time. Because the nodes are quite fast in performing the required calculations, communication time tends to dominate for $N_p > 6$.

A typical $[A][X] = [B]$ non-parallel solver based on LU-Decomposition is available in Numerical Recipes [23]. When the matrix $[A]$ and vector $[B]$ are given, the matrix $[X]$ can be obtained using the LU-Decomposition. The parallel $[A][X] = [B]$ solver SCALAPACK is also based on the LU-Decomposition algorithm. However, one additional step is required for SCALAPACK: the partition of $[A]$, $[X]$, and $[B]$ into the N_p process grid. Unfortunately, SCALAPACK does not perform the matrix partition autonomously. Thus, we have developed the algorithm for the grid-partition. Considering $N_p = 6$, the physical matrix $[A]$ is transformed into the 2×3 process grid, as shown in Fig. 4. Parameters that define this transformation are MB $\times$ NB for the size of the submatrix, and NPROW $\times$ NPCOL for the number of processors (see Fig. 4). The particular parallel solver used for our calculation, called 'pdgesv' [22], can handle the fullly dense matrix, $[A]$. If the matrix $[A]$ is tridiagonal, and 'pddtsv' is used for the efficient calculation. In addition, 'pddbsv' solves a general band system $[A][X] = [b]$. It should be noted that the answer $[X]$ is splitt into 'row' processors. As shown in

Fig. 5, we have combined the answer $[X]$ in the (0,0) processor and broadcast $[X]$ to other processors using the MPI routine.

We have constructed the sample calculation; Laplace equation with the Dirichlet boundary conditions at the side walls and thus $[A]$ is a banded system and 'pdgesv' is used. The sample code can be downloaded at http://roger.ecn.purdue.edu/~ yoons/SCAL.tar.gz

Flow physics at the smaller length scale can be captured using a finer grid under the parallelization. The length scale of our interest is scaled by the momentum thickness, δ_2. A complete calculation takes about one to two weeks: this is long enough real time to obtain all the information about the droplet characteristics of our particular interest.

Superposition

Contributions from the vortex ring can be obtained through the principle of superposition for potential flow. Since Laplace's governing equation is linear, we may superpose the bulk potential flow with the flow due to the vortex ring (i.e. ϕ_v or Ψ_v),

$$\phi_t = \phi + \phi_v \qquad \Psi_t = \Psi + \Psi_v \tag{7}$$

where ϕ and Psi represent the velocity poential and the streamfunction, respectively. Here $(\ )_t$ denotes the 'total' solution of the jet flow. The flow of the vortex ring can be obtained either by applying the Cauchy-Riemann condition to the stream function [24], or by direct evaluation using Biot-Savart law [25]. Traditionally [24, 26, 17], the velocities induced from this flow are computed from the stream function, Ψ:

$$\Psi(z,r) = \frac{\Gamma_v}{2\pi}\sqrt{r_i r}\left[\left(\frac{2}{\sqrt{m}} - \sqrt{m}\right)K(m) - \frac{2}{\sqrt{m}}E(m)\right] \tag{8}$$

where $m = m(r,z)$. Here, Γ_v is the strength of the vortex and $K(m)$ and $E(m)$ are the complete elliptic integrals of the first and second kind, respectively. The velocities can be determined in a standard fashion by differentiating Ψ,

$$u_v = \frac{1}{r}\frac{\partial \Psi}{\partial r} \qquad v_v = -\frac{1}{r}\frac{\partial \Psi}{\partial z} \tag{9}$$

Alternatively, the Biot-Savart law [27, 28, 25] can be evaluated directly for the filament vortex-ring solution,

$$\vec{u}_v = \frac{\Gamma}{4\pi}\int_0^{2\pi}\frac{\vec{dl}\times(\vec{r}-\vec{r}_i)}{|\vec{r}-\vec{r}_i|^3}d\theta_i \tag{10}$$

where $\vec{dl}$ is the path enclosed by the vortex ring. The entire explicit solution of the filament vortex-ring has recently been developed [29].

Free Surface Boundary Conditions

The unsteady Bernoulli equation provides the boundary condition along a free surface [30]. This condition provides a connection between the inertial, hydrostatic, and capillary forces at the interface. Because the surface curvature, κ, depends nonlinearly on the surface shape, the overall expression is nonlinear. Using the nondimensionalization described previously, the appropriate dimensionless form of the Bernoulli equation is given by:

$$\frac{\partial \phi_t}{\partial t} + \frac{1}{2}|\nabla\phi_t|^2 + P_g + \frac{\kappa}{We} - \frac{Bo}{We}z = 0 \tag{11}$$

where P_g is the dimensionless gas-phase pressure (assumed to be zero in the present studies), and We and Bo are the Weber and Bond numbers,

$$We = \frac{\rho U^2 a}{\sigma} \qquad Bo = \frac{\rho g a^2}{\sigma} \tag{12}$$

where σ is the surface tension and g is the gravitational constant. As shown in Fig. 2, the vortex ring is located at the nozzle exit in order to model the vorticity present in the actual flow. While the singularity arises at the vortex ring, the solution at the vortex-ring is also singular and that of the computational nodes near the vortex-ring is not physical. In an effort to overcome the problem, we have separated the

17

governing equation for potential flow from the total solution; the time derivative of the vortex-ring is zero (i.e. $\partial \phi_v / \partial t = 0$) since its strength (or circulation) is assumed constant and its location is fixed. Thus the time derivative of the Eqn. (7) is given by:

$$\frac{\partial \phi_t}{\partial t} = \frac{\partial \phi}{\partial t} \tag{13}$$

Thus Eqn. (11) becomes:

$$\frac{\partial \phi}{\partial t} + \frac{1}{2}|\nabla \phi_t|^2 + P_g + \frac{\kappa}{We} - \frac{Bo}{We}z = 0 \tag{14}$$

The transformation from the Eulerian (i.e. $\partial / \partial t$) to the Lagrangian (i.e. D/Dt) is required as the computational nodes move respect to time, t:

$$\frac{D\phi}{Dt} = \frac{\partial \phi}{\partial t} + \nabla \phi_t \cdot \nabla \phi \tag{15}$$

Combining Eqns. (14) and (15) yields:

$$\frac{D\phi}{Dt} = \nabla \phi_t \cdot \nabla \phi - \frac{1}{2}|\nabla \phi_t|^2 - P_g - \frac{\kappa}{We} + \frac{Bo}{We}z \tag{16}$$

Substitution of Eqn. (7) into Eqn. (16) (for $\nabla \phi$ term) yields:

$$
\begin{aligned}
\frac{D\phi}{Dt} &= \nabla \phi_t \cdot \nabla(\phi_t - \phi_v) - \frac{1}{2}|\nabla \phi_t|^2 - P_g - \frac{\kappa}{We} + \frac{Bo}{We}z \\
&= \nabla \phi_t \cdot \nabla \phi_t - \nabla \phi_t \cdot \nabla \phi_v - \frac{1}{2}|\nabla \phi_t|^2 - P_g - \frac{\kappa}{We} + \frac{Bo}{We}z \\
&= \frac{1}{2}|\nabla \phi_t|^2 - \nabla \phi_t \cdot \nabla \phi_v - P_g - \frac{\kappa}{We} + \frac{Bo}{We}z
\end{aligned}
\tag{17}
$$

Since differential operator (∇) is a linear function, superposition theory holds for the velocity as well:

$$u_t = u + u_v \qquad v_t = v + v_v \tag{18}$$

Combining Eqns. (17) and (18), we obtain more explicit Bernoulli relation for ϕ:

$$\frac{D\phi}{Dt} = \frac{1}{2}|u_t|^2 - \vec{u}_t \cdot \vec{u}_v - \frac{\kappa}{We} - P_g + \frac{Bo}{We}z \tag{19}$$

Now that we have separated the ϕ from the general solution ϕ_t, the entire time marching of the numerical algorithm is related to ϕ only. The effect of the vortex ring comes into play only in Eqn. (18). Bernoulli's Eqn. (19) is the 'nonlinear' boundary condition for the Laplace equation and it is marched in time using a 4th order Runge-Kutta time integration.

The curvature of the highly-distorted surface is determined with 4th-order accuracy [31, 32]. We have used the curvature definition from Smirnov [33]:

$$\kappa = \frac{1}{r}\left(\frac{\partial z}{\partial s}\right) + \left(\frac{\partial r}{\partial s}\right)\left(\frac{\partial^2 z}{\partial s^2}\right) - \left(\frac{\partial^2 r}{\partial s^2}\right)\left(\frac{\partial z}{\partial s}\right) \tag{20}$$

The derivatives are evaluated using centeral differencing with the exception of the ends of the domain where forward or backward derivatives are applied [32].

The location of nodes on the free surface (i.e. z and r) is advanced by integrating the respective velocity components in time:

$$\frac{Dz}{Dt} = \frac{\partial \phi}{\partial z} \qquad\qquad \frac{Dr}{Dt} = \frac{\partial \phi}{\partial r} \tag{21}$$

where

$$\frac{\partial \phi}{\partial z} = \frac{\partial \phi}{\partial s}\cos\beta - q\sin\beta \qquad\qquad \frac{\partial \phi}{\partial r} = \frac{\partial \phi}{\partial s}\sin\beta + q\cos\beta \tag{22}$$

where $q = \partial \phi / \partial n$ is the normal derivative of phi. The surface slope, β, is assumed to be given by the slope of the parabola at the middle node [31].

Smoothing

Nodes are repositioned along the distorted surface using cubic splines [34], and nodes can be added (due to fluid exiting the nozzle) or removed (due to atomization events) without user intervention. The current 'high-speed' atomization simulation is more susceptible to numerical instability than the low-speed atomization (i.e. varicose breakup simulation with smooth surface) due to complex surface shape. In addition, the 'necking' region where a droplet is pinched-off experiences a relatively high velocity (i.e. node velocities reache $2 \sim 7$ times that of the jet speed) and therefore 'node-crossing' or 'not-simply-connected domain' sometimes occurs. Thus numerical smoothing is crucial to prevent the numerical instability [35].

Following the definition for filter function and its transfer function by Spyropoulos and Blaisdell [36]:

$$\hat{f}_j = \sum_{n=0}^{N-1} a_n \frac{f_{j-n} + f_{j+n}}{2} \qquad\qquad G_k = \sum_{n=0}^{N-1} a_n \cos\left(\frac{2\pi k n}{N}\right) \tag{23}$$

where $\hat{f}$ is the filtered function, f is the function prior to the filtering, a_n is the coefficient listed in Table 1 for $N = 2 - -4$, N is the number of points used, G_k is the filter transfer function, and k is the wavenumber. Table 1 provides the coefficients for the various explicit filter functions developed by researchers [37, 11, 35, 38, 36]. In Fig. 6, the transfer filter function, G_k, is plotted as a function of the wavenumber, $2k/N$. The main purpose of using filter is to suppress the relatively large wavenumbers (or small wavelengths). The filters by Hilbing et al [37] and Lundgren and Mansour are not suitable because they do not suppress large wavenumbers sufficiently. The filter by Spyropoulos and Blaisdell [36] is not suitable either as it amplifies some wavenumbers. Since the 3-pt trapezoid filter damps out the small wavenumbers more than other comparable filters, it may be too diffusive for the current use. While we hope to damp out the large wavenumbers and leave the small wavenumbers as they are, we have chosen the filter function by Longuet-Higgins and Cokelet [35]; this filter is designed to eliminate the odd-even mode in the function which contains the highest frequency, known as the Nyquist Rate [39].

Table 1: Coefficients for the various explicit filter functions

	N	a_o	a_1	a_2	a_3
3-pt Trapezoid	2	0.5	0.5	—	—
5-pt Hilbing et al. [37]	3	0.9625	0.05	-0.0125	—
5-pt Lundgren and Mansour [11]	3	0.94	0.08	-0.02	—
5-pt Longuet-Higgin and Cokelet [35]	3	0.625	0.5	-0.125	—
7-pt Lele [38]	4	0.5	0.5625	—	-0.0625
7-pt Spyropoulos and Blaisdell [36]	4	0.5	0.6744132	—	-0.1744132

Vorticity Centroid

The centroid of vorticity of the viscous flow is regarded as the center of the vortex-ring. The definition of the centroid of the vorticity, weighted in the radial direction is given by:

$$\bar{r} = \frac{\int_{r=0}^{r=1} r\omega\, dr}{\int_{r=0}^{r=1} \omega\, dr} \tag{24}$$

and the vorticity, ω, is defined as:

$$\omega = \frac{\partial v}{\partial z} - \frac{\partial u}{\partial r} \tag{25}$$

where u and v are the velocities in the axial and radial direction, respectively. Assuming $\partial v/\partial z \approx 0$, i.e. parallel flow at the orifice exit plane, the centroid can be written as:

$$\bar{r} = \frac{\int_{u(r=0)}^{u(r=1)} r\, du}{\int_{u(r=0)}^{u(r=1)} du} \tag{26}$$

19

Substituting the definition of the displacement thickness, δ_1, [40] into Eqn. (26) and applying integration by parts gives the following result:

$$\bar{r} = 1 - \delta_1 \tag{27}$$

where

$$\delta_1 = \int_0^1 \left(1 - \frac{u(r)}{U}\right) dr \tag{28}$$

δ_1 can be approximated using a Navier-Stokes solution of the internal flow, or appropriate analytical methods such as Blasius solution [40] for a flat-plate or the Thwaites' [41] equation for a converging/diverging nozzle.

The vortex strength Γ_v is defined as the circulation around any path enclosing the vortex-ring, namely:

$$\Gamma_v = \oint \vec{u} \cdot d\vec{I} \tag{29}$$

where $\vec{u}$ is the internal flow velocity of the injector orifice and $\vec{I}$ is the integration path. The integration is taken in a counterclockwise direction around the path. Assuming $\partial u/\partial z = 0$ and a no-slip boundary condition at the wall, the surface integral in Eqn. (29) can be written as follows for the path we have chosen:

$$\Gamma_v = \Delta z \tag{30}$$

where Δz is the length scale which is comparable to the most dominant wavelength, λ. Γ_v is always positive and will induce counterclockwise motion (this is based on the upper half of the flow going from left to right). Eqns. (27) and (30) uniquely determine the location and strength of the vortex from first principles. No additional calibration constants are used in the formulation.

It is possible to set $\Delta z = \lambda$, predicted by Brennen's result [42], since the circulation causes the axisymmetrically disturbed wavelength observed at the nozzle exit. The λ observed in Hoyt and Taylor's case [16] is a function of the momentum thickness δ_2, scaled by the parameter $\gamma = 0.175$. Presuming a high contraction ratio of the nozzle reduces the turbulence fluctuation, Hoyt and Taylor [16] assumed a laminarized flow over a flat plat and therefore they utilized the Blasius [40] solution to approximate the momentum thickness, namely:

$$\Gamma_v = \lambda = \left(\frac{2\pi}{0.175}\right) \delta_2 \tag{31}$$

Another possible choice for the circulation approximation is to use the Kutta-condition [30] from the potential flow theory. It is known that the velocity of the potential flow at a sharp corner is infinite and therefore it is not physically possible. One remedial treatment is that a stagnation point is forced at the sharp corner, known as the 'Kutta-condition'. While the gradient of the inflow velocity of the injector orifice is zero due to the nature of potential flow, one may adjust the strength of vortex-ring Γ_v to be such that the sum of potential velocity and vortex induced velocity in the axial direction to be zero at the sharp corner; this linear relation was applied and solved to find the Γ_v. The closer the vortex-ring is to the wall (i.e. the higher $\bar{r}$), the stronger the vortex induced velocity will be. In order to satisfy the stagnant velocity at the sharp corner with constant potential inflow velocity of 1.0, Γ_v must decrease as $\bar{r}$ increases. It is shown in Fig. 7 that the strength of the vortex-ring condition decreases as $\bar{r}$ increases. One may utilize the cubically interpolated equation of the Kutta-condition in Fig. 7.

The third possible choice is to adjust the strength to be such that the vorticity integral over the radial direction of the real flow matches that of the vortex-ring:

$$\int_{r=0}^{r=1} \omega \, dr = \int_{r=0}^{r=1} \omega_v \, dr \tag{32}$$

It is known that ω_v is infinite at the ring and zero everywhere else. However, the change in the induced axial-velocity over the radial direction is finite (i.e. $\partial u_v/\partial r$). Thus we again assume a parallel flow for the real flow (i.e. $\partial v/\partial z = 0$). Then Eqn. (32) becomes:

$$\int_{u(r=0)}^{u(r=1)} du = \int_{u_v(r=0)}^{u_v(r=1)} du_v \tag{33}$$

This is essentially matching Δu_v to be U and will yield the positive Γ_v. The quadratic interpolation of this approximation is shown in Fig. 7.

20

The variation of Γ_v as a function of the centroid of the vorticity $\bar{r}$ is presented in Fig. 7. It is seen that the Γ_v used is lower than that of the Kutta-condition. The ratio of their Γ_v value varies from 2.8 to 1.0 as a function of $\bar{r}$. It is observed that their difference in Γ_v decreases as $\bar{r}$ increases and eventually yields difference of approximately 3% from one to the other at about $\bar{r} = 0.99$. The reason for such a behavior is that the model accuracy improves when the boundary layer is 'thin'.

In summary, any choice of the three methods is applicable for the circulation approximation not only because Γ_v differs little at high $\bar{r}$ but also because Γ_v by itself does not change the droplet size significantly. However, one needs to use the same approximation consistently when parametric studies are performed. We have used the approximation using Brennen's theory for the case presented in the result section.

Post Processing Formulation for Droplets

The addition of the Biot-Savart Law to the inviscid jet of the BEM formulation is expected to cause instability at the free surface that eventually forms a series of toroidal ligaments pinched off from the main body of the jet. Here the formulations for the cross-sectional area, centroids of the area, volume, and the velocity of the droplets are developed.

Using Gauss's divergence theorem, we have transformed the surface integral to a line or contour integral in order to compute the cross-sectional area of a pinched-off ring:

$$A = \frac{1}{2}\left[\int_C r\,dz + \int_C z\,dr\right] \tag{34}$$

which was discretized using the trapezoid Rule,

$$A = \frac{1}{4}\sum_{j=1}^{N}\left[(r_j + r_{j+1})(z_{j+1} - z_j) - (z_j + z_{j+1})(r_{j+1} - r_j)\right] \tag{35}$$

where N is the last (or maximum) *node* that closes the loop. The centroids of the cross-sectional area are defined as:

$$z_c = \frac{\int_S z\,dA}{A} \qquad\qquad r_c = \frac{\int_S r\,dA}{A} \tag{36}$$

This is also discretized using the trapezoid Rule. Similar to the previous approach, we have found the cross-sectional area can be expressed as:

$$z_c = \frac{1}{12A}\sum_{j=1}^{N}\left[(r_j + r_{j+1})(z_{j+1}^2 - z_j^2) - (z_j + z_{j+1})^2(r_{j+1} - r_j)\right] \tag{37}$$

$$r_c = \frac{1}{12A}\sum_{j=1}^{N}\left[(r_j + r_{j+1})^2(z_{j+1} - z_j) - (z_j + z_{j+1})(r_{j+1}^2 - r_j^2)\right] \tag{38}$$

The theorem of Pappus-Guldinus [43] relates a volume of revolution to its generating cross-sectional area:

$$V = 2\pi A r_c \tag{39}$$

For the velocities of a droplet, we have weighted both velocities u_D (axial) and v_D (radial) in the radial direction. The formulation is as follows:

$$u_D = \frac{\sum_{j=1}^{N}\left(\frac{\partial\phi}{\partial z}\right)_j r_j}{r_c\,N} \qquad\qquad v_D = \frac{\sum_{j=1}^{N}\left(\frac{\partial\phi}{\partial r}\right)_j r_j}{r_c\,N} \tag{40}$$

Modeling Secondary Instability

While the current model is based on an axisymmetric formulation, actual primary atomization is a 3-dimensional phenomenon (see Fig. 8-(a)). The model result of pinch-off, as shown in Fig. 8-(b), is not a droplet but a vortex-ring with a significant amount of circulation around the ring surface. The circulation around the ring surface is large enough to cause instability in the circumferential direction. In reality, this

is the secondary instability which occurs before the vortex-ring pinch-off. The current model assumes that droplets are formed from a secondary instability on annular ligaments shed from the periphery of the jet. This amounts to a decoupling of primary and secondary instability which permits the axisymmetric analysis of the jet itself.

Ponstein[1] investigated the linear stability of a liquid column with circulation Γ_r and radius a_r. Ponstein's result is utilized to predict the dominant wavelength k in the circumferential direction:

$$\omega^2 = \left[\frac{1 - k^2}{We_r} + \left(\frac{\Gamma_r}{2\pi} \right)^2 \right] k \frac{I_1(k)}{I_o(k)} \tag{41}$$

where $We_r = \rho U^2 a_r / \sigma$. Note that the ring radius, a_r, is the non-dimensional variable. This expression is solved to determine the $k = k_{max}$ value attributed to the maximum growth rate, ω for a given ring geometry and circulation. Since Ponstein's analysis was conducted for a liquid column, we assume that the thickness of the ring-shaped ligaments is much less than the nozzle/jet radius (i.e. $a_r << a$). This assumption is confirmed from ligament sizes produced in the calculations. Fig. 9 illustrates how Ponstein's equation is applied to the vortex-ring (annular ligament) with circulation Γ_r.

At the event of vortex-ring pinch-off, all information about the ring is collected (i.e. volume, centroids, etc). Thus we can calculate the circumferential length of the ring, $l = 2\pi r_c$. The most dominant wavelength ($\lambda = 2\pi/k_{max}$) which corresponds to the maximum growth rate is known from Ponstein's Eqn (41). Thus the number of droplets per ring can be estimated (i.e. $N_D = l/\lambda$). The volume of the ring (i.e. V) is known and that of a droplet can be approximated using the definition of a sphere volume, $V_D = V/N_D = \frac{4}{3}\pi \left(\frac{D}{2} \right)^3$. Thus a droplet diameter (D) can be estimated.

RESULTS

Grid Convergence Study

Hoyt and Taylor's case is used for the grid convergence check (i.e. $We = 19057$, $\bar{r} = 0.99$, and $\Gamma_v = 0.139$). Δs is the grid spacing for the BEM node. While Hilbing [32] mentioned that $\Delta s = 0.300$ is fine enough to resolve the low speed "Rayleigh breakup" where waves are of length comparable to the orifice diameter, a much finer grid resolution is required for high speed atomization where the wavelengths are comparable to the boundary layer thickness at the orifice exit. For this reason, the grid resolution for the present studies taxes the current computational capabilities of even advanced Linux-based compute clusters. In Fig. 10, it is shown that the axial location for the first ring pinch-off is reasonably insensitive to mesh spacing for $\Delta s \lesssim 0.030$. However, grid function convergence studies indicate that a smaller mesh spacing is required for the accurate prediction of the droplet characteristics in the atomization regime. About $1000 \sim 3000$ droplets were collected for each run for statistically reliable data and results for drop statistics are shown in Table 2. The Sauter Mean Diameter, SMD, (drop whose diameter replicates the average surface area of drops in the population) is the most frequent measure used in the atomization field. Table 2 shows that the $\overline{N}_D$ per ring, its Standard Deviation, and SMD are converged to a reasonable accuracy at $\Delta s = 0.012$. Thus we have used $\Delta s = 0.016$. In addition, the standard deviation of $\overline{N}_D/ring$ does not change much after $\Delta s \lesssim 0.016$. Similarly, the time-averaged droplet velocities (i.e. $\bar{u}_D$ and $\bar{v}_D$) do not change much either for this mesh spacing. This result also validates the pinch criteria employed for a ligament breakup: a pinch-off is assumed when the distance between binary nodes is less than a certain tolerance, ε. The range of the tolerance is $20 \sim 70\%$ of the mesh spacing. The ligament size is also insensitive to the range of the pinch-off criteria.

It is uncertain when to stop the simulation since the jet can grow indefinitely depending on injection conditions. For the simulations conducted to date, the time required for the first pinching event is typically around $t \approx 1.7$. We found that collecting about 300 to 400 rings provides stastically reliable data. This would give roughly 1000 droplets. Thus we typically stop our calculation at about $t \approx 5.0$. Table 3 shows that the solution is insensitive to what for $t > 4.0$.

Effect of Rankine Vortex Size and Initial Jet Length

In Fig. 1, vortices induce motion/instability near to the nozzle exit (i.e. axisymmetrically disturbed waves) and eventually cause the jet to break up into turbulent flow. However, the flow at the nozzle exit is

Table 2: Grid convergence test

Δs	$\overline{N_D}/ring$	Stnd. Dev.	SMD/d	$\overline{u}_D$	$\overline{v}_D$	$\overline{U}_D$
0.050	10.07	4.68	0.0995	0.608	0.442	0.752
0.040	10.87	8.71	0.0962	0.689	0.430	0.812
0.030	14.20	11.33	0.0841	0.790	0.479	0.924
0.020	12.46	8.46	0.0729	0.770	0.419	0.876
0.016	10.44	6.65	0.0623	0.779	0.404	0.877
0.012	10.87	6.44	0.0588	0.796	0.411	0.896

Table 3: Effect of Calculation Length on Drop Statistics

t	SMD/d	N_D	$\overline{N_D}/ring$	Stnd. Dev.
2.0	0.0628	88	7.97	3.329
3.0	0.0623	856	10.44	6.665
4.0	0.0635	2582	11.08	7.936
5.0	0.0655	5132	11.48	7.985

nearly laminar flow as the flow is laminarized through highly contracted nozzle geometry under a favorable pressure gradient [16]. Since the filament vortex-ring is located exactly at the nozzle exit, the computational nodes near the nozzle exit are induced with the greater motion. This seems contradictory to the observed laminarized flow as shown in Fig. 1. In reality, it takes some time and distance for the rollup motion to develop and therefore the relaxation length is present regardless of the flow regime. For this reason, a cutoff for the superimposition method of the filament vortex-ring is introduced using stationary Rankine vortex model [17]. The size of Rankine vortex (i.e. R_c in Fig. 2), whose center is located at the upper corner of the nozzle exit, has little effect on droplet size and thus this is the parameter that can be set at the users convenience. As shown in Fig. 11, little variation in the axial pinch-off location is observed for $R_c < 0.4$. We have set $R_c = 0.3$ so that the computational nodes at the near nozzle exit are not affected by the induced motion. This is essentially setting the Rankine vortex size to be the relaxation length, $R_c \approx l_r$. It should be noted that the relaxation length can be scaled with the nozzle length, l [44, 45].

The simulation begins with an initially assumed jet shape as shown in Fig. 2. The size of the initial shape seems to have some effect on the first pinch-off. The larger the shape, the earlier the motion/instability is induced. However, the initial shape size seems to have little effect on the axial pinch-off location as shown in Fig. 12.

Comparison with Experiment

The complete simulation of the Hoyt and Taylor's jet [46] is shown in Fig. 13. The jet structure is initially assumed to be a simple cylinder with a hemispherical tip as shown in Fig. 2 and its evolution is simulated via time integration. The simulation is completed at $t = 5.0$. A slight 'swelling' is observed at $t = 1.0$ and the fluctuation of the jet surface is seen at $t > 2.0$. The velocities induced by the bound vortex are large enough to penetrate the jet surface and it results in the primary atomization. It should be noted that most liquid ligaments, pinching from the jet surface, are in the 'rollup' motion in counterclockwise direction while the mean velocity of the ligament is in the streamwise direction. Similar structures are noted in Fig. 8-(a) in a closeup view of the Hoyt and Taylor experiment. The counterclockwise rollup motion is a strong evidence that the boundary layer instability is the fundamental cause of the primary atomization. The mean velocity of most droplets are in streamwise direction as the droplets motion propagates along with the main jet stream, the most dominant convective source.

It was mentioned, in the previous section, that the model takes advantage of Ponstein's Eqn. (41) to model the instability of a pinch-off vortex-ring. Using the Eqn. (41), the number of waves or droplets (N_D) per ring is predicted and plotted as a function of the circulation, Γ_r. Their relationship is parabolic and the least square fit is available in Fig. 14. Thus if Γ_r is known, a rough estimation of N_D can be produced. Fig. 15 illustrates the relation between the number of circumferential waves and the core size of a pinch-off vortex-ring. As the size increases, more waves appear. This is exactly the opposite phenomenon as for the

elliptical instability of Widnall [47] and Sullivan: they observed more waves when the core size decreases. It should be noted that the mechanism of the surface tension driven instability (i. e. liquid vortex-ring in air) is different from the shear layer driven elliptical instability [48, 49, 50, 51], (i.e. liquid into liquid or gas into gas).

It is well known that the droplet size varies significantly within the atomization regime. Wu et al [52] reported the droplet size variation with U for the turbulent water jet into air. Hoyt and Taylor's experiment had been carried out for the Bernoulli pressure $\Delta P < 60\ psi$; no result with higher ΔP is reported [46, 16, 53]. However, we hypothesized the increase in ΔP for the Hoyt and Taylor jet. The result is taken the jet speed up to $U = 40\ m/s$ which corresponds to $\Delta P \approx 116\ psi$ or slightly higher in order to account for some pressure loss within the nozzle. The final result for the Hoyt and Taylor's case [46] is shown in Fig. 16. Using the methodology employed in the previous section with no calibration constants, the model predicts the Sauter Mean Diameter, SMD, with reasonable accuracy. As shown in Fig. 16, there is a steep gradient at a jet speed around $U \approx 20\ m/s$ for the Wu et al. [52] turbulent jet experiment. Our model result overlaps with that obtained by Hoyt and Taylor. It is interesting to observe that Wu et al.'s data is also similar to our result and that of Hoyt and Taylor at about $U \approx 20\ m/s$. While Wu et al. noted this as the region of 'uncertainty', it is possible that the rollup motion was competing with the turbulence and thus the perceptible effect of the rollup motion appears as shown in Fig. 16.

For $U \gtrsim 20\ m/s$, differences between the calculations and the experiments emerge. It is known that linear analysis [54] overpredicts the droplet size (by less than 20%) because it neglects the satellite droplet mass due to the nonlinear effect [55, 56] which yields the multiple crests per wavelength. Ponstein's Eqn. (41) is a linear analysis and thus it also tends to overpredict the droplet size. However, a 20% or smaller SMD difference does not explain the difference we see in Fig. 16 at a higher jet speed. This is due to the fundamental difference between the boundary layer instability jet and the turbulent jet: the boundary layer instability jet is scaled by the momentum thickness [42] and the turbulent jet is scaled by the Kolmogrov length scale, l_k or/and turbulence eddy characteristics length of kinetic energy, l_i [52]. Wu et al. derived the empirical formula using the 'surface kinetic energy' argument which gives SMD scaled by $\sim 1/U^{1.48}$. Thus the governing length scale (i.e. l_k and l_i) decrease significantly at about $U \sim 20\ m/s$. On the other hand, the SMD of the boundary layer instability jet is scaled by δ_2: $SMD \sim 1/U^{0.5}$ and thus its change with respect to U is relatively moderate as shown in Fig. 16.

Another experiment on the boundary layer instability jet is available by McCarthy and Molloy [57]. The rollup motion causes the jet to be atomized when the circulation is large enough to win against other competing forces such as viscous or/and capillary forces. In Fig. 17-(a), the 'stretching' is observed due to capillary force when the jet is atomized. In Fig. 17-(b), the computational result for the case is shown where the similar 'stretching' of the capillary force is observed. For the high speed jet, like that of Hoyt and Taylor [46, 16], the effect of viscosity and capillary force is of little importance because the jet is nearly inviscid. In fact, the large scale motion of Hoyt and Taylor's jet is governed by the Rayleigh inviscid analysis [54] which concludes the most dominant wavelength to be $\lambda = 4.51d$.

CONCLUSIONS

A fully nonlinear model has been developed to simulate primary atomization caused by boundary layer instability using superposition of a ring vortex with a potential jet flow. The axisymmetric model employs a boundary element methodology in which the vorticity in the boundary layer at the orifice exit is used to determine ring vortex strength and radial location at the orifice exit plane. Annular ligaments are pinched off the surface in this case; a secondary linear instability analysis due to Ponstein is used to predict the fractionization of the ligaments into individual droplets.

The SMD of the model result agrees well with the actual droplet size of Hoyt and Taylor's experiment. The result of the current model is also compared with the experimental data of Wu et al. [52]. The comparison confirms that the current model predicts the droplet size satisfactorily.

ACKNOWLEDGMENTS

References

[1] J. Ponstein. Instability of rotating cylindrical jets. *Applied Scientific Research*, 8(6):425–456, 1959.

[2] J. H. Hilbing and S. D. Heister. Droplet size control in liquid jet breakup. *Physics of Fluids*, 8(6):1574–1581, 1996.

[3] J. H. Hilbing and S. D. Heister. Nonlinear simulation of a high-speed, viscous liquid jet. *Atomization and Sprays*, 2:1–24, 1997.

[4] S. D. Heister, M. Rutz, and J. H. Hilbing. Effect of acoustic perturbations on liquid jet atomization. *Journal of Propulsion and Power*, 13:82–88, 1997.

[5] K. Rump and S. D. Heister. Modeling the effect of unsteady chamber conditions on atomization processes. *Journal of Propulsion and Power*, 14:576–578, 1998.

[6] S. D. Heister. Boundary element methods for two-fluid free surface flows. *Engineering Analysis with Boundary Elements*, 19:309–317, 1997.

[7] N. Kamiya and K. Nakayama. Prediction of free surface of die swell using the boundary element method. *Computers and Structures*, 46:387–395, 1993.

[8] M. A. Kelmanson. Boundary integral equation solution of viscous flows with free surfaces. *Journal of Engineering Mathematics*, 17:329–343, 1983.

[9] J. Tanzosh, M. Manga, and H. A. Stone. Boundary integral methods for viscous free-boundary problems: Deformation of single and multiple fluid-fluid interfaces. *Boundary Element Technology VII*, C. A. Brebbia and M. S. Ingber, Editors:19–39, 1992.

[10] N. N. Mansour and T. T. Lundgren. Satellite formation in capillary jet breakup. *Physics of Fluids*, 2:1141–1144, 1990.

[11] T. T. Lundgren and N. N. Mansour. Oscillations of drops in zero gravity with weak viscous effects. *Journal of Fluid Mechanics*, 194:479–510, 1988.

[12] I. F. Murray and S. D. Heister. On a droplet's response to acoustic excitation. *International Journal of Multiphase Flow*, 25:531–550, 1999.

[13] S. S. Yoon, S. D. Heister, J. T. Epperson, and P. E. Sojka. Modeling multi-jet mode electrostatic atomization using boundary element methods. *Journal of Electrostatics*, 50:91–108, 2001.

[14] E. Setiawan and S. D. Heister. Nonlinear modeling of an infinite electrified jet. *Journal of Electrostatics*, 42:243–257, 1997.

[15] V. Y. Shkadov. Wave formation on surface of viscous liquid due to tangential stress. *Fluid Dynamics*, 5:473–476, 1970.

[16] J. W. Hoyt and J. J. Taylor. Turbulence structure in a water jet discharging in air. *Physics of Fluids*, 20(10):S253–s257, 1977.

[17] P. G. Saffman. *Vortex Dynamics*. Cambridge University Press, New York, 1992. pp. 22, 192–195.

[18] J. A. Liggett and P. L.-F. Liu. *The Boundary Integral Equation Method for Porous Media Flow*. George Allen and Unwin, 1983.

[19] M. Abramowitz and F. A. Stegun. *Handbook of Mathematical Functions*. Dover Publications, 1972. pp. 562–566 and 590–592.

[20] S. S. Yoon and S. D. Heister. A fully nonlinear primary atomization. In *15th Annual Conference on Liquid Atomization and Spray Systems*, pages 36–40. ILASS, 2002. held in Madison, Wisconsin.

[21] S. S. Yoon and S. D. Heister. A fully nonlinear primary atomization. In *38th AIAA/ASME/SAE/ASEE Joint Propulsion Conference and Exhibit*, pages AIAA 2002–4179. AIAA, 2002. held in Indianapolis, IN.

[22] L. S. Blackford, J. Choi, A. Cleary, E. D'Azevedo, J. Demmel, I. Dhillon, J. Dongarra, S. Hammarling, G. Henry, A. Petitet, K. Stanley, D. Walker, and R. C. Whaley. *Department of Computer Science.* University of Tennessee, Knoxville, 1997. http://www.netlib.org/scalapack/index.html.

[23] W. H. Press, S. A. Teukolsky, W. T. Vetterling, and B. P. Flannery. *Numerical Recipes in FORTRAN, The Art of Scientific Computing.* Cambridge University Press, New York, 1992.

[24] H. Lamb. *Hydrodynamics.* Dover, New York, 1879. pp. 236–239.

[25] K. Karamcheti. *Principles of Ideal-Fluid Aerodynamics.* John Wiley and Sons, New York, 1966. pp. 526–530, 599.

[26] G. K. Batchelor. *An Introduction to Fluid Dynamics.* Cambridge University Press, New York, 1999. pp. 511–517, 521–526.

[27] W. J. Duncan, A. S. Thom, and A. D. Young. *An Elementary Treatise on the Mechanics of Fluids.* Edward Arnold, London, 1960. pp. 93–94.

[28] A. S. Ramsey. *A Treatise on Hydromechanics.* G. Bell and Sons, London, 1920. pp. 241–244.

[29] S. S. Yoon and S. D. Heister. Analytic solutions for computing velocities induced from potential vortex ring. *AIAA Journal Technical Paper*, 2002. submitted.

[30] I. G. Currie. *Fundamental Mechanics of Fluids.* McGraw-Hill, New York, 1993. Second Edition, pp. 172–174.

[31] D. E. Medina. *On droplets and boundary elements.* Sibley School of Mechanical and Aerospace Engineering, Cornell University, Technical Report FDA-89-12, Ithaca, New York, 1989.

[32] J. H. Hilbing. *Nonlinear Modeling of Atomization Processes.* PhD thesis, Purdue University, 1996.

[33] V. I. Smirnov. *A Course of Higher Mathematics.* Pergamon Press, New York, 1964.

[34] E. Kreyszig. *Advanced Engineering Mathematics.* John Wiley and Sons, New York, 1993. pp. 949–956.

[35] M. S. Longuet-Higgins and E. D. Cokelet. The deformation of steep surface waves on water. *Proceedings of the Royal Society of London A*, 350:1–26, 1976.

[36] E. T. Spyropoulos and G. A. Blaisdell. Evaluation of the dynamic model for simulations of compressible decaying isotropic turbulence. *AIAA Journal*, 34(5):990–998, 1996.

[37] J. H. Hilbing, S. D. Heister, and C. A. Spangler. A boundary-element method for atomization of a finite liquid jet. *Atomization and Sprays*, 5:621–638, 1995.

[38] S. K. Lele. Compact finite difference schemes with spectral-like resolution. *Journal of Computational Physics*, 103:16–42, 1992.

[39] J. G. Proakis and D. G. Manolakis. *Digital Signal Processing.* Prentice-Hall, New Jersey, 1996. pp. 30–31.

[40] F. M. White. *Viscous Fluid Flow.* McGraw Hill, New York, 1991. 2nd Edition pp. 235, 269, 358.

[41] B. Thwaites. *Incompressible Aerodynamics.* Dover, New York, 1960. pp. 30–31.

[42] C. Brennen. Cavity surface wave patterns and general appearance. *Journal of Fluid Mechanics*, 44(1):33–49, 1970.

[43] I. H. Shames. *Engineering Mechanics.* Prentice-Hall, New Jersey, 1993. pp. 306–308.

[44] J. H. Rupe. On the dynamic characteristics of free liquid jets and a partial correlation with orifice geometry. *NASA JPL Technical Report*, 32–207, 1962.

[45] A. M. Sterling and C. A. Sleicher. The instability of capillary jets. *Journal of Fluid Mechanics*, 68(3):477–495, 1975.

[46] J. W. Hoyt and J. J. Taylor. Waves on water jets. *Journal of Fluid Mechanics*, 83:119–127, 1977.

[47] S. E. Widnall and J. P. Sullivan. On the stability of vortex rings. *Proceedings of the Royal Society of London, Series A*, 332(1590):335–353, 1973.

[48] R. R. Kerswell. Elliptical instability. *Annual Review of Fluid Mechanics*, 34:83–113, 2002.

[49] B. J. Bayly. Three-dimensional instability of elliptical flow. *Physical Review Letters*, 34:2160–2163, 1986.

[50] F. Waleffe. On the three-dimensional instability of strained vortices. *Physics of Fluids*, A 2(1):76–80, 1990.

[51] M. J. Landman and P. G. Saffman. The three-dimensional instability of strained vortices in a viscous fluid. *Physics of Fluids*, 30(8):2339–2342, 1987.

[52] P. K. Wu, L. K. Tseng, and G. M. Faeth. Primary breakup in gas/liquid mixing layers for turbulent liquids. *Atomization and Sprays*, 2:295–317, 1992.

[53] J. W. Hoyt and J. J. Taylor. Effect of nozzle boundary layer on water jets discharging in air. In *Jets and Cavities–International Symposium*, pages 93–100. ASME, 1985. held in Miami Beach, Florida, Nov. 17–22.

[54] W. S. Rayleigh. On the instability of jets. *Proc. London Math. Soc.*, 10(4), 1878.

[55] M. C. Yuen. Non-linear capillary instability of a liquid jet. *Journal of Fluid Mechanics*, 33(1):151–163, 1968.

[56] E. F. Goedde and M. C. Yuen. Experiments on liquid jet instability. *Journal of Fluid Mechanics*, 40(3):495–514, 1970.

[57] M. J. McCarthy and N. A. Molloy. Review of stability of liquid jets and the influence of nozzle design. *The Chemical Engineering Journal*, 7:1–20, 1974.
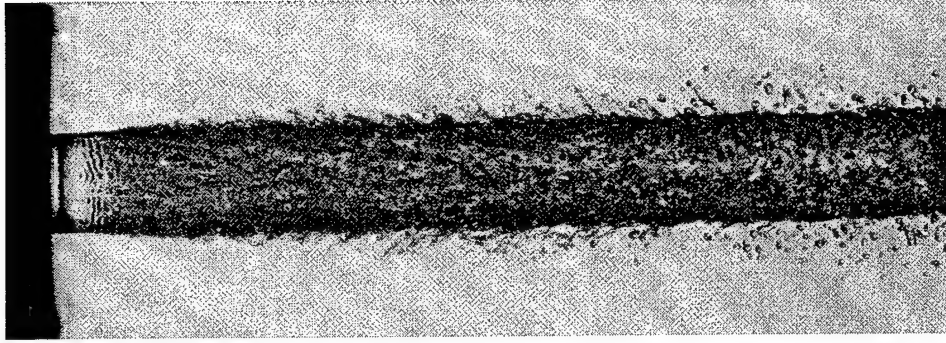
Figure 1: Typical water jet into air in the atomization regime. Experimental image by Hoyt and Taylor [46]. Printed under the permission of *Journal of Fluid Mechanics*.
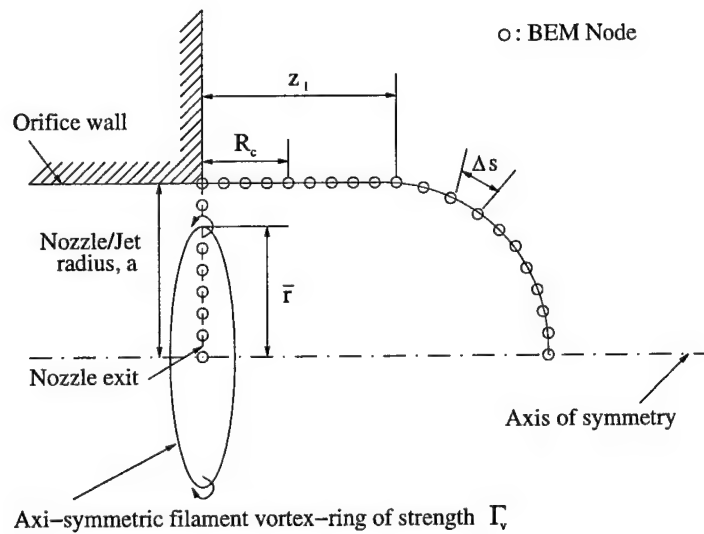

Figure 2: Schematic of the initial jet geometry indicating computational nodes and the axisymmetric ring vortex at the orifice exit plane.
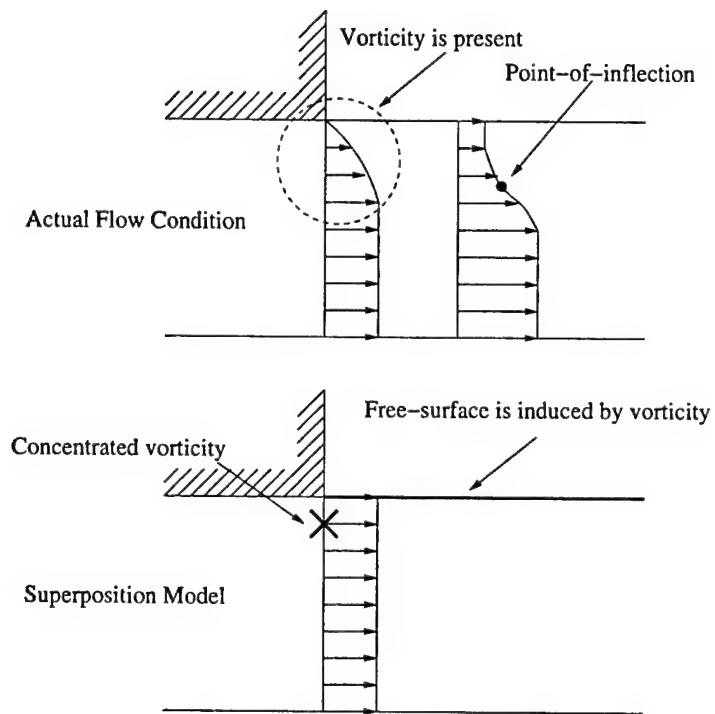
Figure 3: Comparison of the actual physical flow condition with the superposition model in simulating boundary layer relaxation downstream of the orifice exit plane.
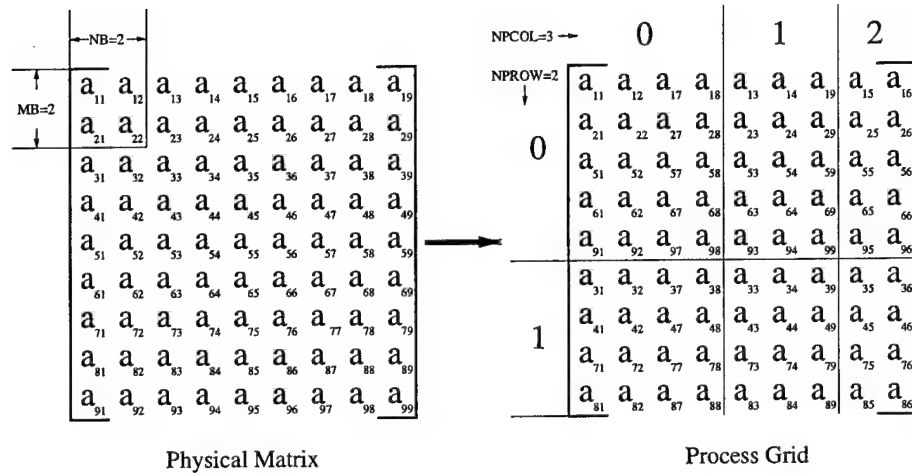
Figure 4: A 9 × 9 matrix decomposition with a 2 × 2 submatrix for a 2 × 3 process grid
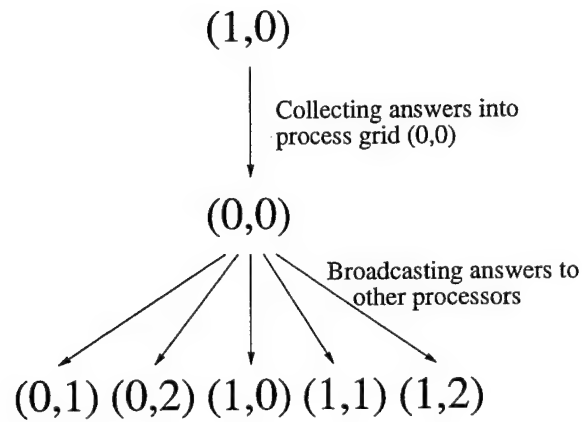
Figure 5: Passing the solution [X] to all other processors is carried out for all processors to share the information of [X].
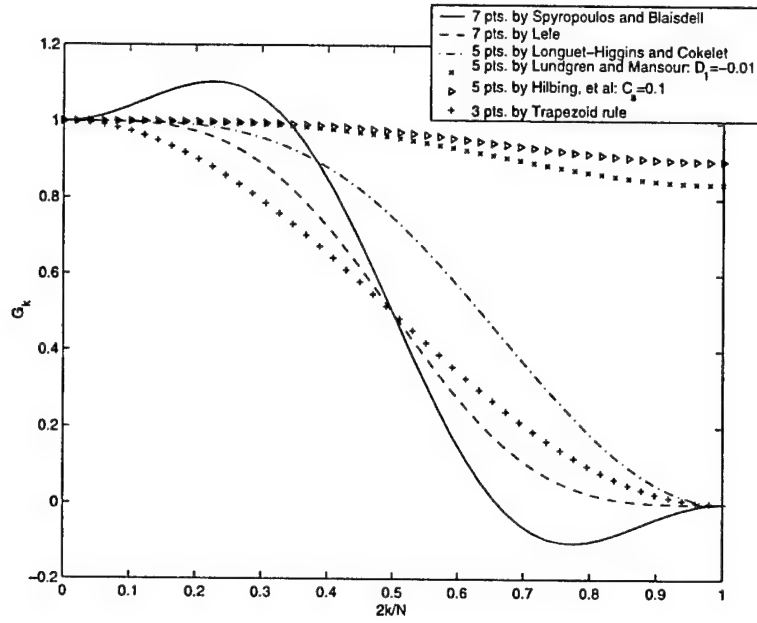
Figure 6: Filter transfer function vs. wavenumber for various filters
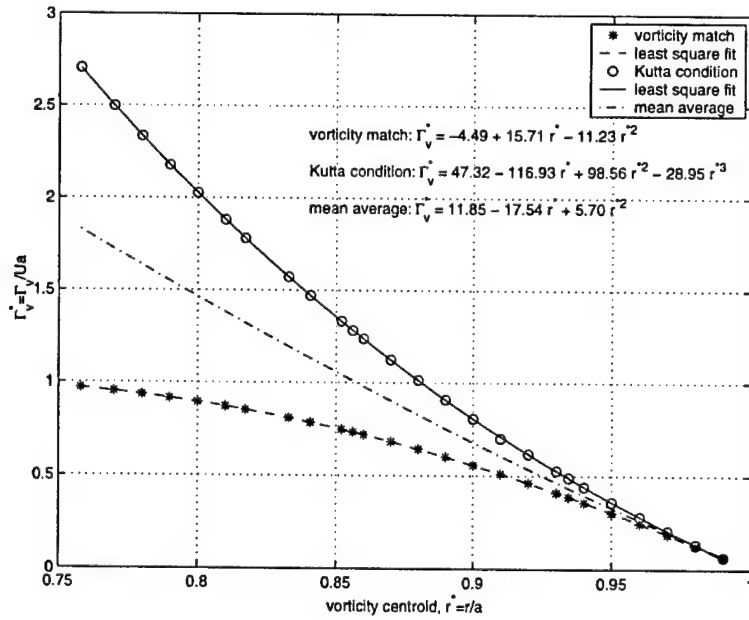
Figure 7: General approximation of circulation for filament vortex-ring using the Kutta condition and vorticity-match method.

(a)

(b)

Figure 8: (a) Closeup of the actual Hoyt and Taylor's water jet [46]. Printed under the permission of *Journal of Fluid Mechanics*. (b) The closeup of the model result for Hoyt and Taylor's water jet.
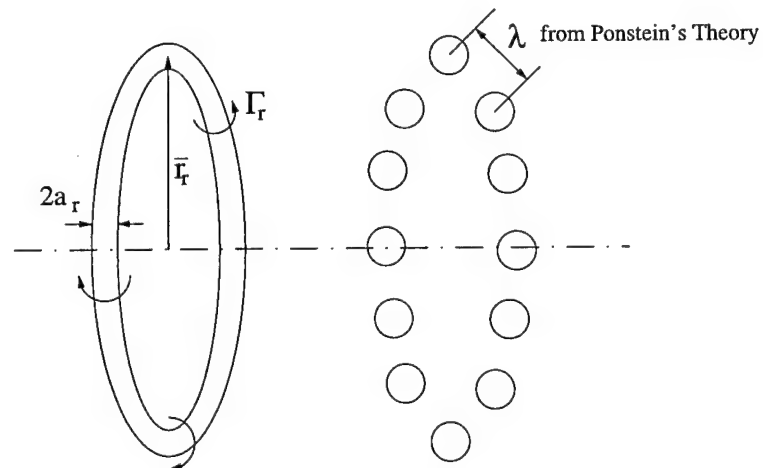
Figure 9: Application of Ponstein's [1] theory for the secondary instability of a pinch-off vortex-ring
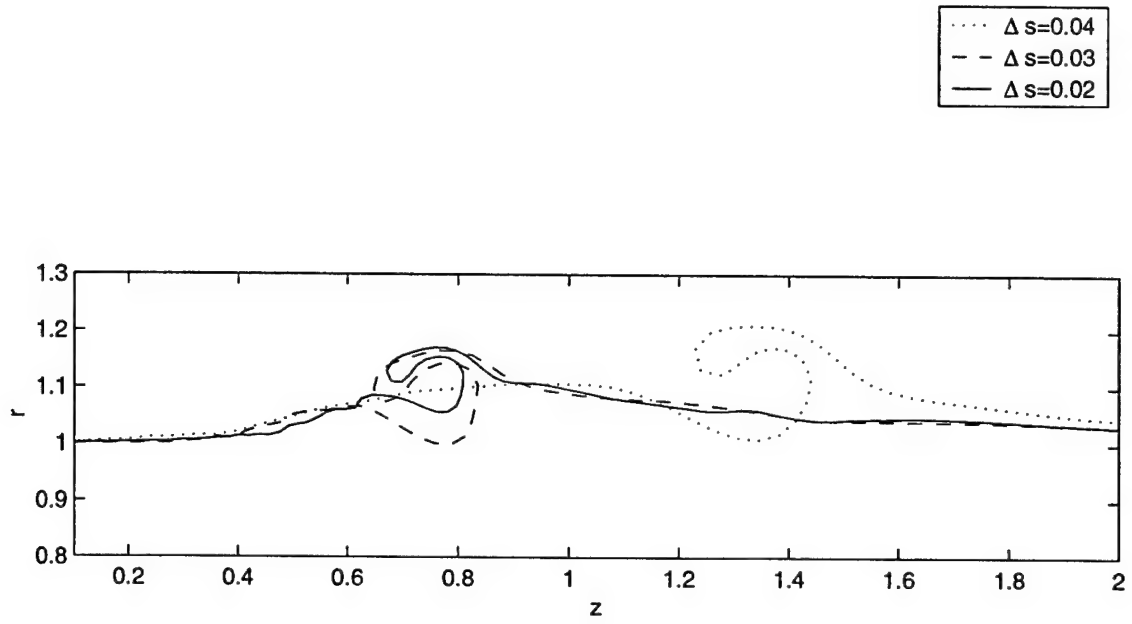
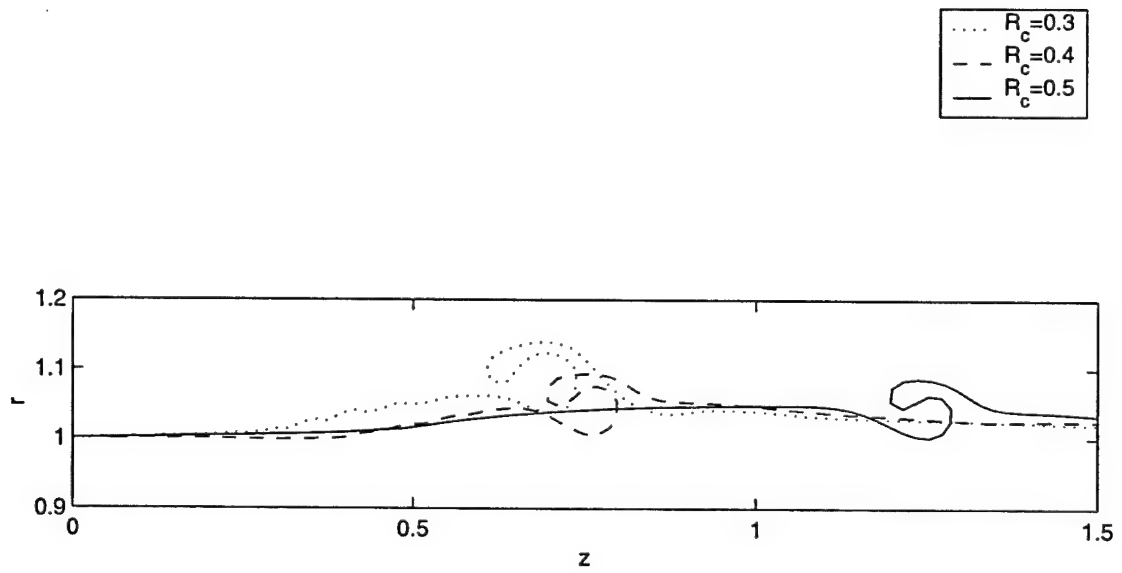Figure 10: Grid convergence study: Effect of nodal spacing, Δs.

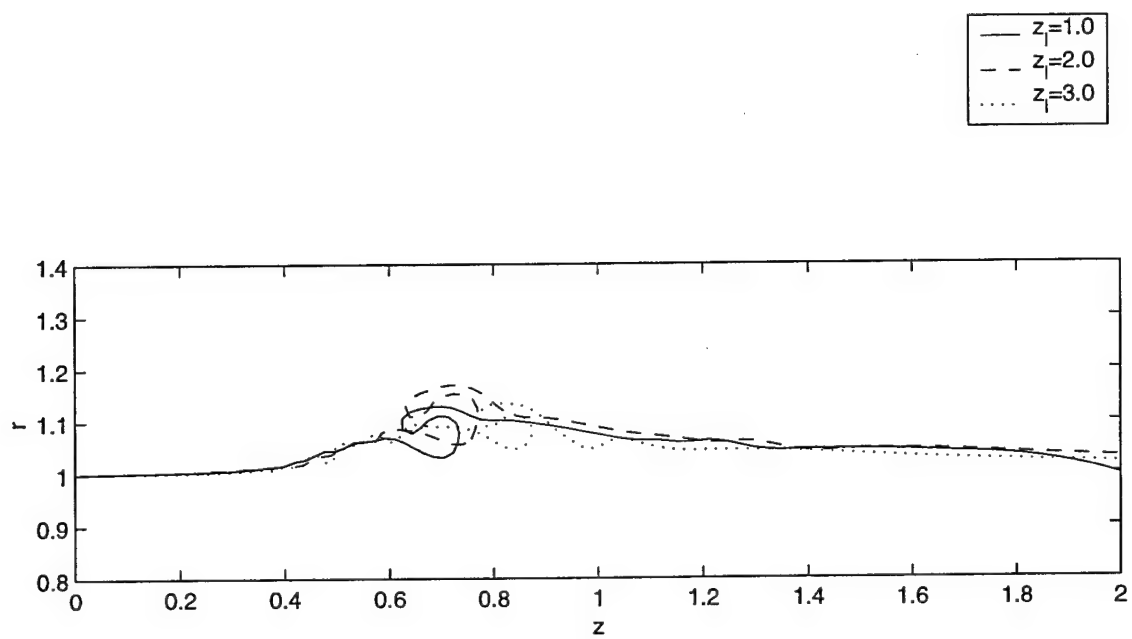Figure 11: Effect of the size of the Rankine vortex, R_c.

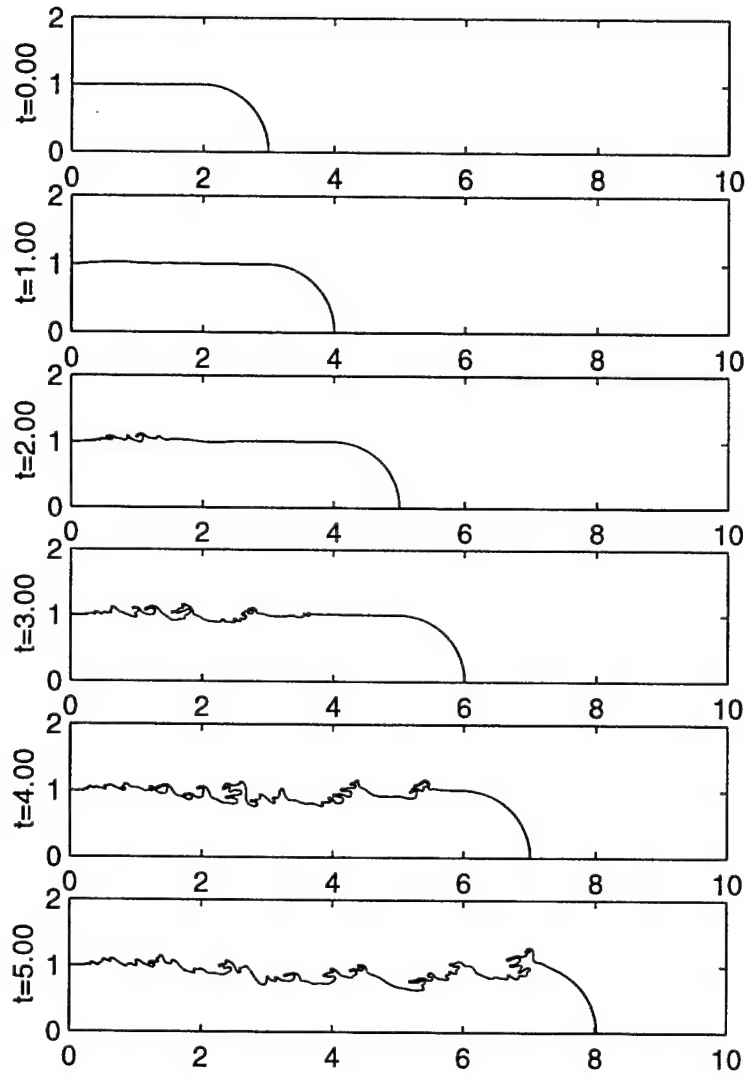Figure 12: Effect of the initially assumed shape

Figure 13: Jet evolution for conditions consistent with Hoyt and Taylors experiment [46]. Annular ligaments which have pinched off from the domain are not shown to improve clarity.
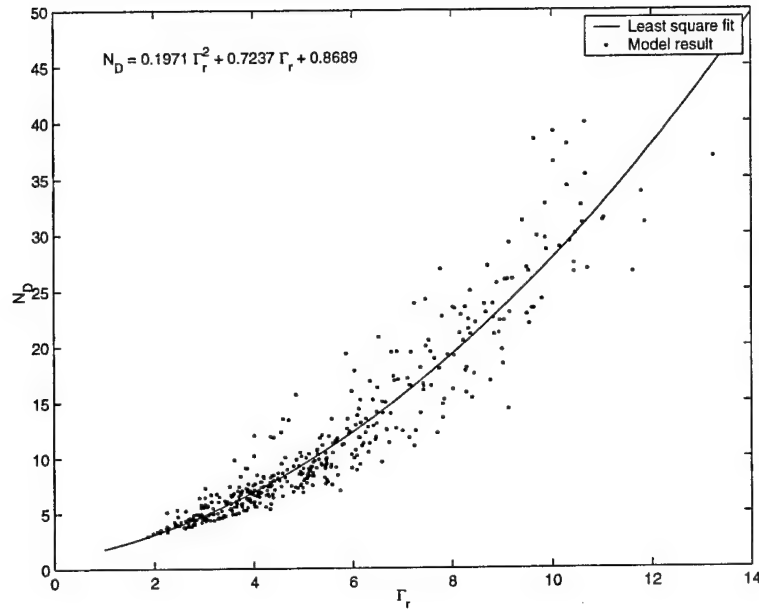
Figure 14: Prediction of cicumferential wave number (or number of droplet) due to circulation around the rotating ring pinched-off from the main liquid stream.
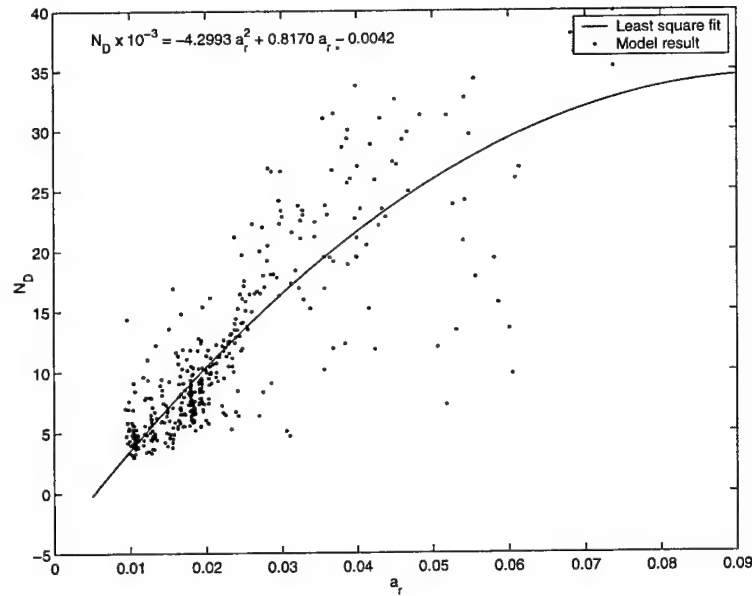

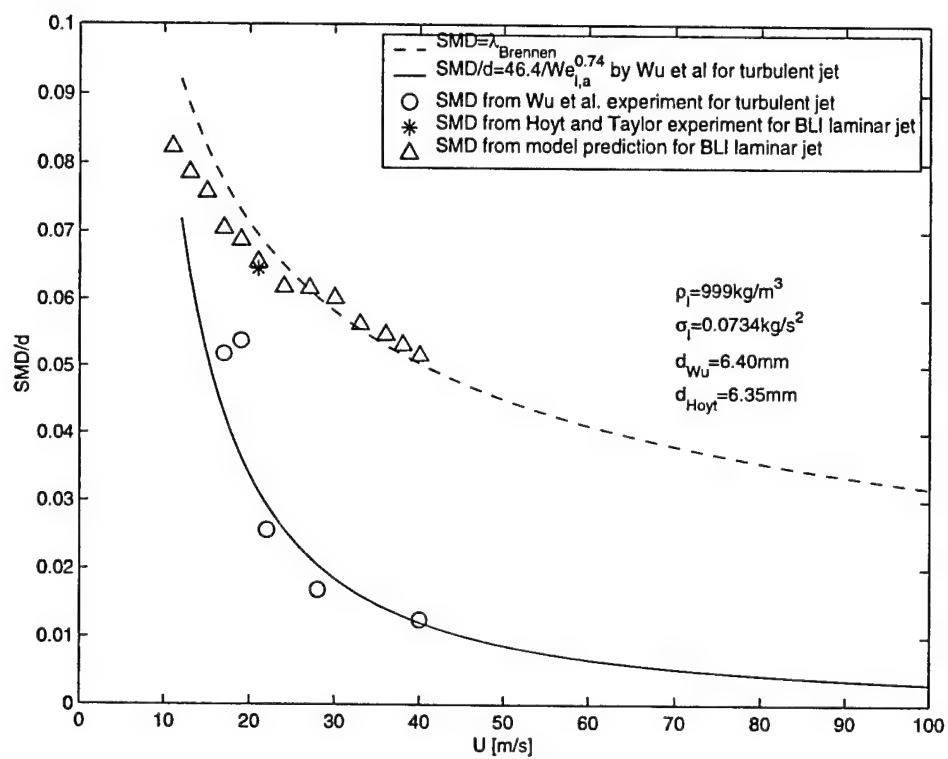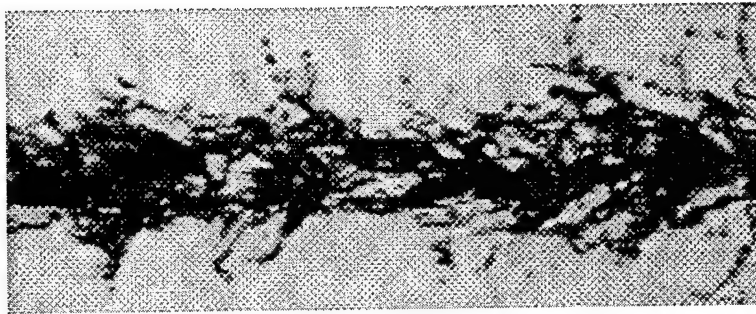Figure 15: Number of waves vs. core thickness of pinch-off vortex-ring

Figure 16: Sauter mean diameter comparison for various jet speed U in $[m/s]$.

(a) Experiment
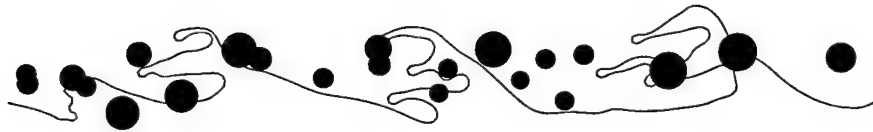
(b) Model result

Figure 17: Liquid: 60% glycerol and 40% water by weight, $\rho = 103\frac{kg}{m^3}$, $\mu = 11cP$, $\sigma = 0.0669\frac{kg}{s^2}$, $U = 20\frac{m}{s}$, $d = 2.54mm$, $We = 781$, $Re = 4750$. Comparison between experiment [57] and model results. The black circles represent the location and the relative size of the pinched-off droplets. Printed under the permission of *Elsevier Science*.

6 Appendix B - Jet Stability Theory

Yoon*, S. S. and Heister, S. D., "Categorizing Linear Theories for Atomizing Jets".

Categorizing Linear Theories for Atomizing Jets

Sam S. Yoon * and Stephen D. Heister[†]

* Graduate Research Assistant, [†] Professor, School of Aeronautics and Astronautics, Purdue University, W. Lafayette, IN

Abstract

This paper compares and contrasts linear stability analyses based on the deformations of an infinite liquid column and due to boundary layer vorticity imparted to the free surface from the orifice exit plane. The bulk of the prior works which date back to Kelvin-Helmholtz [1], Rayleigh [2], Weber [3], Taylor [4], Ponstein [5], Levich [6], Sterling and Sleicher [7], and Reitz and Bracco [8] have focused on the liquid column analysis. Though used to a lesser extent, the boundary layer instability analysis by Brennen's [9] can also be used to predict the dominant wavelength of the laminar jet. Differences between the two approaches are highlighted for sample injection conditions and injector geometries.

1 Introduction

The linear theory associated with primary atomization of a liquid jet is well established and much studied. More recently, nonlinear analyses have served to compliment the linear results and explain the presence of satellite droplets which have frequently been observed in low-speed jets. At higher jet speeds, it becomes more difficult to assess the value of linear theories because turbulence and secondary atomization become important contributers and because the jet surface is often obscured by droplets. In spite of these drawbacks, many of today's atomization models draw heavily from the linear theories based on a column of liquid exposed to a high-velocity gas shear flow.

The biggest drawback from these theories is that there is no mechanism to include effects of the orifice geometry on the possible wavelengths introduced to the liquid surface. A notable exception here is the work of Hoyt and Taylor [10, 11, 12] which focused on the boundary layer behavior at the orifice exit plane as a significant player in the subsequent instabilities observed in the jet. Drawing from a boundary layer-based instability analysis due to Brennen [9], these researchers showed that the wavelengths observed in their carefully-controlled experiment were in agreement with those predicted using Brennen's theory.

The aim of this short paper is to compare and contrast these approaches and to assess potentially important contributions of other researchers which have not been frequently cited in prior literature. In this context, we provide a brief review of linear stability results and highlight similarities and differences in the various approaches. Specific examples are considered to illustrate differences between liquid column-based and boundary layer-based approaches.

2 Lord Rayleigh's Analysis

Probably the most famous and poineering stability analysis for the liquid jet was developed by Lord Rayleigh [2]. Rayleigh considered the infinitely long inviscid column of liquid with negligible influence from the gas phase. He hypothesized the infinitesimal disturbance will cause the jet to breakup under a capillary-based instability. The famous dispersion relation he obtained is as follows:

$$w^2 = \frac{\sigma}{\rho_l a^3}(1 - k^2 a^2)ka\frac{I_1(ka)}{I_o(ka)} \tag{1}$$

where $w = w_r + iw_i$ (i.e. w_r=growth rate, $i = \sqrt{-1}$, and w_i=frequency of oscillation), σ=surface tension of the liquid, ρ_l=liquid density, a=orifice radius, k=wave number=$2\pi/\lambda$ (i.e. λ=wavelength), $I_1(ka)$ and $I_o(ka)$ are modified Bessel functions of the first kind. By expanding the Bessel functions in a power series and computing the maximum of the w vs. ka curve, he obtained the result:

$$w_m = 0.97\sqrt{\frac{\sigma}{\rho_l d^3}} \tag{2}$$

for which the corresponding wavnumber and wavelength are:

$$ka = 0.696 \approx 0.7 \qquad\qquad \lambda = 4.51d \tag{3}$$

There are numerous experimental confirmations of Rayleigh's wavelength appearing in low-speed jets. Many researchers have extended the result to the fully nonlinear regime and assumed that the jet will actually fragment into sections $4.51d$ in length which leads to a predicted droplet diameter of about $1.89d$ as shown in Fig. 1. While such conditions can be generated with a carefully controlled perturbation in an experiment, more commonly the jet is shown to bifurcate into two drops per wavelength; the presence of the satellite drops are not predicted from linear theory, but numerous nonlinear results [13, 14, 15, 16, 17] have confirmed their presence and agree well with size measurements from a variety of experiments.

The Rayleigh jet is of course the simplest of all cases in that aerodynamic interactions with the gas are neglected. The low jet velocities associated with this flow regime also imply that instabilities emanating from the boundary layer inside the orifice are necessarily small. For these reasons, there is good agreement between experiment and theory for a variety of orifice designs.

3   Weber's Equation

Weber [3] extended Rayleigh's analysis by adding the effect of viscosity of the jet which gives:

$$w^2 + \frac{3\mu}{\rho_l a^2}(ka)^2 w = \frac{\sigma}{2\rho_l a^3}(1 - k^2 a^2)k^2 a^2 \tag{4}$$

The coefficient of the w term accounts for viscous effects. McCarthy and Molloy [18] provided the maximum growth rate of Weber's Eq. (4).

$$w_m = \left[\sqrt{\frac{8\rho_l a^3}{\sigma}} + \frac{6\mu a}{\sigma}\right]^{-1} \tag{5}$$

The corresponding most dominant wavelength is

$$\lambda = \sqrt{2}\pi d\sqrt{1 + \frac{3\mu}{\sqrt{2\rho_l a\sigma}}} \tag{6}$$

Nonlinear simulations for viscous [19] and inviscid [13, 20] flows show comparable results for low-speed jets as well; the presence of viscosity only seems to decrease the rate at which the instability grows, not the shape of the wave.

4   Sterling-Sleicher Equation

The greatest shortcoming of Rayleigh and Weber equations is due to the neglect of aerodynamic forces on the liquid jet. Sterling-Sleicher [7] (hereafter referred as 'SS') had developed the dispersion equation that takes into accout the aerodynamic effects; the general SS equation is:

$$\left(\frac{\xi I_o(\xi)}{2I_1(\xi)} + \epsilon\frac{\xi K_o(\xi)}{2K_1(\xi)}\right)w^2 \tag{7}$$

$$+ \left(2i\epsilon\frac{U\xi^2 K_o(\xi)}{2aK_1(\xi)} + \frac{\mu\xi^2}{\rho_l a^2}\left[2\xi\frac{I_o(\xi)}{I_1(\xi)} - 1 + \frac{2\xi^2}{\xi_1^2 - \xi^2}\left(\xi\frac{I_o(\xi)}{I_1(\xi)} - \xi_1\frac{I_o(\xi_1)}{I_1(\xi_1)}\right)\right]\right)w$$

$$= \frac{\sigma}{2\rho_l a^3}(1 - \xi^2)\xi^2 + \epsilon\frac{U^2\xi^3}{2a^2}\frac{K_o(\xi)}{K_1(\xi)}$$

where

$$\xi = ka \qquad \xi_1^2 = \xi^2 + \frac{wa^2\rho}{\mu} \qquad \epsilon = \frac{\rho_g}{\rho_l} \tag{8}$$

41

In the absence of gas phase and viscosity (i.e. $\epsilon = \mu = 0$), the SS Eq. (7) reduces to Rayleigh's result. In addition, the general SS Eq. (7) can be written as the following for the inviscid case:

$$\left(\frac{\xi I_o(\xi)}{2I_1(\xi)} + \epsilon\frac{\xi K_o(\xi)}{2K_1(\xi)}\right)w^2 + \left(i\epsilon\frac{U\xi^2 K_o(\xi)}{aK_1(\xi)}\right)w = \frac{\sigma}{2\rho_l a^3}(1 - \xi^2)\xi^2 + \epsilon\frac{U^2\xi^3}{2a^2}\frac{K_o(\xi)}{K_1(\xi)} \tag{9}$$

Sterling-Sleicher considered the case where $\xi = ka < 1.0$ which implies the wavenumber is small or the wavelength (i.e. $\lambda = 2\pi/k$) is large enough that it is on the order of the nozzle radius, a. In this case, the general SS equation is simplified substantially:

$$w^2 + \frac{3\mu\xi^2}{\rho_l a^2}w = \frac{\sigma}{2\rho a^3}(1 - \xi^2)\xi^2 + \epsilon\frac{U^2\xi^3}{2a^2}\frac{K_o(\xi)}{K_1(\xi)} \tag{10}$$

It should be noted that a typoghraphical error is present in the original Sterling-Sleicher paper in the 'ϵ' term. It should be U^2 while it was typed as just U. Here U is the 'constant' and 'uniform' jet speed. In the limit of $\xi \to \infty$ for an inviscid case, the SS Eq. (7) is essentially the same as the Kelvin-Helmholtz equation, which is used to predict the smaller wavelengths (detailed proof of this claim is available in the following section).

5 Reitz-Bracco Equation

Further extention of the SS equation was presented by Reitz-Bracco [21] with the assumption that the liquid jet velocity is also a function of the radial direction (i.e. $U = U_g(r)$), as in the Orr-Sommerfeld equation [22, 23]. This equation of Reitz-Bracco (hereafter referred as 'RB') seems to be the most general dispersion expression available in the literature for the axisymmetric case.

$$w^2 + 2\nu k^2 \left(\frac{I_1'(\xi)}{I_o(\xi)} - \frac{2kl}{k^2 + l^2}\frac{I_1(\xi)}{I_o(\xi)}\frac{I_1'(la)}{I_1(la)}\right)w \tag{11}$$

$$= \frac{\sigma k}{\rho_l a^2}(1 - \xi^2)\left(\frac{l^2 - k^2}{l^2 + k^2}\right)\frac{I_1(\xi)}{I_o(\xi)} + \epsilon\left(U - \frac{iw}{k}\right)^2 k^2\left(\frac{l^2 - k^2}{l^2 + k^2}\right)\frac{I_1(\xi)}{I_o(\xi)}\frac{K_o(\xi)}{K_1(\xi)}$$

where

$$\nu = \mu/\rho_l \qquad\qquad l^2 = k^2 + w/\nu \qquad\qquad \lim_{\nu\to 0}\left(\frac{l^2 - k^2}{l^2 + k^2}\right) = 1.0 \tag{12}$$

It should be noted that Levich [6] had performed a similar analysis the result of which is exactly the same as the RB equation except that Levich had omitted the terms $\rho_g w^2$ and $\rho_g ikUw$ of gas by assuming the two terms are negligible compared to the terms $\rho_l w^2$ and $\rho_l ikUw$ of liquid. In the absence of viscosity and the gas phase (i.e. $\nu = \epsilon = 0$), the RB Eq. (11) also recovers Rayleigh's result. Further, the RB Eq. (11) becomes the following if inviscid (i.e. $\nu = 0$):

$$\left(\frac{\xi}{2} + \epsilon\frac{\xi K_o(\xi)}{2K_1(\xi)}\right)w^2 + \left(i\epsilon\frac{U\xi^2 K_o(\xi)}{aK_1(\xi)}\right)w = \frac{\sigma}{2\rho_l a^3}(1 - \xi^2)\xi^2 + \epsilon\frac{U^2\xi^3}{2a^2}\frac{K_o(\xi)}{K_1(\xi)} \tag{13}$$

This is exactly the same as the inviscid case of the SS Eq. (9) except for the coefficient of w^2. This difference originated from Sterling-Sleicher's uniform jet speed (i.e. $U = constant$) assumption which differs from Reitz-Bracco's jet velocity approximation with the gas velocity as a function of the radial direction. It is interesting to note that both the inviscid SS Eq. (9) and that of RB Eq. (13) are reduced to the following expression in the limit as $\xi \to \infty$:

$$w^2 = \epsilon U^2 k^2 - \frac{\sigma k^3}{\rho_l} \tag{14}$$

where we have used the approximations $\lim_{\xi\to\infty} I_o(\xi)/I_1(\xi) = 0$, $\lim_{\xi\to\infty} K_o(\xi)/K_1(\xi) = 1$ (see Pearson [24]), and $\rho_l \gg \rho_g$. This Eq. (14) is essentially the Kelvin-Helmholtz equation [25, 1].

6 Ponstein's Equation

In this section, the linear theory of Ponstein [5] is discussed. His work published in 1959 in Applied Scientific Research, Deutch Journal, has not been well recognized in the atomization community. The work not only had extended Rayleigh's [2, 26] analysis to include gas-phase effects, but also considered column rotation (swirl) in an analysis published long before the Sterling-Sleicher (1975), and even before Levich (1962).

Ponstein had considered two cases: a rotating liquid column in gas-phase and a rotating bubble (or gas) column in a liquid surrounding for the second case. A uniform liquid column in vacuum is well known by Rayleigh [2] who predicted the most dominant wavelength, $\lambda = 4.51d$. Rayleigh [26] also considered a uniform bubble column in liquid whose solution is:

$$\omega^2 = \frac{\sigma}{\rho_l a^3}(1 - k^2 a^2)\xi\frac{K_1(\xi)}{K_o(\xi)} \tag{15}$$

This equation predicts a most unstable wavelength, $\lambda = 6.48d$. For an axisymmetric rotating bubble column (based on $e^{\omega t}$), Ponstein gives the following result:

$$\omega^2 = \left[\frac{\sigma}{\rho_l a^3}(1 - k^2 a^2) - \left(\frac{\Gamma}{2\pi a^2}\right)^2\right]\xi\frac{K_1(\xi)}{K_o(\xi)} \tag{16}$$

where Γ is the circulation around the ring (or column) which can be estimated as $\Gamma = (2\pi a)V_\theta$ from Saffman [27]. Here V_θ is the tangential velocity of the ring surface. For a non-rotating case (i.e. $\Gamma = 0$), Eq. (16) recovers the Rayleigh's result in Eq. (15). In this case, circulation has a stabilizing influence as indicated by the negative sign on the Γ term. The faster it rotates, the more stable the bubble ring is. The detailed discussion of Eq. (16) is available in Lundgren and Mansour [28] where they had modeled the evolution of the bubble vortex-ring using boundary integral method. An interesting example of the bubble vortex-ring of Dolphin is discussed in Shariff [29].

Ponstein gives the following result for the second case he had considered, a rotating liquid column in gas:

$$\omega^2 = \left[\frac{\sigma}{\rho_l a^3}(1 - k^2 a^2) + (1 - \epsilon)\left(\frac{\Gamma}{2\pi a^2}\right)^2\right]\xi\frac{I_1(\xi)}{I_o(\xi)} + \epsilon U^2 k^2\frac{I_1(\xi)}{I_o(\xi)}\frac{K_o(\xi)}{K_1(\xi)} \tag{17}$$

If we consider non-rotating (i.e. $\Gamma = 0$) and non-aerodynamic effect (i.e. $U = \epsilon = 0$), Rayleigh's result is recovered. Here, circulation has a destabilizing effect as indicated by the positive sign on the Γ term. The faster the column rotates, the more unstable it becomes. Increasing gas density ϵ serves to aid in stabilizing the column circulation term, but destabilizes the dominant aerodynamic (U^2) term.

Considering the non-rotating case with aerodynamic effect, Ponstein's Eq. (17) can be written as:

$$\omega^2 = \frac{\sigma}{\rho_l a^3}(1 - k^2 a^2)\xi\frac{I_1(\xi)}{I_o(\xi)} + \epsilon U^2 k^2\frac{I_1(\xi)}{I_o(\xi)}\frac{K_o(\xi)}{K_1(\xi)} \tag{18}$$

For $\xi < 1.0$, it is known that $I_1(\xi)/I_o(\xi) \approx (\xi)/2$. Applying this identity, Eq. (18) is re-written as:

$$\omega^2 = \frac{\sigma}{2\rho_l a^3}(1 - k^2 a^2)(\xi)^2 + \epsilon\frac{U^2(\xi)^3}{2a^2}\frac{K_o(\xi)}{K_1(\xi)} \tag{19}$$

This result is exactly the same as the inviscid case of the dispersion relation derived by Sterling-Sleicher in Eq. (10).

7 Taylor's Equation

Taylor [4] derived the following relation based on his aerodynamic theory:

$$\frac{w}{kU} = \sqrt{\frac{\rho_g}{\rho_l}} \, 2xg(x) \tag{20}$$

43

where x is the nondimensional wavelength of Reitz and Bracco [21] and $g = g(x)$ is the function of the Taylor's number, T_a.

$$x = \frac{\rho_g U^2}{\sigma k} \qquad\qquad T_a = \frac{\rho_l}{\rho_g}\left(\frac{\sigma}{\mu U}\right)^2 = \frac{\rho_l}{\rho_g}\left(\frac{Re}{We_{l,d}}\right)^2 \tag{21}$$

with $Re = \rho_l U d/\mu$ and $We_{l,d} = \rho_l U^2 d/\sigma$. The RB Eq. (11) in the limit of $\xi \to \infty$ with viscosity (i.e. $\nu \neq 0$) is as follows:

$$(w + 2\nu k^2)^2 + \frac{\sigma k^3}{\rho_l} - 4\nu^2 k^3\sqrt{k^2 + \frac{w}{\nu}} + \frac{\rho_g}{\rho_l}(w + iUk)^2 = 0 \tag{22}$$

This equation is modified in the form of the Taylor's Eq. (20) assuming $\rho_l \gg \rho_g$,

$$\frac{w}{Uk} = \sqrt{\frac{\rho_g}{\rho_l}}\, h(x) \tag{23}$$

where

$$h(x) = \sqrt{1 - \frac{1}{x} + \frac{\rho_l \chi}{U^2 k^2 \rho_g}} \qquad \chi = 2\left(2\nu^2 k^3\sqrt{k^2 + \frac{w}{\nu}} - 2\nu k^2 w - 2\nu^2 k^4\right) \tag{24}$$

If we hypothesized the RB Eq. (23) were the same as Taylor's Eq. (20), the following relation can be set:

$$2\, x\, g(x) = h(x) \tag{25}$$

Reitz and Bracco [21] also defined a function $f(x) = x\, g(x)$. The numerical solution of Eq. (23) was given by Reitz and Bracco. The most dominant nondimensional wavelength x_m was found to be 1.5 and thus $f(x_m) = \sqrt{3}/6 \approx 0.2887$ as $T_a \geq 1.0$ (see Bracco [30]). Though the value of $f(x_m) = \sqrt{3}/6$ was first found by G. I. Taylor [4] and was mentioned in Ranz's paper [31], it seems that the most dominant nondimensional wavenumber $x_m = 1.5$, which gives $f(x_m) = \sqrt{3}/6$, as noted by Reitz and Bracco [21]. The same results have been found using KH Eq. (14) which is significantly simpler than Eq. (23). KH Eq. (14) can be written in the form of Taylor's Eq. (20):

$$\frac{w}{kU} = \sqrt{\frac{\rho_g}{\rho_l}}\left(1 - \frac{1}{x}\right)^{1/2} \tag{26}$$

Note that KH Eq. (14) is valid under inviscid (i.e. $\nu = 0$) assumption. If this were the same as Taylor's Eq. (20), $2xg(x) = (1 - \frac{1}{x})^{1/2}$ can be set:

$$g(x) = \frac{1}{2x}\left(1 - \frac{1}{x}\right)^{1/2} \tag{27}$$

The $f(x)$ and $g(x)$ as a function of the nondimensional wavelength x are plotted in Fig. 2. The $g(x_m)$ can be found by taking derivative of Eq. (27) with respect to x.

$$\frac{dg(x)}{dx} = \frac{1 - 2xy}{4x^3 y^{1/2}} \tag{28}$$

where $y = 1 - \frac{1}{x}$. Let $1 - 2xy = 0$ to find the most dominant nondimensional wavenumber, x_m. This gives the following analytical results:

$$x_m = 1.5 \qquad\qquad f(x_m) = x_m\, g(x_m) = \frac{\sqrt{3}}{6} \tag{29}$$

This shows that the viscosity is of little importance since no difference is seen in x_m and $f(x_m)$ values between Reitz and Bracco's numerical result and our analytical results using KH Eq. (14) (see Fig. 2).

Wu et al [8] assumed that the initial droplet diameter, D, might be proportional to the length of the most unstable wavelength, λ

$$D = B\lambda \tag{30}$$

where

$$\lambda = \frac{2\pi}{k_m} = \frac{2\pi}{\frac{U^2 \rho_g}{\sigma x_m}} = \frac{2\pi\sigma}{U^2 \rho_g}x_m = \frac{2\pi\sigma}{U^2 \rho_g}(1.5) = \frac{3\pi\sigma}{U^2 \rho_g} \tag{31}$$

44

B is a constant that is empirically approximated. Wu, Reitz and Bracco [8] gave $B \approx 4.5$, based on the curve-fit of their experimental data. Applying this Eq. (31) to Hoyt and Taylor's case [11] which is discussed in detail in the next section (i.e. $\sigma_{H_2O} = 0.0734 kg/s^2$, $\rho_{air} = 1.23 kg/m^3$, $U = 21m/s$, and $d = 6.35mm$, thus $We_g = 46.9$), the most unstable wavelength is $\lambda \approx d/5$. The wavelength overpredicts the value observed in Hoyt and Taylor's experiment (i.e. $\lambda \approx d/13.8$). It should be noted that Eq. (31) is capable of producing very small wavelengths with large U and ρ_g, which is the case of Wu et al [8]; this aerodynamic theory works well for their atomizing jets of the shear layer driven instability.

8 Boundary Layer Instability Analysis

None of the conventional linear stability theories can account for the largely axisymmetric waves observed by Hoyt and Taylor [11] in their famous 1977 experiments. In this experiment, a carefully machined nozzle was used to provide a favorable pressure gradient to a reasonably high-speed jet such that turbulence effects were minimized. The resultant waves formed on the surface of the water jet showed wavelengths $\lambda \approx d/13.8$ which is not predicted well by the linear theories discussed above. These researchers theorized that the thickness of the boundary layer at the orifice exit plane could play a significant role in explaining the observed wavelength. It was suspected that the point of inflection due to change in velocity profile from a no-slip to a free-surface edge condition was responsible for the instability and the subsequent wave growth. Shkadov [32] was another researcher working on this theory at the time.

For this reason, we review the classical boundary layer instability based on the Orr-Sommerfeld equation. Using (i) the solution by Betchov and Criminale [33] for the fully developed 2D steady parallel laminar flow, (ii) the perturbation method [22], (iii) and the linearization, the 2D Navier-Stokes equations can be written as follows:

$$(u - c)\left[\hat{v} - \frac{1}{\alpha^2}\hat{v}''\right] + \frac{1}{\alpha^2}\hat{v}u'' = \frac{1}{Re_{\delta_2}\,i\alpha}\left[2\hat{v}'' - \alpha^2\hat{v} - \frac{1}{\alpha}\hat{v}''''\right] \tag{32}$$

where $u = u(y)$ is the axial velocity profile in y direction, $c = c_r + ic_i$ is the growth-rate, α is the wavenumber, $\hat{v} = \hat{v}(y)$ is the amplitude of the radial perturbation in y direction, and $Re_{\delta_2} = U\delta_2/\nu$. This is called 'Orr-Sommerfeld' equation. Sometimes different notations (i.e. $\hat{v}(y) = -i\alpha\phi(y)$) are used by researchers (see Panton [23] and/or Schlichting [22]). It should also be noted that $\phi(y)$ is not velocity potential but complex amplitude function for the streamfunction. There is no analytic solution to Eq. (32) but the numerical solution for a wide range of values of frequency and Re_{δ_2} is available by Jordinson [34].

Considering the inviscid case of Orr-Sommerfeld Eq. (32) (i.e. $Re_{\delta_2} \to \infty$), the following equation is obtained:

$$(u - c)\left[\hat{v} - \frac{1}{\alpha^2}\hat{v}''\right] + \frac{1}{\alpha^2}\hat{v}u'' = 0 \tag{33}$$

This is called 'Rayleigh Equation'. Lord Rayleigh (1880-1913) provided a theorem based on his Eq. (33), "Velocity profiles with points of inflection are unstable". Rayleigh proved that the presence of a *point-of-infection* is a *necessary* (though it is not *sufficient*) condition for the appearance of unstable waves. This is a powerful statement as it can be used to classify the flow regime: laminar to turbulent flows. For example, the velocity profile contains no point-of-inflection under favorable pressure gradient (i.e. $\partial P/\partial x < 0$). Generally, it is fair to state that the flow is laminar in such case. On the other hand, point-of-inflection can be found in adverse pressure gradient (i.e. $\partial P/\partial x > 0$) where the flow is sometimes unstable and eventually this may lead to turbulent flow.

The influence of gas density, and hence aerodynamic forces on the interface, has been widely investigated experimentally. Reitz and Bracco [21] observed a substantial difference in the atomization mechanism when the liquid jet was injected in different gases (i.e. $\rho_{N_2} = 6\ kg/m^3$ and $\rho_{Xe} = 23\ kg/m^3$). Wu et al [35] have reported a change in droplet size for primary atomization when a different gas density was tested for the same liquid jet. From this basis one may conclude that the aerodynamic interaction at the surface of the jet does alter wave growth, i.e. that aerodynamic forces are of sufficient magnitude to contribute to the instability. Shkadov's theory [32] states that the velocity profile of liquid is independent of gas density, which seems contradictory to the experimentally observed trend. This dilemma is probably due to the high gas-liquid density ratio which causes the growth rate due to the aerodynamic term to dominate as compared to the growth rate due to the vortices, thereby invalidating Shkadov's theory. In addition, the droplet sizes are strongly dependent on secondary atomization at high jet speed and high gas density conditions.

Clearly the influence of the gas is regime dependent, but the fundamental instability mechanism is present in all regimes. The fundamental questions which should be asked are, "Will instability occur in the absence of gas phase? If so, where is that instability mechanism originating from?"

Hoyt and Taylor[10] did not observe differences in wave structure with differing external airflows in their experiments. The axisymmetrically disturbed short wavelength observed near the nozzle exit is present regardless of magnitude or direction of the air velocity. Hoyt and Taylor concluded that this phenomenon has "no discernible effect of relative air velocity". In spite of Hoyt and Taylor's effort in this regard, their result has not well been recognized in the atomization community. For many years, the notion that vorticity at the nozzle exit being responsible for the atomization has been over-shadowed by the aerodynamic linear theory and the experiment which showed a significant difference in spray structure with the change in gas density.

Shkadov [32] provides the solution of the Rayleigh's Eq. (33) and proves that the amplitude of surface waves grows in the downstream direction, as the jet velocity profiles relaxes. This eigenvalue problem is also solved by Brennen [9]. Brennen provided the boundary layer instability analysis. He considered separated boundary layer flow over the planar plate using Gaussian velocity profile. This resulted in:

$$\gamma = 2\pi f \frac{\delta_2}{U} \tag{34}$$

where γ is the nondimensional frequency, f is the dimensional frequency in $[Hz]$, δ_2 is the momentum thickness in $[m]$, and U is the speed of the uniform flow in $[m/s]$. Brennen concluded that $\gamma = 0.175$ was to be the nondimensional frequency which would give maximum amplification at the flow separation point.

Applying $\gamma = 0.175$ to Hoyt and Taylor case [11]

$$f = \frac{\gamma}{2\pi} \frac{U}{\delta_2} = \left(\frac{0.175}{2\pi}\right) \left(\frac{21m/s}{1.2 \times 10^{-5}m}\right) = 48,741 Hz \tag{35}$$

Note that the boundary layer momentum thickness, δ_2, can be approximated using Blasius solution [36] for laminar flow assuming that $\delta_2 << a$:

$$\frac{\delta_1}{x} = \frac{1.721}{\sqrt{Re_x}} \qquad\qquad \frac{\delta_2}{x} = \frac{0.664}{\sqrt{Re_x}} \tag{36}$$

where $Re_x = \frac{Ux}{\nu}$ and δ_1 is the displacement thickness. Assuming that the wave speed is about the same as that of the liquid jet U,

$$\lambda \approx \frac{U}{f} = \frac{21m/s}{48741Hz} = 0.43 \ mm = \frac{d}{14.8} \tag{37}$$

While this was a theoretically predicted value, Hoyt and Taylor's experimental observation of the axisymmetrically disturbed wavelength was about $\lambda \approx 0.46 \ mm = d/13.8$ as shown in Fig. 3 (note: $d = 6.35 \ mm$). The comparison between theory and experiment was excellent.

McCarthy and Molloy [18]'s experiment provides further confirmation of the role of the momentum thickness in wave formation at the orifice exit plane. They varied the nozzle-to-diameter ratio (i.e. l/d) and observed the effect of l/d on 'laminar' jet structure. In their paper [18], it was not mentioned that the jets had distinctive axisymmetric waves for different orifice designs, yet the experimental images do contain these structures as shown in Fig. 4 excerpted from their paper. In the further downstream, the jets become turbulent (see Case $l/d = 5$ and 10 in Fig. 5) and result in the primary atomization.

To compare the McCarthy and Molloy results with Brennan's theory, we assume boundary layer development inside the passage can be approximated by boundary layer growth on a flat plate. Clearly, this assumption becomes poor when the boundary layer is a substantial fraction of the orifice radius, but one could use a numerical analysis or more elaborate theory to more accurately ascertain momentum thicknesses at the orifice exit plane. The errors result from freestream pressure gradients which develop as the boundary layer builds in the passage. A thorough review of turbulent momentum thickness is available by Klein [37]. Given this caveat, the predicted δ_2 values using this technique, when implemented in Brennen's equation, show good agreement with the observed wavelengths from the McCarthy and Molloy experiments as presented in Table 1. One can also note from Table 1 that the δ_2 values are all quite small relative to the orifice radius, thereby lending credence to the simple approach of assuming flat plate boundary layer growth.

Table 1: Summary for McCarthy and Molloy's Experiment [18]

l/d^*	$Re_x^\dagger$	δ_1/d	δ_2/d	Re_{δ_2}	$f^\natural$ [Hz]	$\lambda^\sharp$	λ_{exp}
1	4748	1/40.04	1/103.8	46	22758	d/2.9	d/2.8
5	23738	1/17.90	1/46.41	102	10178	d/1.3	d/1.4
10	47477	1/12.66	1/32.82	145	7197	1.1 d	1.0 d

* l/d=nozzle length to diameter ratio
† $Re_x = Ul/\nu$ $^{\natural,\sharp}$ Brennen's Eqs. (35) and (37), respectively
note: Blasius solution is used for δ_1 and δ_2 estimation

9 Comparison of the Linear Models

It is useful to compare the wavelengths predicted by the liquid column theories and the boundary layer theory for the same atomizer. In Fig. 6, wavelength predicted by Brennen's theory is plotted as a function of jet speed for various l/d and is compared with the SS and KH liquid column-based analyses.

The results obtained by Sterling-Sleicher Eq. (10) and that obtained by Kelvin-Helmholtz Eq. (14) are essentially the same at the higher jet speeds indicating that the KH mechanism is dominant for atomizing jets. The Reitz and Bracco Eq. (13) (though not plotted in Fig. 6) gives results very similar to the Sterling and Sleicher result as noted in prior discussion. These column-based results show a strong dependence on jet velocity at the lower speeds, with an asymptotic behavior at the high jet speeds. The boundary layer-based results are also provided in Fig. 6 for various orifice lengths. These results show a more modest variation in critical wavelength at the lower injection velocities with a similar asymptotic behavior at the high jet speeds. Results from the boundary layer-based analysis show a strong influence of orifice l/d, while the column-based analysis does not include this parameter. In general, the boundary layer-based results predict smaller wavelengths at the low jet speeds and larger wavelengths at the higher jet speeds as compared to the column-based results.

Unfortunately, the influence of turbulence, especially at the higher jet speeds, makes it difficult to perform experiments to compare the two theories. The axisymmetrically perturbed waves are not observable when the jet flow is already turbulent flow at the nozzle exit (see Figure-1 of Wu et al [38]). However, the flow at Hoyt and Taylor nozzle exit is nearly laminar flow as the flow is laminarized through highly contracted nozzle geometry under the favorable pressure gradient [11]. Their carefully conducted experiment, which had substantially reduced all other possible perturbation sources (i.e. such as turbulence and cavitation), has made the observation of the boundary layer waves possible. For their water jet (laminar at the nozzle exit), the Reynolds number based on the momentum thickness (Re_{δ_2}) is about 225 while the Blasius solution indicates that the flow should be turbulent for $Re_{\delta_2} > 200$.

This dilemma is probably because that the favorable pressure gradient has shifted the shape factor (i.e. $H = \delta_1/\delta_2$) and thus the critical Reynolds number ($Re_{\delta_2,crit}$) has increased. It should be noted that a slight decrease in H can result in a substantial increase in $Re_{\delta_2,crit}$ [36, 39]. At this stage of the research, it is not clear where the $Re_{\delta_2,crit}$ lies for the liquid jet. In Fig. 7, we have considered a laminar water jet into an air. It is shown that Re_{δ_2} increases with increasing l/d. In reality, it is not guaranteed that the flow at the nozzle exit is laminar for high l/d. However, one will have a better chance of observing the boundary layer waves if $Re_{\delta_2} < Re_{\delta_2,crit}$. It certainly would be interesting to generate additional experimental data for these conditions.

10 Conclusions

Linear analyses based on liquid column and boundary layer-based methodologies are compared and contrasted. The boundary layer-based analysis has the advantage that it addresses the orifice geometry as a primary influence in determining the most unstable wavelength. The column-based theories are shown to be largely equivalent in the atomization regime due to the dominance of the Kelvin-Helmholtz instability mechanism at these conditions. In performing a sample comparison of the two methods for a water jet, the boundary layer-based scheme tends to predict smaller critical wavelengths at low speed conditions and larger critical wavelengths at high injection speeds. While the column-based analysis has received more attention in the community, the boundary layer-based approach is shown to have merit based on limited experiments

aimed at addressing this mechanism.

Acknowledgements

References

[1] P. G. Drazin and W. H. Reid. *Hydrodynamic Stability.* Cambridge University Press, New York, 1981. pp. 14–28.

[2] W. S. Rayleigh. On the instability of jets. *Proc. London Math. Soc.*, 10(4), 1878.

[3] C. Weber. Zum zerfall eines flussigkeitsstrahles. *Z. Angew. Math. Mech.*, 11:138–145, 1931.

[4] G. K. Batchelor (Editor). *Collected Works of G. I. Taylor.* Cambridge University Press, Cambridge, MA, 1958.

[5] J. Ponstein. Instability of rotating cylindrical jets. *Applied Scientific Research*, 8(6):425–456, 1959.

[6] V. G. Levich. *Physicochemical Hydrodynamics.* Prentice Hall, New Jersey, 1962. pp. 639–646.

[7] A. M. Sterling and C. A. Sleicher. The instability of capillary jets. *Journal of Fluid Mechanics*, 68(3):477–495, 1975.

[8] K. J. Wu, R. D. Reitz, and F. V. Bracco. Measurements of drop size at the spray edge near the nozzle in atomizing liquid jets. *Physics of Fluids*, 29(4):941–951, 1986.

[9] C. Brennen. Cavity surface wave patterns and general appearance. *Journal of Fluid Mechanics*, 44(1):33–49, 1970.

[10] J. W. Hoyt and J. J. Taylor. Waves on water jets. *Journal of Fluid Mechanics*, 83:119–127, 1977.

[11] J. W. Hoyt and J. J. Taylor. Turbulence structure in a water jet discharging in air. *Physics of Fluids*, 20(10):S253–s257, 1977.

[12] J. W. Hoyt and J. J. Taylor. Effect of nozzle boundary layer on water jets discharging in air. In *Jets and Cavities–International Symposium*, pages 93–100. ASME, 1985. held in Miami Beach, Florida, Nov. 17–22.

[13] N. N. Mansour and T. T. Lundgren. Satellite formation in capillary jet breakup. *Physics of Fluids*, 2:1141–1144, 1990.

[14] P. Lafrance. Nonlinear breakup of a laminar liquid jet. *Physics of Fluids*, 18:428, 1975.

[15] D. F. Rutland and G. J. Jameson. Theoretical prediction of the sizes of drops formed in the breakup of capillary jets. *Chemical Engineering Science*, 25:1689–1698, 1970.

[16] C. A. Spangler, J. H. Hilbing, and S. D. Heister. Nonlinear modeling of jet atomization in the wind-induced regime. *Physics of Fluids*, 7:964, 1995.

[17] D. F. Rutland and G. J. Jameson. A non-linear effect in the capillary instability of liquid jets. *Journal of Fluid Mechanics*, 46(2):267–271, 1971.

[18] M. J. McCarthy and N. A. Molloy. Review of stability of liquid jets and the influence of nozzle design. *The Chemical Engineering Journal*, 7:1–20, 1974.

[19] D. W. DePaoli, T. C. Scott, and O. A. Basaran. Oscillation frequencies of droplets held pendant on a nozzle. *Separation Science and Technology*, 27(15):2071–2082, 1992.

[20] C. A. Spangler, J. H. Hilbing, and S. D. Heister. Nonlinear modeling of jet atomization in the wind-induced regime. *Physics of Fluids*, 7(5):964–971, 1995.

[21] R. D. Reitz and F. V. Bracco. Mechanism of atomization of a liquid jet. *Physics of Fluids*, 25(10):1730–1742, 1982.

[22] H. Schlichting. *Boundary Layer Theory.* McGraw-Hill, New York, 1979. pp. 461–463.

[23] R. L. Panton. *Incompressible Flow.* John Wiley and Sons, 1996. Second Edition, pp. 460–470, 718–727, 739–741.

[24] C. E. Pearson. *Handbook of Applied Mathematics.* Van Nostrand Reinhold Company, New York, 1974. pp. 349–350, 361.

[25] G. K. Batchelor. *An Introduction to Fluid Dynamics.* Cambridge University Press, New York, 1999. pp. 511–517, 521–526.

[26] W. S. Rayleigh. On the instability of cylindrical fluid surfaces. *Philosophical Magazine*, 34(207), 1892.

[27] P. G. Saffman. The number of waves on unstable vortex rings. *Journal of Fluid Mechanics*, 84(4):625–639, 1978.

[28] T. T. Lundgren and N. N. Mansour. Vortex ring bubbles. *Journal of Fluid Mechanics*, 224:177–196, 1991.

[29] K. Marten, K. Shariff, S. Psarakos, and D. J. White. Ring bubbles of dolphins. *Scientific American*, pages 82–87, 1996. August.

[30] F. V. Bracco. Modeling of engine sprays. *SAE Transactions, Fuels and Lubricants*, 94(850394):144–167, 1985.

[31] W. E. Ranz. Some experiments on orifice sprays. *Can. Journal of Chemical Engineering*, 36:175, 1958.

[32] V. Y. Shkadov. Wave formation on surface of viscous liquid due to tangential stress. *Fluid Dynamics*, 5:473–476, 1970.

[33] R. Betchov and W. O. Criminale. *Stability of Parallel Flows.* Academic Press, New York, 1967. 2nd Edition pp. 235.

[34] R. Jordinson. The flat plate boundary layer. part 1. numerical integration of the orr-sommerfeld equation. *Journal of Fluid Mechanics*, 43:801–811, 1970.

[35] P. K. Wu and G. M. Faeth. Aerodynamic effects on primary breakup of turbulent liquids. *Atomization and Sprays*, 3:265–289, 1993.

[36] F. M. White. *Viscous Fluid Flow.* McGraw Hill, New York, 1991. 2nd Edition pp. 235, 269, 358.

[37] A. Klein. Review: Turbulent developing pipe flow. *Journal of Fluids Engineering*, 103:243–249, 1981.

[38] P. K. Wu, L. K. Tseng, and G. M. Faeth. Primary breakup in gas/liquid mixing layers for turbulent liquids. *Atomization and Sprays*, 2:295–317, 1992.

[39] A. R. Wazzan, C. Gazley Jr, and A. M. O. Smith. Tollmien-schlichting waves and transition. *Prog. Aerosp. Sci.*, 18(2):351–392, 1979.

[40] A. Hart-Davis. http://www.freeimages.co.uk/. In *Jet Flow in Rayleigh Regime*, 2001. http://www.hd.org/Damon/photos/.
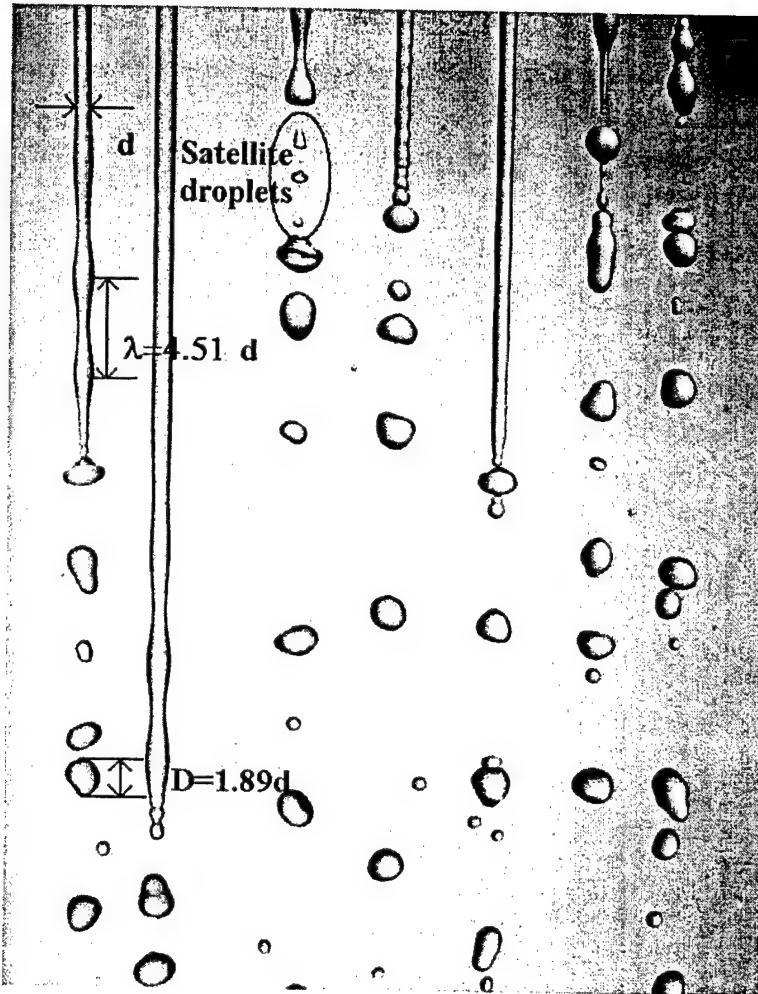
Figure 1: Typical low speed jet in the Rayleigh regime. Experimental image by Adam Hart-Davis [40]. Printed under the permission of Adam Hart-Davis.
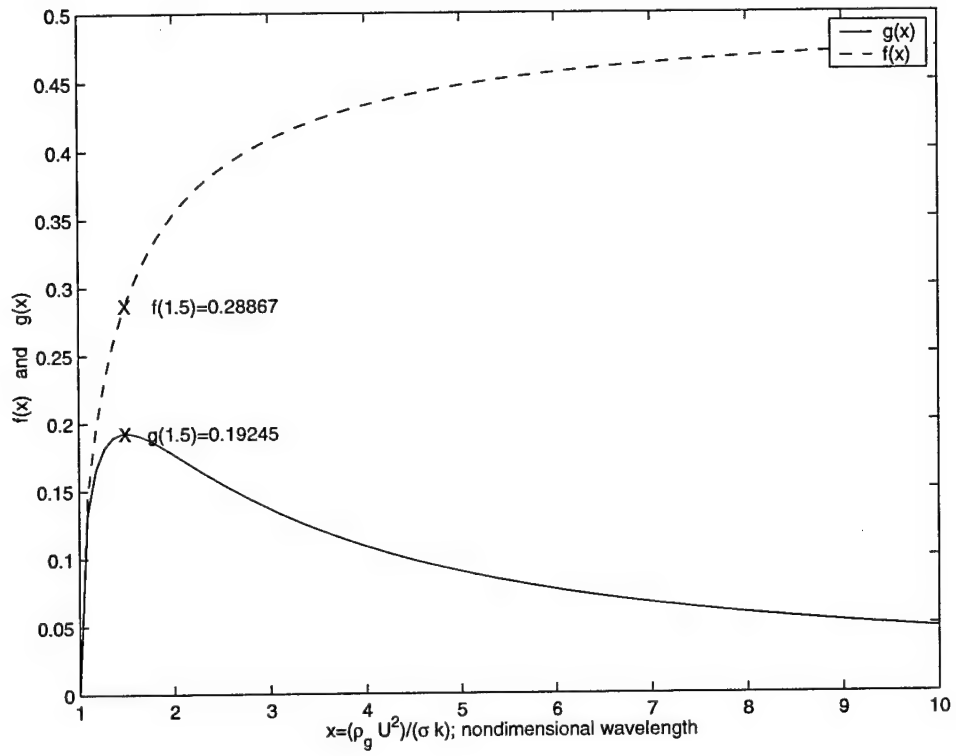
Figure 2: The functions $g(x)$ by Taylor [4] and $f(x) = xg(x)$ by Reitz and Bracco [21] as a function of nondimensional wavenumber $x = (\rho_g U^2)/(\sigma k)$.
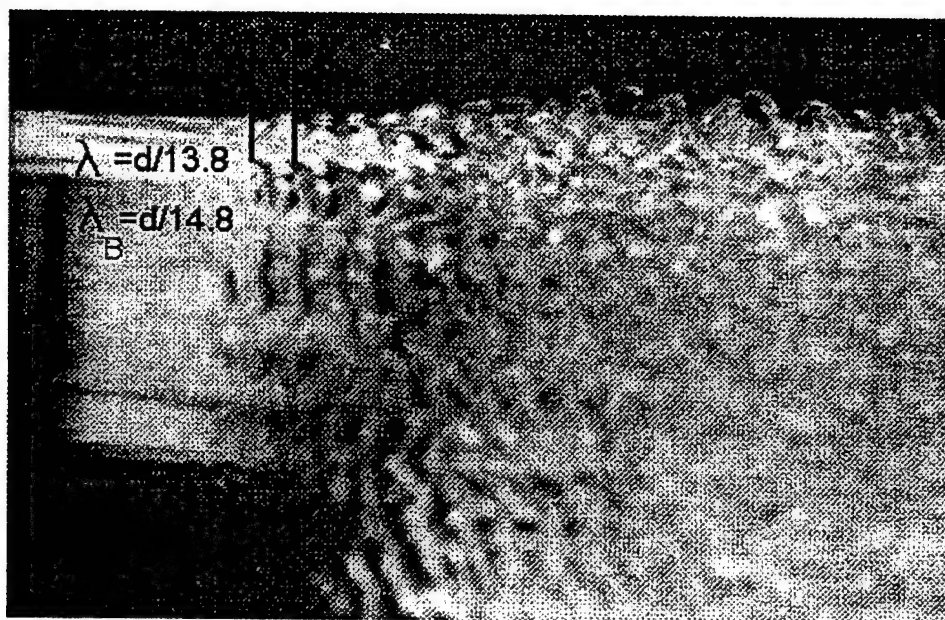
Figure 3: Typical water jet into air in the atomization regime. Experimental image by Hoyt and Taylor [10]. which shows the most dominant wavelength $\lambda = d/13.8$ while Brennen's theory predicts $\lambda_B = d/14.8$. Printed under the permission of *Journal of Fluid Mechanics*.
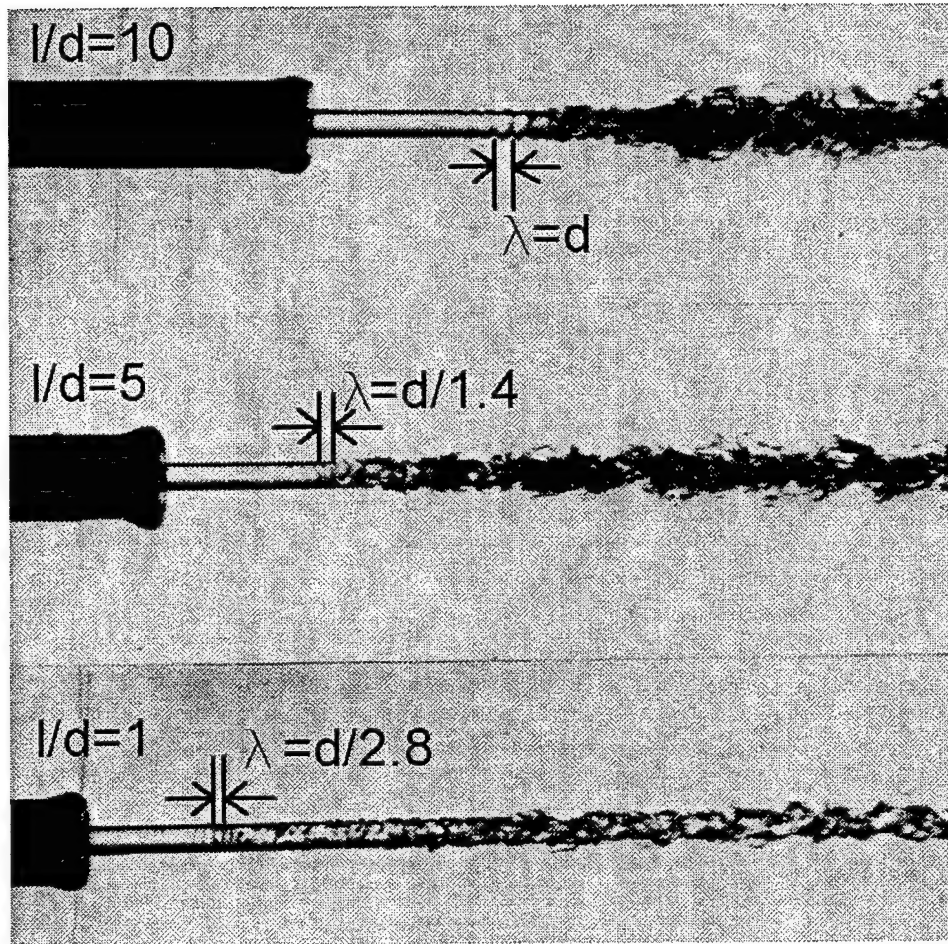
Figure 4: McCarthy and Molloy's experiment [18] for l/d=10, 5, and 1: The most dominant wavelength appears subsequent to laminar region which can be scaled by the Brennen's [9] theory. Printed under the permission of *Elsevier Science*.
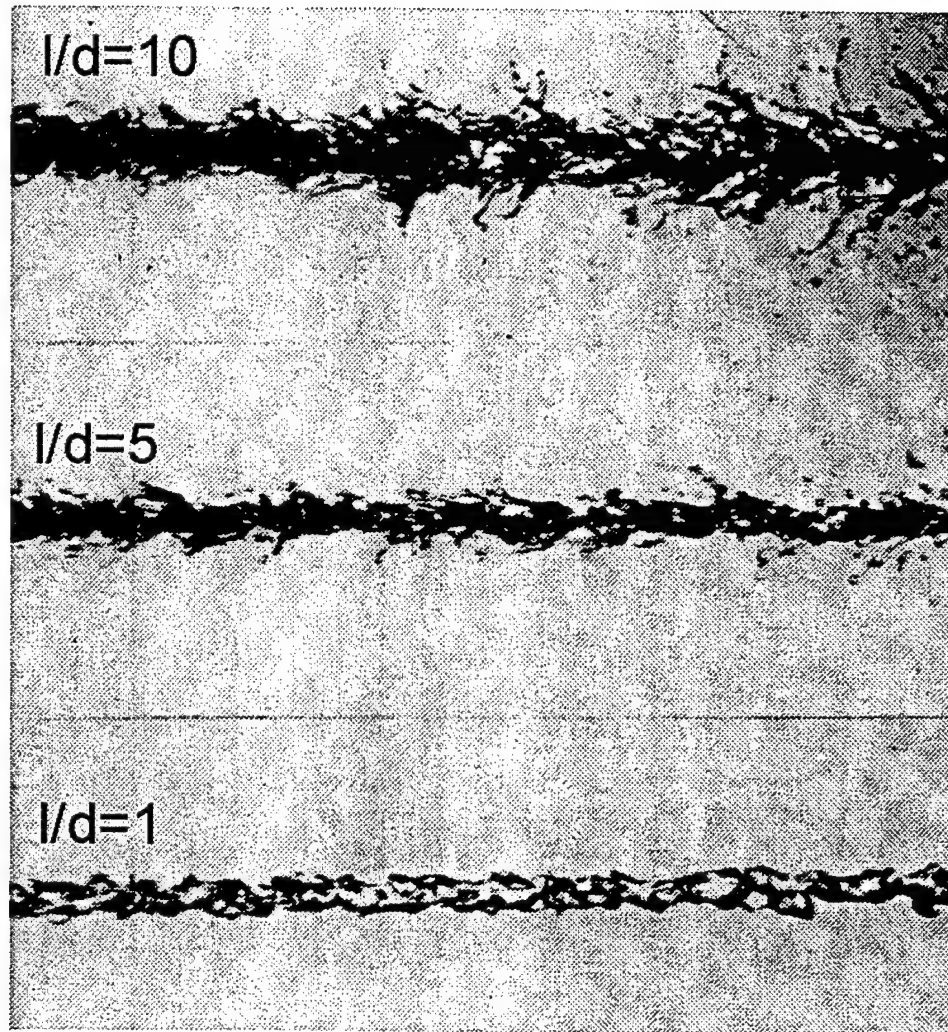
Figure 5: McCarthy and Molloy's experiment [18] for l/d=10, 5, and 1 in the further downstream. Droplet size is not scaled by the most dominant wavelength. Printed under the permission of *Elsevier Science*.
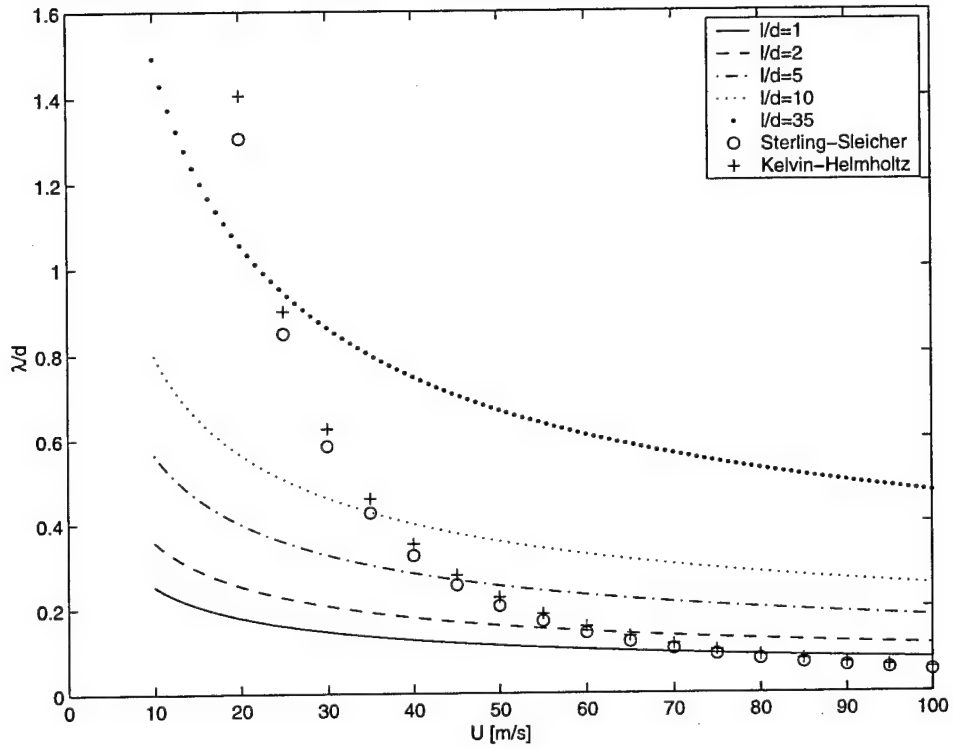
Figure 6: Variation of the theoretically predicted boundary layer waves as well as that of Sterling-Sleicher Eqs. (10) and Kelvin-Helmholtz Eq. (14) as a function of jet speed for various l/d. Water jet into air is considered: $\nu = 1.12 \times 10^{-6} m^2/s$ and $d = 1\ mm$. 2nd wind-induced regime for $26.76\ m/s < U < 48.86\ m/s$ and atomization regime for $U > 48.86\ m/s$.
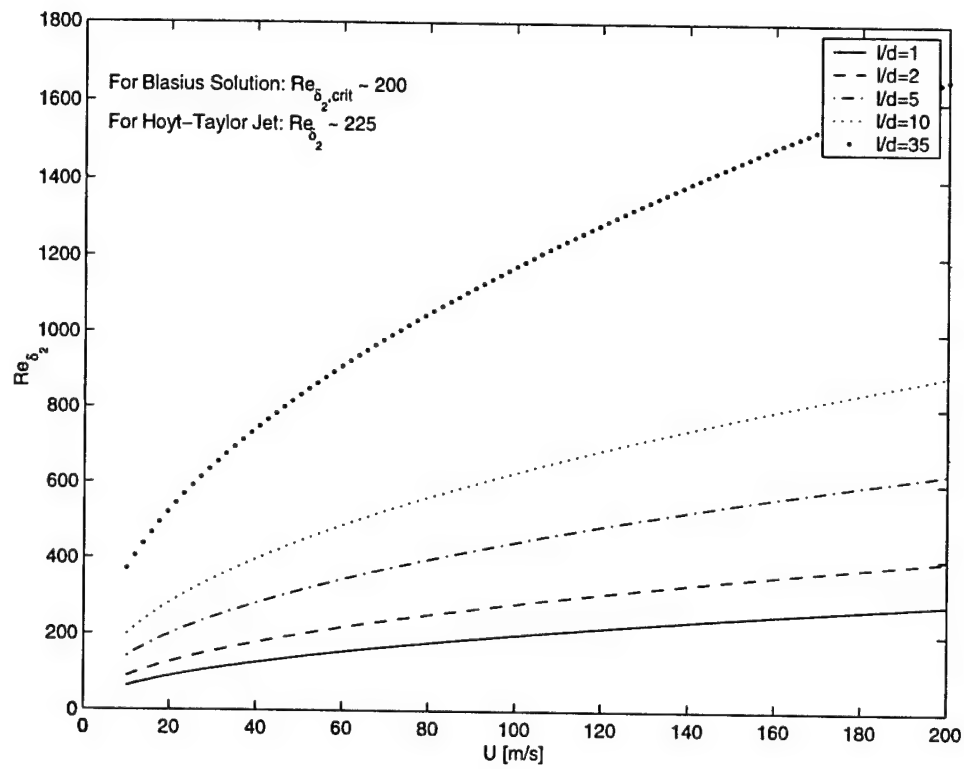
Figure 7: Variation of the theoretically predicted Reynolds number based on the momentum thickness as a function of jet speed for various l/d. The same case mentioned in Fig. 6.

7   Appendix C - Acoustic Interactions with Liquid Jet

Yoon*, S. S. and Heister, S. D., "Modeling Atomizing Jet due to Boundary Layer Instabilities".

Modeling Atomizing Jet due to Boundary Layer Instability

Sam S. Yoon [*] and Stephen D. Heister[†]

[*] Graduate Research Assistant, [†] Professor, School of Aeronautics and Astronautics, Purdue University, W. Lafayette, IN

Abstract

A nonlinear model has been developed to assess the time evolution of an axisymmetric liquid jet using a boundary-element method. Vorticity transported from the boundary layer in the orifice passage to the free surface is modeled using a potential ring vortex placed at the orifice exit plane. The vortex strength is uniquely determined from the Kutta condition and information regarding the boundary layer thickness at the orifice exit plane. It is shown that primary breakup can occur even in the absence of the gas phase. Using a secondary stability analysis after Ponstein [1], the size of the droplets is estimated based on the size of the ring-type structures shed from the periphery of the jet. Computed droplet sizes are in reasonable agreement with experimental data, although turbulence effects obscure some comparisons.

1 Introduction

The hydrodynamic instability of liquid jet flow has been of great interest to fluid dynamicists for more than a hundred years. Despite the numerous analytical, experimental and numerical studies over the years, the jet flow is too complex to be understood completely. While the flow in the first few diameters downstream from the nozzle exit greatly depends on the internal flow effect, the relative motion between the main liquid stream and the gas plays an important role farther downstream. Droplets pinched off from the liquid stream experience drag and therefore result in breakup. In addition, collision between one droplet and another enhances the complexities of the jet atomization process. These phenomena are greatly dependent on the initial flow condition near the nozzle exit.

Two upstream flow conditions that may affect the initial flow condition at the nozzle exit are turbulence and cavitation. While DeJuhasz [2] claimed that turbulence may be the most important factor in jet breakup process, it was later shown by Bergwerk [3] that the turbulence eddy viscosity in the applicable range of Reynolds numbers is not large enough to cause the disintegration of the jet. Bergwerk suspected that cavitation was the main source that produces an amplitude large enough to cause the jet breakup.

In the absence of cavitation and the substantial reduction of turbulence fluctuations through the use of a nozzle geometry promoting highly favorable pressure gradients [4] atomization is still known to occur. This suggests that there are other mechanisms that lead to the disintegration of the jet. Rupe [5] observed the velocity profile relaxation has a key role in influencing the jet breakup. The boundary layer instability analysis by Shkadov [6] predicted the unstable short wavelength of the free surface of the jet. In the sudden absence of nozzle wall and ignoring jet divergence (i.e. parallel flow), the jet velocity at the free surface will start to accelerate from the stagnant condition consistent with the no slip boundary condition inside the nozzle. This condition results in a point of inflection in the velocity profile, which is inviscidly unstable according to Rayleigh's theorem (see Schlichting [7] and Panton [8]); vortices start to form at the point of inflection and cause a roll-up at the critical layer and eventually the instability.

The influence of gas density, and hence aerodynamic forces on the interface, has been widely investigated experimentally. Reitz and Bracco [9] observed a substantial difference in the atomization mechanism when the liquid jet was injected in different gases (i.e. $\rho_{N_2} = 6$ kg/m^3 and $\rho_{Xe} = 23$ kg/m^3). Wu et al [10] have reported a change in droplet size for primary atomization when a different gas density was tested for the same liquid jet. From this basis one may conclude that the aerodynamic interaction at the surface of the jet does alter wave growth, i.e. that aerodynamic forces are of sufficient magnitude to contribute to the instability. However, Hoyt and Taylor[4] did not see differences in wave structure with differing external airflows in their experiments. The axisymmetrically disturbed short wavelength observed near the nozzle exit is present regardless of magnitude or direction of the air velocity as noted in Fig. 1–(a). Hoyt and Taylor

59

concluded that this phenomenon has "no discernible effect of relative air velocity". In spite of Hoyt and Taylor's effort in this regard, their issue has not well been recognized in the atomization community.

Shkadov's theory states that the velocity profile of liquid is independent of gas density, which seems contradictory to the experimentally observed trend. This dilemma is probably due to the high gas-liquid density ratio which causes the growth rate due to the aerodynamic term to dominate as compared to the growth rate due to the vortices, thereby invalidating Shkadov's theory. In addition, the droplet sizes are strongly dependent on secondary atomization at high jet speed and high gas density conditions. For many years, the notion that vorticity at the nozzle exit being responsible for the atomization has been overshadowed by the aerodynamic linear theory and the experiment which showed a significant difference in spray structure with the change in gas density. Clearly the influence of the gas is regime dependent, but the fundamental instability mechanism is present in all regimes.

In a later paper by Hoyt and Taylor [11], they claimed that the axisymmetrically disturbed wavelength shown in cavitating flow over bluff body in Fig. 2 is similar to the wavelength seen in their water jet experiment. Brennen had performed linear boundary layer instability analysis of Rayleigh's equation and provided the nondimensionalized frequency, $\gamma = 0.175$, to be the one that gives the maximum amplification at flow separation point. Using $\gamma = 0.175$ for Hoyt and Taylor's case, the theoretically predicted wavelength was $\lambda = (1/14.8)d$ and the experimentally observed wavelength was $\lambda = (1/13.8)d$ as shown in Fig. 1–(b). The comparison between theory and experiment was excellent.

Based on the evidence that Hoyt and Taylor had presented, the notion that boundary layer instability is responsible for the axisymmetrically disturbed waves near nozzle exit is too compelling to ignore. For this reason, we have investigated the effect of boundary layer thickness at the nozzle exit on the liquid jet. While the entire numerical method is based on the potential theory, it may sound contradictory to model the effect of viscosity with the current numerical model. However, our intention is to 'lump' the vortices at the nozzle exit and therefore simulate the abrupt change in boundary condition for the liquid jet. This is traditionally known as superposition theory and is somewhat similar to what has been known as the 'vortex-method' (see Chorin [12, 13, 14]) of series of singular vortices.

A complete summary of the boundary layer instability is discussed and contrasted in the recent study by Yoon and Heister [15]. Table 1 provides the summary of all flow regimes mentioned in this paper.

Table 1: Characteristics of various flow regimes

Flow Regime	Rayleigh	1st WI	2nd WI	Atomization
Reitz's Criteria	$We_g < 0.4$	$0.4 < We_g < 12$	$12 < We_g < 40$	$We_g > 40$
Reitz-Bracco's Recom.[a]	Rayleigh	Sterling-Sleicher[b]	Kelvin-Helmholtz	Reitz-Bracco[c] (Taylor)
Wavelength Range[d]	$\lambda > 4.12d$	$0.73d < \lambda < 4.12d$	$0.24d < \lambda < 0.73d$	$\lambda < 0.73d$
Dominant Force[e]	Capillary	Cap., visc., dynm.	Moderate dynamic	Strong dynamic
Dominant Inst. Mech.[f]	Capillary	BLI	BLI	BLI & turbulence
BLI Effect	None	S BL: Wiggles		Finger-like droplets, lam.[g]
		M BL: Moderate rollup & stretching		Weak BLI, transitional
		L BL: Strong rollup & stretching		turbulence dominates

WI: wind induced   [a] applicable eqn. for shear layer driven instability
[b] for $ka < 1.0$ [c] for $ka \rightarrow \infty$
[d] based on Reitz-Bracco's recommendation using Reitz's criteria
[e,f] for $\rho_l / \rho_g > 500$; shear layer driven instability is negligible [16]
BLI: boundary layer instability   S: small M: medium L: large
note: the range of S,M,L cannot be determined because they differ at different nozzle geometry and flow condition
[g] this flow is governed by inviscid Orr-Sommerfeld eqn.

2 Modeling

The model is based on an unsteady axisymmetric potential flow of a liquid exiting a round orifice in the absence of a gas-phase medium. A bound ring vortex is utilited to simulate viscous effects associated with vorticity in the boundary layer formed in the orifice passage. Carefully controlled experiments have shown a reasonably axisymmetric structure during the early stages of the free surface instability. Fig. 3 provides a schematic representation of the geometry and appropriate nomenclature. The size of Rankine vortex [17] is defined as R_c which will be discussed in detail in a later section. A vortex ring of strength Γ_v and overall radius $\bar{r}$ is assumed to lie at the orifice exit plane. A computational domain represented by a simple

cylindrical column of length z_l with a hemispherical cap is selected to initialize the calculation. Constant nodal spacing, Δs is employed along this domain and nodes are added as the jet issues forth from the orifice. Fig. 4 compares the actual flow condition and the current superposition modeling. The concentrated vortices at the filament vortex-ring are transported to the free surface and therefore the jet surface is untable. We choose the liquid density, ρ, jet average exit velocity, U, and orifice radius, a as dimensions in the problem.

The formulation of the BEM starts with the integral representation of Laplace's equation, $\nabla^2 \phi = 0$, with ϕ being the velocity potential. Following Liggett and Liu [18], the integral form for this relation is:

$$\alpha\phi(\vec{r}_i) + \int_\Omega \left[\phi\frac{\partial G}{\partial \hat{n}} - qG\right] d\Omega = 0 \tag{1}$$

where $\phi(\vec{r}_i)$ is the value of the potential at a point $\vec{r}_i$, Ω is the boundary of the 3D domain, and G is the free space Green's function corresponding to Laplace's equation. The detailed procedures for solving Eq. (1) using BEM is available in the literature [19, 20, 21, 22].

The unsteady Bernoulli equation provides the boundary conditions along a free surface [23]. This condition provides a connection between the inertial, hydrostatic, and capillary forces at the interface. Because the surface curvature, κ depends nonlinearly on the surface shape, the overall expression is nonlinear. Using the nondimensionalization described previously, the appropriate dimensionless form is:

$$\frac{D\phi}{Dt} = \frac{1}{2}|u_t|^2 - \vec{u}_t \cdot \vec{u}_v - \frac{\kappa}{We} - P_g + \frac{Bo}{We}z \tag{2}$$

where P_g is the dimensionless gas-phase pressure (assumed to be zero in the present studies), and We and Bo are the Weber and Bond numbers characterizing the flow: $We = \rho U^2 a/\sigma$ and $Bo = \rho g a^2/\sigma$. This Bernoulli Eq. (2) is the 'nonlinear' free surface boundary condition for the Laplace equation. This equation is marched in time using a 4th order Runge-Kutta time integration. The curvature (κ) of the highly-distorted surface is determined with full 4th-order accuracy as well [24] We have used the curvature definition from Smirnov [25]. The location of nodes on the free surface (i.e. z and r) is calculated by integrating the respective velocity components in time.

Contributions from the ring vortex can be obtained through the principle of superposition for potential flow. Since the Laplacian governing equation is linear, we may superpose the bulk potential flow with the potential vortex-ring:

$$\phi_t = \phi + \phi_v \qquad\qquad u_t = u + u_v \tag{3}$$

where $\vec{u}_v$ is the induced velocities due to vortex ring that can be obtained from the Biot-Savart law [26, 27, 28]. The entire explicit solution of the filament vortex-ring has recently been developed [29]. Here $(\ )_t$ represents the general or 'total' solution of the jet flow. The solution of the vortex ring can be obtained by direct evaluation of Biot-Savart law [28]. The entire explicit solution of the filament vortex-ring has recently been developed [29].

Nodes are repositioned along the distorted surface using cubic splines [30], and nodes can be added (due to fluid exiting the nozzle) or removed (due to atomization events) without user intervention. The current 'high-speed' atomization simulation is more susceptible to numerical instability than the low-speed atomization (i.e. varicose breakup simulation with smooth surface) due to complex surface shape. In addition, the 'necking' region where a droplet is pinched-off experiences a relatively high velocity (i.e. node velocities reach $2 \sim 7$ times that of the jet speed) and therefore 'node-crossing' or 'not-simply-connected domain' sometimes occurs. Thus numerical smoothing is crucial to prevent the numerical instability [31]. We have chosen the filter function by Longuet-Higgins and Cokelet [31]; this filter is designed to eliminate the odd-even mode in the function which contains the highest frequency, known as the Nyquist Rate [32].

The centroid of the vorticity of the viscous flow is regarded as the center of the vortex-ring. The definition of the centroid of the vorticity, weighted in the radial direction is:

$$\bar{r} = \frac{\int_{r=0}^{r=1} r\omega dr}{\int_{r=0}^{r=1} \omega dr} \tag{4}$$

and the vorticity, ω, is defined as:

$$\omega = \frac{\partial v}{\partial z} - \frac{\partial u}{\partial r} \tag{5}$$

where u and v are the velocities in axial and radial direction respectively. Assuming $\partial v/\partial z \approx 0$, i.e. parallel flow at the orifice exit plane, the centroid can be written as:

$$\bar{r} = \frac{\int_{u(r=0)}^{u(r=1)} r\,du}{\int_{u(r=0)}^{u(r=1)} du} \tag{6}$$

Substituting the definition of the displacement thickness, δ_1, [33] into Eq. (6) and applying integration by parts give the following result:

$$\bar{r} = 1 - \delta_1 \tag{7}$$

δ_1 can be approximated using a Navier-Stokes solution of the internal flow, or appropriate analytical methods such as Blasius solution [33] for a flat-plate or Thwaites [34] equation for a converging/diverging nozzle.

The vortex strength Γ_v is defined as the circulation that is taken about any path enclosing the vortex-ring.

$$\Gamma_v = \oint \vec{u} \cdot d\vec{I} \tag{8}$$

where $\vec{u}$ is the internal flow velocity of the injector orifice and $\vec{I}$ is the integration path. The integration is taken in counterclockwise around the path. Assuming $\partial u/\partial z = 0$ and a no-slip boundary condition at the wall, the surface integral in Eq. (8) can be written as follows for the path we have chosen:

$$\Gamma_v = \Delta z \tag{9}$$

where Δz is the length scale which is comparable to the most dominant wavelength, λ. Γ_v is always positive and will induce counterclockwise motion (this is based on the upper half of the flow going from left to right). Eqs. (7) and (9) uniquely determine the location and strength of the vortex from first principles. No additional calibration constants are used in the formulation.

It is possible to set $\Delta z = \lambda$, predicted by Brennen's result [35] since the circulation causes the axisymmetrically disturbed wavelength observed at the nozzle exit. The λ observed in Hoyt and Taylor's case [11] is a function of the momentum thickness δ_2, scaled by the parameter $\gamma = 0.175$. Presuming a high contraction ratio of the nozzle reduces the turbulence fluctuation, Hoyt and Taylor [11] assumed a laminarized flow over a flat plat and therefore they utilized the Blasius [33] solution to approximate the momentum thickness.

$$\Gamma_v = \lambda = \left(\frac{2\pi}{0.175}\right)\delta_2 \tag{10}$$

Addition of the Biot-Savart Law to the inviscid jet of BEM is expected to cause instability at the free surface that eventually forms a series of toroidal ligaments pinched off from the main body of the jet. Using Gauss's divergence theorem, we have transformed the surface integral to a line or contour integral and therefore have obtained the cross-sectional area of the ligaments as well as the centroids of the area. We have obtained the volume of the ligaments using the theorem of Pappus-Guldinus [36] which relates a volume of revolution to its generating cross-sectional area.

While the current model is based on an axisymmetric formulation, actual primary atomization is a 3-dimensional phenomenon (see Fig. 5-(a)). The model result of pinch-off, as shown in Fig. 5-(b), is not a droplet but a vortex-ring with a significant amount of circulation around the ring surface. The circulation around the ring surface is large enough to cause instability in circumferential direction. In reality, this is the secondary instability which occurs before the vortex-ring pinch-off. The current model assumes that droplets are formed from a secondary instability on annular ligaments shed from the periphery of the jet. This amounts to a decoupling of primary and secondary instability which permits the axisymmetric analysis of the jet itself.

Ponstein[1] investigated the linear stability of a liquid column with circulation Γ_r and radius a_r. Ponstein's result is utilized to predict the dominant wavelength k in the circumferential direction:

$$\omega^2 = \left[\frac{1-k^2}{We_r} + \left(\frac{\Gamma_r}{2\pi}\right)^2\right] k\frac{I_1(k)}{I_0(k)} \tag{11}$$

where $We_r = \rho U^2 a_r/\sigma$. Note that the ring radius, a_r, is the non-dimensional variable. This expression is solved to determine the $k = k_{max}$ value attributed to the maximum growth rate, ω for a given ring geometry and circulation.

3 Results and Discussion

3.1 Grid Convergence Study

Hoyt and Taylor's case is used for the grid convergence study (i.e. $We_{l,a} = 19057$, $\bar{r}^* = 0.99$, and $\Gamma_v^* = 0.139$). Let Δs represent the grid spacing for BEM nodes. While Hilbing [24] mentioned that $\Delta s = 0.300$ is fine enough to resolve the low speed "Rayleigh's breakup" where waves are of length comparable to the orifice diameter, much finer grid resolution is required for high speed atomization where the wavelengths are comparable to the boundary layer thickness at the orifice exit. For this reason, the grid resolution for the present studies taxes the current computational capabilities of even advanced Linux-based compute clusters. In Fig. 6, it is shown that the axial location for the first ring pinch-off is reasonably insensitive to mesh spacing for $\Delta s < 0.030$. However, grid function convergence studies indicate that a smaller mesh spacing is required for the accurate prediction of the droplet characteristics in the atomization regime. About 3000 $\sim$ 5000 droplets were collected for each run for statistically reliable data; results for drop statistics are shown in Table 2. The Sauter Mean Diameter, SMD, (drop whose diameter replicates the average surface area of drops in the population) is the most frequent measure used in the atomization field. Table 2 shows that the $\overline{N}_D$ per ring, its Standard Deviation, and SMD are converged to a reasonable accuracy at $\Delta s/a = 0.012$. Thus we have used $\Delta s/a = 0.016$. In addition, the standard deviation of $\overline{N}_D/ring$ does not change much after $\Delta s/a < 0.016$. Similarly, the time-averaged droplet velocities (i.e. $\bar{u}_D$ and $\bar{v}_D$) do not change much either for this mesh spacing. This result also validates the pinch criteria employed for a ligament breakup: a pinch-off is assumed when the distance between binary nodes is less than a certain tolerance, ε. The range of the tolerance is 20 $\sim$ 70% of the mesh spacing. The ligament size is also insensitive to the range of the pinch-off criteria.

Table 2: Grid convergence test

$\Delta s/a$	$\overline{N}_D/ring$	Stnd. Dev.	SMD/d	$\bar{u}_D/U$	$\bar{v}_D/U$	$\overline{U}_D/U$
0.050	10.07	4.68	0.0995	0.608	0.442	0.752
0.040	10.87	8.71	0.0962	0.689	0.430	0.812
0.030	14.20	11.33	0.0841	0.790	0.479	0.924
0.020	12.46	8.46	0.0729	0.770	0.419	0.876
0.016	10.44	6.65	0.0623	0.779	0.404	0.877
0.012	10.87	6.44	0.0588	0.796	0.411	0.896

It is uncertain when to stop the simulation since the jet can grow indefinitely depending on injection conditions. For the simulations conducted to date, the time required for the first pinching event is typically around $t^* \approx 1.7$. We found that collecting about 300 to 400 rings provides stastically reliable data. This would give roughly 3000 $\sim$ 5000 droplets. Thus we typically stop our calculation at about $t^* \approx 5.0$. Table 3 shows that the solution is insensitive when $t^* > 4.0$.

Table 3: Effect of calculation length on drop statistics

t^*	SMD/d	N_D	$N_D/ring$	Stnd. Dev.
2.0	0.0628	88	7.97	3.329
3.0	0.0623	856	10.44	6.665
4.0	0.0635	2582	11.08	7.936
5.0	0.0655	5132	11.48	7.985

3.2 Hoyt and Taylor's Case

The complete simulation of the Hoyt and Taylor's jet [4] is shown in Fig. 7. The jet structure is initially assumed to be a simple cylinder with a hemispherical tip as shown in Fig. 3 and its evolution is simulated via time integration. The simulation is completed at $t^* = 5.0$. A slight 'swelling' is observed at $t^* = 1.0$ and a fluctuation of the jet surface is seen at $t^* > 2.0$. The velocities induced by the bound vortex are large

enough to penetrate the jet surface and it results in primary atomization. It should be noted that most liquid ligaments pinching from the jet surface are in the 'roll-up' motion in counterclockwise direction while the mean velocity of the ligament is in the stream-wise direction. Similar structures are noted in Fig. 5-(a) in a closeup view of the Hoyt and Taylor experiment. The mean velocity of most droplets are in stream-wise direction as droplets motion propagates along with the main jet stream, the most dominant convective source. The counterclockwise roll-up motion is a strong evidence that the boundary layer instability is the fundamental cause of the primary atomization. The counterclockwise roll-up motion would not have been observed if the jet were turbulent (see Figure–(1) of Wu et al. [16]). The mean velocity of most droplets are in stream-wise direction as droplet motion propagates along with the main jet stream, the most dominant convective source.

It is interesting to note that the liquid core appears naturally as a consequence of the calculation. While the current model is based on the axisymmetric formulation (2D), the real instability is three-dimensional (3D). It is obvious that the loss of liquid mass of the model prediction is noticeably greater than that of actual 3D jet and, thus, it forms the liquid core. Another possibility for accounting for the difference in the actual jet and the model jet may be due to the incomplete simulation of the actual jet. Presumably, the entire jet should be streaming down far away from near nozzle exit region.

All droplets pinched-off within $t^* < 5.0$ are shown in Fig. 7. It is seen that droplets are pinched-off as soon as the primary instability is initiated; this may seem contradictory while experiment shows, in Fig. 1–(a), that the primary instability undergoes the transitional process to result in the primary breakup of the secondary instability. The difference is observed because: the model is based on axisymmetrical formulation and does not include viscous effects. During the transitional region, the viscous force holds the fluid together untill the vorticities are greater to win over the viscous force.

Nevertheless, the model predicts the droplet diameter (i.e. $d/10 < D < d/20$) which is well within the order of the actual SMD of Hoyt and Taylor's experiment (i.e. $SMD_{exp} \approx d/15.5$), as shown in Fig. 13. Though the loss of mass in the simulation is larger than that observed experimentally, the circulation around the pinch-off ring (Γ_r) is large enough to give the short wavelength which, in return, accounts for the less loss of mass in the 3D actual jet.

The pinch-off droplet velocity vs. its location is plotted in Fig. 8. It is shown that the total droplet velocity ($U_D = \sqrt{u_D^2 + v_D^2}$) increases slightly with respect to the pinch-off axial-location (z) because both u_D and v_D increase with z. This is consistent with Wu et al's observation [16] (see Figure–(3) of Wu et al. [16]). While our axial velocity (i.e. $u_D = 0.809$) is in excellent agreement with Wu et al's result (i.e. $u_D = 0.760$) our model over-predicts the radial velocity (i.e. $v_D = 0.424$) as compared to the experimental result (i.e. $v_D = 0.07$). The difference is probably due to (i) the recording location of the data: while our data was recorded at the droplet pinch-off location, Wu et al's data was recorded at a few nozzle diameter away from the centerline (i.e. $r/d \sim 2$ or 3) where droplet had already experienced drag. This could possibly reduce the droplet speed.

Newton's 2nd law is applied to describe the motion of a droplet assuming drag to be the only external force acting on a droplet. The equation of motion of a droplet can be written as:

$$m\frac{D\vec{u}_D}{Dt} = \frac{1}{2}\rho_g C_D A_p \mid \vec{u}_g - \vec{u}_D \mid (\vec{u}_g - \vec{u}_D) \tag{12}$$

where A_p is the projected area of a droplet $\vec{u}_g$ and $\vec{u}_D$ are gas and droplet velocity, respectively. C_D is the drag coefficient correlation for the solid-sphere given by Hwang et al [37] below:

$$C_{D,S} = \begin{cases} \frac{24}{Re_D}\left(1 + \frac{1}{6}Re_D^{2/3}\right) & Re_D \leq 1000 \\ 0.424 & Re_D > 1000 \end{cases} \tag{13}$$

where $Re_D = UD/\nu_{air}$. The dynamics of a droplet of Hoyt and Taylor's case is shown in Fig. 9. It indicates that the droplet must travel a distance of 47 d to reduce the initial radial droplet speed (i.e. $v_D = 0.424\,U$) to $v_D = 0.2\,U$. Thus the drag alone cannot explain the difference between our model result (i.e. $v_D = 0.424\,U$) and the experimental observation (i.e. $v_D = 0.07U$). (ii) It is possible that the drag coefficient is greater than $C_D = 0.518$ for a solid-sphere from Hwang et al [37] because C_D of an elliptically distorted droplet in shape is usually greater than that of a solid-sphere. (iii) Another possibility is that the absence of viscosity in our model may have induced extremely high radial velocity during the pinch-off event, especially at the 'necking' computational node; only the viscosity effect can reduce the local pinch-off velocity.

We have observed that the droplet size (D) is independent (or more likely random) of the axial location, a smaller D is observed with larger radial location. We have enlarged the photo of Fig. 1–(a) and were able to confirm that the droplet closer to the surface is larger than the one farther away from the surface.

It was mentioned in the previous section that the model takes advantage of Ponstein's Eq. (11) to model the instability of a pinch-off vortex-ring. Using Eq. (11), the number of waves or droplets (N_D) per ring is predicted and plotted as a function of the circulation, Γ_r. Their relationship is parabolic and the least square fit is available in Fig. 10. Thus if Γ_r is known, a rough estimate of N_D can be produced. Fig. 11 illustrates the relation between the number of circumferential waves and the core size of a pinch-off vortex-ring. As the size increases, a larger number of waves appear. This is exactly the opposite phenomenon of the elliptical instability of Widnall [38] and Sullivan: they observed a larger number of waves when the core size decrease. It should be noted that the mechanism of surface tension driven instability (i. e. liquid vortex-ring in air) is different from the shear layer driven elliptical instability [39, 40, 41, 42] (i.e. liquid into liquid or gas into gas).

Hoyt and Taylor [4, 11, 43] reported dramatic changes in jet configuration even with small (i.e. 10 ppm) polymer addition to the water. As a result of anisotropically stretched macromolecules in the fluid [44, 45], the surface drag is greatly reduced and small-scale surface disturbances are eliminated. However, the polymer addition does not reduce the large-scale disturbances. In fact, Hoyt et al [43] reported that the polymer solution amplified the large-scale disturbances while damping out the small-scale disturbances. The instability of the large-scale waves is governed by Rayleigh's breakup, $\lambda = 4.51d$, in sinuous mode even for high speed jet. Since potential superposition theory cannot account for the complex governing physics of the polymer fluids, only non-polymer jet flow is simulated in this report.

3.3 Effect of Weber Number for Fully Developed Flow

We may consider a very long pipe flow with constant diameter (i.e. $l/d = \infty$) which would result in a fully-developed flow regardless of the jet speed, U. In this case, the jet speed determines the regime of the jet instability because the momentum thickness is fixed (and therefore the circulation amount is constant) for all speeds. Thus, more atomization is expected in a flow with the high jet speed.

Eventually, the boundary layer instability disturbance will result in jet breakup regardless of the jet speed. If U is small that $We_{l,a} = 100$, the jet similar to Rayleigh's breakup is observed as shown in Fig. 12 (note: no atomization is observed for $t^* < 5.0$). If U increases up to $We_{l,a} = 1,000$, the boundary layer instability effect is more eminent; 'stretching' is observed while BLI is competing with σ. When $We_{l,a} = 10,000$, the surface tension force is greatly reduced and therefore the atomization event occurs at a faster rate (little competing behavior since dynamics force is dominant).

Table 4: Effect of Weber number on drop statistics. Collected Data up to $t^* = 5.0$

$We_{l,a}$	SMD/d	N_D	$\overline{N_D}/ring$	Stnd. Dev.
1,000	0.1034	1514	3.03	1.96
10,000	0.0733	5172	8.66	5.87

3.4 Effect of Jet Speed

Wu et al [16] provided both an empirical model and experimental observations for the Sauter Mean Diameter (SMD). Their model is based on Kolmogorov length scale [46]:

$$\frac{SMD}{\lambda} = \frac{133}{We_{l,\lambda}^{0.74}} \tag{14}$$

Note that Wu et al [16] introduced $\lambda = d/8$ from Hinze [47]. The above expression then becomes:

$$\frac{SMD}{d} = \frac{77.5}{We_{l,d}^{0.74}} \qquad\qquad \frac{SMD}{d} = \frac{46.4}{We_{l,a}^{0.74}} \tag{15}$$

Here SMD is defined as:

$$SMD = \frac{\sum_{i=1}^{N_D} D_i^3}{\sum_{i=1}^{N_D} D_i^2} \qquad (16)$$

where N_D is the number of droplet collected.

It is well known that the droplet size varies significantly within the atomization regime. Wu et al [16] reported the droplet size variation with U for turbulent water jet into air. Hoyt and Taylor's experiment had been carried out for the Bernoulli pressure $\Delta P < 60 \ psi$; no result with higher ΔP is reported [4, 11, 48]. However, we hypothesized the increase in ΔP for Hoyt and Taylor jet. The result has taken the jet speed up to $U = 40 \ m/s$ which corresponds to $\Delta P \approx 116 \ psi$ or slightly higher for accounting some pressure loss within the nozzle. The final result for Hoyt and Taylor's case [4] is shown in Fig. 13. Using the methodology employed in the prior section with no calibration constants, the model predicts the Sauter Mean Diameter, SMD, with reasonable accuracy. As shown in Fig. 13, there is a steep gradient at jet speed around $U \approx 20 \ m/s$ for Wu et al [16] turbulent jet experiment. Our model result overlaps with that obtained by Hoyt and Taylor. It is interesting to observe that Wu et al's data is also similar to our result and that of Hoyt and Taylor at about $U \approx 20 \ m/s$. While Wu et al noted this as the region of 'uncertainty', it is possible that the roll-up motion was competing with the turbulence and thus the perceptible effect of the roll-up motion appears as shown in Fig. 13.

As $U > 20 \ m/s$, differences between the calculations and the experiments merge. It is known that linear analysis [49] overpredicts the droplet size (by less than 20%) because it neglects the satellite droplet mass due to the nonlinear effect [50, 51] which yields multiple crests per wavelength. Ponstein's Eq. (11) is a linear analysis and thus it also may tend to overpredict the droplet size. However, 20% or smaller SMD difference does not explain the difference we see in Fig. 13 at higher jet speed. It is due to the fundamental difference between the boundary layer instability jet and the turbulent jet: Boundary layer instability jet is scaled by the momentum thickness [35] and the turbulent jet is scaled by the Kolmogrov length scale, l_k or/and turbulence eddy characteristics length of kinetic energy, l_i [16]. Wu et al derived the empirical formula using the 'surface kinetic energy' argument which gives SMD scaled by $\sim 1/U^{1.48}$. Thus the governing length scale (i.e. l_k and l_i) decrease significantly at about $U \sim 20 \ m/s$. On the other hand, SMD of the boundary layer instability jet is scaled by δ_2: $SMD \sim 1/U^{0.5}$ and thus its change with respect to U is relatively moderate as shown in Fig. 13.

It is noted that, in reality, cavitation might occur at the sharp corner of the nozzle entry during this high speed flow ($U \sim 40 \ m/s$) because it is known that the cavitation magnitude increases as the jet speed increases [52]. In addition, the jet may become turbulent if $Re_{\delta_2} > Re_{\delta_2, crit}$ due to increase in U (i.e. $Re_{\delta_2} \propto U^{1/2}$). In Fig. 14, the jet becomes more stable (or less atomization) as U increases. This is consistent with Rupe's observation [5]. As U increases, the nozzle exit velocity profile becomes flatter which contains less circulation. One may imagine the limiting case of such condition: $U \to \infty$ ($Re_d \to \infty$) and thus inviscid flow with the perfectly flat velocity profile which contains no circulation at the nozzle exit. In this limiting case, the jet is unconditionally stable unless it is perturbed by other instability mechanisms. If the circulation at the nozzle exit increases, the jet is more unstable. However, the greater stability of the higher speed BLI jet structure does not necessarily mean that the higher speed jet produces lesser number of droplets. In fact, the circulation of the pinch-off ring for the higher speed jet is greater and therefore it results in the smaller droplet size and more total number of droplets up to a certain limit (note: the limit has not yet been determined in this study). In Fig. 15, it is shown all droplet statistics (i.e. total number of droplets, N_D, and its value per ring, N_D/ring, and its standard deviation) increase with increasing U. This indicates that the droplet statistics becomes more unstable as U increases.

In summary,

- The SMD of the boundary layer jet is scaled by $1/U^{0.5}$ while that of the turbulent jet is scaled by $1/U^{1.48}$.

- The smaller circulation with increasing U at the nozzle exit yields more stable jet structure.

- On contrary, the circulation around the pinch-off ring contains the larger circulation with increasing U. Thus it yields the smaller droplet size and more unstable droplet statistics.

3.5 Effect of Exit Plane Boundary Layer Thickness

Changing the ratio of nozzle length-to-diameter (l/d) is essentially the same as changing the boundary layer thickness for the constant diameter pipe flow. The effect of l/d for the jet breakup has been investigated by many researchers [53, 54, 55, 9, 56].

For the Rayleigh and 1st wind-induced regime $(We_g < 2.55)$, Sterling-Sleicher's experimental data shows that the breakup (or jet) length, L, decreases with increasing nozzle length, l. This indicates that the velocity profile with thicker boundary layer breaks up faster due to larger roll-up motion at the critical layer. They had also observed the important effect of the velocity profile relaxation as they reduced the aerodynamic effect by decreasing the ambient pressure from 0.98 to 0.2 atm.

For the 2nd wind-induced regime, McCarthy and Molloy [56] also investigated the effect of l/d on atomization mechanism as shown in Fig. 16. The jet is shown up to $z/d < 70$ and the jet speed remains constant. The flow operating condition was: Liquid: 60% glycerol and 40% water by weight, $\rho_l = 103\frac{kg}{m^3}$, $\mu_l = 11cP$, $\sigma_l = 0.0669\frac{kg}{s^2}$, $U = 20\frac{m}{s}$, $d = 2.54mm$, $We_{l,a} = 781$, $Re_d = 4750$, and $We_g = 18.7$ for l/d=0, 1, 5, and 10. We can see that the flow is in the low part of the 2nd wind-induced regime and thus no definite dominating instability mechanism exist (see Table 1). The boundary layer instability is competing with other instabilities such as capillary and viscous force. As to which force should be dominant is determined by the boundary layer thickness during this flow regime. For instance: the instability was not observed for $l/d = 0$. For $l/d = 1$, the relaxation length was about $l_r/d \approx 4.7$. The axisymmetrically disturbed waves (due to primary instability) were seen at this point but the viscous force is large enough to pull the surface structure intact. Only wiggles appear on the surface due to the competition between vorticity and viscosity. For $l/d = 5$, the relaxation length is increased to $l_r/d \approx 5.7$ and the primary atomization is observed (due to secondary instability). For $l/d = 10$, the relaxation length is, again, increased to $l_r/d \approx 6.4$. SMD does not seem to change much from the previous case while the atomizing motion became more amplified due to larger roll-up motion. The increase in relaxation length with larger boundary layer appears to be reasonable; it takes longer distance for the critical layer to develop the roll-up motion for the thicker boundary layer. The roll-up motion causes the jet to be atomized when the circulation is large enough to win against other competing forces such as viscous or/and capillary force. In Fig. 17-(top), the 'stretching' is observed due to capillary force when the jet is atomized. In Fig. 17-(bottom), the computational result for the case is shown where the similar 'stretching' of the capillary force is observed. For the high speed jet like that of Hoyt and Taylor [4, 11], the effect of viscosity and capillary force is of little importance because the jet is nearly inviscid. In fact, the large scale motion of Hoyt and Taylor's jet is governed by the Rayleigh's inviscid analysis [49] which concludes the most dominant wavelength to be $\lambda = 4.51d$.

If the viscosity is strong enough to damp out the 'thin' or small boundary layer instability and thus competing behavior, wiggles on the surface are observed. It is known that the viscosity generally damps out the instability (even though sometimes the instabilities arise due to the viscosity, such as Tollmien-Schlichting waves [7]). In other words, the circulation of the 'thin' boundary layer is not strong enough to result in the atomization in the 2nd wind-induced regime (though 'thin' boundary layer in the atomization regime is strong enough to result in the atomization due to the absence of ν and small σ). The model cannot predict this behavior due to the absence of viscosity, as noted in Table 1. The model, which assumes the inviscid flow, is more unstable than the actual flow due to the absence of viscosity. Perhaps the inviscid flow with rotationality is intrinsically unstable unless the surface tension is relatively large enough to suppress the rotationality or/and dynamic force of the fluid. However, the model predicts that 'stretching' atomization occurs with the 'thick' boundary layer within the 1st or/and 2nd wind-induced regime, as shown in Fig. 17-(bottom). In this case, the atomization occurs in a 'stretching' pattern while the roll-up motion is enhanced by the surface tension force, σ, which tends to keep the surface stable. McCarthy and Molloy's experiment is summarized in Table 5, which shows an excellent agreement between the wavelength predicted by Brennen's boundary layer analysis and the experimental results.

For the atomization regime $(We_g > 40)$, Reitz and Bracco [9] show, in Fig. 6 in their paper, that the cone angle increases with increasing l/d. This trend is evident only in the high gas density environment and with high cavitation in the internal flow. It is well known that increasing gas density results in higher cone angle. It is probably that the radial velocity of droplets (v_D) increases with the gas density, which makes the cone angle greater; Wu et al [10] had observed that v_D increases with increasing gas density. This suggests that increasing l/d for the Reitz and Bracco's case might have had the similar effect (i.e. causing the higher v_D) to cause the higher cone angle.

Table 5: Summary for McCarthy and Molloy's experiment [56]

l/d	Re_x^a	δ_1/d	δ_2/d	Re_{δ_2}	f^b [Hz]	λ^c	λ_{exp}
1	4748	1/40.04	1/103.8	46	22758	d/2.9	d/2.8
5	23738	1/17.90	1/46.41	102	10178	d/1.3	d/1.4
10	47477	1/12.66	1/32.82	145	7197	1.1 d	1.0 d

^{a} where $Re_x = Ul/\nu$ $\quad$ ^{b,c} Brennen's Eqs. (??) and (??), respectively

note: Blasius solution is used for δ_1 and δ_2 estimation

In another experiment for the atomization regime, Hiroyasu et al [54] (i.e. water jet into air) shows that the increase in l/d causes the breakup length L to be smaller (This is consistent with Sterling and Sleicher's observation even though the flow regime is different). However, beyond the maximum value at about $U \approx 60\ m/s$, their behavior shows no clear trend. In addition, this trend could not be observed when Hiroyasu et al [54, 55] changed the ambient pressure from 0.1 to 3.0 MPa; aerodynamic effect is greater.

We have learned that the influence of l/d is difficult to investigate according to these researchers work. The reason is that there are many other mechanisms (i.e. cavitation, turbulence, and aerodynamics) that may be coupled with the effect of l/d. In addition, the influence of l/d becomes less perceptible when the flow regime approaches to the atomization regime. However, we have noticed one clear trend (even though we may draw different conclusion from the work of these researchers): "Thicker boundary layers are more unstable".

For this reason, we have investigated the effect of boundary layer thickness: Three cases for different boundary layer thickness are conducted using the current model (i.e. $l/d = 1$, 2, and ∞). The configuration of the test cases for the Hoyt and Taylor's nozzle is shown in Fig. 18. Only the boundary layer thickness changes while everything else remains constant (i.e. Reynolds and Weber numbers). It is shown in Fig. 19 that the increase in δ_2 results in a larger fluctuation at the early stage of the atomization (even though its effect fades away as t^* increases in Fig. 22). A good explanation for the faster instability growth with larger δ_2 is depicted in Fig. 20: as the critical-layer moves away from the parallel line, it allows a larger roll-up motion which results in larger fluctuation of the jet structure. Note that Lin [57, 58] shows that the critical-layer is located at the point-of-inflection of the velocity profile. Table 6 summarizes the results of three cases considered. A slight increase in SMD is seen with increasing δ_2. This is due to larger droplets arising from larger roll-up motion. The larger fluctuation gives more dispersive N_D distribution as its RMS value increases from Case-1 to Case-3. This dispersive behavior with larger δ_2 is seen in Fig. 21. One may suspect the limiting case of such behavior with the fully developed flow: δ_2 is a maximum under such conditions. A fully developed flow is likely to contain substantial turbulence fluctuation as the laminarized flow is limited only in the entry region. Turbulent flow is expected to have the most dispersive behavior in the droplet distribution. As time progresses, it is difficult to observe the difference between Cases 1 to 3 as shown in Fig. 22. In addition, little change in SMD is found (see Table 6). This is the similar difficulty that the previous researchers [54, 55] had experienced. Even though our current model is not influenced by other effects (i.e. turbulence, cavitation, or/and aerodynamics), we have to agree that the influence of the boundary layer itself is difficult to observe when the spray is in the atomization regime. However, it is clear, as shown in Fig. 23, that Case 3 of 'thicker' boundary layer results in more unstable condition with more atomizations.

Table 6: Model predictions for different boundary layer. Collected data up to $t^* = 5.0$

Case	l/d	δ_1/d	δ_2/d	SMD/d	N_D	$\overline{u}_D$	$\overline{v}_D$	$N_D/ring$	Stnd. Dev.
1	1.0	1/200	1/518	1/15.27	3884	0.809	0.424	11.48	7.98
2	2.0	1/141	1/367	1/15.19	5879	0.817	0.428	11.59	8.25
3	∞	1/6	1/24	1/14.81	8133	0.811	0.457	11.69	8.40

4   Conclusions

A fully nonlinear model has been developed to simulate primary atomization caused by boundary layer instability using superposition of a ring vortex with a potential jet flow. The axisymmetric model employs a boundary element methodology in which the vorticity in the boundary layer at the orifice exit is used to determine ring vortex strength and radial location at the orifice exit plane. Annular ligaments are pinched off the surface in this case; a secondary linear instability analysis due to Ponstein is used to predict the fractionization of the ligaments into individual droplets.

The SMD of the model result agrees well with the actual droplet size of Hoyt and Taylor's experiment. The result of the current model is also compared with the experimental data of Wu et al. [16]. The comparison confirms that the current model predicts the droplet size satisfactorily.

ACKNOWLEDGMENTS

References

[1] J. Ponstein. Instability of rotating cylindrical jets. *Applied Scientific Research*, 8(6):425–456, 1959.

[2] K. J. DeJuhasz. Dispersion of sprays in solid injection oil engines. *Trans. A.S.M.E.*, 53:65, 1931.

[3] W. Bergwerk. Flow patterns in diesel nozzle spray holes. *Proc. Inst. Mech. Eng.*, 173:655, 1959.

[4] J. W. Hoyt and J. J. Taylor. Waves on water jets. *Journal of Fluid Mechanics*, 83:119–127, 1977.

[5] J. H. Rupe. On the dynamic characteristics of free liquid jets and a partial correlation with orifice geometry. *NASA JPL Technical Report*, 32–207, 1962.

[6] V. Y. Shkadov. Wave formation on surface of viscous liquid due to tangential stress. *Fluid Dynamics*, 5:473–476, 1970.

[7] H. Schlichting. *Boundary Layer Theory*. McGraw-Hill, New York, 1979. pp. 461–463.

[8] R. L. Panton. *Incompressible Flow*. John Wiley and Sons, 1996. Second Edition, pp. 460–470, 718–727, 739–741.

[9] R. D. Reitz and F. V. Bracco. Mechanism of atomization of a liquid jet. *Physics of Fluids*, 25(10):1730–1742, 1982.

[10] P. K. Wu and G. M. Faeth. Aerodynamic effects on primary breakup of turbulent liquids. *Atomization and Sprays*, 3:265–289, 1993.

[11] J. W. Hoyt and J. J. Taylor. Turbulence structure in a water jet discharging in air. *Physics of Fluids*, 20(10):S253–s257, 1977.

[12] A. J. Chorin. Numerical study of slightly viscous flow. *Journal of Fluid Mechanics*, 57:785–796, 1973.

[13] A. J. Chorin and P. S. Bernard. Discretization of a vortex sheet. *Journal of Computational Physics*, 13:423–429, 1973.

[14] A. J. Chorin. Vortes sheet approximation of boundary layers. *Journal of Computational Physics*, 27:428–442, 1978.

[15] S. S. Yoon and S. D. Heister. Categorizing linear theories for atomizing jets. *Atomization and Sprays*, 2002. submitted.

[16] P. K. Wu, L. K. Tseng, and G. M. Faeth. Primary breakup in gas/liquid mixing layers for turbulent liquids. *Atomization and Sprays*, 2:295–317, 1992.

[17] P. G. Saffman. *Vortex Dynamics*. Cambridge University Press, New York, 1992. pp. 22, 192–195.

[18] J. A. Liggett and P. L.-F. Liu. *The Boundary Integral Equation Method for Porous Media Flow*. George Allen and Unwin, 1983.

[19] S. D. Heister. Boundary element methods for two-fluid free surface flows. *Engineering Analysis with Boundary Elements*, 19:309–317, 1997.

[20] I. F. Murray and S. D. Heister. On a droplet's response to acoustic excitation. *International Journal of Multiphase Flow*, 25:531–550, 1999.

[21] S. S. Yoon, S. D. Heister, J. T. Epperson, and P. E. Sojka. Modeling multi-jet mode electrostatic atomization using boundary element methods. *Journal of Electrostatics*, 50:91–108, 2001.

[22] S. S. Yoon and S. D. Heister. A fully nonlinear model for atomization of high-speed jets. *Engineering Analysis with Boundary Elements*, 2002. submitted.

[23] I. G. Currie. *Fundamental Mechanics of Fluids*. McGraw-Hill, New York, 1993. Second Edition, pp. 172–174.

[24] J. H. Hilbing. *Nonlinear Modeling of Atomization Processes.* PhD thesis, Purdue University, 1996.

[25] V. I. Smirnov. *A Course of Higher Mathematics.* Pergamon Press, New York, 1964.

[26] W. J. Duncan, A. S. Thom, and A. D. Young. *An Elementary Treatise on the Mechanics of Fluids.* Edward Arnold, London, 1960. pp. 93–94.

[27] A. S. Ramsey. *A Treatise on Hydromechanics.* G. Bell and Sons, London, 1920. pp. 241–244.

[28] K. Karamcheti. *Principles of Ideal-Fluid Aerodynamics.* John Wiley and Sons, New York, 1966. pp. 526–530, 599.

[29] S. S. Yoon and S. D. Heister. Analytic solutions for computing velocities induced from potential vortex ring. *AIAA Journal Technical Paper,* 2002. submitted.

[30] E. Kreyszig. *Advanced Engineering Mathematics.* John Wiley and Sons, New York, 1993. pp. 949–956.

[31] M. S. Longuet-Higgins and E. D. Cokelet. The deformation of steep surface waves on water. *Proceedings of the Royal Society of London A,* 350:1–26, 1976.

[32] J. G. Proakis and D. G. Manolakis. *Digital Signal Processing.* Prentice-Hall, New Jersey, 1996. pp. 30–31.

[33] F. M. White. *Viscous Fluid Flow.* McGraw Hill, New York, 1991. 2nd Edition pp. 235, 269, 358.

[34] B. Thwaites. *Incompressible Aerodynamics.* Dover, New York, 1960. pp. 30–31.

[35] C. Brennen. Cavity surface wave patterns and general appearance. *Journal of Fluid Mechanics,* 44(1):33–49, 1970.

[36] I. H. Shames. *Engineering Mechanics.* Prentice-Hall, New Jersey, 1993. pp. 306–308.

[37] S. Hwang, Z. Liu, and R. D. Reitz. Breakup mechanisms and drag coefficients of high speed vaporizing liquid drops. *Atomization and Sprays,* 6:353–376, 1996.

[38] S. E. Widnall and J. P. Sullivan. On the stability of vortex rings. *Proceedings of the Royal Society of London, Series A,* 332(1590):335–353, 1973.

[39] R. R. Kerswell. Elliptical instability. *Annual Review of Fluid Mechanics,* 34:83–113, 2002.

[40] B. J. Bayly. Three-dimensional instability of elliptical flow. *Physical Review Letters,* 34:2160–2163, 1986.

[41] F. Waleffe. On the three-dimensional instability of strained vortices. *Physics of Fluids,* A 2(1):76–80, 1990.

[42] M. J. Landman and P. G. Saffman. The three-dimensional instability of strained vortices in a viscous fluid. *Physics of Fluids,* 30(8):2339–2342, 1987.

[43] J. W. Hoyt, J. J. Taylor, and C. D. Runge. The structure of jets of water and polymer solution in air. *Journal of Fluid Mechanics,* 63(4):635–640, 1974.

[44] S. Kumar and G. M. Homsy. Direct numerical simulation of hydrodynamic instabilities in two- and three-dimensional viscoelastic free shear layers. *Journal of Non-Newtonian Fluid Mechanics,* 83:251–278, 1999.

[45] H. Haj-Hariri and G. M. Homsy. Three-dimensional instability of viscoelastic elliptic vortices. *Journal of Fluid Mechanics,* 353:357–381, 1997.

[46] H. Tennekes and J. L. Lumley. *A First Course in Turbulence.* M.I.T. Press, Cambridge, MA, 1975. pp 248–286.

[47] J. O. Hinze. *Turbulence.* McGraw-Hill, New York, 1975. 2nd Edition, pp. 625–631, 427.

[48] J. W. Hoyt and J. J. Taylor. Effect of nozzle boundary layer on water jets discharging in air. In *Jets and Cavities-International Symposium*, pages 93–100. ASME, 1985. held in Miami Beach, Florida, Nov. 17–22.

[49] W. S. Rayleigh. On the instability of jets. *Proc. London Math. Soc.*, 10(4), 1878.

[50] M. C. Yuen. Non-linear capillary instability of a liquid jet. *Journal of Fluid Mechanics*, 33(1):151–163, 1968.

[51] E. F. Goedde and M. C. Yuen. Experiments on liquid jet instability. *Journal of Fluid Mechanics*, 40(3):495–514, 1970.

[52] C. Xu. *Simulation of Orifice Internal Flows Including Cavitation and Turbulence.* PhD thesis, Purdue University, 2002.

[53] A. M. Sterling and C. A. Sleicher. The instability of capillary jets. *Journal of Fluid Mechanics*, 68(3):477–495, 1975.

[54] H. Hiroyasu, M. Shimizu, and M. Arai. The breakup of high speed jet in a high pressure gaseous atmosphere. In *Proceedings of the 2nd International Conference on Liquid Atomization and Spray Systems*, pages 69–74. ICLASS, 1982. held in Madison, Wisconsin.

[55] M. Arai, M. Shimizu, and H. Hiroyasu. Breakup length and spray angle of high speed jet. In *Proceedings of the 3rd International Conference on Liquid Atomization and Spray Systems*, pages 1B/4/1–10. ICLASS, 1985. held in London, United Kingdom.

[56] M. J. McCarthy and N. A. Molloy. Review of stability of liquid jets and the influence of nozzle design. *The Chemical Engineering Journal*, 7:1–20, 1974.

[57] C. C. Lin. On the stability of two-dimensional parallel flows, parts i, ii, iii. *Quart. Applied Mathematics*, 3:117–42, 218–34, 277–301, 1945.

[58] C. C. Lin. *The Theory of Hydrodynamic Stability.* Cambridge Press, New York, 1955.

(a)
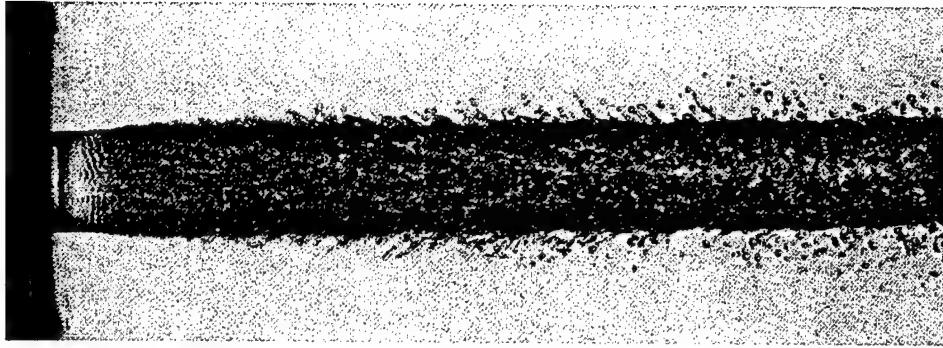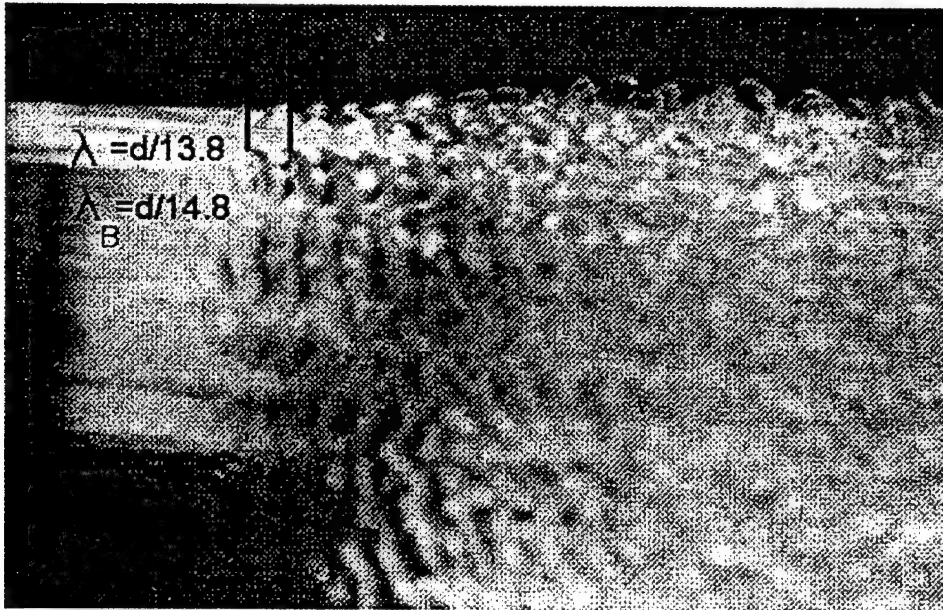
$\lambda = d/13.8$

$\lambda_B = d/14.8$

(b)

Figure 1: (a) Typical water jet into air in the atomization regime. Experimental image by Hoyt and Taylor [4]. (b) Closeup picture shows the most dominant wavelength $\lambda = d/13.8$ while Brennen's theory predicts $\lambda_B = d/14.8$. Printed under the permission of *Journal of Fluid Mechanics*.
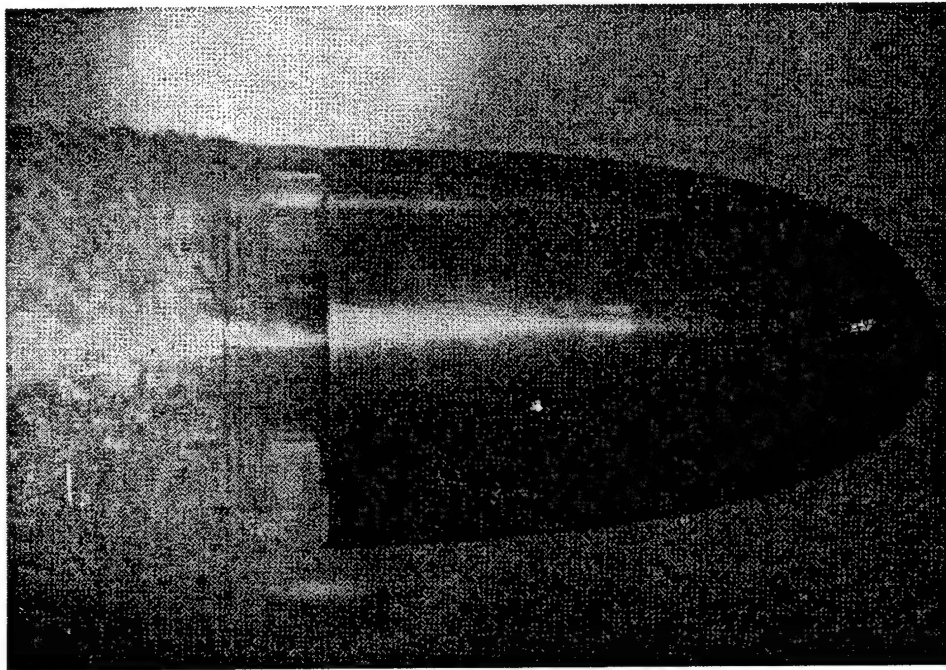
Figure 2: Typical cavitating flow over bluff body (ogive). Experimental image by Brennen [35]. Printed under the Permission of *Journal of Fluid Mechanics*.
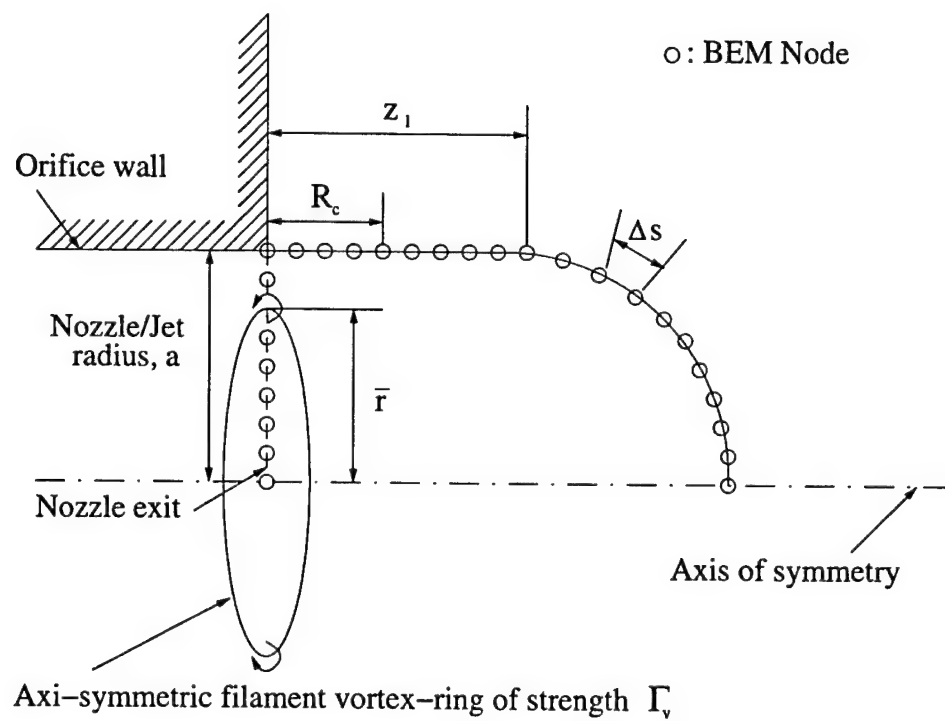
Figure 3: Schematic of the initial jet geometry indicating computational nodes and the axisymmetric ring vortex at the orifice exit plane.
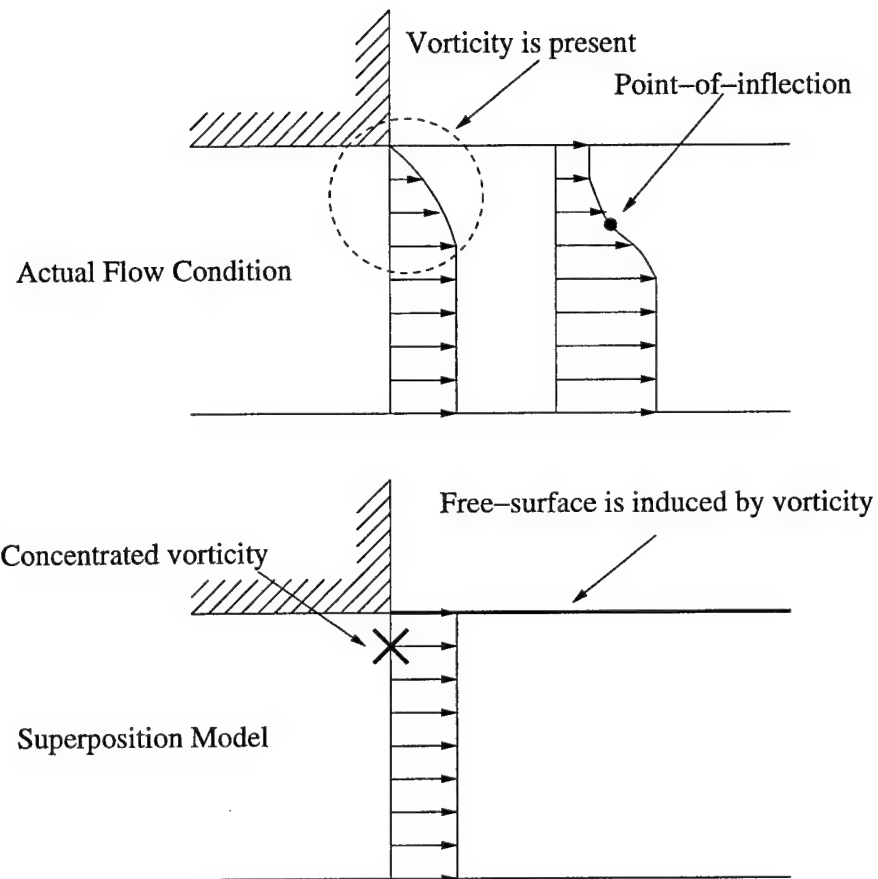
Figure 4: Comparison of the actual physical flow condition with the superposition model in simulating boundary layer relaxation downstream of the orifice exit plane.

(a)

(b)

Figure 5: (a) Closeup of the actual Hoyt and Taylor's water jet [4]. Printed under the permission of *Journal of Fluid Mechanics*. (b) The closeup of the model result for Hoyt and Taylor's water jet.
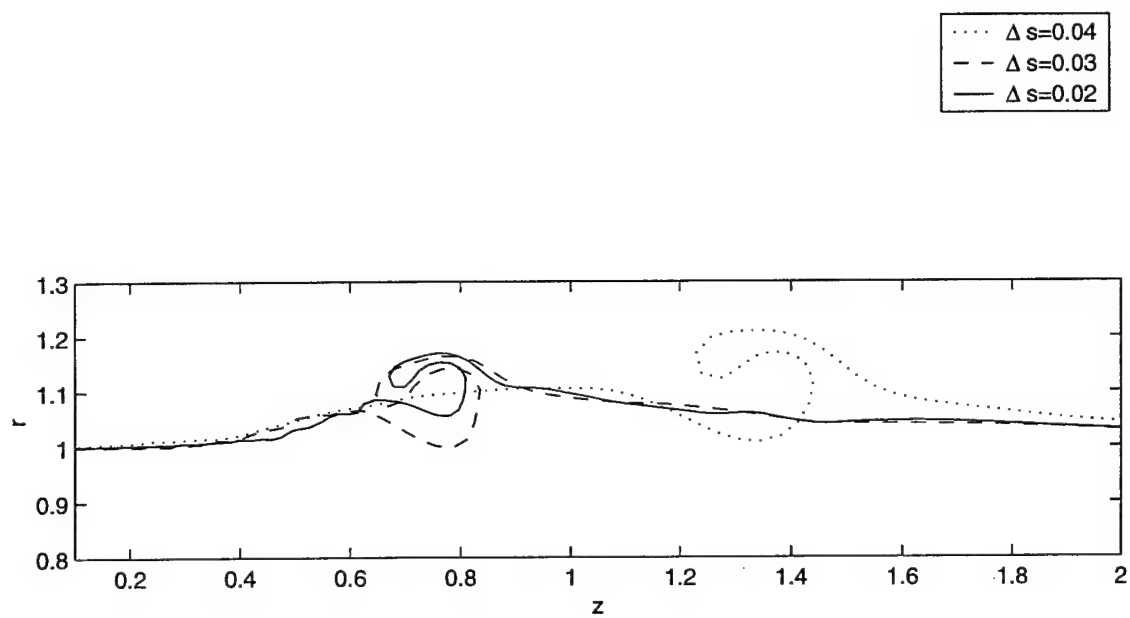
Figure 6: Grid convergence study: Effect of nodal spacing, Δs.
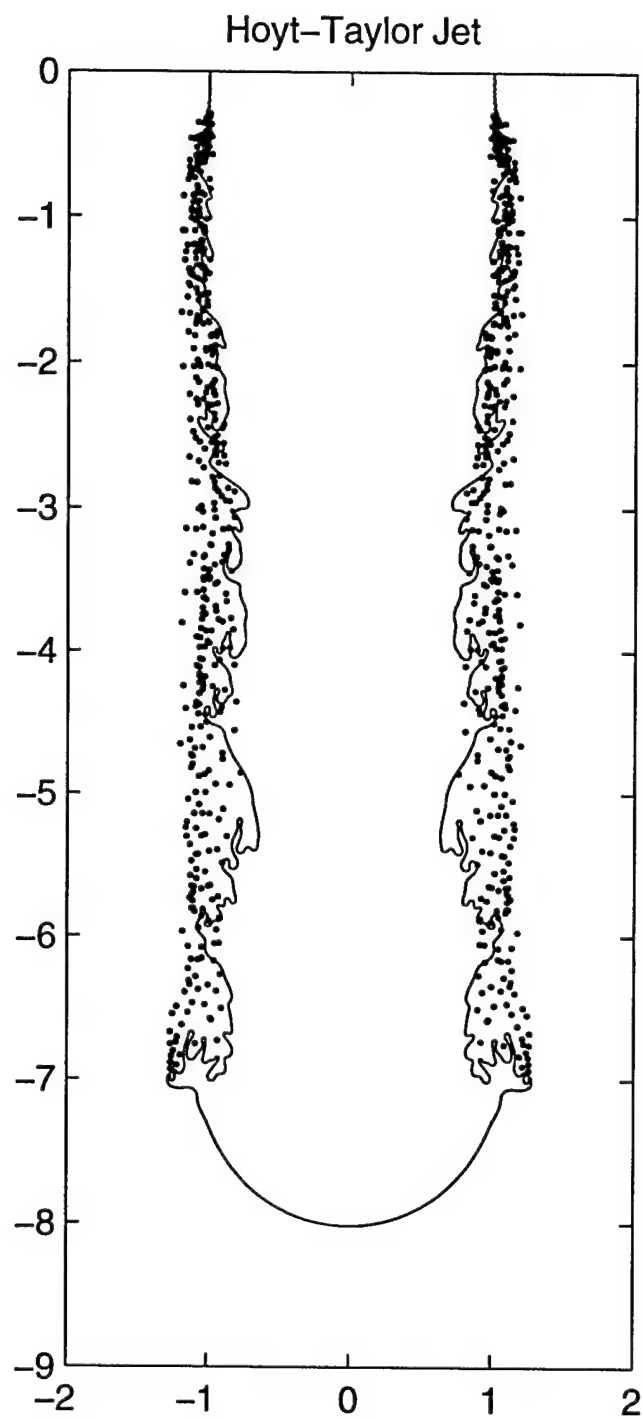
Figure 7: Hoyt-Taylor jet with atomized droplets at $t^* = 5.0$.
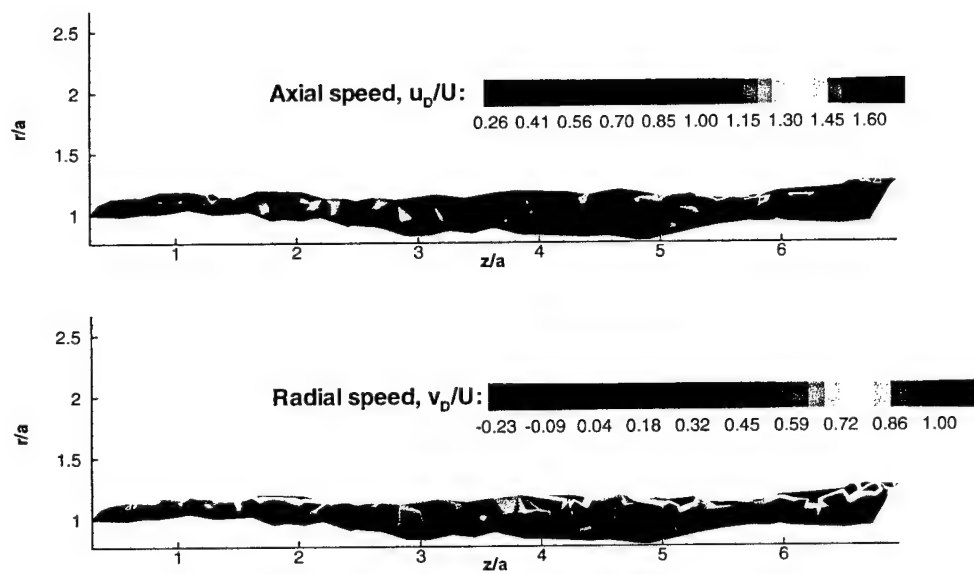
Figure 8: Model result: velocity contour in axial and radial direction for the Hoyt-Taylor case [11]
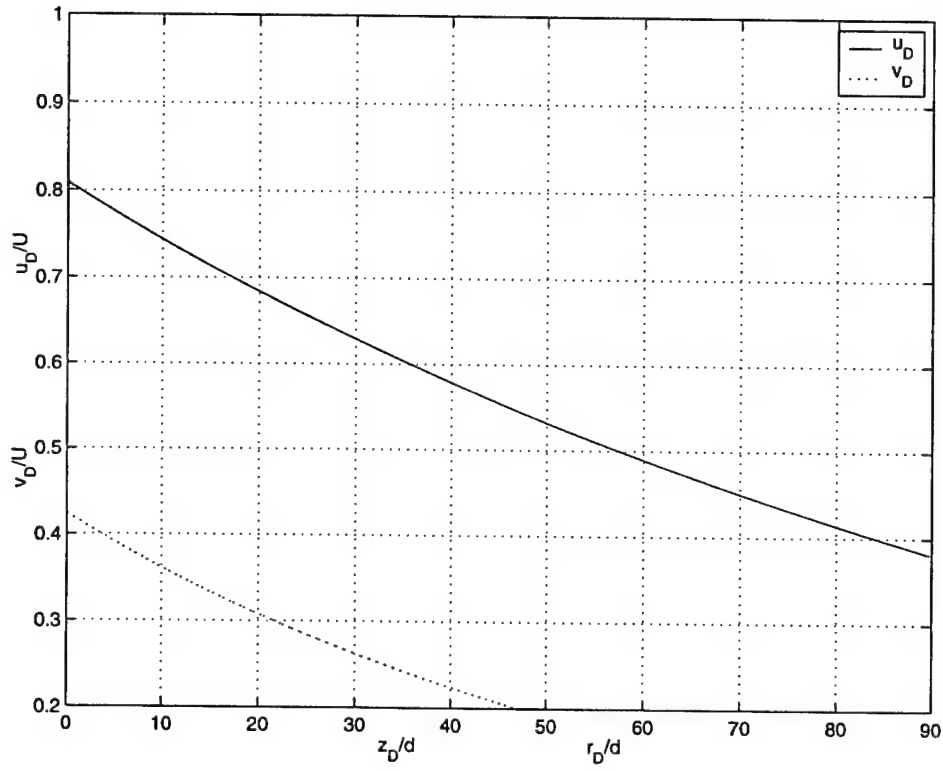
Figure 9: Dynamics of a droplet of Hoyt and Taylor's case: $d = 6.35\ mm$, $D = d/15.5$, $U = 21\ m/s$, $Re_D = UD/\nu_{air} = 589$, $u_D = 0.809\ U$, $v_D = 0.424\ U$, $\rho_l = 999\ kg/m^3$, $\rho_g = 1.23\ kg/m^3$, and $C_D = 0.518$.
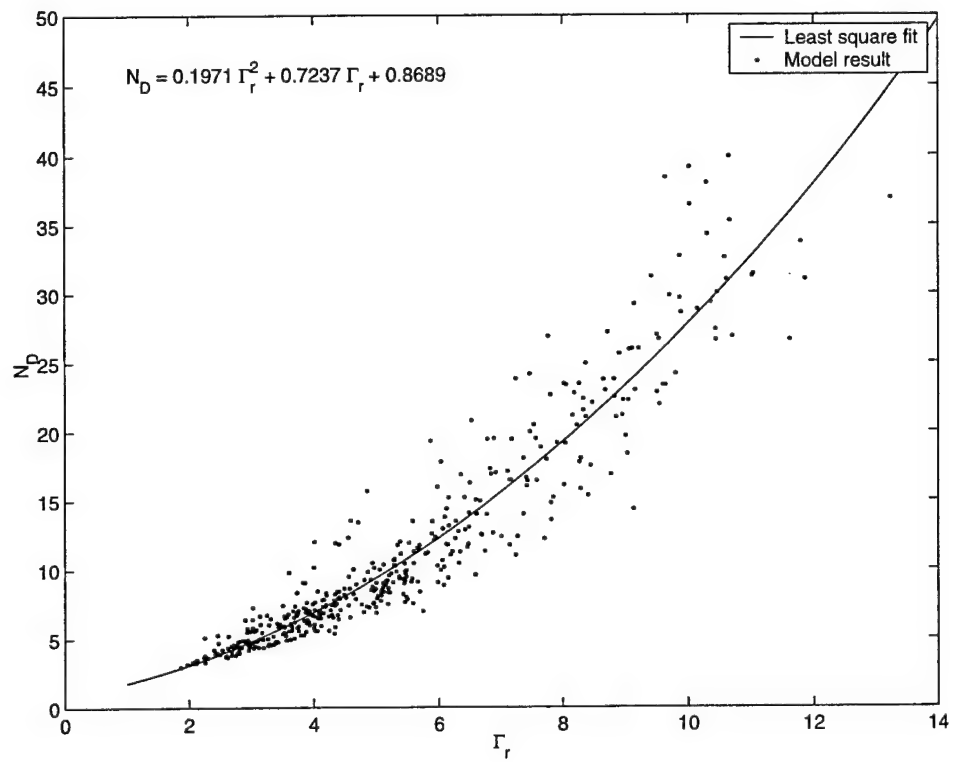
Figure 10: Prediction of cicumferential wave number (or number of droplet) due to circulation around the rotating ring pinched-off from the main liquid stream.
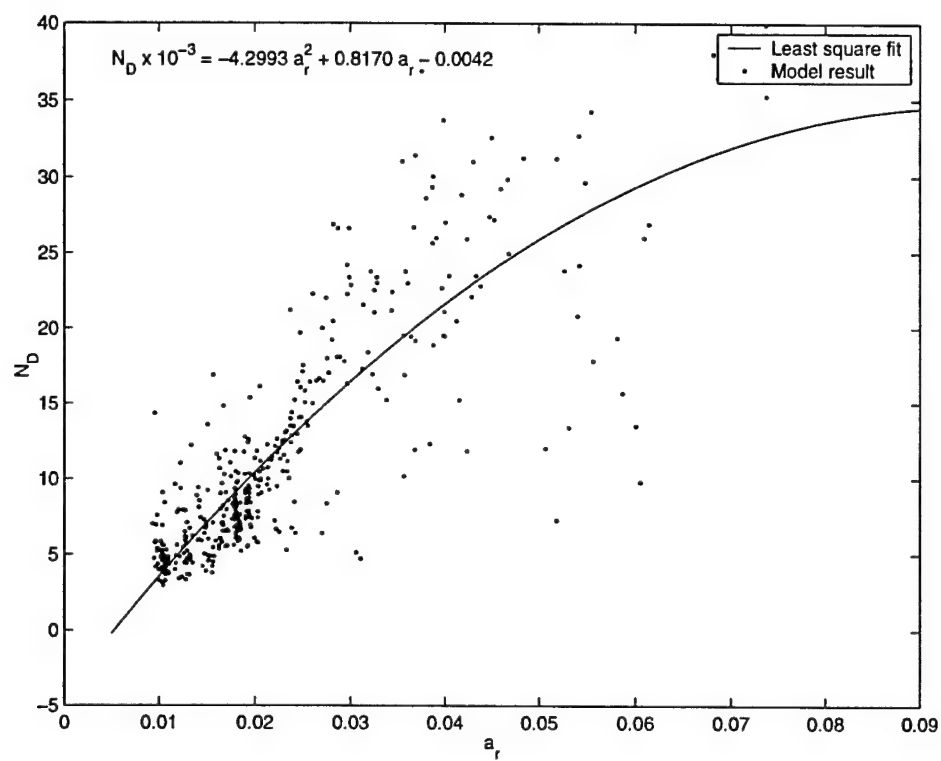
Figure 11: Number of waves vs. core thickness of pinch-off vortex-ring
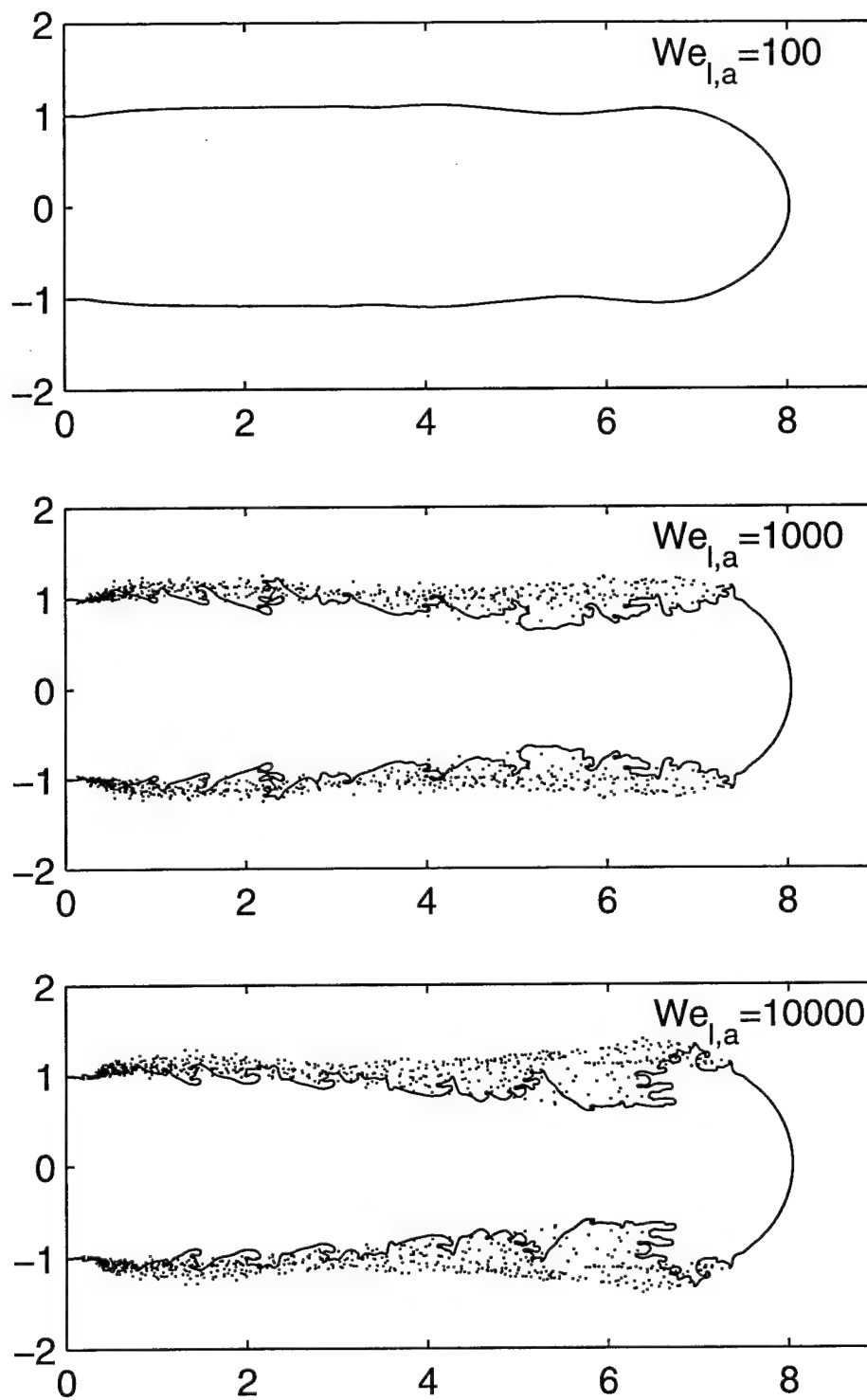
Figure 12: Effect of Weber number on atomization of fully-developed flows.
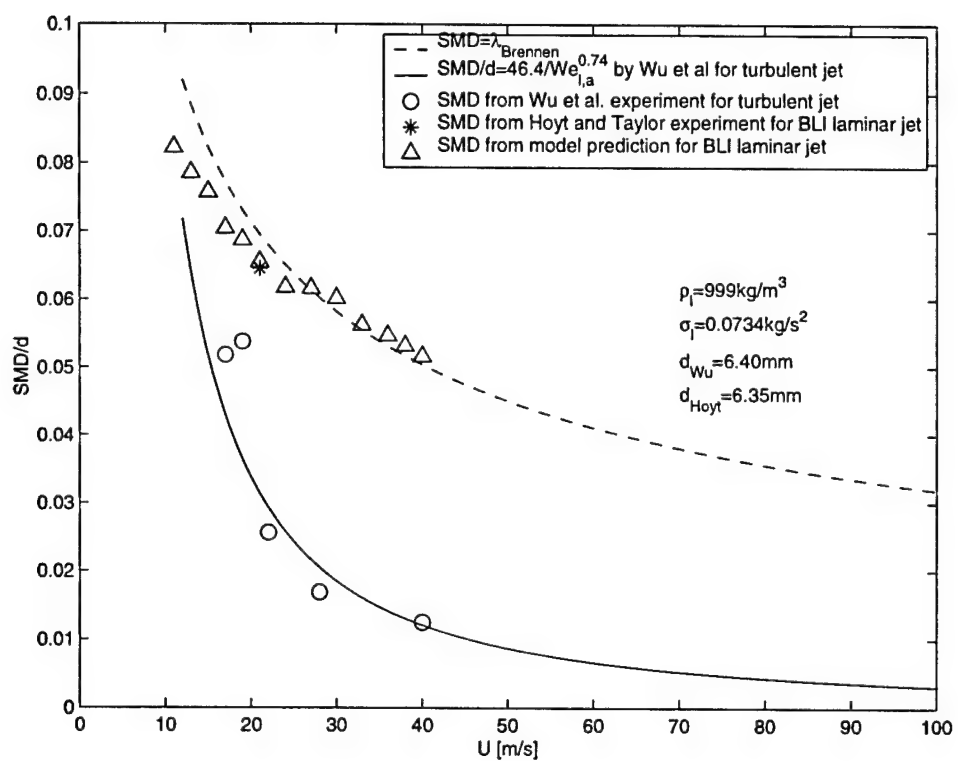
Figure 13: Sauter mean diameter comparison for $U \sim 20m/s$
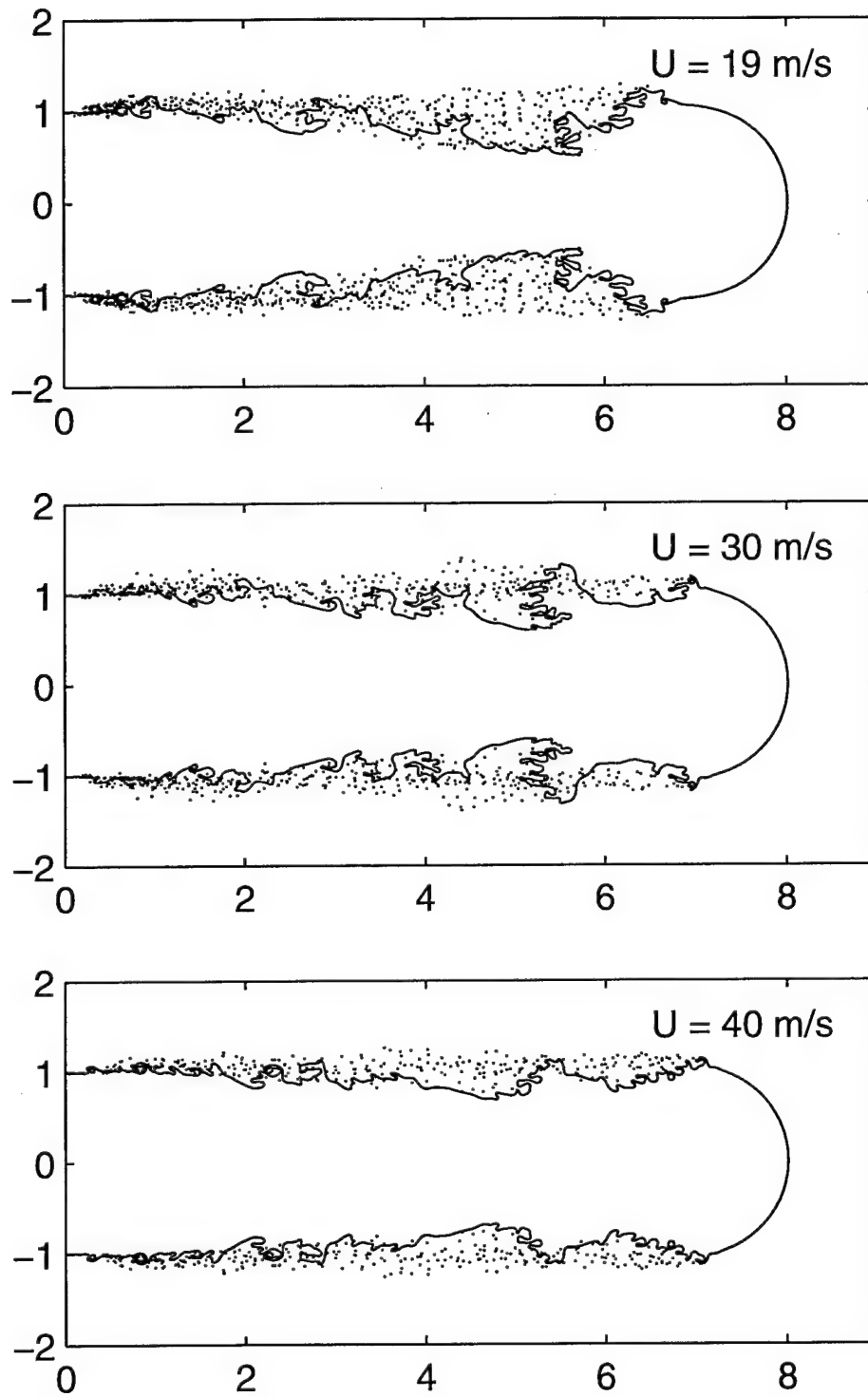
Figure 14: Effect of jet speed on jet surface structure of Hoyt-Taylor's jet. Due to larger circulation contained in the velocity profile, more unstable jet structure appears in the lower speed case.
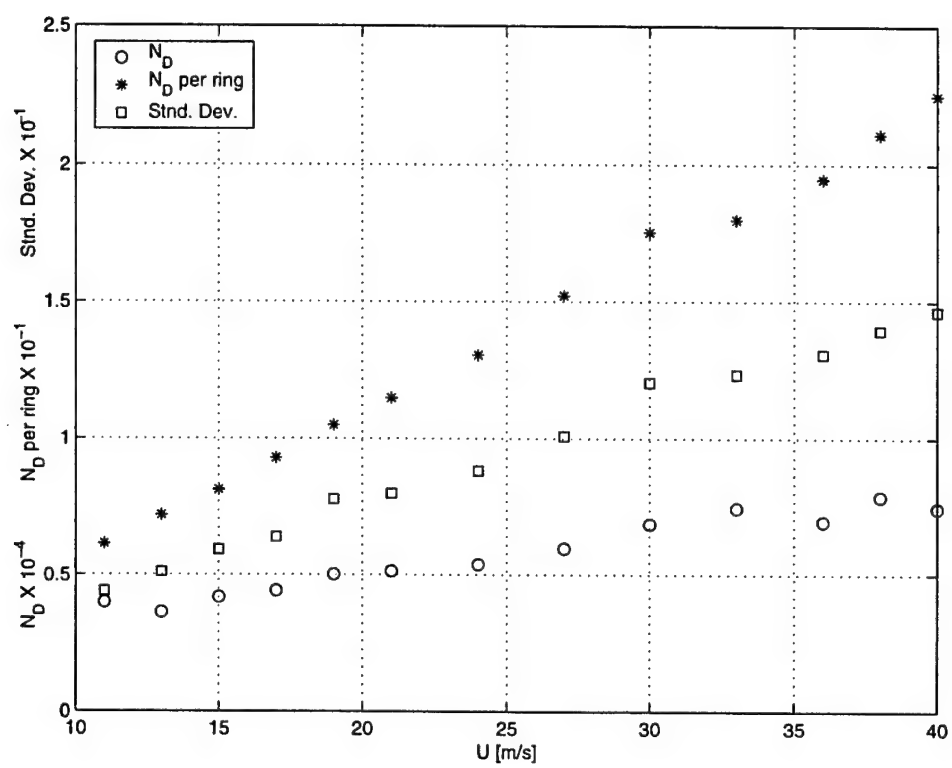
Figure 15: Effect of jet speed, U, on drop statistics
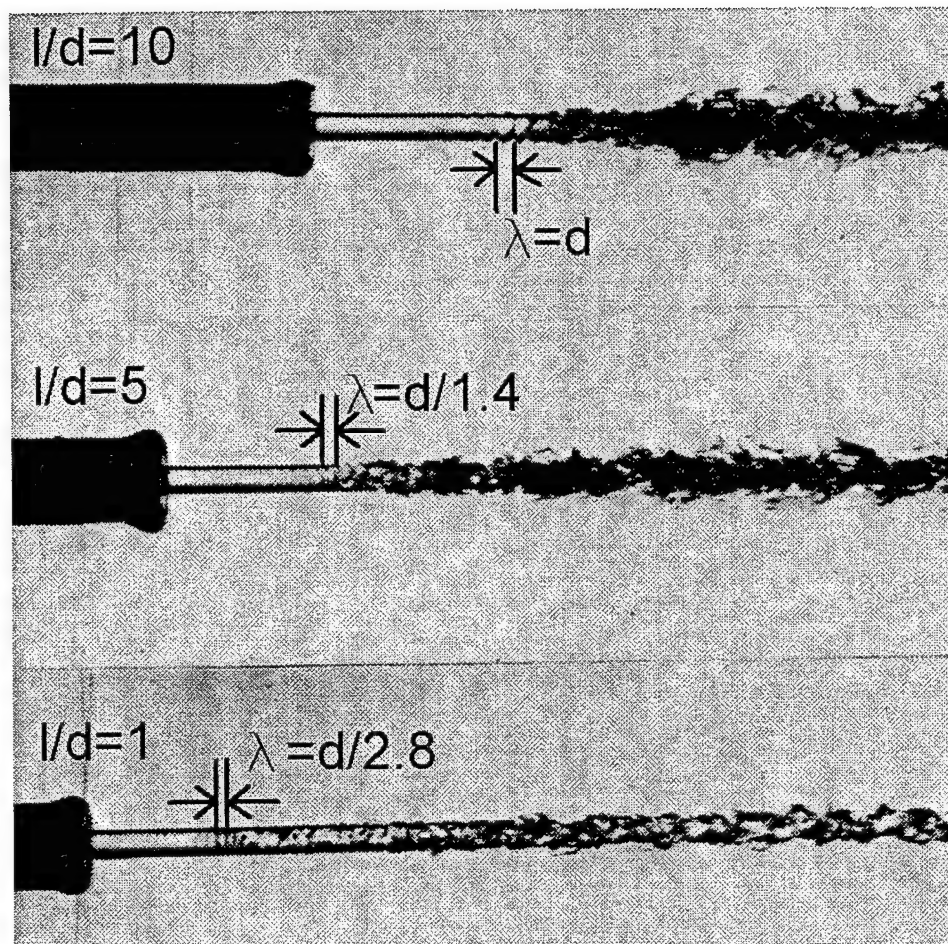
Figure 16: McCarthy and Molloy's experiment [56] for l/d=10, 5, and 1: The most dominant wavelength appears subsequent to laminar region which can be scaled by the Brennen's [35] theory. Printed under the permission of *Elsevier Science*.

(a) Experiment
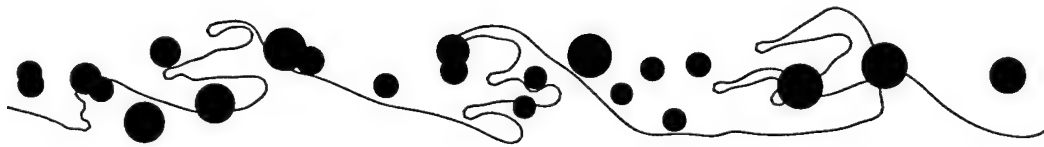
(b) Model result

Figure 17: Liquid: 60% glycerol and 40% water by weight, $\rho = 103\frac{kg}{m^3}$, $\mu = 11cP$, $\sigma = 0.0669\frac{kg}{s^2}$, $U = 20\frac{m}{s}$, $d = 2.54mm$, $We = 781$, $Re = 4750$. Comparison between experiment [56] and model results. The black circles represent the location and the relative size of the pinched-off droplets. Printed under the permission of *Elsevier Science*.
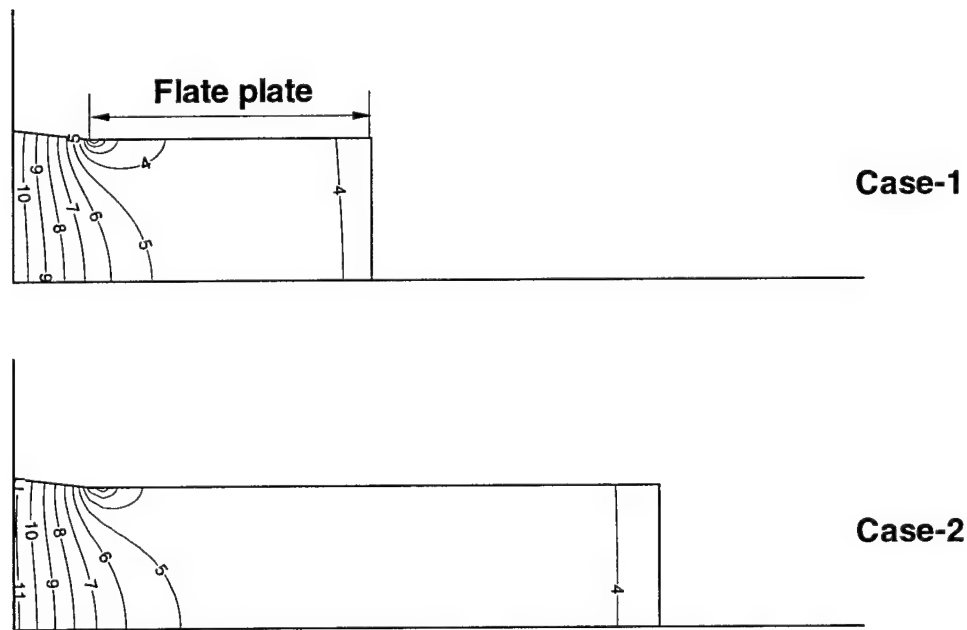
Figure 18: Pressure distribution of Hoyt-Taylor's nozzle [11] for three different nozzle lengths. Note that 'Case-3' is the fully-developed flow (i.e. $l/d = \infty$).
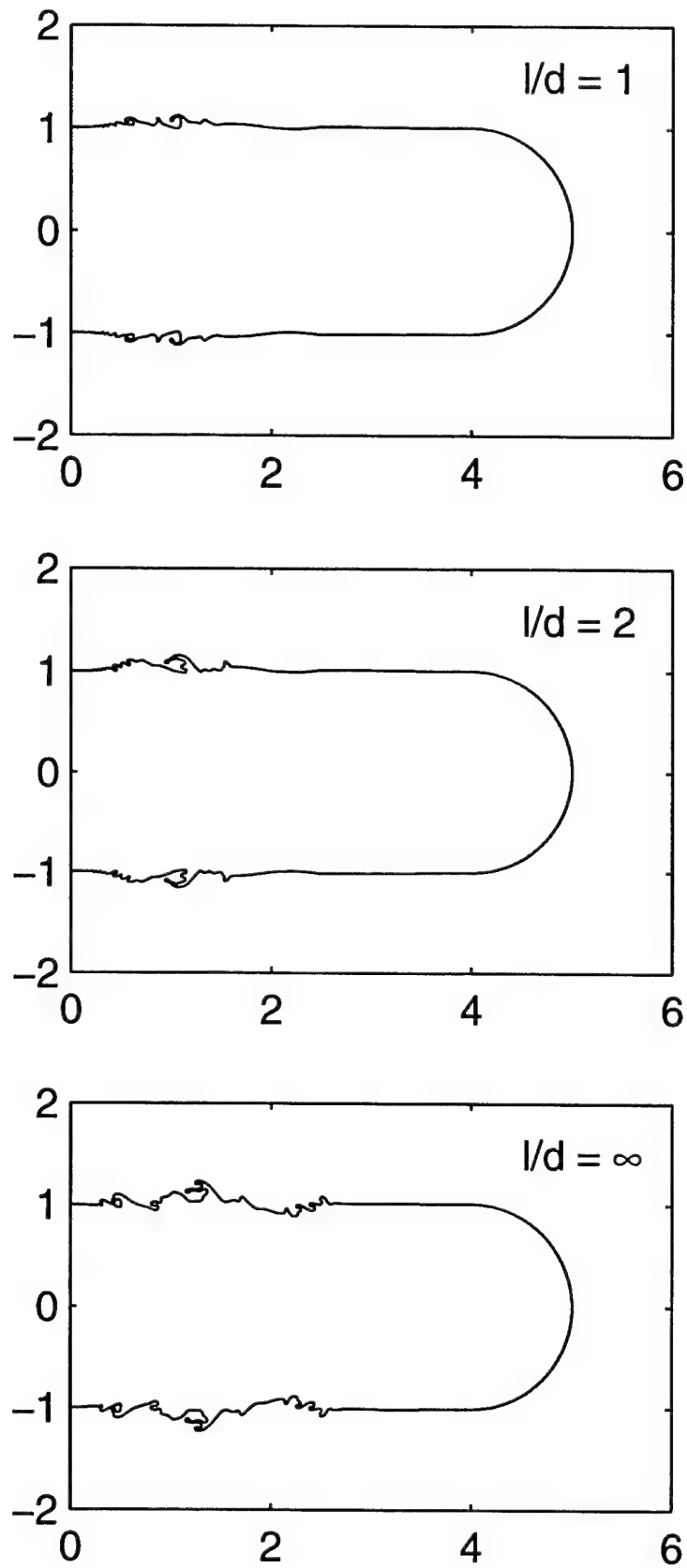
Figure 19: Boundary layer effect at $t^* = 2.0$. Larger fluctuation as δ_2 increases.
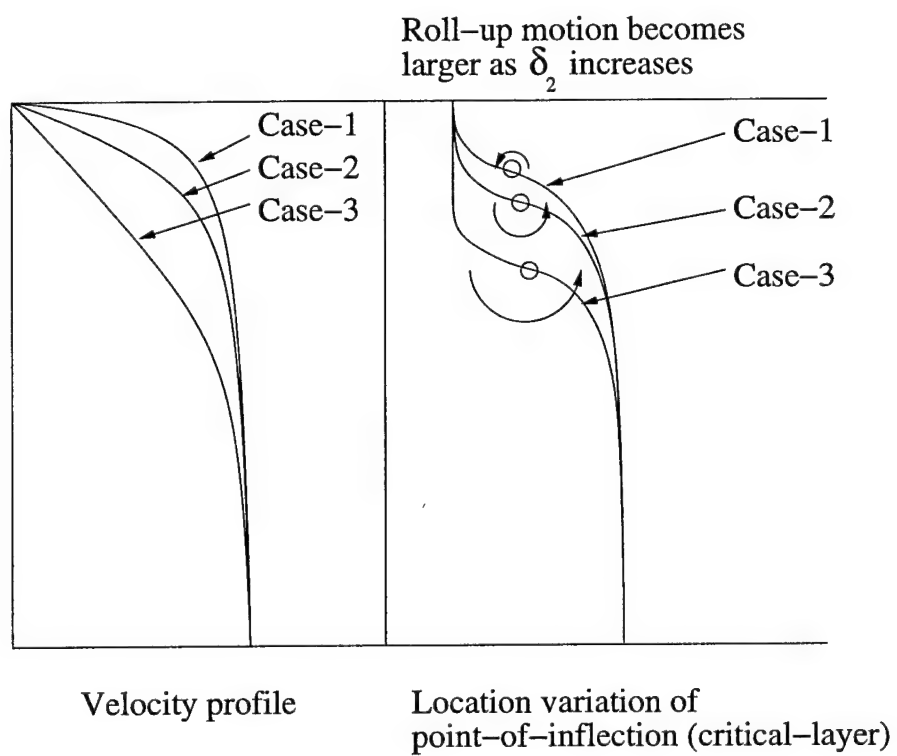
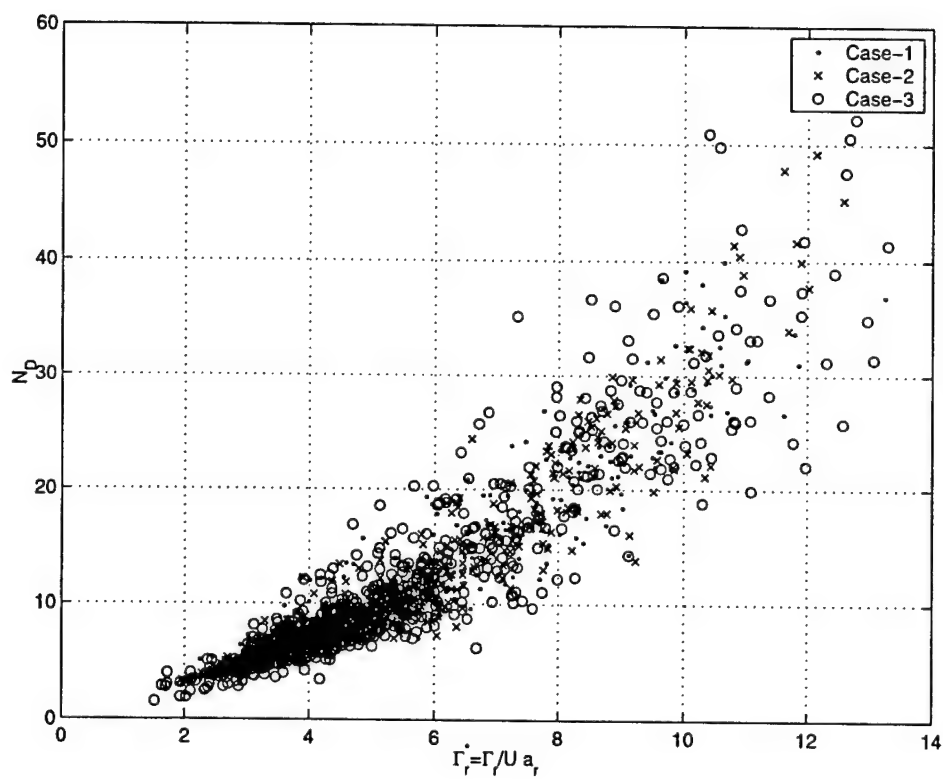Figure 20: Schematic of rollup motion at critical layer for the three cases.

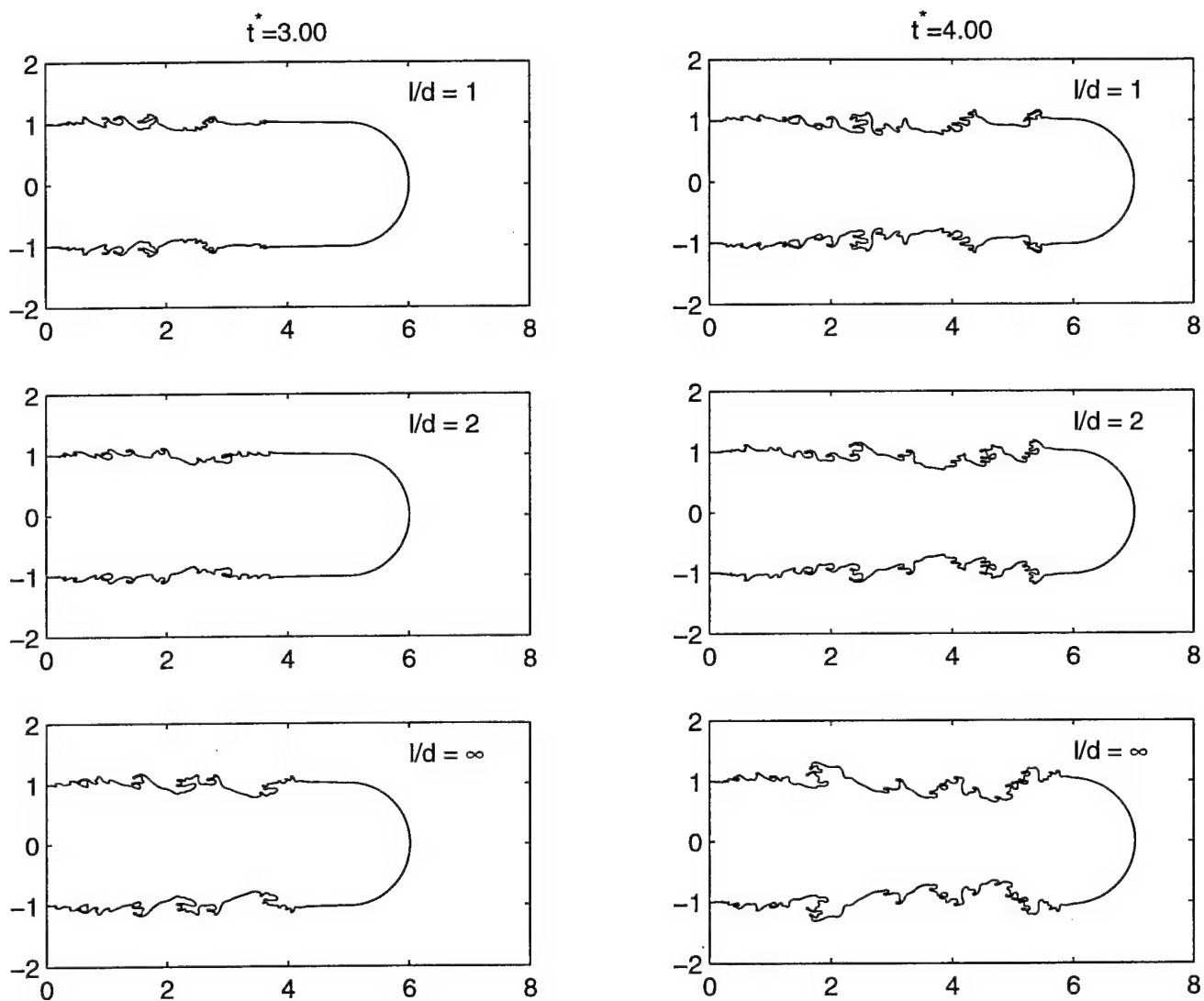Figure 21: Larger fluctuation due to increase in δ_2 leads more dispersive N_D distribution as nozzle length is increased.

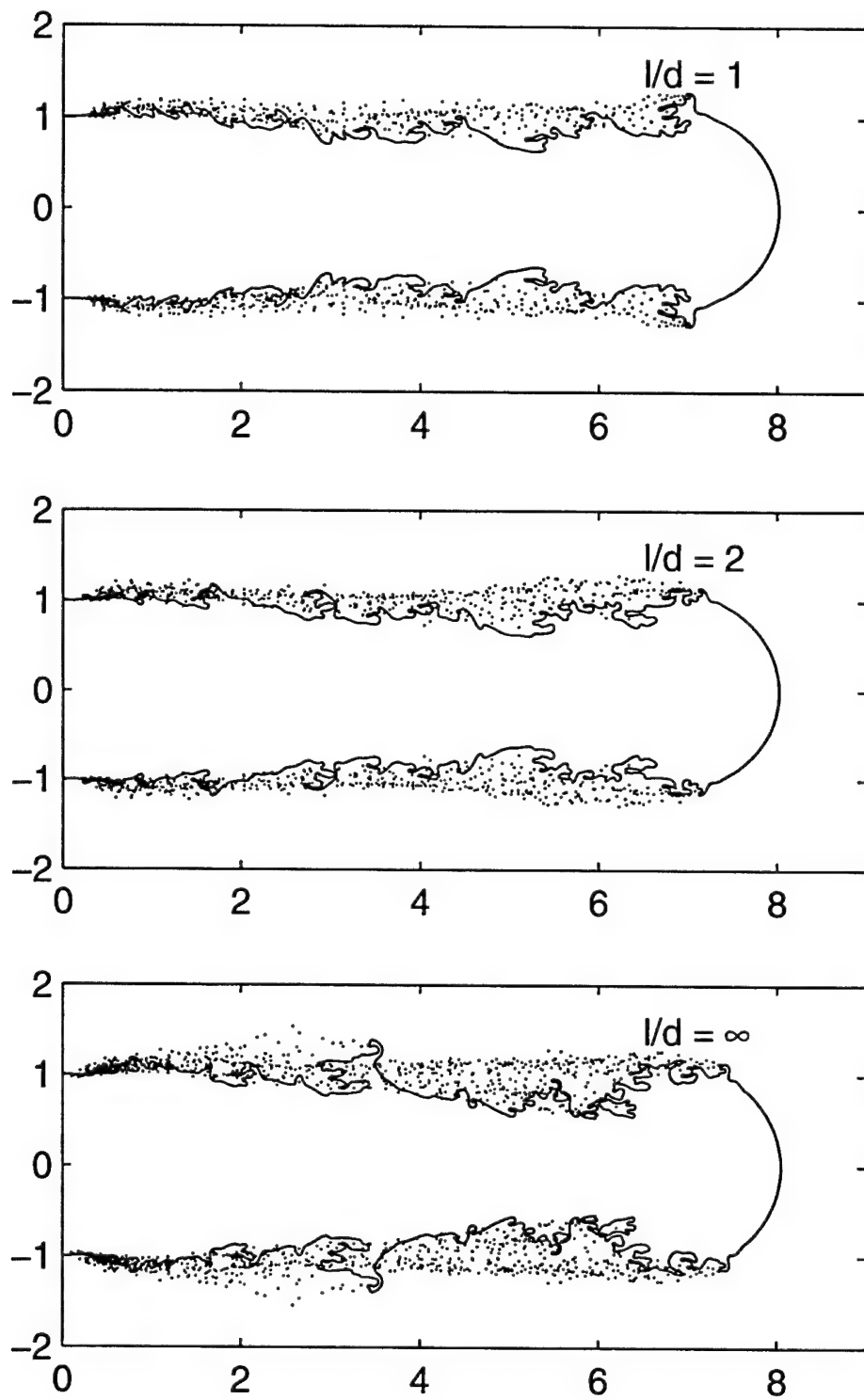Figure 22: Boundary layer effect fades away as t^* increases

Figure 23: Boundary layer effect at $t^* = 5.0$

95

8   Appendix D - Coaxial Injector Simulations

Kim*, B and Heister, S. D., "Two-phase Modeling of Hydrodynamic Instabilities in Coaxial Injectors".

Two-phase Modeling of Hydrodynamic Instabilities in Coaxial Injectors

Byoung-Do Kim *, Stephen D. Heister †

* Graduate Research Assistant, † Professor,
School of Aeronautics and Astronautics,
Purdue University, W. Lafayette, IN

Abstract

The hydrodynamic instability of coaxial injector with recessed inner fluid posts have been investigated using a homogeneous flow method with pseudo-density model in a time-dependent, viscous calculation. The present study focuses on unsteady self-oscillation mode in the coaxial injector. The Kelvin-Helmholtz instability mechanism due to velocity discontinuity between gas and liquid phase is investigated as a source of unsteadiness which could contribute to combustion instabilities. A 2-D analogue is investigated in these initial studies. A series of parametric studies have been completed to assess the amplitude and frequency of oscillations under a variety of design conditions. Effect of the thickness of the inner post has been studied as well.

Introduction

In many coaxial injectors, liquid flowing down a central post is atomized by a high-velocity gas passing around the outer annulus. In many applications, the liquid post is submerged somewhat from the orifice exit plane to provide flame holding in combustion systems such as liquid rocket engines. High-frequency oscillation of the jet spray has been observed by various researchers' experiments of coaxial injectors with the submerged liquid post. [1,2,3,6-8,21] These disturbances could couple to the dynamics of the jet breakup process and potentially provide amplification of oscillations within the combustion chamber. Bazarov [1,2] dubbed this phenomenon as *'Self-Oscillation'* and suggested this as a cause of decreased combustion efficiency and a source of high amplitude noise during combustion. Combustion instabilities of this nature can have severe impact on the performance of the engine and can in some cases lead to catastrophic failures.

Hutt and Rocker [4] investigated the high frequency combustion instability associated with coaxial injectors. They classified the instability phenomena in the chamber as injection-coupled and intrinsic mechanism. The injection coupling implies chamber pressure/temperature variation as a

key contributor in the change of flow dynamics through the injector. In the other hand, the intrinsic mechanism occurs in the flowfield due to its own flow dynamics with negligible feed system effect. However, it should be noted that injection coupling is never independent of the intrinsic subprocesses, such as atomization, propellant heatup, vaporization, and mixing because these processes determine the relationship between the injector response and the chamber response.

Bazarov [1,2] studied the self-oscillation phenomena along with the self-pulsation mode of jet instability in coaxial injector. He postulated that the self-oscillation occurs when the gas-liquid interaction forms a cavity inside nozzle, leading to jet swirling around the nozzle exit. The self-pulsation of the liquid jet mixed with the gas flow depends on the pressure drop at liquid and gas phase, correlating with the time of liquid propagation through the injector nozzle [5]. In addition to external disturbances from combustion chamber and feed system during engine operation, injectors can generate self-pulsation under certain conditions by its own intrinsic unsteadiness leading to random modeification of the spray formation process.

Mayer and his research group have done a significant amount of work on the coaxial injector in terms of the combustion instability. Mayer and Krulle [6] investigated coaxial flow mixing phenomena in terms of chamber pressure variation, density/velocity ratio changes and surface tension effect. By increasing chamber pressure gas density is increased, magnifying the aerodynamic interaction between the liquid and gas phases and resulting in a faster, finer atomization. Increasing surrounding gas velocity also leads to an increase of surface wave growth and to macroscopic instabilities of the liquid jet. They claimed the initiation of the jet surface deformation was due to internal liquid turbulence delivering energy transform in forms of eddy structures, approximately a size of 10-30% of the LOX post diameter. In other works of Mayer [7,8], the coaxial injector flow was studied under firing engine condition at supercritical chamber pressure (higher than 5 MPa). The study revealed a remarkable difference between subcritical spray formation and the supercritical injection and mixing. At subcritical condition, the liquid jet shows similar flow pattern to the cold flow test forming ligaments off the liquid jet surface and producing droplets before evaporation. Upon approaching and exceeding supercritical pressure, droplets no more exist and the liquid jet rapidly dissolves. The flame from combustion chamber was anchored at the tip of LOX post by flow recirculation eddies serving as flame holder for steady-state combustion. The asymmetric flow oscillation was also reported in all experiments, but the source of the oscillation was not clearly stated.

Instability mechanisms in coaxial injectors were also investigated experimentally under non-combusting conditions by Glogowski et al. [9,10] Their experimental results showed that for the coaxial injector with a liquid oxygen (LOX) post recessed into the fuel annulus, the injector transitioned into a condition of resonance characterized by a whistling noise. Significant modification to the overall structure of the spray due to the strong acoustic coupling between injector hydrodynamics and spray formation was also found. Without the recessed region, the injector operation

produced a near resonance condition with a lower amplitude whistling noise but did not make considerable change in spray structure. The recirculation by reverse flow near the recessed LOX post exit was also showed in this study. The effort to measure flow properties within the recessed region was not successful due to optical constraints and the small spatial and temporal scales involved.

Eroglu and Chigier [11] focused on the wave characteristics of liquid jet from coaxial air-blast injector. They measured frequency and wavelength of the jet issuing from the injector, and found two dominant wave type; spanwise(dilational) and stream-wise(sinuous) waves. The spanwise wave showed at a low relative jet velocity between gas and liquid-phase and the stream-wise wave showed at a high relative jet velocity. Average wavelengths decreased with liquid and gas velocity. The frequency band of the jet oscillation increased with the liquid jet velocity.

Mansour and Chigier [12] also conducted similar research on the liquid sheet instability issuing from the two-dimensional air-assisted nozzle. The results showed the same pattern with the Eroglu and Chigier's study. However, Mansour and Chigier's study probed higher velocity cases, and confirmed that the frequency of the liquid sheet oscillation increased with coflowing gas velocity. This also indicates that the aerodynamic interaction between gas and liquid flow is the dominant factor for the flow oscillation.

In general, for the flow at high velocity, most of researchers agree that the principal source introducing instability to the jet is from aerodynamic forces arising from the interaction of the liquid jet with the surrounding gas flow. Reynolds and Weber numbers are generally very high in these atomizers and aerodynamic forces are several orders of magnitude larger than capillary forces. The interaction between the liquid and gas phases mainly comes from different velocities of each phase. The velocity discontinuity in a homogeneous fluid results wave growth on the interface, which is a common *Kelvin-Helmholtz* instability.

Most of the previous research works summarized here mainly contributed to the investigation of flow phenomena outside of injector after the injection. None of them addressed the inner flow structure in a recessed region of the coaxial injector, especially using numerical simulation. Since the upstream flow in a injector provides the initial condition for the entire spray atomization process and combustion chamber acoustic characteristics, research work on this area is highly desirable. In this paper, the 2-D analogue (a liquid sheet in a channel) of the coaxial injector will be studied numerically to characterize amplitude and frequency of oscillations of the inner liquid sheet. The model is described briefly in the following section; results of parametric studies are then summarized in the latter part of the paper along with the result of finite LOX post thickness modeling.

Linear Analysis

Liquid sheet instabilities have been analyzed by many researchers over the past several decades. Among those investigations, Squire's [17] analysis was among the first fundamental studies on the instability of inviscid liquid film. Based on the Squire's analysis, Dombroski and Johns [18] investigated the aerodynamic instability of viscous liquid film subject to symmetric and asymmetric waves. Li and Tankin [19] also studied viscous liquid sheets and provided an analysis for aerodynamic and viscosity-enhanced instability modes. However, most previous efforts have focused on a moving liquid sheet in a semi-infinite stagnant gas. Since the jet inside coaxial injector encounters higher velocity gas phase and the outside nozzle wall provides a finite region for the gas, the mathematical formulation for this special case needs to be derived. In this section, an analytical approach based on the linear theory is presented for the coaxial injector case.

It should be noted that the approach based on the linear stability theory can only evaluate the beginnings on the instability. As the amplitude of the disturbance grows, the linear assumptions soon become invalid. In addition, the presence of a finite-length domain makes the connection to an infinite sheet stability analysis somewhat tenuous: i.e., the injection exit plane is not treated in periodic boundary conditions typically used in linear studies. Even though the theoretical approach doesn't allow us to describe the jet instability in a complete structure, it provides a good starting point for predicting unstable, wave-type behavior of the jet with disturbances.

Consider a two-dimensional liquid sheet with density ρ_l, surface tension σ and uniform thickness $2h$, moving at velocity U_l through an inviscid moving gas medium of density ρ_g at velocity U_g as illustrated in Figure 1. The coordinates are chosen such that the direction of the x-axis is parallel to the direction of the velocity U_l and U_g, and the y-axis is normal to the liquid sheet with its origin located at the mid-plane of the liquid sheet. Let the relative velocity ΔU represents the velocity difference between gas and liquid phase, $U_g - U_l$, that is, the reference frame is attached to the liquid phase. Finally, let h represent the sheet thickness and nh represent the distance to the channel wall, where n measure the number of sheet thicknesses to the wall.

For anti-symmetrical disturbances, the displacements of corresponding points on the two surfaces are equal in magnitude and in the same direction. Hence, the two interfaces are regarded to have the following form :

$$y = \pm h + \eta \tag{1}$$

$$\eta = \eta_0 e^{(\omega t + ikx)} \tag{2}$$

where $y = \pm h$ are the equilibrium positions of the two interfaces, i.e. the position with no disturbances; η_0 is the initial amplitude of the wave, and is taken to be much smaller than the half-width of the sheet, h; k is the wave number of the disturbance, and $k = 2\pi/\lambda$, where λ is the wavelength of the disturbance; $\omega = \omega_r + i\omega_i$ is a complex variable. The real part ω_r represents the rate of

growth or decay of the disturbance; its imaginary part ω_i is 2π times the disturbance frequency; and $-\omega_i/k$ is the wave propagation speed of the disturbance.

Let $\phi = \phi_g + \Delta U x$ be the velocity potential of the gas phase where the ϕ_g is the perturbation potential and ϕ_l is the perturbation velocity potential of the liquid phase. We will neglect viscosity for this analysis since the Reynolds numbers are quite high in practical devices. Therefore, the Laplace equation governs the process:

$$\frac{\partial^2 \phi}{\partial x^2} + \frac{\partial^2 \phi}{\partial y^2} = 0 \tag{3}$$

where ϕ is the velocity potential with ϕ_l and ϕ_g for the individual liquid and gas phases, respectively. The linearized kinematic boundary condition for liquid phase is

$$\frac{\partial \phi_l}{\partial y} = \frac{\partial \eta}{\partial t} \tag{4}$$

and for gas phase

$$\frac{\partial \phi_g}{\partial y} = \frac{\partial \eta}{\partial t} + \Delta U \frac{\partial \eta}{\partial x} \tag{5}$$

which are to be satisfied at $y = \pm h$. The dynamic boundary condition from unsteady Bernoulli's equation gives the following relation for the pressure at the interface:

$$P_l - P_g = -\rho_l \left(\frac{\partial \phi_l}{\partial t} \right) + \rho_g \left(\frac{\partial \phi_g}{\partial t} + \Delta U \frac{\partial \phi_g}{\partial x} \right) \tag{6}$$

Since the pressure induced by surface tension σ is,

$$P_l - P_g = \frac{\sigma}{R} \cong -\sigma \frac{\partial^2 \eta}{\partial x^2} \tag{7}$$

to 2nd order in η. Here, R is the radius of curvature of the interfaces. Considering the disturbances given in Equation (2), it is assumed that ϕ_l and ϕ_g take the following form:

$$\phi_l = F(y)e^{(\omega t + ikx)} \tag{8}$$

$$\phi_g = G(y)e^{(\omega t + ikx)} \tag{9}$$

Equation (8) and (9) can be solved by performing a Fourier analysis. The velocity potential for the liquid phase becomes

$$\phi_l = \eta_0 \left(\frac{\omega}{k} \right) tanh(kh)e^{(\omega t + ikx)} \tag{10}$$

and the velocity potential for the gas phase is:

$$\phi_g = \frac{\eta_0}{k} \left[\frac{cosh(ky) - tanh(nkh)sinh(ky)}{sinh(ky) - tanh(nkh)cosh(ky)} \right] (\omega + ik\Delta U)e^{(\omega t + ikx)} \tag{11}$$

Substitution of Equation (10), (11) and (7) into Equation (6) for $y = h$ leads to the following dispersion relation between the complex growth rate ω and the disturbance wave number k :

$$\omega^2(\rho_l tanh(kh)D_h - \rho_g N_h) - \omega(2ik\Delta U \rho_g N_h) + k^2\Delta U^2 \rho_g N_h + \sigma k^3 D_h = 0 \qquad (12)$$

where

$$N_h = cosh(kh) - tanh(nkh)sinh(kh) \qquad (13)$$
$$D_h = sinh(kh) - tanh(nkh)cosh(kh) \qquad (14)$$

Equation (12) represents a complex quadratic equation for growth rate ω as a function of wave number k.

The dispersion relation can be nondimensionalized using liquid density ρ_l, liquid phase velocity U_l and the jet thickness h as dimensions. Assuming Weber number $We \gg 1$ due to the high liquid-phase velocity, the normalized dispersion relation becomes:

$$\omega^2(tanh(k)D_h - \epsilon N_h) - \omega(2ik\Delta U \epsilon N_h) + k^2\epsilon\Delta U^2 N_h = 0 \qquad (15)$$

and since

$$\frac{N_h}{D_h} = \frac{cosh(k) - tanh(nk)sinh(k)}{sinh(k) - tanh(nk)cosh(k)} = \frac{1 - tanh(nk)tanh(k)}{tanh(k) - tanh(nk)} \qquad (16)$$

by letting N_h/D_h be Θ, the dispersion relation becomes :

$$\omega^2(tanh(k) - \epsilon\Theta) - \omega(2ik\Delta U \epsilon\Theta) + k^2\epsilon\Delta U^2\Theta = 0 \qquad (17)$$

Since the condition for instability is where the real part of growth rate is positive, solving this dispersion relation for growth rate and evaluating the effect of changing the three main parameters (h, ϵ, ΔU) can provide us basic idea of how the liquid sheet will behave.

In order to verify this analytic solution, infinite distance between the liquid sheet surface and the nozzle wall is applied, i.e., $n \to \infty$. In this limit, the hyperbolic tangent term, $tanh(nk)$ has an approximate value of 1, and the Equation(16) becomes:

$$\frac{N_h}{D_h} = \Theta = \frac{1 - tanh(k)}{tanh(k) - 1} = -1 \qquad (18)$$

Under the long wave assumption, Equation (17) becomes :

$$\omega^2(1 + \epsilon) + \omega(2ik\Delta U \epsilon) - k^2\epsilon\Delta U^2 = 0 \qquad (19)$$

This result is identical to Squire's result in the long wave limit. The parameter Θ really measures the effect of the finite channel height. Therefore, solving Equation (17) identifies the influence of the finite channel height of interest in this work.

Figure 2 shows the nondimensional growth rate, ω_r for anti-symmetrical disturbances when the relative velocity, ΔU varies. Here the density ratio, ϵ is 0.01 and the channel width to sheet thickness ratio, n is 5. Cases of $U_g/U_l = 2, 4$ and 8 are investigated. As shown in the result, the liquid sheet instability grows rapidly as the gas velocity grows. Due to the high speed of the gas phase surrounding liquid sheet, the Kelvin-Helmholtz instability governs the behavior of the liquid sheet. While the growth rate increases indefinitely as the wave number grows, viscosity and surface tension in actual flows will reduce the growth rate in large wave number region.

Figure 3 illustrates the effect of gas/liquid density ratio on growth rate. Here $\Delta U = 3$ and $n = 2$ for all cases, and density ratio ϵ values of 0.1, 0.01 and 0.001 are considered. As gas phase density increases, the gas imparts more momentum to the liquid surface. Therefore, the growth rate of disturbance increases when the density ratio gets higher.

The effect of channel width to jet thickness ratio, n is shown in Figure 4. The density ratio, ϵ is 0.01 and the relative velocity, ΔU is 3, and n values of 2, 5, and 10 are considered. This result shows that the instability grows rapidly as the sheet gets thicker (channel gets smaller). However, in the small wave number region ($k < 0.07$) the growth rate exhibits the opposite pattern. The presence of the cavity wall has a stabilizing effect on the very long wave instabilities. This behavior is most important in assessing the growth rate response since the long wavelength instabilities are presumed to be the most harmful to overall injector performance in combustion system. Therefore, one can conclude that the presence of wall can either be a stabilizing or destabilizing effect depending on the wavelength of the instability.

Modeling Description

A two-dimensional incompressible, unsteady, viscous flow solver has been developed utilizing a finite volume implementation of the Marker and Cell discretization method. The current model is based on homogeneous flow two-phase treatment in which the single phase Navier-Stokes equations are solved using a fictitious "pseudo" density which varies in amplitude between the liquid and gas extremes. This provides a mechanism to compute the local droplet number density without having to solve the flow-field around all the individual droplets. The single fluid model can be achieved by assuming locally homogeneous flow (LHF) in which the relative velocity and temperature between two-phases are small enough in comparison to variation of the overall flow field that is to be predicted. Under the LHF assumption, and by providing a proper constitutive relation for the pseudo-density of the homogeneous flow, the model is able to handle the two-phase flow with less computational resources than traditional two-fluid modeling. However, capillary forces are not resolved using this approach because the interface is not known as part of the solution methodology. For the high Reynolds and Weber numbers characterizing the injectors of interest, this simplification is deemed appropriate. The development of the homogeneous fluid model is

discussed in detail in prior works [13-15].

The two-dimensional, viscous, unsteady, Navier Stokes equations are expressed in the following form:

$$\frac{\partial \rho}{\partial t} + \frac{\partial \rho u}{\partial x} + \frac{\partial \rho v}{\partial y} = 0 \tag{20}$$

$$\frac{\partial \rho u}{\partial t} + \frac{\partial \rho u^2}{\partial x} + \frac{\partial \rho u v}{\partial y} + \frac{\partial P}{\partial x} = \frac{\partial}{\partial x}\mu\frac{\partial u}{\partial x} + \frac{\partial}{\partial y}\mu\frac{\partial u}{\partial y} \tag{21}$$

$$\frac{\partial \rho v}{\partial t} + \frac{\partial \rho u v}{\partial x} + \frac{\partial \rho v^2}{\partial y} + \frac{\partial P}{\partial y} = \frac{\partial}{\partial x}\mu\frac{\partial v}{\partial x} + \frac{\partial}{\partial y}\mu\frac{\partial v}{\partial y} \tag{22}$$

The Lagrangian form of the continuity equation is also required :

$$\frac{D\rho}{Dt} + \rho(\frac{\partial u}{\partial x} + \frac{\partial v}{\partial y}) = 0 \tag{23}$$

Because of the two-phase treatment, the viscosity can vary spatially. According to Kubota et al. [16], the viscosity of mixture can be written:

$$\mu = \alpha\mu_g + (1 - \alpha)\mu_l \tag{24}$$

where μ_g and μ_l are the gas and liquid viscosities, and α is the void fraction. Since the non-dimensional pseudo-density is volume fraction of mass per unit cell volume, the Equation (24) can be written as:

$$\mu(\rho) = \rho\mu_l + (1 - \rho)\mu_g \tag{25}$$

This mixture viscosity is substituted back into Equation (21) and (22) for non-dimensionalization. The channel width, liquid inflow velocity and liquid density are chosen as dimensions in nondimensionalizing the equations. Rearranging the equations for flux calculation through cell faces yield the following momentum equations:

$$\frac{\partial \rho u}{\partial t} + \frac{\partial}{\partial x}\left[\rho u^2 - \frac{1}{Re^*}\frac{\partial u}{\partial x}\right] + \frac{\partial}{\partial y}\left[\rho u v - \frac{1}{Re^*}\frac{\partial u}{\partial y}\right] = -\frac{\partial p}{\partial x} \tag{26}$$

$$\frac{\partial \rho v}{\partial t} + \frac{\partial}{\partial x}\left[\rho u v - \frac{1}{Re^*}\frac{\partial v}{\partial x}\right] + \frac{\partial}{\partial y}\left[\rho v^2 - \frac{1}{Re^*}\frac{\partial v}{\partial y}\right] = -\frac{\partial p}{\partial y} \tag{27}$$

where

$$\frac{1}{Re^*} = \frac{\rho}{Re_l} + \frac{\rho_g(1 - \rho)}{\rho_l}\frac{1}{Re_g} \tag{28}$$

which includes the both liquid and gas phase viscous effect in one term. The second and third terms in left hand side of the Equation (26) and (27) are the main terms for calculation of momentum

104

fluxes in x and y directions in the code. Here Re_l and Re_g represent Reynolds numbers of liquid and gas-phase respectively.

Since ρ is a non-physical variable, an additional constitutive relation is required in place of an equation of state which would normally close the set of governing equations. In this case, we envision a group of droplets convecting through a gas media. If we assume all droplets are of the same size and neglect fission or fusion processes, then the local number density sets the pseudo-density for a given computational cell. Consequently, one can conclude from the above assumptions that the density evolves in time by simply considering a Lagrangian tracking of the droplet field as specified by a continuity equation as:

$$\frac{D\rho}{Dt} = \frac{\partial \rho}{\partial t} + u\frac{\partial \rho}{\partial x} + v\frac{\partial \rho}{\partial y} = 0 \tag{29}$$

This equation is basically a statement that the droplet mass is invariant along a path line in the fluid. By taking account for the flow direction, the pseudo-density is updated based on mass flux calculation as follows :

$$\rho^{n+1} = \rho^n - \frac{\Delta t}{V_c}\left[\left(\dot{m}_{out}\right)_{x,y} - \left(\dot{m}_{in}\right)_{x,y}\right] \tag{30}$$

where V_c is volume of a given cell and $\dot{m}$ is mass flowrate corresponding x and y directions. The flux of the mass through a given cell are calculated by a standard upwind scheme. While this provides a locally first order solution in the region adjacent to the discontinuity in density, it provides for a stable approach to account for the large density gradients near the interface. Since the interface region will undoubtedly contain droplets in these very high convective environments, a shock-type density discontinuity would not be consistent with a homogeneous flow representation. The scheme is second-order accurate with the exception of the points adjacent to the interface, and convergence is verified in the next section. Figure 5 illustrates the basic geometry of a coaxial injector. The computational domain is the recessed region inside the nozzle, and the structured mesh employed 100×200 grid points in transverse (y) and axial (x) directions respectively. Exponential stretching is applied in the transverse direction to enhance resolution near the walls.

For boundary conditions, the liquid and gas-phase velocities are defined at inflow boundary. The pressure is extrapolated with zero gradient for inflow boundary. No slip conditions for velocities are defined on both walls. Finally, constant pressure condition is set for outflow boundary while the velocities are extrapolated at this location.

A series of grid convergence studies have verified that this mesh (100×200) is adequate to resolve the unsteady sheet flow. When the velocities for the liquid sheet and surrounding gas flow in upper and lower sides are balanced in exact symmetry, the flow field reaches a steady state after a certain period of time. This steady state condition provides us an opportunity for relatively simple grid function convergence test.

A center point in the computational domain has been picked for a flow-representative-position. Time histories of density, pressure and liquid velocity have been observed until the flow solution reaches to the steady state. Figure 6 shows the each flow property history at the center point for three grid sizes: 100×50, 200×100 and 400×200 in x and y axis respectively. Result shows that the 200×100 grid provides accuracy comparable to the fine grid. In Figure 7 and 8, the density and velocity distribution over y axis at the nozzle exit are depicted after reaching steady state. The coarse grid reaches steady state when $t = 3.7$, and the medium and fine grids achieve steady state at $t = 5.15$, $t = 4.75$ respectively. These figures also show the good agreement between the medium grid and fine grid while the coarse grid still has some errors as compared to the other two grids. In overall, the 200×100 grid is expected to generate flow solution in a good resolution while reducing running time in a significant order. A typical calculation takes three to four hours for the 200×100 grid on Pentium II 450MHz machine. The 400×200 grid runs about 48 hours even on 64-bits RISC Alpha chip (500MHz) machine until the flow solution reaches to the steady state.

Since it takes substantially long time until the liquid sheet develops the instability, an artificial disturbance is introduced in order to initiate the oscillation at ealier stage. This has been done via setting up unbalanced velocities on upper and lower side of liquid surface grid points at initial time step($t = 0.0$) only. The result shows that a certain level of small disturbance can cause the violent oscillation of the liquid sheet inside the channel after a short transient time. Since the flow field is solved by a system of elliptic-parabolic governing equations, the numerical disturbance causing the oscillation is initial condition dependent. However, by no means of measuring the magnitude of the artificial disturbance quantitatively at the time the oscillation is initiated, a direct comparison between the cases with and without the initial disturbance is not possible. The best one can do at the moment is to make sure that the code predicts, at least qualitatively, all characteristics of the flow.

Numerical Results

A baseline case is presented to provide the reader with insight into the unsteady jet oscillation inside a coaxial injector nozzle. The injector schematic is shown in Figure 5. The channel width, D_0, is assumed to be $0.005m$ and the liquid sheet width, D_i, is $0.001m$. The length of recessed region L is $0.01m$ which is twice the channel diameter. The thickness of liquid injector structure is neglected since the computational domain is outside of the liquid injector and the gas and liquid flows interact each other right after coming out of the exit. The gas and liquid phase velocities are $80m/s$ and $20m/s$ respectively. The Reynolds numbers are $Re_g = 2.22 \times 10^5$ for gas and $Re_l = 9.98 \times 10^4$ for liquid. Here, density of water has been used for the liquid phase and a gas/liquid density ratio of 0.01 is assumed to be realistic with high pressure injector operation.

The overall behavior of the instability is shown in Figure 9 which depicts pseudo-density con-

tours at various times during the calculation. Here, the outermost contour is for $\rho_g = 0.01$ and the innermost contour is for $\rho_l = 1.0$. After some chaotic oscillations during early phases of the calculation, the sheet enters a quasi-periodic oscillation. The velocity streamlines and velocity profiles at the exit are shown in Figure 10.

By plotting the location of maximum density at the exit plane as a function of time, the character of the oscillation becomes apparent as seen in Figure 11 which shows a very high amplitude oscillation (channel walls are at $r = 0,\ 1$) as evidenced in the pseudo-density contours in Figure 9.

The oscillation is also quasi-periodic; by taking the Fast Fourier Transform of the signal in Figure 11, we can identify its fundamental frequencies. Results of this calculation are shown in Figure 12. The peak near $f = 0$ is attributed to the transient during the start of the calculation. The first peak with frequency of 0.6836 indicates the fundamental frequency, and the second peak corresponds to the first harmonic mode at frequency of 1.3867. The development of multiple harmonics takes longer than for a single tone. There is some activity at higher harmonics, but at a much lower energy level than the primary tone and the first harmonic. Under the nondimensionalization employed, a frequency of 2.0 would correspond to the time it takes a liquid fluid element to traverse the channel according to the definition of Strouhal number. The primary tone would correspond to a period of roughly three times the channel transit time.

Converting these nondimensional frequency values into physical ones, the primary harmonic is at 2740 Hz and the second harmonic is near 5600 Hz. These are frequencies within the range of acoustic modes within liquid rocket engine combustion chambers. A series of experimental result by Eroglu and Chigier [11] also showed that the frequencies of jet oscillation of airblast coaxial injector at similar water-air velocities fall into the same frequency band. In principal, the numerical analysis does support the conclusion that jet instability in the submerged region could reinforce instabilities in the combustion chamber. However, the jet submergence is much larger here than that typically used in rocket engine injectors. For this reason, a parametric study was initiated to classify the instability over a range of design and operating conditions.

Parametric Study

A parametric study has been conducted in order to evaluate the influence of gas/liquid density ratio, velocity ratio, sheet thickness, sheet submergence, and Reynolds number. Results are compared by plotting the amplitude of the oscillation (basically the difference between the upper peaks and lower peaks in Figure 11) as a function of time for the various parameters investigated.

Density ratio effects

Four simulations at various gas/liquid density ratios with all other inputs fixed ($U_g/U_l = 4$, $L/D = 2$, $h = 0.2$, $Re = 10^5$) have been conducted in order to assess the influence of this parameter. The

oscillation amplitude histories for these cases are summarized in Figure 13 for gas/liquid density ratios, $\epsilon = 0.005$, 0.01, 0.02, and 0.1. The primary frequency, f, of each case is also noted in the legend in Figure 13. Results indicate that both the amplitude and the frequency of the oscillation increase with gas density. Physically, this is attributed to the fact that the gas is capable of imparting more momentum to the liquid when it is of higher density. This behavior is completely consistent with the linear Kelvin-Helmholtz theory.

Effect of gas/liquid velocity ratio

Three different velocity ratio cases have been studied for other conditions consistent with the baseline case described previously. Here, $U_g/U_l = 2$, 4, and 8 were investigated; results are depicted in Figure 14. The case with $U_g/U_l = 2$ shows very little activity as the sheet deviates little from its initial height. The case with $U_g/U_l = 8$ setting shows a chaotic oscillation which essentially encompasses the entire width of the channel. In this case, it appears that the sheet breaks up because of the unusually high gas velocity and the liquid fragments disintegrated from the liquid core keep hitting walls and generate non-periodic, high frequency vibration rather than wave type oscillation. For this reason, no frequency value is reported for this condition.

Physically, the gas dynamic pressure which drives the instability scales as the square of the gas velocity. The results obtained in this study is consistent with this general nonlinear behavior.

Effect of varying sheet thickness

Geometric variations were also investigated in the studies. Figure 15 depicts the influence of the thickness of the liquid sheet at other conditions corresponding to the baseline case. Sheet thicknesses (h) corresponding to 20, 40, 60, and 80% of the channel width were considered in the study. Physically, this would correspond to thicknesses of 1, 2, 3, and 4 mm in the baseline injector design. In general, the oscillation frequencies were not strongly dependent on the thickness of the sheet. The amplitude of the oscillations tends to decrease with increasing h, presumably due to the fact that the liquid inertia grows with the sheet thickness.

Linear analyses indicate that the presence of the walls has a destabilizing effect which is the opposite of the trends noted in the nonlinear calculations. The long wave instabilities which govern the calculations are indeed damped by the presence of channel walls. High frequency, short wave instabilities are not resolved in the present model since capillary forces are neglected and the pseudo-fluid treatment does not support a sharp discontinuity at the interface. This area would require further study with a separate flow two-phase model in order to more fully resolve this issue.

108

Channel length effects

The effect of liquid injector submergence is addressed in Figure 16. Here, the liquid injector was recessed at four separate distances, 1, 1.5, 2, and 3 channel heights ($L/D = 1$, 1.5, 2, 3) with other conditions remaining identical to the baseline configuration. When the channel width is the same as the recess length ($L/D = 1$), there is little activity, and a straight sheet comes out of the exit. As the submergence length is increased, the $L/D = 1.5$ case shows the sheet starts to oscillating but the magnitude of the oscillation is smaller than the baseline case and damps out gradually as time goes on. At $L/D = 2$, large amplitude oscillations are noted.

At $L/D = 3$, the oscillation becomes unpredictable with varying magnitude. In this case, the liquid sheet breaks up before it reaches to the exit, and the liquid fragments from the disintegration near the exit are shot out at somewhat irregular intervals. The radical change of the amplitude of this case can be explained by this behavior. In general, these trends are in agreement with the linear theory since increased submergence increases the time for instabilities to grow within the channel. Since most liquid rocket injectors of this type use very small submergence lengths, the present analysis shows little evidence of instability from the mechanism investigated in this work.

In general, the frequency of the instability tends to decrease with increased submergence. However, the FFT of the $L/D = 3$ case is interesting in that two distinct frequencies with similar energy content are noted. A short frequency consistent with a long-wave instability is present in addition to a higher frequency representative of clumps of disintegrated fluid. For very short submergence lengths there simply isn't time to grow instabilities to any appreciable level under the Kelvin-Helmholtz mechanism.

Reynolds number effects

The influence of viscous interactions were investigated through a series of simulations at Reynolds numbers between 10^3 and 10^7. Once again, the other input parameters were maintained at values selected in the baseline configuration. As we can see from the Figure 17, the amplitude of the oscillation is only slightly affected over this substantial Reynolds number range. In cases of high Reynolds numbers, however, two distinct frequencies appear in the oscillation; a fundamental frequency and a first harmonic mode at a lower energy level. The higher frequency is created by liquid fragments separated from the liquid sheet breakup near the exit. Since the liquid fragments come out of the nozzle exit in a very regular manner, the short wave pattern at high frequency is developed. The amplitude of the oscillation at high Reynolds number decreases slightly because of energy loss caused by the harmonic mode development.

This result is consistent with general nonlinear behavior since decreased viscous interaction generates higher frequency mode in addition to the primary oscillation.

Effect of Liquid Post Thickness

In this section the "baseline" flow conditions are considered with a liquid sheet with a finite post thickness. This structure is often referred to as the "LOX post" in coaxial injectors involving this cryogenic propellant. When we consider a finite thickness of the post, the flow must now expand/recirculate to fill the region immediately downstream of the post tip. A pair of counter-rotating vortices become apparent immediately downstream of the upper and lower posts. The recirculation region has approximately the same thickness as the post tip thickness (t_{LOX}) at the nozzle exit and tapers to zero at some downstream point. This recirculation area serves as flame holder in combusting system and stabilizes the liquid jet inside the injector by anchoring the jet to the nozzle exit.

Moon [20] investigated coaxial injector and showed that the recirculation region exists immediately after the LOX post exit. He explained that the recirculation region is caused by at least two mechanisms: viscous mixing and pressure gradient. Since static pressure is not constant throughout the flow, the recirculation zone forms a pseudo-diffuser, causing a low pressure region to exist near the post tip. Viscous effects cause a slightly more rapid decrease in velocity at the jet boundary.

Recently, Glogowski and Micci [10] conducted a series of experiments and investigated the flow near the LOX post region. Unfortunately, measurement of the flow inside the recessed region didn't produce favorable results due to difficulties involved in characteristically high signal-to-noise ratio in this area. However, they did verify the recirculation region near the LOX post by measuring mean axial velocity and showing that there exists negative mean velocity at the post tip. For the condition where the LOX post thickness is not negligible, they agreed that macroscopic instability within the liquid jet arise from both static pressure perturbation and aerodynamic viscous forces. In another research of Glogowski et al. [9], the flow characteristics of recessed LOX post area was investigated. They found that the injection operation with tapered LOX post recessed into fuel annulus produced a resonance condition characterized by a whistling noise and a significant modification to the overall spray structure. The non-tapered (straight) post exhibited a lower amplitude whistling noise but did not affect the spray structure.

All the flow properties used in the previous baseline case are preserved except to let the liquid post has a finite thickness with solid wall no-slip boundary conditions. In order to improve resolution in liquid post exit area, the spacing in x direction is exponentially stretched by using the same strategy used in y direction stretching. The smallest grid size is applied to the area between gas and liquid-phase where the most interaction is expected. The liquid post thickness here is 0.1 each in unit channel width. Dimensional conversion gives each $0.5mm$ thickness of upper and lower post in $5mm$ channel width. It should be noted that no slip boundary condition is defined on the post tip in y direction. The other boundary conditions remain the same as the baseline case without

liquid post thickness.

Figure 18 shows pseudo-density contours at various times. The liquid sheet develops symmetric disturbances on its surface due to expansion of the flow into the bluff region downstream of the posts (a). The length of this region is about 5 or 6 times the post tip thickness. After this calculation startup period, the liquid sheet enters a fiber-type breakup mode (Chigier[21]) which creates continuous surface vortices showing aerodynamic viscous effects (b). This limit cycle, bounded-oscillation state lasts until instability of the liquid sheet itself becomes prominent and starts to generate asymmetric wave (c). This wave grows rapidly, and the liquid sheet oscillates in a quasi-periodic manner (d), (e). When compared with the baseline case without liquid post thickness, the oscillation is larger in magnitude and has a shorter wavelength, leading to a higher frequency.

Velocity streamlines and exit velocity profiles are shown in Figure 19. The flow recirculation at the liquid post exit is obvious in this figure. Symmetric recirculation regions are developed on upper and lower surfaces during the initial and bounded oscillating state period (a), (b). The velocity profiles at the injector exit in this period show the momentum deficit in the radial areas corresponding to the upper and lower posts. During this period, one can see the assumed plug-flow velocity distribution in the liquid is largely maintained. Once the liquid sheet starts to oscillate, the velocity profile goes through a corresponding oscillation. Note that the highest density region is actually convected out of the channel with the highest velocity in parts (d) and (e) even though the liquid is injected at lower velocity than the gas. These velocity profile characteristics show the same qualitative behavior as the results of the measurements by Moon [20] and Glogowski et al.[9].

Two different liquid post thickness have been evaluated in order to assess the influence of this parameter. Posts of twice ($t_{LOX} = 0.2$) and half ($t_{LOX} = 0.05$) of the baseline thickness were considered. The magnitude of oscillation of each LOX post thickness are plotted with the previous baseline case without finite post thickness in Figure 20. Note that the lines are plotted only for the oscillation period, i.e., the initial point ($t = 0.0$) is when the quasi-periodic oscillation starts. For the thicker post case, larger surface vortices are formed initially due to bigger recirculation region at the post tip. The liquid sheet then undergoes a quasi-periodic oscillation with an amplitude much less than that of the $t_{LOX} = 0.1$ case. The intact length of the liquid sheet from the base of liquid post is increased in this case and the frequency of the oscillation is lower than the $t_{LOX} = 0.1$ case. In the thinner liquid post configuration, the long-wave disturbance appears almost immediately and the magnitude of the oscillation grows to about the same level as the $t_{LOX} = 0.1$ case, but with a significantly higher frequency of oscillation.

In comparing these results to the case from the prior section where the post thickness was neglected altogether, we see an interesting behavior. The thicker post shows a stabilizing effect, while the two thinner posts show amplification in the instability as compared to the case where a zero post thickness was assumed. These results indicate that that the thickness of the post can play a strong role in the instability and can in principle explain the significant differences in spray

character noted by Glogowski, et. al. when tapered and untapered posts were used.

Conclusions

A homogeneous flow model has been developed to assess hydrodynamic instabilities of coaxial atomizers in which a liquid jet/sheet is submerged slightly in an annular gas stream. The calculations have been performed in a 2-D analogue to this geometry; a liquid sheet with coflowing gas on upper and lower extremities. Kelvin-Helmholtz type instabilities are noted under conditions where the gas velocity is substantially greater than that of the liquid. Parametric studies indicate the amplitude of the instability increases with gas velocity, gas density, and sheet recess/submergence length inside the channel. Increasing sheet thickness tended to decrease the amplitude of the oscillation. The frequencies observed are consistent with the channel transit time of the liquid.

A series of liquid post thicknesses were investigated to assess the effects of this parameter. Flow recirculation at the post tip is observed in accordance with prior experimental observations. Thin posts show greater amplitude instabilities than the zero-thickness case, while a thicker post proved to damp the amplitude of the oscillation. In addition, the thinner posts created much higher oscillation frequencies than the case of a zero-thickness post. These results are indicative of the effects noted experimentally; strong differences in exit flow can be attributed to fairly minor changes in post thickness.

Acknowledgement

Nomenclature

D - Channel width

f - Nondimensional frequency

h - Liquid sheet thickness from center line

k - Wave number L - Channel length

$\dot{m}$ - Nozzle massflow rate

P - Pressure

Re - Reynolds number

t_{LOX} - Liquid post thickness

u, v - Velocity

V - Computational cell volume

We - Weber number

x - Cartesian coordinate, x-direction

y - Cartesian coordinate, y-direction

α - Void fraction

ΔU - Velocity difference between liquid and gas phase

ϵ - Density ratio (ρ_g/ρ_l)

η - amplitude of wave disturbance

μ - Viscosity

ϕ - Velocity potential

ρ - Fluid pseudo-density

σ - Surface tension

ω - Growth rate

Subscripts

c - Computational cell

g - Gas-phase

l - Liquid-phase

i - Inlet

o - Outlet

References

1. V. G. Bazarov and Vigor Yang, "Liquid-Propellant Rocket Engine Injectors Dynamics," *Journal of Propulsion and Power*, Vol. 14, No. 5, pp. 797-806, 1998.

2. V. G. Bazarov and L.A. Lyul'ka, "Nonlinear Interactions in Liquid Propellant Rocket Engine Injectors," *AIAA 98-4039*, 1998.

3. T. Arai and H. Hashimoto, "Disintegration of a Thin Liquid Sheet in a Cocurrent Gas Stream", *ICLASS-85*, Vol 1B, pp. 1-7, 1985.

4. J. J. Hutt and M. Rocker, "High-Frequency Injector-Coupled Combustion", *Liquid Rocket Engine Combustion Instability*, Vol. 169, Progress in Astronautics and Aeronautics, pp. 345-356, 1995.

5. V. G. Bazarov, "Self-Pulsations in Coaxial Injectors with Central Swirl Stage," *AIAA 95-2358*, 1995

6. W. Mayer and G. Krulle, "Rocket Engine Coaxial Injector Liquid/Gas Interface Flow Phenomena", *Journal of Propulsion and Power*, Vol. 11, No. 3, pp. 513-518, 1995.

7. W. Mayer and H. Tamura, "Flow Visualization of Supercritical Propellant Injection in a Firing LOX/GH2 Rocket Engines", *AIAA 95-2433*, 1995

8. W. Mayer, A. Schik, and M. Schaffler, "Injection and Mixing Processing in High-Pressure Liquid Oxygen/Gaseous Hydrogen Rocket Combustors", *Journal of Propulsion and Power*, Vol. 16, No. 5, pp. 823-828, 2000.

9. M. Glogowski, M. Bar-Gill, et al. "Shear Coaxial Injector Instability Mechanisms", *AIAA 94-2774*, 1994

10. M. Glogowski and M. M. Micci, "Shear Coaxial Spray Characterization Near the LOX post Tip Region", *AIAA 95-2552*, 1995.

11. H. Eroglu and N. Chigier, "Wave Characteristics of Liquid Jets from Airblast Coaxial Atomizers", *Atomization and Sprays*, Vol. 1, pp. 349-366, 1991.

12. Adel Mansour and Norman Chigier, "Dynamic behavior of liquid sheet", *Physics of Fluids A*, Vol. 3(12), pp. 2971-2980, 1991.

13. Chen Y., and Heister S. D., "Modeling Hydrodynamic Non-Equilibrium in Bubbly and Cavitating Flows," *Journal of Fluids Engineering*, Vol. 118, No. 1, pp. 172-178, 1995.

14. Bunnell R. A. *Unsteady, Viscous, Cavitating Simulation of Injector Internal Flows*, Ph. D. Thesis, School of Aeronautics and Astronautics, Purdue University, West Lafayette, IN, August 1999.

15. Bunnell, R. A., Heister S. D., Yen C. and Collicott S. H., "Cavitating Injector Flows: Validation of Numerical Models and Simulations of Pressure Atomizers," *Atomization and Sprays*, Vol. 9, pp. 445-465, 1999.

16. Akihiro Kubota et al., "A New Modeling of Cavitating Flows : A Numerical Study of Unsteady Cavitation on a Hydrofoil Section", *Journal of Fluid Mechanics*, Vol. 240, pp. 59-96, 1992.

17. H. B. Squire, "Investigation of the Instability of a Moving Liquid Film", *British Journal of Applied Physics*, Vol. 4, pp. 167-169, 1953.

18. N. Dombroski and W. R. Johns, "The Aerodynamic Instability and Disintegration of Viscous Liquid Sheet", *Chemical Engineering Science*, Vol. 18, pp. 203-214, 1963.

19. Xianguo Li and R. S. Tankin, "On the Temporal Instability of a Two-dimensional Viscous Liquid Sheet", *J. of Fluid Mechanics*, Vol. 226, pp. 425-443, 1991

20. L. F. Moon, "Pressure and Velocity in a Developing Coaxial Jet", *AIAA Journal* Vol. 14, No. 1, pp. 43-49, 1976.

21. Norman Chigier and Rolf D. Reitz, "Regimes of Jet Breakup and Breakup Mechanisms (Physical Aspect)", *AIAA*, Vol. 3(12), pp. 109-135, 1995.

Figure Captions

1. Nomenclature for linear stability analysis for anti-symmetric jet oscillations in a channel

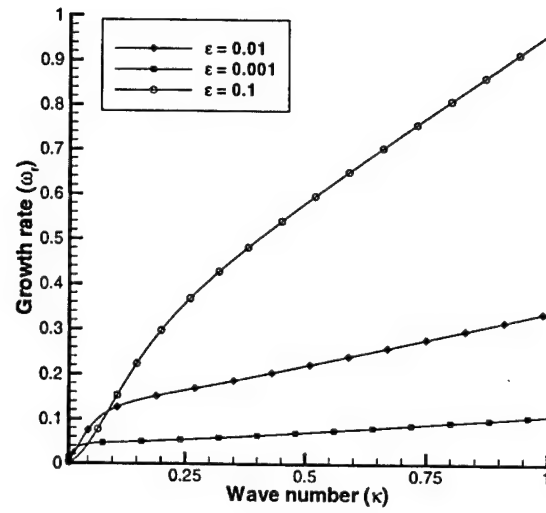2. Effect of gas velocity on growth rate: $\epsilon = 0.01, n = 5$

3. Effect of gas/liquid density ratio, ϵ on growth rate: $\Delta U = 3, n = 5$
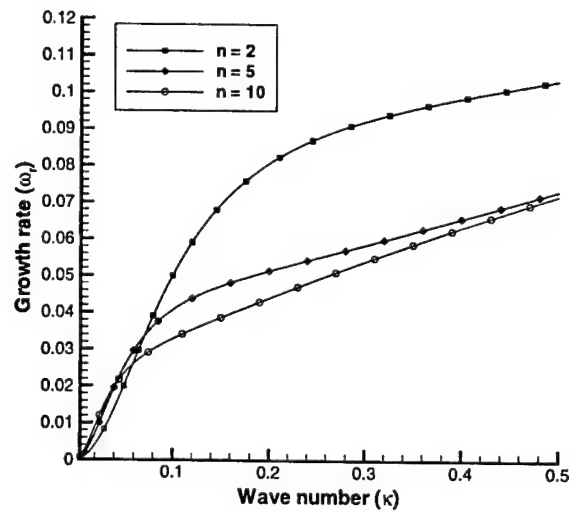
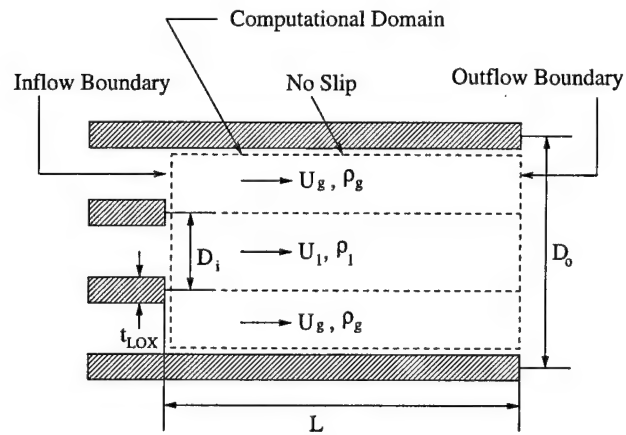4. Effect of channel width on growth rate: $\epsilon = 0.01, \Delta U = 3$
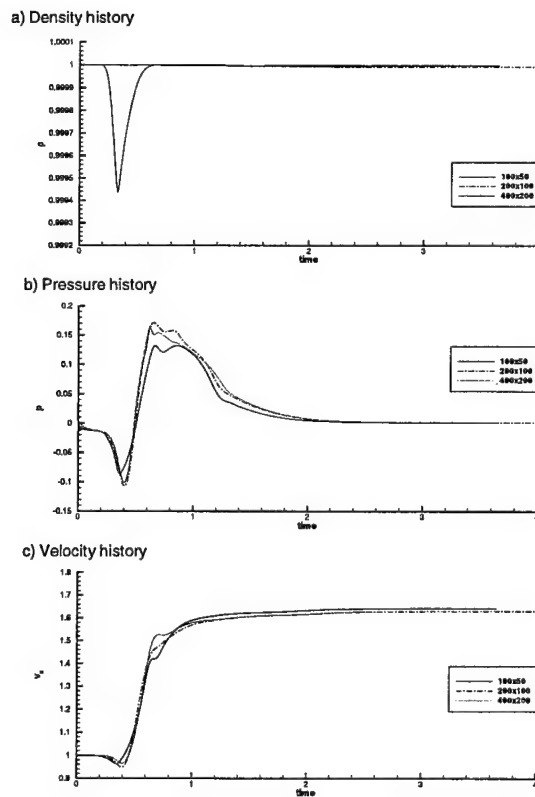
5. Coaxial injector schematic noting design variables.

6. Effect of grid size on density, pressure, and velocity at a point on the centerline of the domain $(U_g/U_l = 4, L/D = 2, h = 0.2, Re_l = 10^5)$

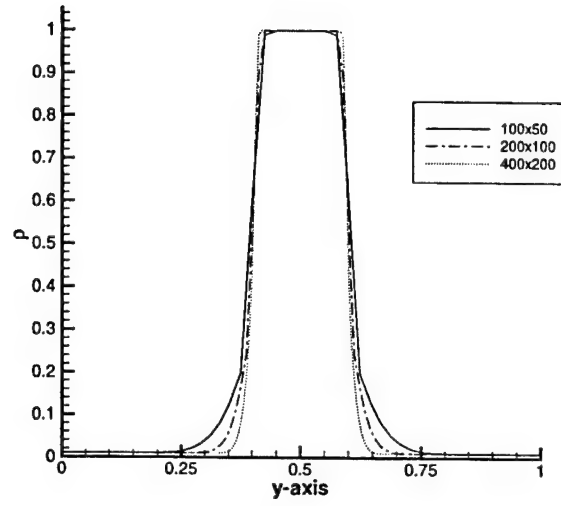7. Density distribution at exit at steady state

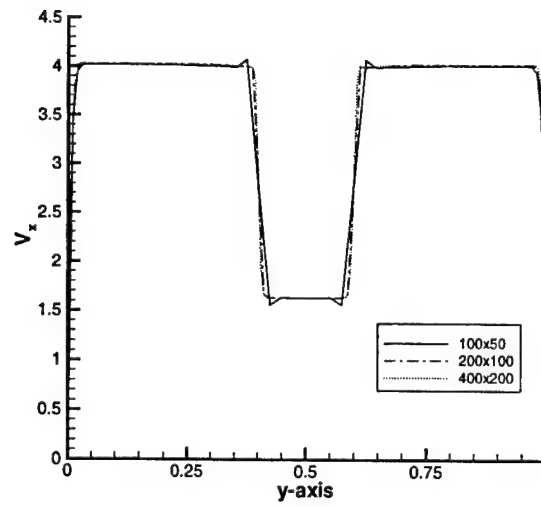8. Velocity distribution at exit at steady state
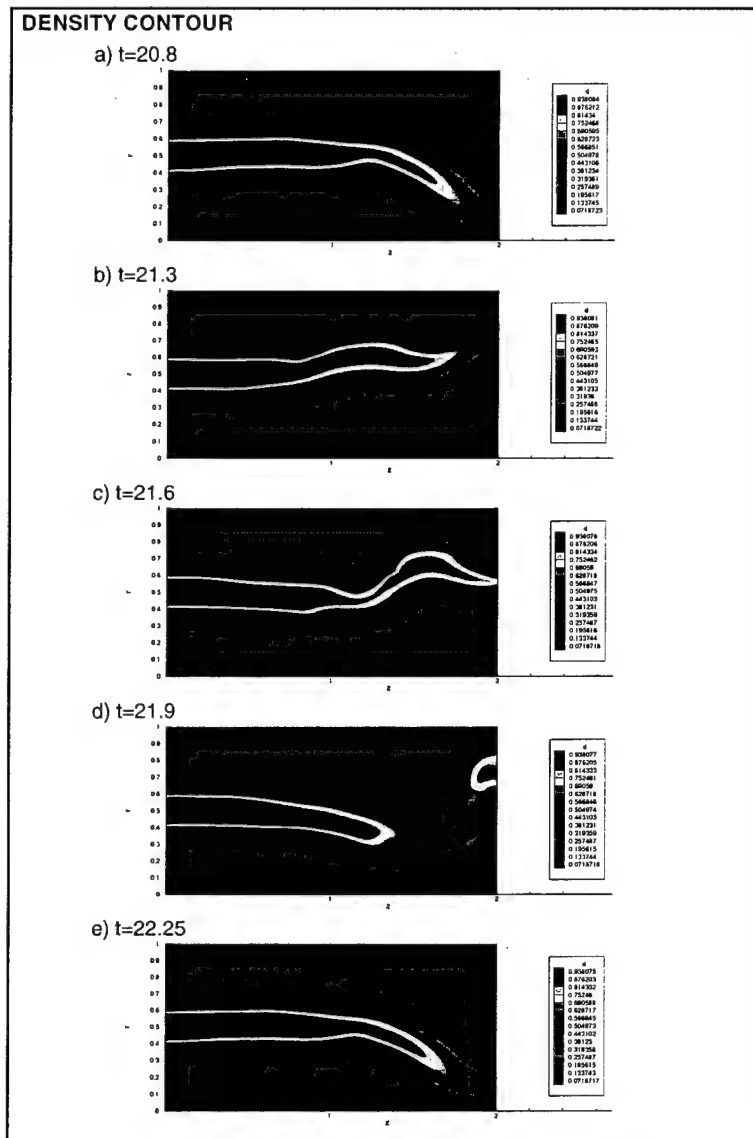
9. Density contours in a typical jet oscillation
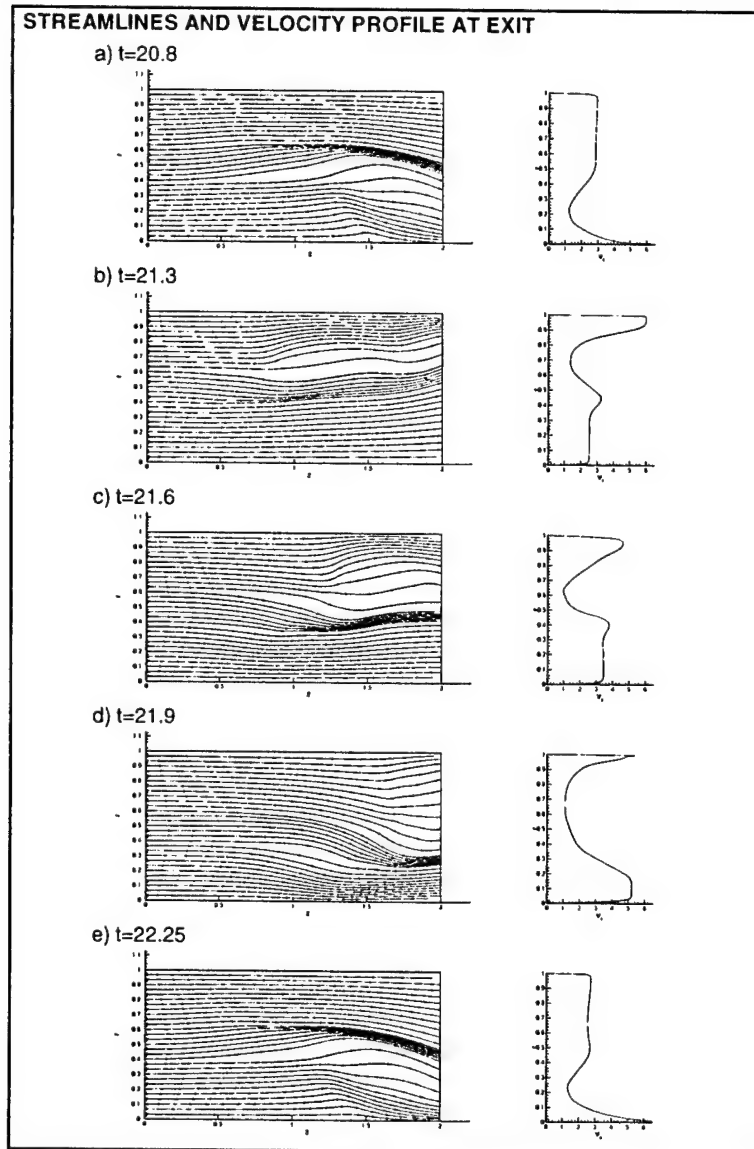
10. Velocity streamlines and exit velocity profiles in a typical jet oscillation

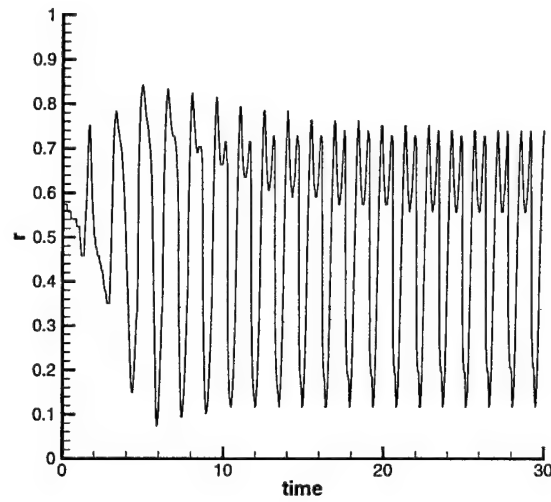11. Liquid sheet oscillation : Maximum density location at channel exit $(U_g/U_l = 4, L/D = 2, h = 0.2, Re_l = 10^5)$

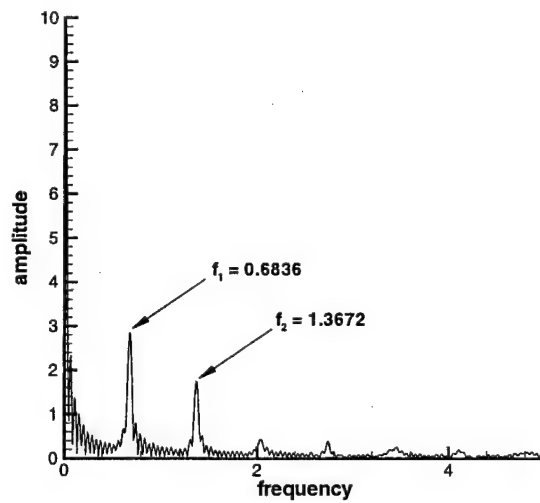12. Fast Fourier Transform analysis of liquid sheet oscillation

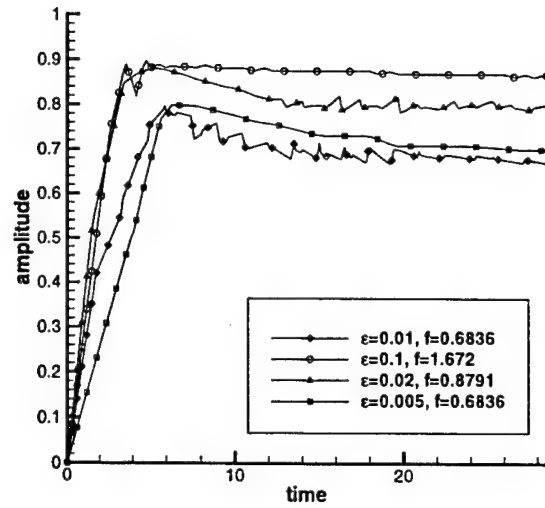13. Effect of density ratio on amplitude of the sheet oscillation $(U_g/U_l = 4, L/D = 2, h = 0.2, Re_l = 10^5)$

14. Effect of velocity ratio on amplitude of the sheet oscillation $(\epsilon = 0.01, L/D = 2, h = 0.2, Re_l = 10^5)$

15. Effect of jet thickness on amplitude of the sheet oscillation $(U_g/U_l = 4, \epsilon = 0.01, L/D = 2, Re_l = 10^5)$

16. Effect of channel length on amplitude of the sheet oscillation $(U_g/U_l = 4, \epsilon = 0.01, h = 0.2, Re_l = 10^5)$

17. Effect of gas Reynolds number on amplitude of the sheet oscillation $(U_g/U_l = 4, \epsilon = 0.01, L/D=2, h = 0.2)$

18. Density contours liquid sheet oscillation with liquid post thickness, $t_{LOX} = 0.1$

Figure 1: Nomenclature for linear stability analysis for anti-symmetric jet oscillations in a channel
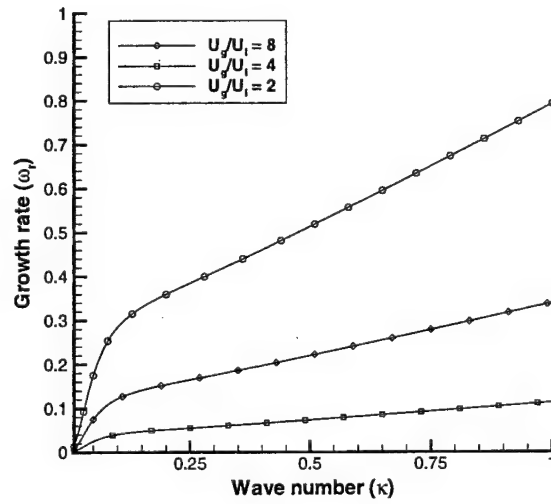
Figure 2: Effect of gas velocity on growth rate: $\epsilon = 0.01, n = 5$

Figure 3: Effect of gas/liquid density ratio, ϵ on growth rate: $\Delta U = 3, n = 5$

Figure 4: Effect of channel width on growth rate: $\epsilon = 0.01, \Delta U = 3$

119

Figure 5: Coaxial injector schematic noting design variables

Figure 6: Effect of grid size on density, pressure, and velocity at a point on the centerline of the domain ($U_g/U_l = 4$, $L/D = 2$, $h = 0.2$, $Re_l = 10^5$)

Figure 7: Density distribution at exit at steady state

Figure 8: Velocity distribution at exit at steady state

DENSITY CONTOUR

Figure 9: Density contours in a typical jet oscillation

Figure 10: Velocity streamlines and exit velocity profiles in a typical jet oscillation

Figure 11: Liquid sheet oscillation : Maximum density location at channel exit ($U_g/U_l = 4$, $L/D = 2$, $h = 0.2$, $Re_l = 10^5$)

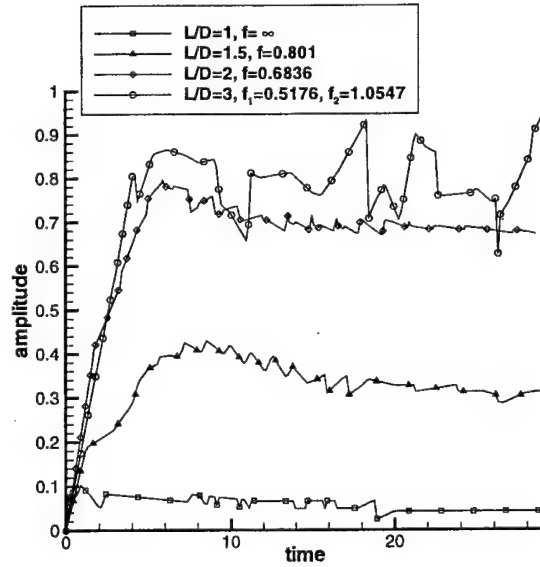Figure 12: Fast Fourier Transform analysis of liquid sheet oscillation

124

Figure 13: Effect of density ratio on amplitude of the sheet oscillation ($U_g/U_l = 4$, $L/D = 2$, $h = 0.2$, $Re_l = 10^5$)
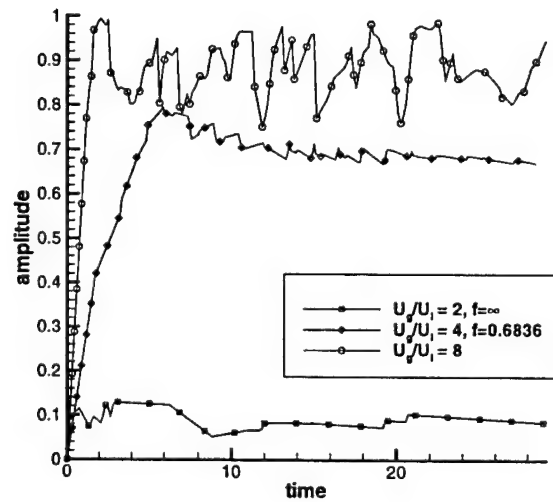
Figure 14: Effect of velocity ratio on amplitude of the sheet oscillation ($\epsilon = 0.01$, $L/D = 2$, $h = 0.2$, $Re_l = 10^5$)

125
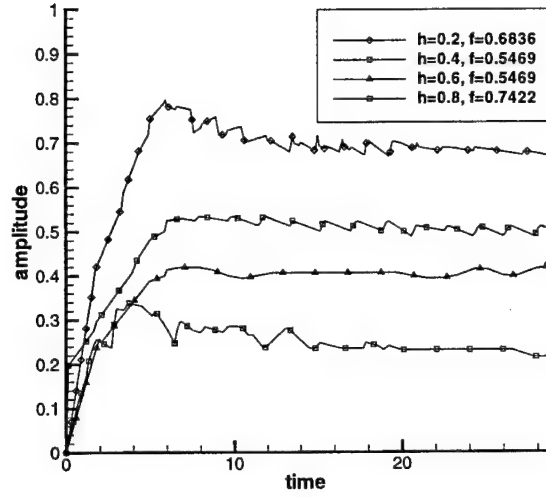
Figure 15: Effect of jet thickness on amplitude of the sheet oscillation ($U_g/U_l = 4$, $\epsilon = 0.01$, $L/D = 2$, $Re_l = 10^5$)
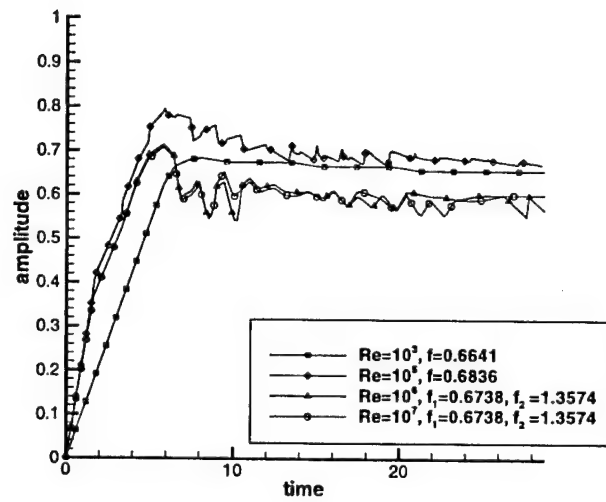

Figure 16: Effect of channel length on amplitude of the sheet oscillation ($U_g/U_l = 4$, $\epsilon = 0.01$, $h = 0.2$, $Re_l = 10^5$)

126

Figure 17: Effect of gas Reynolds number on amplitude of the sheet oscillation ($U_g/U_l = 4$, $\epsilon = 0.01$, L/D=2, $h = 0.2$)
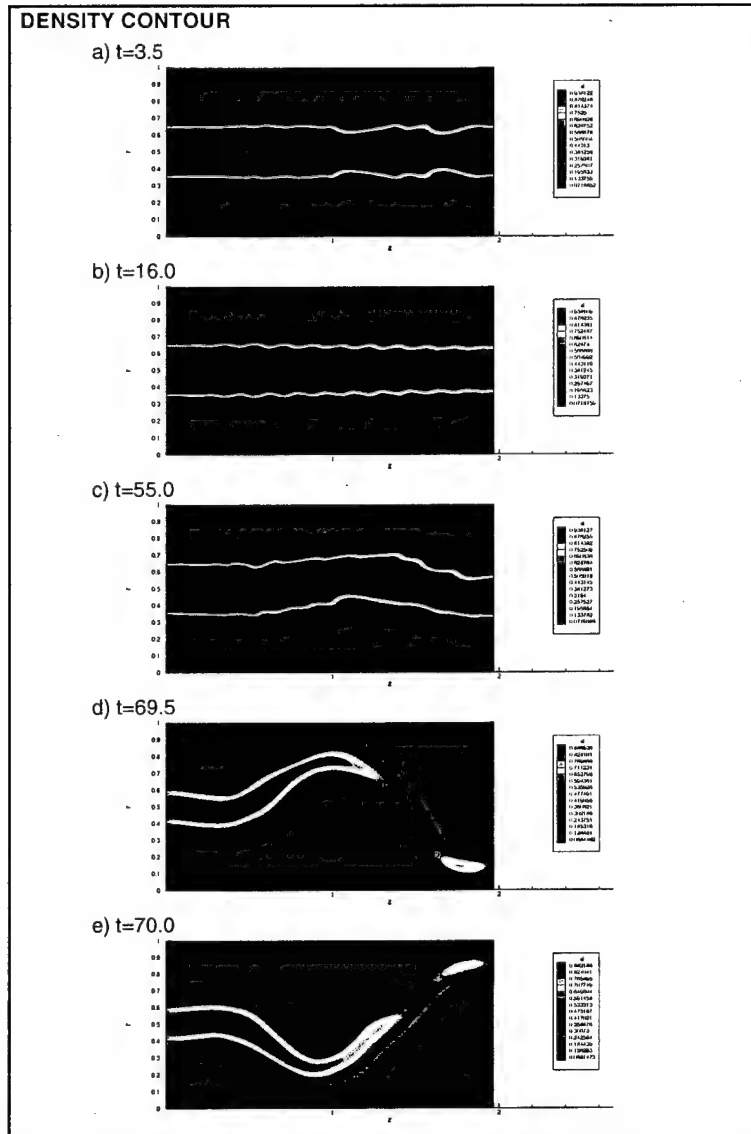
Figure 18: Density contours liquid sheet oscillation with liquid post thickness, $t_{LOX} = 0.1$
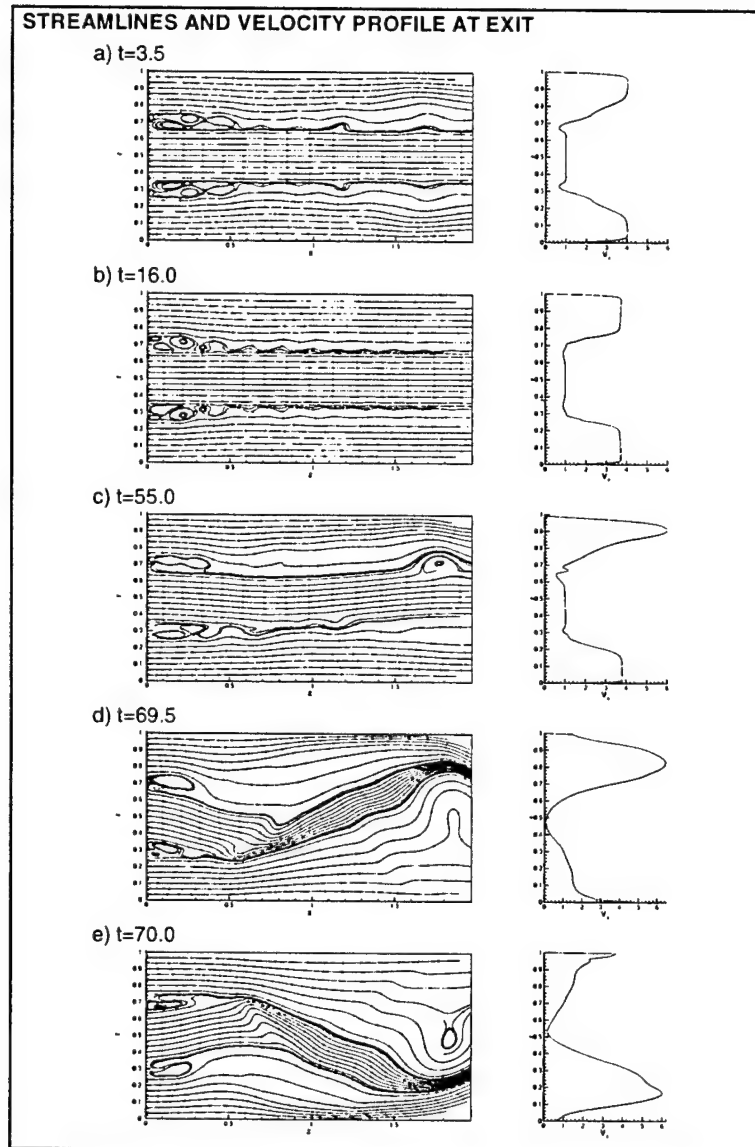
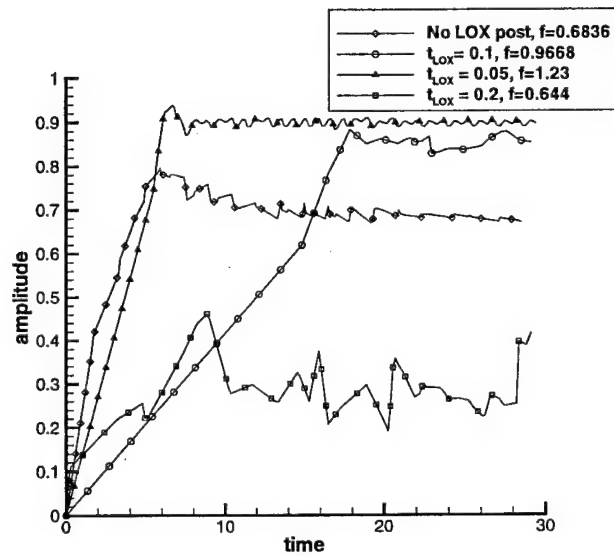Figure 19: Velocity streamlines and exit velocity profiles with liquid post thickness, $t_{LOX} = 0.1$

Figure 20: Effect of liquid post thickness on amplitude of oscillation ($U_g/U_l = 4$, $L/D = 2$)

9   Appendix E - Three-Dimensional Coaxial Injector Modeling

Kim*, B. and Heister, S. D., "Three-dimensional Simulations of Flow within the Recessed Region in a Coaxial Injector".

Three-Dimensional Flow Simulations in Recessed Region of a Coaxial Injector

Byoung-Do Kim [*], Stephen D. Heister [†], Steven H. Collicott [‡]

[*] Graduate Research Assistant, [†] Professor, [‡] Associate Professor

School of Aeronautics and Astronautics,

Purdue University, W. Lafayette, IN

Abstract

A three-dimensional, two-phase, unsteady Navier-Stokes solver has been developed to investigate fluid dynamic instabilities within the recessed region of a shear coaxial injector element. Here, the main emphasis is to study applications related to liquid rocket engine injectors using the gas/liquid shear-coaxial element in which the inner liquid cylindrical post is submerged slightly with respect to the overall exit plane of the device. Since most of the previous works focus on spray structure outside of the injector, this study provides readers with insight into unsteadiness resulting from hydrodynamic instabilities within the internal nozzle flow upstream of the combustion chamber.

The present study focuses on unsteady 'self-oscillations' which have been theorized by various researchers. The Kelvin-Helmholtz instability mechanism due to velocity discontinuity between gas and liquid phase is investigated as a source of unsteadiness which could contribute to combustion roughness or instabilities. Massflow variations of the order of 30-40% are shown to exist as a result of this highly nonlinear process; fundamental frequencies are also identified for a range of conditions.

Introduction

The liquid-oxygen/gaseous-hydrogen coaxial injectors have been widely used in the liquid rocket engines. The concentric-orifice coaxial injector was used in rocket engine testing as early as the 1940s and later became the general choice on most of cryogenic liquid rocket engines. The mechanism of typical shear coaxial injector is that the liquid oxydizer is fed through the central tube and the gaseous hydrogen is coflowing around the outer annulus. Often times, the liquid oxygen post structure is recessed from the injector face in order to improve the combustion stability. Inner liquid turbulence and gas to liquid interactions cause the liquid to be stripped away from the jet and entrained into the surrounding gasflow. Disturbances from inside the combustion chamber

or outside vibrations during engine operations, along wioth the intrinsic jet instability inside the nozzle, create a certain circumstance that the liquid jet cannot maintain a uniform distribution of atomized spray. The spray jet in the recessed region then could produce periodic fluctuations in the combustion zone which may or may not couple to the dynamics within the combustion chamber, possibly followed by severe combustion instability.

In general, for the flow at high velocity, most of researchers agree that the principal source introducing instability to the jet is from aerodynamic forces arising from the interaction of the liquid jet with the surrounding gas flow. Reynolds and Weber numbers are generally very high in these atomizers and aerodynamic forces are several orders of magnitude larger than capillary forces. The interaction between the liquid and gas phases mainly comes from different velocities of each phase. The velocity discontinuity in a homogeneous fluid results wave growth on the interface, which is a common *Kelvin-Helmholtz* instability.

The historical review of the development of various coaxial injectors used in liquid engines can be found in Ref. 1 and 2. Theoretical and numerical modeling efforts on the coaxial injector atomization is also summarized in the paper of Vingert et al.[3] along with experimental results. Their work mainly devoted to the drop size prediction by using those experimental data. In the paper of Hulka and Hutt [1] the review focused on instability phenomena associated with combustion chamber feed system. Series of injector testing revealed that injection velocity ratio, pressure drop after the injection and fuel injection temperature are the key parameters defining combustion instability.

According to the Ref. 2, the combustion instability with high frequency is categorized into acoustic instability and hybrid instability. The acoustic instability shows dominant wave-type oscillation in the main chamber, but is independent of the feed system. With the hybrid form of instability, the wave character of the oscillation is strongly coupled between the feed system and the combustion chamber. Hutt and Rocker [4] also investigated the high frequency combustion instability associated with coaxial injectors. They classified the instability phenomena in the chamber as injection-coupled and intrinsic mechanism. The injection coupling implies chamber pressure/temperature variation as a key contributor in the change of flow dynamics through the injector. In the other hand, the intrinsic mechanism occurs in the flowfield due to its own flow dynamics with negligible feed system effect. However, a general agreement does not exist in term of categorizing those instability mechanism due to the involvement of various subprocesses occurring after the injection at different time scales. It should be noted that injection coupling is never independent of the intrinsic subprocesses, such as atomization, propellant heatup, vaporization, and mixing because these processes determine the relationship between the injector response and the chamber response.

Mayer and his research group have done a significant amount of work on the coaxial injector in terms of the combustion instability. Mayer and Krulle [5] investigated coaxial flow mixing phe-

nomena in terms of chamber pressure variation, density/velocity ratio changes and surface tension effect. By increasing chamber pressure gas density is increased, magnifying the aerodynamic interaction between the liquid and gas phases and resulting in a faster, finer atomization. Increasing surrounding gas velocity also leads to an increase of surface wave growth and to macroscopic instabilities of the liquid jet. They claimed the initiation of the jet surface deformation was due to internal liquid turbulence delivering energy transform in forms of eddy structures, approximately a size of 10-30% of the LOX post diameter. Their global spray simulation combining primary and secondary jet breakup showed qualitative match with their experimental results. In other works of Mayer [6,7], the coaxial injector flow was studied under firing engine condition at supercritical chamber pressure (higher than 5 MPa). The study revealed a remarkable difference between subcritical spray formation and the supercritical injection and mixing. At subcritical condition, the liquid jet shows similar flow pattern to the cold flow test forming ligaments off the liquid jet surface and producing droplets before evaporation. Upon approaching and exceeding supercritical pressure, droplets no more exist and the liquid jet rapidly dissolves. The flame from combustion chamber was anchored at the tip of LOX post by flow recirculation eddies serving as flame holder for steady-state combustion. The asymmetric flow oscillation was also reported in all experiments, but the source of the oscillation was not clearly stated.

For analysis of the wave-type, asymmetric jet oscillation many researchers studied its theoretical aspects and conducted numerous experiments. Eroglu and Chigier [9] focused on the wave characteristics of liquid jet from coaxial air-blast injector. They measured frequency and wavelength of the jet issuing from the injector, and found two dominant wave type; spanwise(dilational) and stream-wise(sinuous) waves. The spanwise wave showed at a low relative jet velocity between gas and liquid-phase and the stream-wise wave showed at a high relative jet velocity. Average wavelengths decreased with liquid and gas velocity. The frequency band of the jet oscillation increased with the liquid jet velocity. Mansour and Chigier [10] also conducted similar research on the liquid sheet instability issuing from the two-dimensional air-assisted nozzle. The results showed the same pattern with the Eroglu and Chigier's study. However, Mansour and Chigier's study probed higher velocity cases, and confirmed that the frequency of the liquid sheet oscillation increased with coflowing gas velocity. This also indicates that the aerodynamic interaction between gas and liquid flow is the dominant factor for the flow oscillation.

Instability mechanisms in coaxial injectors were investigated experimentally by Glogowski et al. [13-15] under noncombusting conditions. Their experiment results showed that for the coaxial injector with the liquid oxygen (LOX) post recessed into the fuel annulus, the injector transitioned into a condition of resonance characterized by a whistling noise and significant modification to the overall structure of the spray due to the strong acoustic coupling between injector hydrodynamics and spray formation. Without the recessed region, the injector operation produced a near resonance condition with a lower amplitude whistling noise but did not make considerable changes in the

134

spray structure. The recirculation by reverse flow near the recessed LOX post exit also confirmed in the study. A try for getting oscillation frequency data in the submergence region of the coaxial injector was not successful due to optical restraint with small scales involved.

Bazarov [16–18] investigated coaxial injector flow dynamics in engine operating conditions. He identified "self-oscillation" and "self-pulsation" modes of liquid jet characteristics and suggested them as sources of high amplitude noise during combustion, leading to combustion inefficiency. He claimed that those high frequency instability occurred because of the intrinsic unsteadiness of flowfield and interactions with the combustion chamber and feed system dynamics since the injector element operates in strong feedback loops coupling chamber response and injection feed system. However, it was not clear which mechanism had more serious influence on the jet oscillation/pulsation.

Most of the previous research works summarized here mainly contributed to the investigation of flow phenomena outside of injector after the injection. None of them addressed the inner flow structure in a recessed region of the coaxial injector, especially using numerical simulation. Since the upstream flow in a injector provides the initial condition for the entire spray atomization process and combustion chamber acoustic characteristics, research work on this area is highly desirable.

Motivated by Bazarov's research, Kim and Heister [19–21] developed a 2-D numerical model investigating the coaxial liquid sheet behavior. The simulation demonstrated the self-oscillation mode caused by the Kelvin-Helmholtz instability. A series of parametric study had been done in order to analyze the effects of several key parameters including velocity/density ratio, recess length changes and the LOX post thickness. The results showed that increasing density and velocity ratio produced higher oscillation frequency and increasing the recess length also increased the natural frequency of the liquid sheet oscillation, leading to the sheet breakup. These results showed the same tendency that was predicted by linear theory analysis. Recent experimental study of Branam [22] provided the same qualitative match to the overall liquid jet behavior. Based on the 2-D results, a three-dmensional model has also developed and a series of has been conducted using Space Shuttle Main Engine's injector geometry and its flow properties. In this paper, the hydrodynamic instability of the coaxial jet in the recessed region is presented using the three dimensional direct numerical simulation. The results indicate that the recess length to injector orifice diameter has a significant effect on spray structure over the velocity and gas ratio changes. Unfortunately, none of experimental data for exact comparison exists due to very small spartial and temporal scales involved in the area. However, some of recent experimental data provide good measure in a macroscopic point of view for the instability frequency as explained later in this paper.

Modeling Description

Numerics

A fully unsteady, three dimensional, two-phase simulation has been developed utilizing a finite volume implementation of the Marker and Cell discretization method. The current model is based on locally homogeneous flow (LHF) assumption in which the relative velocity and temperature between two-phases are small enough in comparison to variation of the overall flow field that is predicted. Additional constituitive relation for desity field has been implemented in order to provide a mechanism of solving two-phase flow with a single phase Navier-Stokes equations set. This fictious "pseudo" density varies in amplitude between the liquid and gas extream. The LHF assumption and the pseudo-density implementation allow the current model to handle the two-phase flow field with one governing equations set rather than to compute separate governing equation sets for each flow phase, liquid and gas in this case.

Formulation of the three dimensional governing equations for computation are given as follows.

$$\frac{\partial \rho}{\partial t} + \frac{\partial \rho u}{\partial x} + \frac{\partial \rho v}{\partial y} + \frac{\partial \rho w}{\partial z} = 0 \tag{1}$$

$$\frac{\partial \rho u}{\partial t} + \frac{\partial \rho u^2}{\partial x} + \frac{\partial \rho u v}{\partial y} + \frac{\partial \rho u w}{\partial z} + \frac{\partial P}{\partial x} = \frac{\partial}{\partial x}\mu\frac{\partial u}{\partial x} + \frac{\partial}{\partial y}\mu\frac{\partial u}{\partial y} + \frac{\partial}{\partial z}\mu\frac{\partial u}{\partial z} \tag{2}$$

$$\frac{\partial \rho v}{\partial t} + \frac{\partial \rho u v}{\partial x} + \frac{\partial \rho v^2}{\partial y} + \frac{\partial \rho v w}{\partial z} + \frac{\partial P}{\partial y} = \frac{\partial}{\partial x}\mu\frac{\partial v}{\partial x} + \frac{\partial}{\partial y}\mu\frac{\partial v}{\partial y} + \frac{\partial}{\partial z}\mu\frac{\partial v}{\partial z} \tag{3}$$

$$\frac{\partial \rho w}{\partial t} + \frac{\partial \rho u w}{\partial x} + \frac{\partial \rho v w}{\partial y} + \frac{\partial \rho w^2}{\partial z} + \frac{\partial P}{\partial y} = \frac{\partial}{\partial x}\mu\frac{\partial w}{\partial x} + \frac{\partial}{\partial y}\mu\frac{\partial w}{\partial y} + \frac{\partial}{\partial z}\mu\frac{\partial w}{\partial z} \tag{4}$$

The Lagrangian form of the continuity equation is also required :

$$\frac{D\rho}{Dt} + \rho\left(\frac{\partial u}{\partial x} + \frac{\partial v}{\partial y} + \frac{\partial w}{\partial z}\right) = 0 \tag{5}$$

Under the two-phase flow condition, the viscosity can vary spatially. According to Kubota et al. [26], the viscosity of mixture can be written:

$$\mu = \alpha\mu_g + (1 - \alpha)\mu_l \tag{6}$$

where μ_g and μ_l are the gas and liquid viscosities, and α is the void fraction. Since the non-dimensional pseudo-density is volume fraction of mass per unit cell volume, the Equation (6) can be written as:

$$\mu(\rho) = \rho\mu_l + (1 - \rho)\mu_g \tag{7}$$

136

This mixture viscosity is substituted back into Equation (2) through (4) for non-dimensionalization. The channel width, liquid inflow velocity and liquid density are chosen as dimensions in nondimensionalizing the equations. Then the momentum equations (2 - 4) can be arranged as follows for the momentum flux calculation.

$$\frac{\partial \rho u}{\partial t} + \frac{\partial}{\partial x}\left[\rho u^2 - \frac{1}{Re^*}\frac{\partial u}{\partial x}\right] + \frac{\partial}{\partial y}\left[\rho uv - \frac{1}{Re^*}\frac{\partial u}{\partial y}\right]$$
$$+ \frac{\partial}{\partial z}\left[\rho uw - \frac{1}{Re^*}\frac{\partial u}{\partial z}\right] = -\frac{\partial p}{\partial x} \tag{8}$$

$$\frac{\partial \rho v}{\partial t} + \frac{\partial}{\partial x}\left[\rho uv - \frac{1}{Re^*}\frac{\partial v}{\partial x}\right] + \frac{\partial}{\partial y}\left[\rho v^2 - \frac{1}{Re^*}\frac{\partial v}{\partial y}\right]$$
$$+ \frac{\partial}{\partial z}\left[\rho vw - \frac{1}{Re^*}\frac{\partial v}{\partial z}\right] = -\frac{\partial p}{\partial y} \tag{9}$$

$$\frac{\partial \rho w}{\partial t} + \frac{\partial}{\partial x}\left[\rho uw - \frac{1}{Re^*}\frac{\partial w}{\partial x}\right] + \frac{\partial}{\partial y}\left[\rho vw - \frac{1}{Re^*}\frac{\partial w}{\partial y}\right]$$
$$+ \frac{\partial}{\partial z}\left[\rho w^2 - \frac{1}{Re^*}\frac{\partial w}{\partial z}\right] = -\frac{\partial p}{\partial z} \tag{10}$$

where the Reynolds number for mixture Re^* is defined as follow:

$$\frac{1}{Re^*} = \frac{\rho}{Re_l} + \frac{\rho_g(1-\rho)}{\rho_l}\frac{1}{Re_g} \tag{11}$$

which includes the both liquid and gas phase viscous effect in one term. Here Re_l and Re_g represent Reynolds numbers of liquid and gas-phase respectively.

An additional constituitive relation for the non-physical pseudo-density variable is required in place of an equation of state in order to close the set of governing equations. Basically, the droplets in gas media are assumed to be the same size, i.e. the droplet volume does not change due to the pressure variation of the flow field. Coalescence or collision between the droplets are neglected, nor the secondary breakup of droplet is considered. Consequently, one can conclude from the above assumptions that the density evolves in time by simply considering a Lagrangian tracking of the droplet field as specified by a continuity equation as:

$$\frac{D\rho}{Dt} = \frac{\partial \rho}{\partial t} + u\frac{\partial \rho}{\partial x} + v\frac{\partial \rho}{\partial y} + w\frac{\partial \rho}{\partial z} = 0 \tag{12}$$

This equation is basically a statement that the droplet mass is invariant along a path line in the fluid. By taking account for the flow direction, the pseudo-density is updated based on mass flux calculation as follows :

$$\rho^{n+1} = \rho^n - \frac{\Delta t}{V_c}\left[\left(\dot{m}_{out}\right)_{x,y,z} - \left(\dot{m}_{in}\right)_{x,y,z}\right] \tag{13}$$

137

where V_c is volume of a given cell and $\dot{m}$ is mass flowrate corresponding x, y and z directions. The flux of the mass through a given cell are calculated by a standard upwind scheme. While this provides a locally first order solution in the region adjacent to the discontinuity in density, it provides for a stable approach to account for the large density gradients near the interface. Since the interface region will undoubtedly contain droplets in these very high convective environments, a shock-type density discontinuity would not be consistent with a homogeneous flow representation. The scheme is second-order accurate with the exception of the points adjacent to the interface, and convergence is verified in the next section. One can find more details on development of the numerical solver in Bunnell's work [25]. In this study, the 3-D coaxial jet modeling work will be presented focusing on hydrodynamic instability of shear coaxial jet.

Parallelization

The code runs on a state-of-art Beowulf Linux cluster that is equipped with 104 processors and fast ethernet network. One run usually requires 12 to 24 processors depending on mesh discretization. Since the cluster is dedicated to the modeling, each run makes use of nearly 100% of CPU power and network bandwidth. Even with this superb environment, one run up to 150,000 time steps takes about three weeks.

Parallel processing using MPI (Message Passing Interface) has been implemented in order to run the 3-D model in a timely manner. Even with the large number of 1.2GHz AMD Athlon processors used in the study, running a full 3-D CFD model in a timely, economic manner still remains as a challenge. The MPI has become a standard method for the parallel processing along with PVM (Parallel Virtual Machine). For this study, the MPI has been adopted due to its easy-to-use and built-in libraries in many standard Linux distributions such as RedHat.

MPI libraries provide two basic routines, a function for sending data and one for receiving, along with a multitude of other useful functions that provide the collective communication operations that are necessary for a group of processors running parallel processing jobs.

For the present 3-D atomization modeling, the computational domain is split up in axial direction for the desired number of processors, n. While each processor solves a flow field of subdivided domain, the boundary conditions of each subdomain are transfered to neighboring domain through message passing. All the processors involved in this procedure perform the same calculation in each step by copying the original task to other processors but solving different subdomains and boundary conditions. This type of parallelism is called SPMD, which stands for Single-Program-Multiple-Data. A typical example of using the SPMD parallel process is to solve the Poisson equation.

In the finite volume Marker and Cell method used in this study, the mesh discretization is such that the calculation of primitive variables, P, ρ, V, and the Lagrangian derivative $D\rho/Dt$, only depend on values at neighboring nodes. Thus, it is required that boundary values on a neighboring

node be known for the calculation of primitive variables, and the data along the boundary of a given domain must be passed to its neighbor. Physically, the problem being solved in parallel on 'n' processors can be viewed as 'n' separate flow field problems each being solved with different set of boundary conditions. However, the boundary conditions for each problem are dependent on the flow field in each domain. For processor CP_1 the inlet boundary condition is a constant flow field condition, as is the exit boundary condition for the flow field being solved by CP_{n-1}. Here, the CP_i in this section denotes the computing processor corresponding to each subdomain to be solved. The inner domain boundary conditions are function of time at the inlet and exit and are functions of the surrounding domain flow field.

Figure 1 shows the schematic of computational domain discretization. Assuming that computational domain has $m2 \times n2$ grid points in $i-$ and $j-$ directions, which represent x and y coordinates respectively in physical domain along with $k-$ for z direction, and that "$m2$" in axial ($i-$) direction is evenly divisible by number of processor "n",then each domain will contain $(m2/n)*n2$ grid points in the streamwise direction. Since the boundary values at the sides of a given domain are needed by other processors due to differencing scheme used, the data size for one primitive value in each domain will be $((m2/n) + 2) * n2$. Here, the initial and last data array where $i = 1$ and $i = (m2/n) + 2$ would be locations for the boundary data that is passed between processors, and the arrays between those two locations (from $i = 2$ to $i = (m2/n) + 1$) would be the domain to be solved. A 3-D problem requires the passing of arrays for the boundary condition transmission while 2-D problem requires the passing of vectors. The total data size required for all processes would be $n * ((m2/n) + 2) * n2 * nbyte$ bytes, which depending on whether the variables are declared as single precision or double precision, $nbytes$ would be equal to 2 or 4 bytes respectively.

Another issue associated with parallelization in this modeling is the Poisson solver for calculation of pressure field. The system of sparse linear equations has to be solved in such a way that the solution satisfies each process domain. The original solution algorithm in 2-D simulations [19,20] relies on a Successive Line Over Relaxation (SLOR) method, and the parallelized solver takes the same methodology. The SLOR technique is applied to each subdomain independently, and yet each subdomain is linked to others through the message passing. The procedure is outlined as follows referring to Figure 1;

- Sweep the first column in each domain.

- Pass the result from CP_{n+1} to CP_n.

- Finish the sweep across the domain.

- Pass the result from CP_n to CP_{n+1}.

This provides linkage of the domains at the boundaries since the SLOR sweep requires knowing the value of P at locations "$i + 1$" and "$i - 1$" of each domain. The communication requirements are such that two calls to MPI subroutines, MPI_SEND and MPI_RECV, must be made for each iteration. References 28 - 32 provide background information on MPI.

Despite the large number of processors available, speed was maximized when 6 grid points (minimum number of grid points decided due to differential schemes used in the solver) in axial direction for each individual processors are used, resulting 12 processors of use for $72 \times 71 \times 71$ mesh. With the individual processors at this speed (1.2 GHz chips), the computation becomes communcation limited when larger number of nodes are employed.

Grid Refinement Tests

The computational domain consists of the liquid oxydizer (LOX) and gaseous hydrogen flow path from the LOX post exit to the injector orifice exit, which is the combustion chamber face. To account for the variation in the flowfield, the domainu is devided into numerous grid cells such that the volume of a computational cell is much smaller than the wavelength of the highest frequency acoustic mode to be considered.

The computational structured mesh generation consists of two parts; one is inner circle for liquid-phase, and the other is outer annulus for gas-phase flow. Due to the liquid post structure configured between the liquid cylinder and gaseous fuel annular passage, the circular shape of physical domain has to be fixed. However, a polar coordinate mesh cannot be used due to the condition of maintaining $n \times n$ sparse matrix solver. The inner circle meshing begins with the meshing of a square. The square mesh is then deformed making use of polynomial stretching of order n in order to form a quarter of a circle. A mirror image is then symmetrically projected until it forms a complete circle. The reason that we do not extend this out to the nozzle wall is because we have to have complete the circle configuration for the liquid post structure. For the outer gas-phase domain, circles surround the inner liquid part while lines in y and z directions are extended from the nodes on outest circle of inner domain to the nozzle wall side. A complete cross-sectional view of a coarse computational mesh is shown in Figure 2. Grid points in the diagonal directions create challenges since the $n \times n$ matrix size should be kept due to the flow solver algorithm. This problem was solved by deploying two lines in both y and z directions from the diagonal nodes to external circumference, resulting nearly triangular-shaped cells on the diagonal directions. The liquid post tip area has the smallest grid size to resolve the recirculation zone immediately downstream of the post.

A grid convergence test has been conducted in order to find an adequate mesh size. Three mesh sizes: $30 \times 30 \times 30$, $60 \times 60 \times 60$ and $90 \times 90 \times 90$ in x, y and z direction respectively are tested and the result is shown in Figure 3. However, due to the run-time constraint, the test is limited to a short period of time up to 10,000 time steps. Figure 3 depicts the time history of mass flow

through the injector nozzle exit for each mesh size. While the coarse grid (30 × 30 × 30) shows unacceptable behavior with too much of diffusion, the middle size grid (60 × 60 × 60) matches fairly well with the fine grid (90 × 90 × 90). Though running with the fine grid or even finer grid would be desirable, the cost for running those fine grids requires unbearable run-time (more than one month up to 10,000 time steps for 90 × 90 × 90 grid size). Therefore, the middle grid size has been adopted for the 3-D modeling. Actual 3-D simulations have used a 72 × 71 × 71 mesh by increasing the number of grid points as many as possible without sacrificing a reasonable run-time.

Boundary conditions are applied to the domain as follows: Along the wall of the injector, the no-slip condition is used. The liquid post tip area at the inlet plane also requires a no-slip condition. On the inflow boundary, constant liquid/gas-phase velocities are defined. The pressure is extrapolated with zero gradient for the inlet. At the exit, constant pressure is set while the velocities are extrapolated with zero gradient. It should be noted that the inflow boundary condition only holds for the initial processor used in the calculation. Similarly, the exit boundary condition applies only to the last processor assigned in the parallel processing. Additional boundary conditions on both sides of each subdomains are a function of time and neighboring domains.

Numerical Results

A total of five 3-D unsteady calculations are presented. The Space Shuttle Main Engine's (SSME) coaxial injector has been chosen for baseline modeling case. First, the injector of the SSME main combustion chamber (MCC) has been investigated. Further simulations have been performed for the MCC injector with a longer recess length and lower velocity ratio in order to assess the impact of these parameters. In addition, a simulation of SSME preburner injector has been conducted. The both injectors use liquid oxygen (LOX) and gaseous hydrogen (GH_2) as an oxidizer and fuel respectively, but have different geometries and physical properties consistent with the fuel-rich preburner gases entering the main combustion chamber. Figure 4 illustrates the schematic of three dimensional coaxial injector with geometries of main burner and preburner injectors. The physical properties of each injector flow in operating condition are provided in Table 1.

SSME main burner coaxial injector

The nondimensionalization was based on the geometries in Figure 4 and Table 1 by using fuel annulus diameter D_f, liquid-phase velocity U_l and liquid density ρ_l as nondimensional parameters. Under this nondimensionalization, the LOX post inner diameter has a value of 0.55, the post tip thickness (t_{LOX}) is 0.05 and the recess length (L) is 0.75. The present result assumes a gas/liquid density ratio of 0.02 consistent with high pressure combustion conditions. As discussed in the grid refinement study, a mesh size of 72 × 71 × 71 is used for this case. With parallel processing, 12 processors are used and the computational mesh is split into 12 sets, resulting 8 × 71 × 71

141

of subdomain mesh assigned to each processor. Typically, a 150,000 time step calculation with a timestep $\Delta t = 0.0001$ (0.3$msec$) takes about three weeks.

The results exhibit characteristics termed "self-pulsation" and "self-oscillation" as theorized by Bazarov [16-17]. Pulsations are evident in changes in the flowrate with time, while oscillations are evidenced by azimuthal motion of the central liquid core about the annulus. Prior 2-D simulations [19,20] have shown similar behavior, although the azimuthal motion cannot be resolved with this decreased degree of freedom.

The overall density field behavior of the liquid jet for conditions roughly equivalent to the SSME MCC injector is illustrated in Figure 5. Unfortunately, the model could not be run at the gas/liquid density ratio of this injector, but converged calculations were demonstrated at a density ratio approximately double that in the actual engine. Other simulations at the lower density ratio were obtained and will be discussed subsequent to this case. The left column in Fig. 6 depicts density contours in a cutaway view interpretation of the motion of the jet. The right column shows the density contours at the exit plane.

The resultant highly nonlinear, quasi-periodic oscillation occurs naturally as a result of the Kelvin-Helmholtz instability mechanism. There is no oscillation in the inflow, yet strong oscillations/pulsations develop as a result of the large relative dynamic pressure between the gas and liquid streams. The development of self-pulsation mode of the liquid jet is apparent in those figures.

Pressure contour plots at times corresponding to those in the density plots are shown in Figure 6. Initially, we start the calculations assuming uniform pressure in the recessed region assessed in the computations as shown in the t=0 contour. Nonlinear wave growth occurs quite rapidly and a highly 3-D field develops after initial trasient period. High pressure regions develope in accordance with azimuthal and axial motion of the structures on the jet. Longitudinal wave motion is apparent in the low pressures at times t=8.15, 8.75 vs. the high pressure at t=8.45. Multiple high pressure regions can be formed at different azimuthal locations within the gas annulus as evidenced in the t=8.90 and t=14.60 images.

Velocity streamlines of the jet in $x - y$, $x - z$ and $y - z$ planes are shown in Figure 7 along with velocity contours at exit plane. Only three time frames corresponding to the last three in each density plot are shown here. The asymmetric flow recirculations in the region just downstream of the LOX post are shown in left and middle columns. The far right column illustrates axial velocity contours at the exit plane. While vortices shed from the separated flow region at the base of the LOX post are evident, the velocity contours show that the jet comes out of the orifice exit at an average velocity across the entire exit plane except near the wall and flow recirculation area. This agrees with the experiment of Mayer, Schik and Schaffler [6] which verified the rapid vanishing of relative velocity between the central liquid jet and annular gaseous jet at the downstream of LOX post tip area. In the right column of the figure, streamlines at the orifice exit plane are depicted to

indicate the complex cross-currents which develop in the channel.

One interesting bulk measure of orifice performance is the massflow delivered at the orifice exit plane as a function of time. This quantity can be computed by quadrature of the density-axial velocity product over the exit plane area. Figure 8 shows the time history of mass flow for the density field computed in Fig. 5 and the attendant velocity field. The unsteadiness (self-pulsations) of the jet are quite evident in this figure; massflow variations of 39% about the mean flow are apparent.

Spectral analysis of the data is performed in a manner common for experimentaldata. Because the massflow rate was recorded only for every hundredth iteration, aliasing is expected to be a problem. That is, just as in experiments, there is reason to believe that physical processes are happening at frequencies in excess of the Nyquist frequency for the data stream. Thus, an anti-aliasing filter was convolved with the signal, the the signal was windowed, and the mean subtracted out. The power spectrum was computed through use of an FFT. Spectra computed without this method showed significantly worse signal to noise ratio when compared to those presented here. The spectral content of the mass fluctuation signal provides information regarding the frequency spectrum present. Using a Fast Fourier Transform, the spectral content is shown in Figure 9. There is a significant energy content over a range of dimensionless frequencies with a maximum at $f = 2.2074$, which represent around 73,000 Hz in dimensional units. This frequency is about triple the frequency at which liquid is replaced in the submergence region.

Along with the primary frequency at $f = 2.2074$, the first harmonic frequency at $f = 4.4816$ is also shown in this figure. This higher frequency corresponds to the small peak variation at the top of primary mass flow fluctuation signal in Figure 8, which is caused by small surface vortices coming out of the nozzle exit in an irregular manner.

In a recent study of Smith and Mayer [6], the liquid core jet oscillation in a coaxial injector was observed, and the frequency of flame flickering in a combustion chamber was reported as near 7000 Hz, which falls within the same frequency band of the SSME main burner coaxial injector's case. The same velocity and density ratios were used with similar geometry. Even though their coaxial injector was not exactly the same one used in this study, their experimental study provides some evidence that the liquid jet oscillation/pulsation plays a significant role in combustion response within the chamber. This is an important finding requiring further experimental verification.

SSME MMC injector: lower velocity ratio

A case of lower velocity ratio, $U_g/U_l = 6$, has been investigated in order to assess the influence of this parameter. As the gas-phase velocity is reduced to $180 m/s$, the corresponding Reynolds number of the gas-phase is 4.5×10^5, but the density ratio of default value (0.01) for SSME's MCC was used for this simulation. The time history of mass flow is plotted in Figure 10. A small magnitude self-pulsation appears during the initial time period but it decays gradually without showing any

surface vortices or wave-type instability. The spectral content of the damping fluctuation signal is depicted in Figure 11. A primary frequency at $f = 2.2704$ with very small amplitude is observed in this case; a value similar to that computed for the baseline case.

In prior 2-D simulations [19,20], reductions in the relative gas/liquid velocity also showed a stabilizing influence since the dynamic pressure forcing the instability scales with the square of this velocity. However, the conclusion that the $U_g/U_l = 6$ case is stable for this injector is somewhat tenuous as our present simulation assumes a completely steady flow entering both streams. A more comprehensive analysis or confirmation via experimental data would be required to confirm the relative stability of this (or any) case.

SSME MCC injector: longer recess length

The recess length (depth) is an important paramater governing this flow process, so a calculation was performed to assess the impact of lengthening the recess by 50% ($L = 1.25$) keeping all other parameters fixed as in the baseline MCC calculation described previously. In order to keep the same grid aspect ratio and to stay within a reasonable run-time, a mesh of $132 \times 75 \times 75$ is used with 22 processors. With the increased number of processors, each processor handles the same mesh size of subdomain ($8 \times 75 \times 75$) as set in the baseline case. This methodology provided an acceptable run-time of about three weeks.

Density contours in 3-D cylinder and at exit plane are depicted in Fig. 12. The development of self-pulsations is very clear from the beginning and it continues to be strong through the entire modeling. Azimuthal oscillations become apparent in latter part of simulation as shown in exit plane density contours in the left column. The liquid core moves more actively in an irregular pattern than the baseline case. In this simulation, the liquid jet shows a more structured wave-type motion in the axial direction. The additional flowpath length permits the longer wave instability to become more pronounced; the internal liquid jet is even seen to break up within the submerged region as shown in image (b) in the left hand column of the figure.

The last three time frames in density contour plots are used to show velocity streamlines and axial velocity contours at the orifice exit plane in Figure 13. Flow recirculations are shown in $x - y$ and $x - z$ plane in the first and second columns while velocity contours at exit plane are depicted in the third column with velocity streamlines in cross-stream directions. Vortex structures shed from the base of the LOX post are also evident in this case.

Figures 14 and 15 show the time history of mass flow and the spectral content of this signal, respectively. The magnitude of pulsation is larger, showing oscillating components of the order of 48% of the mean flow. The frequency of oscillation is lower than that observed in the baseline geometry. The larger magnitude pulsation can be explained by the development of wave-type oscillation due to the longer recess length. The primary frequency is decreased to $f = 1.1352$, but this value is still consistent with the prior observation in that it is still roughly triple the frequency

at which the liquid traverses the submerged region. Similar trends have been observed in prior 2-D simulations [19,20]; increasing submergence length increases the time available for instabilities to grow.

SSME pre-burner coaxial injector

The SSME's preburner geometry is shown in Figure 4 and flow properties are tabulated in Table 1. The preburner injector has a shorter recess length ($L = 0.5$) and three times thicker LOX post thickness ($t_{LOX} = 0.15$) than main burner injector. The LOX post diameter (D_i) is 0.45, reducing the mixture ratio of liquid to gas-phase significantly. The density ratio is much higher ($\epsilon = 0.04$) due to the higher pressures in this combustor, but the velocity ratio is identical to the SSME MCC baseline case. The same mesh size of $72 \times 71 \times 71$ is used for the preburner case, so the axial resolution is somewhat better due to the reduced submergence length.

The simulation showed signs of weak pulsation/oscillation activity during the initial transient, but these oscillations were damped and an essentially undisturbed jet issued from the orifice at long times. In prior 2-D simulations [19-21], increasing gas density magnified the aerodynamic interaction, resulting in a faster and finer atomization. However, thickening the LOX post and reducing the submergence length both had stabilizing influences on the instability. In this case, those stabilizing effects overwhelmed the instability caused by the aerodynamic interaction at higher gas density, therefore the overall jet appears as stable.

As noted previously, the present simulations assume idealized conditions at the entry to the submerged region and that the real device may indeed exhibit unsteadiness. More comprehensive simulations would be necessary to fully illuminate this issue.

Main burner injector geometry with preburner flow properties

Having the previous result with preburner injector case raises questions about relation between flow properties and injector geometry. In order to investigate the reciprocal effects between those parameters, a simulation has been conducted using the MCC injector geometry with the preburner flow properties. In summary, the recess length L is 0.75 with LOX post diameter, $D_i = 0.55$ and thickness, $t_{LOX} = 0.05$. The density ratio ϵ is 0.04 and velocity ratio stays at 12. The numbers in Table 1 are used for the Reynolds numbers for gas and liquid-phase. The Reynolds numbers for this case should have been changed based on the main burner injector geometry with the preburner flow properties, but the same values of the preburner case has been used in error. However, the Reynolds numbers are in the same order of magnitude even with the change and it was decided that the time invested in the expensive calculation was such that the values used would be suitable. In prior 2-D parametric studies [19,20], Reynolds number had only a minor influence on results. Therefore, the result of this case is still valid to predict qualitative behavior of the liquid jet.

Figure 16 illustrates the limit-cycle behavior of the density contours in the passage. Pulsations and oscillations similar to those in the baseline MCC simulation are observed. One interesting observation from this case is that the pulsations/oscillations become weaker in magnitude after a certain transient period. This behavior is evidenced in the orifice massflow history shown in Fig. 17. The main difference between this case and the MCC baseline case discussed in Figs. 5-9 is that the density ratio is twice as large. In prior 2-D simulations, increased gas density served to increase the magnatude and frequency of the instability presumably due to the fact that the gas can impart more inertia to the liquid. Here, in the 3-D case, we see a reduction in pulsations with increased gas density.

The spectral content of the waveform shown in Fig. 18 are shown in Figure 19 provides a partial explanation for the reduction in magnatude of the oscillation for this higher gas density case. Significant energy content is stored in a number of frequencies; i.e. the oscillation is not organized at a single frequency so its overall amplitude is lower than the baseline MCC case. The same primary frequency that was observed in the baseline main burner case is present ($f = 2.0$), but in general the fluctuation is very irregular and unpredictable. Further parametric studies are required to illuminate this complex issue.

Summary and Conclusions

A 3-D incompressible, unsteady, viscous Navier-Stokes solver for two-phase flow has been developed for full three dimensional simulations of coaxial injectors in liquid rocket engines. The Space Shuttle Main Engine's (SSME) main burner and preburner injectors served as baseline modeling cases.

High amplitude hydrodynamic instabilities are observed in the recessed region where computations are made. The resulting frequencies and massflow variations for the 5 simulations are summarized in Table 2. The parameter whose effect was investigated is underlined. The massflow of the device oscillates as much as 48% about the mean flow for the cases studied indicating a strong presence of "self pulsations" as theorized by other researchers. Oscillations of the liquid core jet about the gas annulus are also observed in some of the cases. Reduction in the length of the recess region or the velocity difference between the streams serves as a stabilizing influence. Increases of gas density introduced complex effects in terms of spectral content and amplitude of the massflow oscillations.

For the SSME main combustion chamber injector, the primary harmonic frequency was about 7300 Hz. Recent experiments at DLR at comparable conditions indicated flickering of the flame at a similar frequency of 7000 Hz. For this reason, there may be strong connections between hydrodynamic instabilities and the resultant combustion processes. Additional studies are recommended for complete verification of this important conclusion.

Acknowledgement

Nomenclature

D - Channel width

L - Channel length

h - Liquid sheet thickness from center line

t_{LOX} - Liquid post thickness

ΔU - Velocity difference between liquid and gas phase

ϵ - Density ratio (ρ_g/ρ_l)

$\dot{m}$ - Nozzle massflow rate

P - Pressure

Re - Reynolds number

α - Void fraction

μ - Viscosity

ρ - Fluid pseudo-density

CP_i - Computational processor

Subscripts

i - Inlet

o - Outlet

l - Liquid-phase

g - Gas-phase

References

1. J. Hulka and J. J. Hutt, "Instability Phenomena in Liquid Oxygen/Hydrogen Propellant Rocket Engines", *Liquid Rocket Engine Combustion Instability*, Vol. 169, Progress in Astronautics and Aeronautics, pp. 39-72, 1995.

2. G. S. Gill and W. H. Nurick, "Liquid Rocket Engine Injectors", NASA Lewis Research Center, NASA SP-8089, 1976

3. L. Vingert, P. Gicquel, and D. Lourme, "Coaxial Injector Atomization", *Liquid Rocket Engine Combustion Instability*, Vol. 169, Progress in Astronautics and Aeronautics, pp. 145-190, 1995.

4. J. J. Hutt and M. Rocker, "High-Frequency Injector-Coupled Combustion", *Liquid Rocket Engine Combustion Instability*, Vol. 169, Progress in Astronautics and Aeronautics, pp. 345-356, 1995.

5. W. Mayer and G. Krulle, "Rocket Engine Coaxial Injector Liquid/Gas Interface Flow Phenomena", *Journal of Propulsion and Power*, Vol. 11, No. 3, pp. 513-518, 1995.

6. W. Mayer and H. Tamura, "Flow Visualization of Supercritical Propellant Injection in a Firing LOX/GH2 Rocket Engines", *AIAA 95-2433*, 1995

7. W. Mayer, A. Schik, and M. Schaffler, "Injection and Mixing Processing in High-Pressure Liquid Oxygen/Gaseous Hydrogen Rocket Combustors", *Journal of Propulsion and Power*, Vol. 16, No. 5, pp. 823-828, 2000.

8. N. Dombroski and W. R. Johns, "The Aerodynamic Instability and Disintegration of Viscous Liquid Sheet", *Chemical Engineering Science*, Vol. 18, pp. 203-214, 1963.

9. H. Eroglu and N. Chigier, "Wave Characteristics of Liquid Jets from Airblast Coaxial Atomizers", *Atomization and Sprays*, Vol. 1, pp. 349-366, 1991.

10. A. Mansour and N. Chigier, "Dynamic behavior of liquid sheet", *Physics of Fluids A*, Vol. 3(12), pp. 2971-2980, 1991.

11. N. Chigier and R. D. Reitz, "Regimes of Jet Breakup and Breakup Mechanisms (Physical Aspect)", *Recent Advances in Spray Combustion*, Vol. 166, Progress in Astronautics and Aeronautics, pp. 109-135, 1995.

12. Emmanuel Villermaux, "Mixing and Spray Formation in Coaxial Jet", *Journal of Propulsion and Power*, Vol. 14, No. 5, pp. 807-817, 1998.

13. T. Kaltz, M. Milicic, M. Glogowski, "Shear Coaxial Injector Spray Characterization", *AIAA 93-2190*, 1993

14. M. Glogowski, M. Bar-Gill, et al. "Shear Coaxial Injector Instability Mechanisms", *AIAA 94-2774*, 1994

15. M. Glogowski, M. M. Micci, "Shear Coaxial Injector Spray Characterization Near the LOX post Tip Region", *AIAA 95-2552*, 1995

16. V. G. Bazarov and Vigor Yang, "Liquid-Propellant Rocket Engine Injectors Dynamics", *Journal of Propulsion and Power*, Vol. 14, No. 5, pp. 797-806, 1998.

17. V. G. Bazarov and L.A. Lyul'ka, "Nonlinear Interactions in Liquid Propellant Rocket Engine Injectors", *AIAA 98-4039*, 1998.

18. V. G. Bazarov, "Self-Pulsations in Coaxial Injectors with Central Swirl Stage", *AIAA 95-2358*, 1995

19. B. Kim, *Study of Hydrodynamic Instability of Shear Coaxial Injector Flow in a Recessed Region*, Ph.D. Thesis, School of Aeronautics and Astronautics, Purdue University, West Lafayette, IN, December, 2002.

20. B. Kim and S. D. Heister, " Two-phase Modeling of Hydrodynamic Instabilities in Coaxial Injectors", *Journal of Propulsion and Power*, under review.

21. B. Kim and S. D. Heister, "Two-phase Modeling and Hydrodynamic Instability Study of Shear Coaxial Injector Flow", AIAA 2002-3696, 2002.

22. R. Branam, et al. "Injection Characteristics on the Surface of a Coaxial Jet", *AIAA 2002-3695*, 2002

23. C. Yen and S. D. Heister, "Modeling Hydrodynamic Non-Equilibrium in Bubbly and Cavitating Flows", *Journal of Fluids Engineering*, Vol. 118, No. 1, pp. 172-178, 1995.

24. R. A. Bunnell, *Unsteady, Viscous, Cavitating Simulation of Injector Internal Flows*, Ph.D. Thesis, School of Aeronautics and Astronautics, Purdue University, West Lafayette, IN, August 1999.

25. R. A. Bunnell, S. D. Heister, C. Yen and S. H. Collicott, "Cavitating Injector Flows: Validation of Numerical Models and Simulations of Pressure Atomizers", *Atomization and Sprays*, Vol. 9, pp. 445-465, 1999.

26. A. Kubota et al., "A New Modeling of Cavitating Flows : A Numerical Study of Unsteady Cavitation on a Hydrofoil Section", *Journal of Fluid Mechanics*, Vol. 240, pp. 59-96, 1992.

27. J. Smith, D. Klimenko, W. Claus and W. Mayer, "Supercritical LOX/Hydrogen Rocket Combustion Investigations Using Optical Diagnostics", *AIAA-2002-4033*, 2002.

28. Message Passing Interface Forum, "MPI: A Message-Passing Interface Standard", *International Journal of Supercomputing Applications*, Vol. 8, No. 3/4, 1994 available from ftp://netlib2.cs.utk.edu/mpi/mpi-reprot.ps

29. W. Gropp and E. Lusk, "Installation Guide to mpich, a Portable Implementaion of MPI", Mathematics and Computer Science Division, Argonne National Laboratory, 1996. ANL-96/5.

30. W. Gropp and E. Lusk, "User's Guide for mpich, a Portable Implementation of MPI", Mathematics and Computer Science Division, Argonne National Laboratory, 1996. ANL-96/6.

31. PACS Training Group, "Introduction to MPI", National Center for Supercomputing Applications (NCSA) at University Illinois.

32. P. S. Pacheco, *Parallel Programming with MPI*, Morgan Kaufman Publishers, Inc. 1997.

Figure Captions
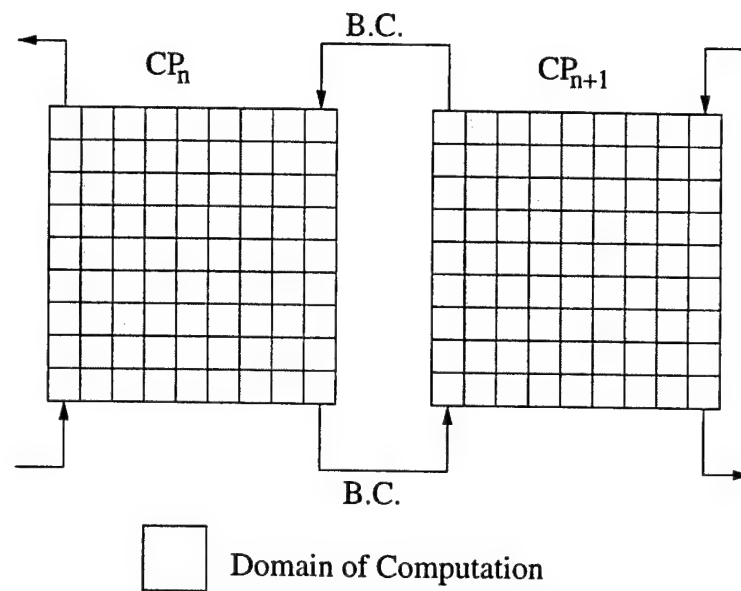
1. Schematic of domain splitting used in parallel processing.
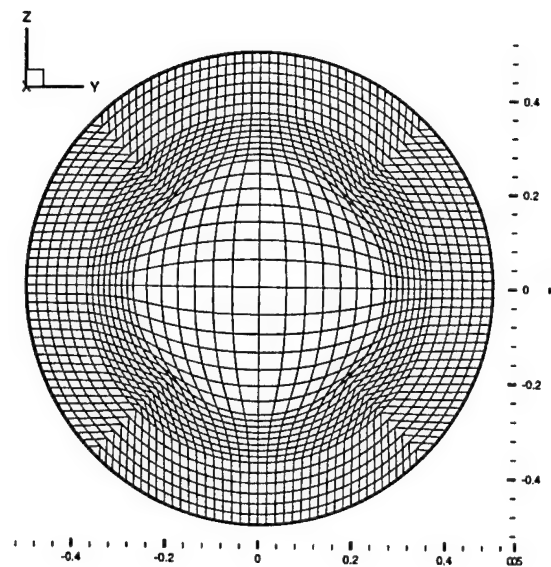
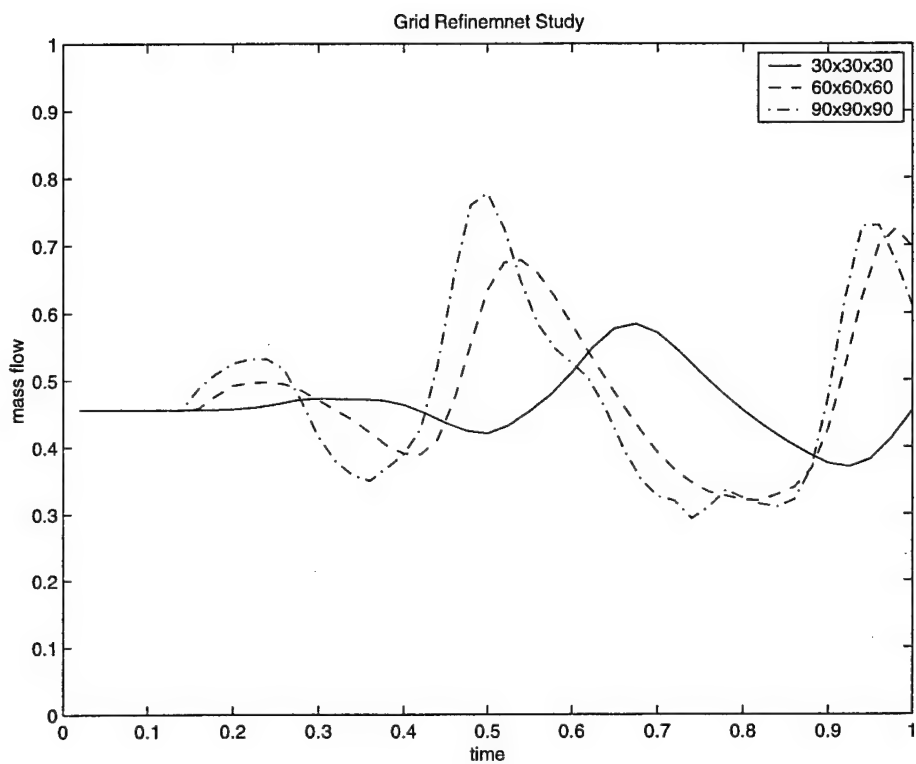2. Cross-sectional view of 3-D computational mesh: Axial direction.

3. Grid refinement study on three different mesh sizes (SSME main burner condition: $\epsilon = 0.02$, $U_g/U_l = 12$, $L/D = 0.75$, $Re_l = 1.1 \times 10^6$, $Re_g = 9.0 \times 10^5$)

4. Schematic of SSME coaxial injector and summary of critical dimensions.

5. Cutaway view (left column) and orifice exit plane (right column) of density contours showing typical Self-Pulsation: SSME Mainburner injector, $\epsilon = 0.02$, $U_g/U_l = 12$, $L/D = 0.75$, $Re_l = 1.1 \times 10^6$, $Re_g = 9.0 \times 10^5$

6. Cutaway view (left column) and orifice exit plane (right column) of pressure contours in 3-D cylinder at various times: SSME Mainburner injector, $\epsilon = 0.02$, $U_g/U_l = 12$, $L/D = 0.75$, $Re_l = 1.1 \times 10^6$, $Re_g = 9.0 \times 10^5$

7. Velocity streamlines in cross-sectional view (left and middle columns) and orifice exit plane (right column): SSME Mainburner injector, $\epsilon = 0.02$, $U_g/U_l = 12$, $L/D = 0.75$, $Re_l = 1.1 \times 10^6$, $Re_g = 9.0 \times 10^5$

8. Time history of mass flow at exit plane: SSME Mainburner injector, $\epsilon = 0.02$, $U_g/U_l = 12$, $L/D = 0.75$, $Re_l = 1.1 \times 10^6$, $Re_g = 9.0 \times 10^5$

9. Spectral analysis of mass flow fluctuation: SSME Mainburner injector, $\epsilon = 0.02$, $U_g/U_l = 12$, $L/D = 0.75$, $Re_l = 1.1 \times 10^6$, $Re_g = 9.0 \times 10^5$

10. Time history of mass flow at exit plane: lower velocity ratio, $\epsilon = 0.01$, $U_g/U_l = 6$, $L/D = 0.75$, $Re_l = 1.1 \times 10^6$, $Re_g = 4.5 \times 10^5$

11. Spectral analysis of mass flow fluctuation: lower velocity ratio, $\epsilon = 0.01$, $U_g/U_l = 6$, $L/D = 0.75$, $Re_l = 1.1 \times 10^6$, $Re_g = 4.5 \times 10^5$

12. Density field evolution for injector with a longer recess length: $\epsilon = 0.01$, $U_g/U_l = 12$, $L/D = 1.25$, $Re_l = 1.1 \times 10^6$, $Re_g = 9.0 \times 10^5$

13. Velocity streamlines and contours with a longer recess length: $\epsilon = 0.01$, $U_g/U_l = 12$, $L/D = 1.25$, $Re_l = 1.1 \times 10^6$, $Re_g = 9.0 \times 10^5$

14. Time history of mass flow at exit plane: longer recess length, $\epsilon = 0.01$, $U_g/U_l = 12$, $L/D = 1.25$, $Re_l = 1.1 \times 10^6$, $Re_g = 9.0 \times 10^5$

15. Spectral analysis of mass flow fluctuation: longer recess length, $\epsilon = 0.01$, $U_g/U_l = 12$, $L/D = 1.25$, $Re_l = 1.1 \times 10^6$, $Re_g = 9.0 \times 10^5$

16. Density contours in initial development of Self-pulsation: $\epsilon = 0.04$, $U_g/U_l = 12$, $L/D = 0.75$, $Re_l = 6.6 \times 10^5$, $Re_g = 3.37 \times 10^6$ post thickness, $t_{LOX} = 0.1$

17. Density contours in small magnitude Self-pulsation mode: $\epsilon = 0.04$, $U_g/U_l = 12$, $L/D = 0.75$, $Re_l = 6.6 \times 10^5$, $Re_g = 3.37 \times 10^6$

18. Time history of mass flow at exit plane: main burner geometry with preburner flow properties, $\epsilon = 0.04$, $U_g/U_l = 12$, $L/D = 0.75$, $Re_l = 6.6 \times 10^5$, $Re_g = 3.37 \times 10^6$

19. Spectral analysis of mass flow fluctuation: $\epsilon = 0.04$, $U_g/U_l = 12$, $L/D = 0.75$, $Re_l = 6.6 \times 10^5$, $Re_g = 3.37 \times 10^6$

Table 1: Physical properties of SSME coaxial injectors in operating conditions

Physical properties	SSME mainburner	SSME preburner
Chamber pressure (MPa)	19.3	34.1
Liquid injection velocity (m/s)	31.3	30
Liquid density (kg/m^3)	1117	1125
Liquid Reynolds No.	1.1×10^6	6.60×10^5
Gas injection velocity (m/s)	360.6	360
Gas density (kg/m^3)	9.47	42.5
Gas Reynolds No.	9.0×10^5	3.37×10^6
Density ratio (ρ_g/ρ_l)	0.0085	0.038
Velocity ratio (U_g/U_l)	12	12
Mixture ratio (liq./gas)	0.89	0.98

Table 2: Summary of 3-D simulations results

CASE	ϵ	U_g/U_l	L/D	t_{LOX}	$\Delta\dot{m}/\dot{m}$	frequency
MCC	0.02	12	0.75	0.05	39	2.2 (7300Hz)
MCC-U	0.01	<u>6</u>	0.75	0.05	Near 0	2.27 (7500Hz)
MCC-L	0.01	12	<u>1.25</u>	0.05	48	1.14 (3800Hz)
PB	0.04	12	<u>0.5</u>	<u>0.15</u>	Near 0	N/A
MCC-PB	<u>0.04</u>	12	0.75	0.05	24	0.5/1.4/2.0/4.7/5.1

Figure 1: Schematic of domain splitting used in parallel processing

Figure 2: Cross-sectional view of 3-D computational mesh: Axial direction

Figure 3: Grid refinement study on three different mesh sizes (SSME main burner condition: $\epsilon = 0.02$, $U_g/U_l = 12$, $L/D = 0.75$, $Re_l = 1.1 \times 10^6$, $Re_g = 9.0 \times 10^5$
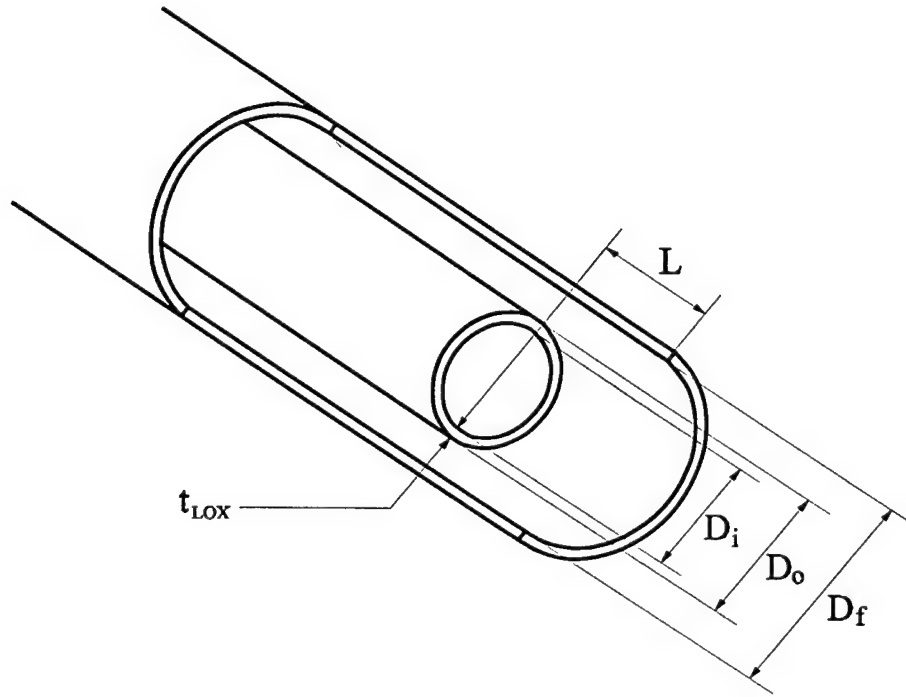
| Injector Geometric Parameters	SSME Preburner	SSME Mainburner
Fuel Annulus Diameter, D_f	5.03mm	8.84mm
LOX Post Outer Diameter, D_o	3.76mm	6.60mm
LOX Post Inner Diameter, D_i	2.26mm	4.77mm
Post Tip Thickness, t_{LOX}	0.76mm	0.92mm
Recess Length, L	2.54mm	6.48mm

Figure 4: Schematic of SSME coaxial injector and summary of critical dimensions
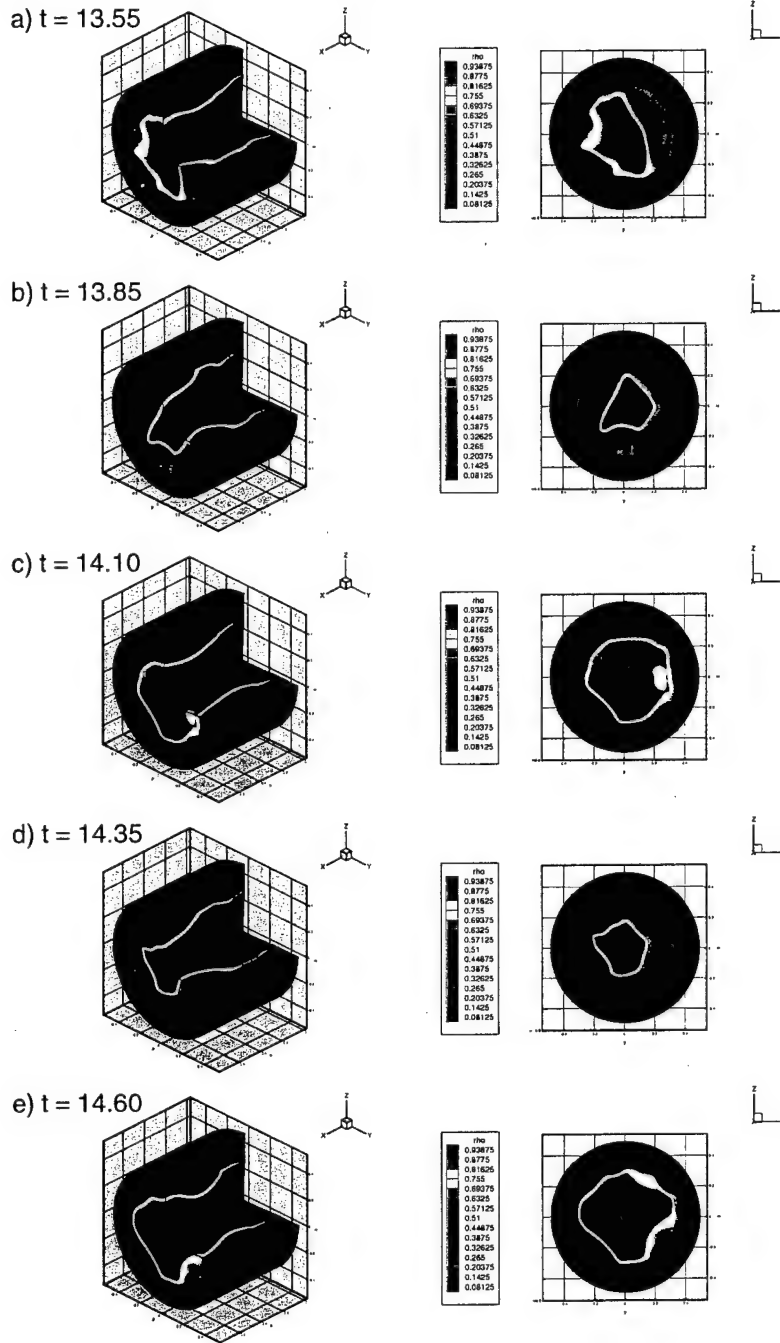
Figure 5: Cutaway view (left column) and orifice exit plane (right column) of density contours showing typical Self-Pulsation: SSME Mainburner injector, $\epsilon = 0.02$, $U_g/U_l = 12$, $L/D = 0.75$, $Re_l = 1.1 \times 10^6$, $Re_g = 9.0 \times 10^5$
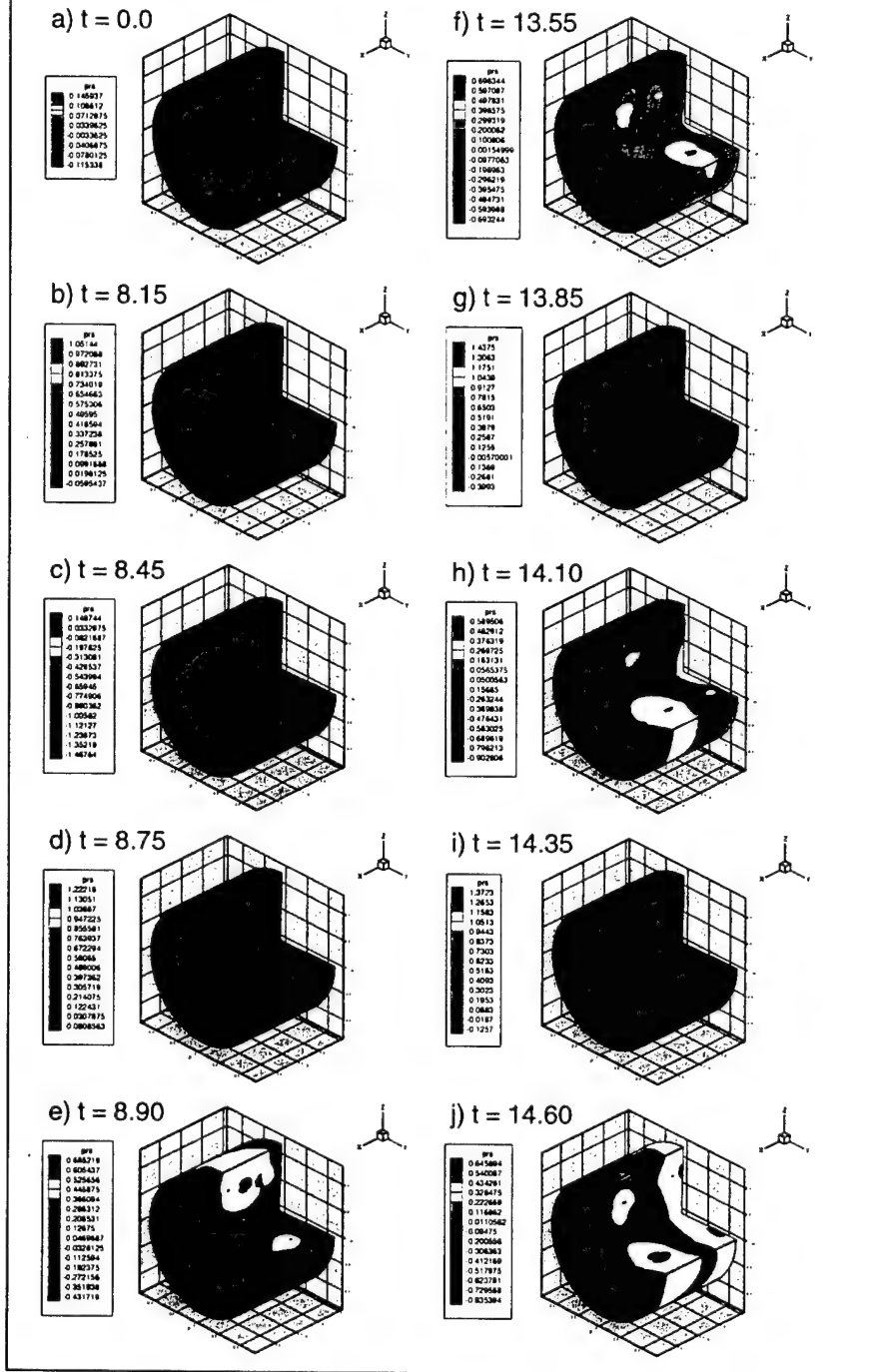
Figure 6: Cutaway view (left column) and orifice exit plane (right column) of pressure contours in 3-D cylinder at various times: SSME Mainburner injector, $\epsilon = 0.02$, $U_g/U_l = 12$, $L/D = 0.75$, $Re_l = 1.1 \times 10^6$, $Re_g = 9.0 \times 10^5$
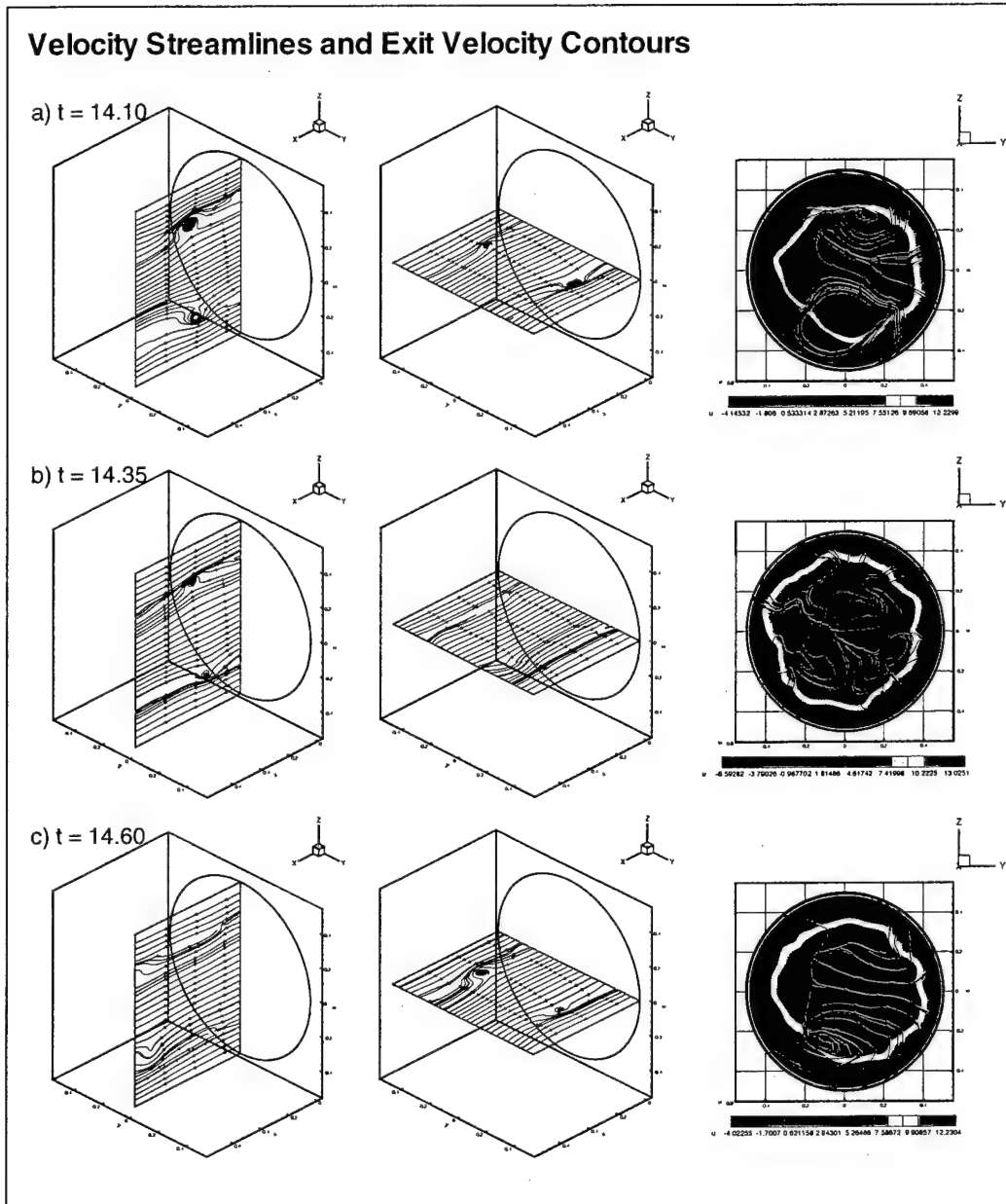
Figure 7: Velocity streamlines in cross-sectional view (left and middle columns) and orifice exit plane (right column): SSME Mainburner injector, $\epsilon = 0.02$, $U_g/U_l = 12$, $L/D = 0.75$, $Re_l = 1.1 \times 10^6$, $Re_g = 9.0 \times 10^5$
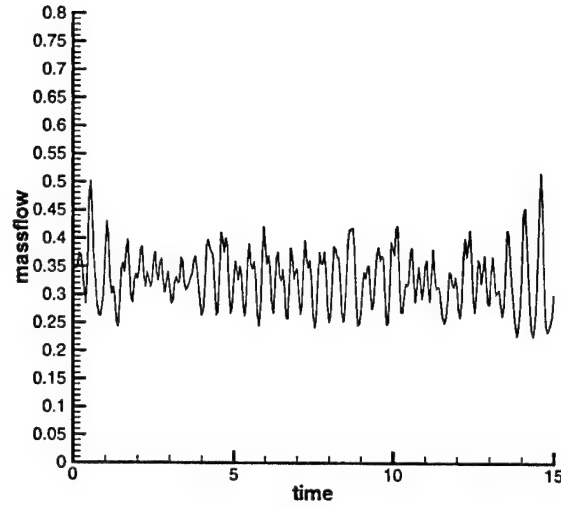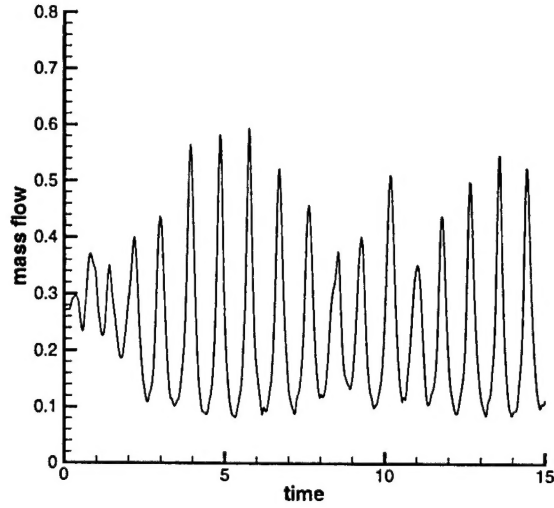
Figure 8: Time history of mass flow at exit plane: $\epsilon = 0.02$, $U_g/U_l = 12$, $L/D = 0.75$, $Re_l = 1.1 \times 10^6$, $Re_g = 9.0 \times 10^5$
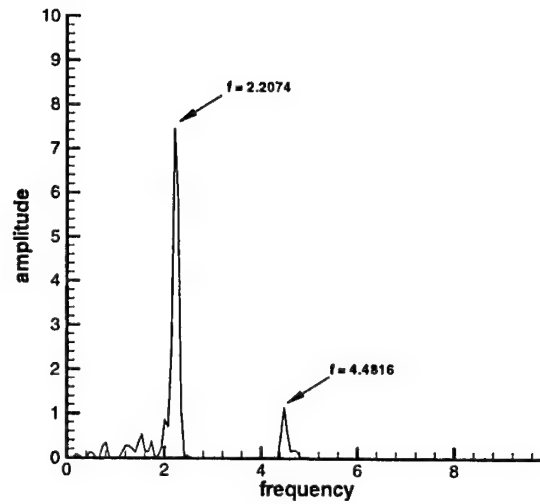
Figure 9: Spectral analysis of mass flow fluctuation: $\epsilon = 0.02$, $U_g/U_l = 12$, $L/D = 0.75$, $Re_l = 1.1 \times 10^6$, $Re_g = 9.0 \times 10^5$
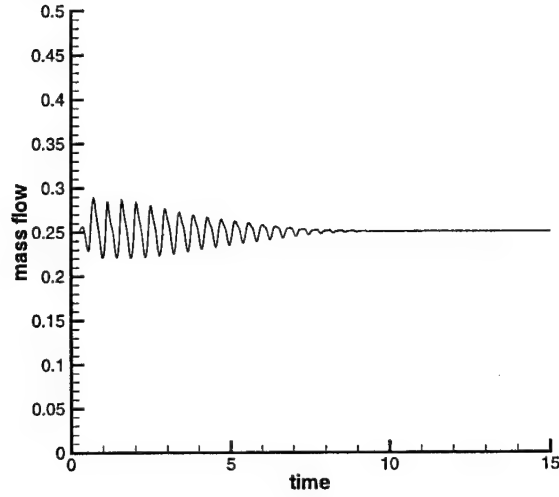
Figure 10: Time history of mass flow at exit plane: lower velocity ratio, $\epsilon = 0.01$, $U_g/U_l = 6$, $L/D = 0.75$, $Re_l = 1.1 \times 10^6$, $Re_g = 4.5 \times 10^5$
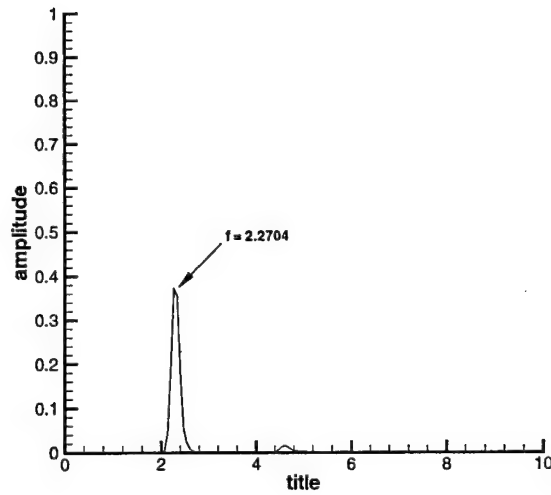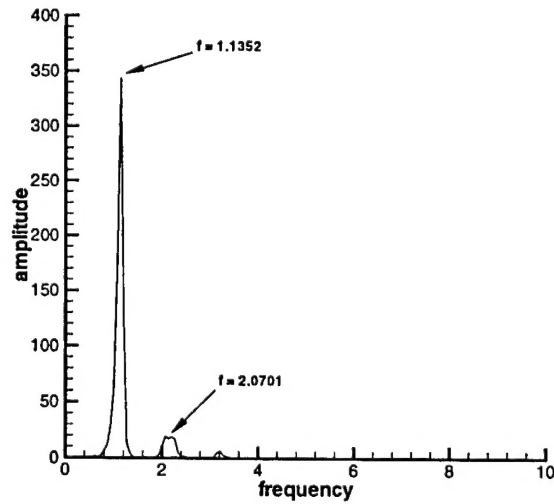

Figure 11: Spectral analysis of mass flow fluctuation: lower velocity ratio, $\epsilon = 0.01$, $U_g/U_l = 6$, $L/D = 0.75$, $Re_l = 1.1 \times 10^6$, $Re_g = 4.5 \times 10^5$
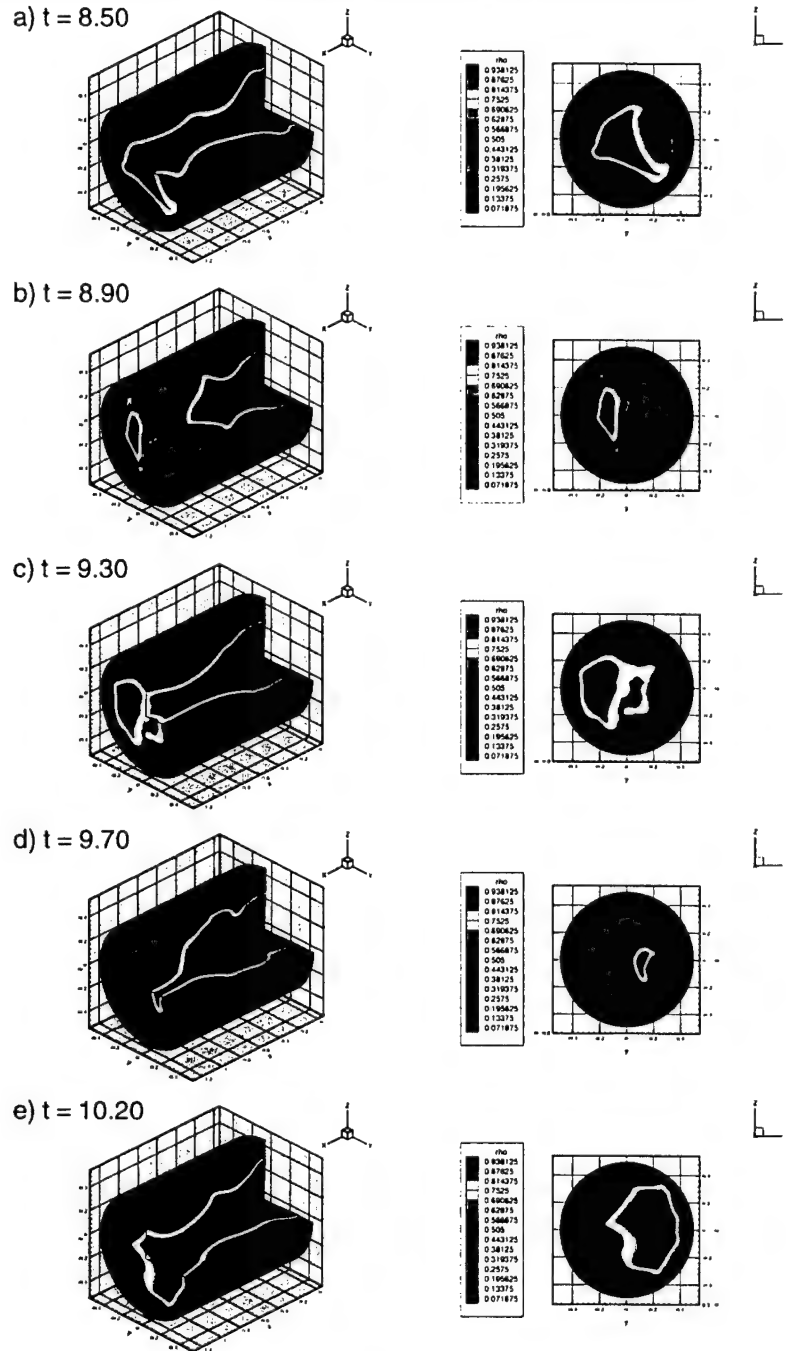
Figure 12: Density field evolution for injector with a longer recess length: $\epsilon = 0.01$, $U_g/U_l = 12$, $L/D = 1.25$, $Re_l = 1.1 \times 10^6$, $Re_g = 9.0 \times 10^5$
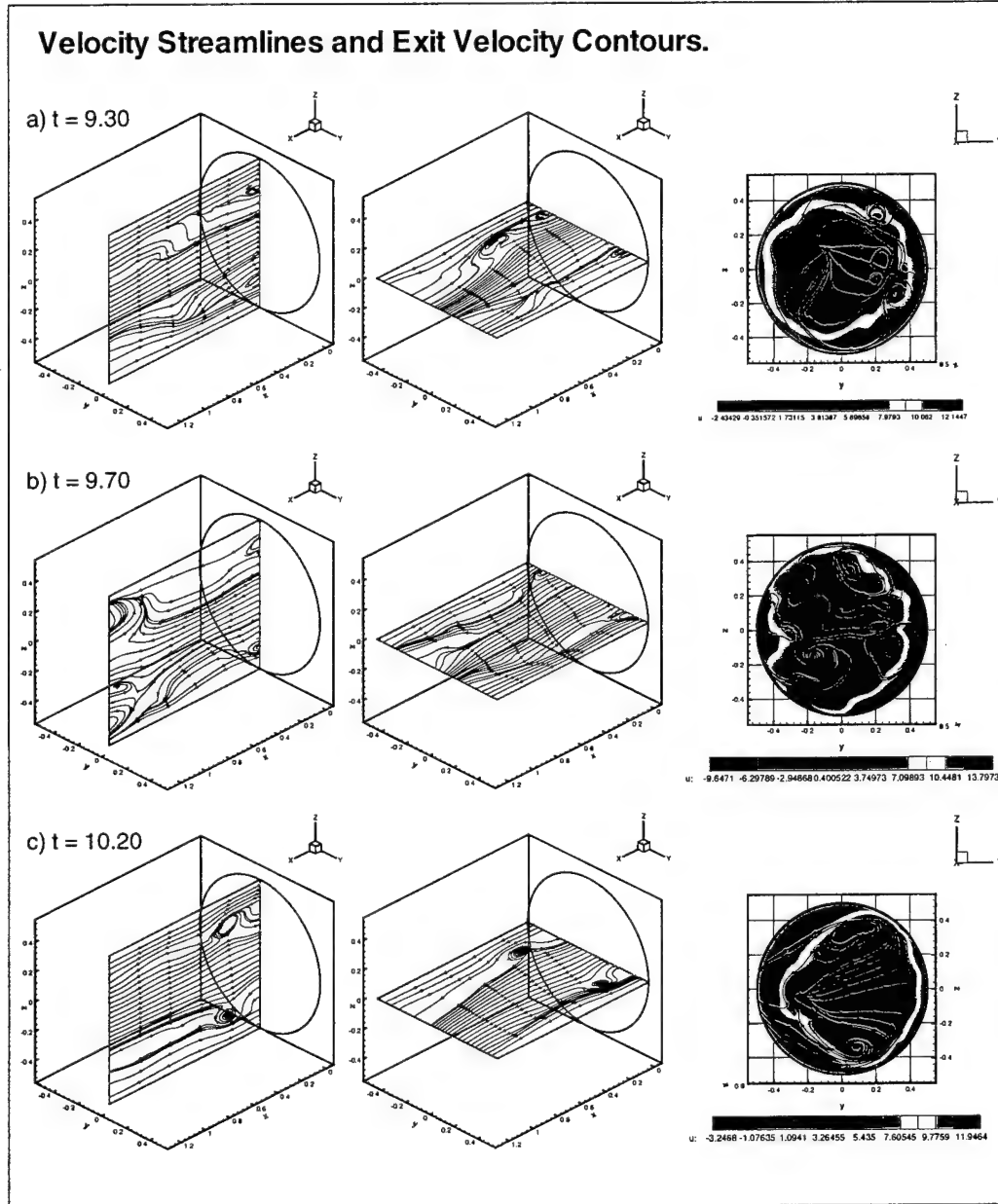
Figure 13: Velocity streamlines and contours with a longer recess length: $\epsilon = 0.01$, $U_g/U_l = 12$, $L/D = 1.25$, $Re_l = 1.1 \times 10^6$, $Re_g = 9.0 \times 10^5$

Figure 14: Time history of mass flow at exit plane: longer recess length, $\epsilon = 0.01$, $U_g/U_l = 12$, $L/D = 1.25$, $Re_l = 1.1 \times 10^6$, $Re_g = 9.0 \times 10^5$

Figure 15: Spectral analysis of mass flow fluctuation: longer recess length, $\epsilon = 0.01$, $U_g/U_l = 12$, $L/D = 1.25$, $Re_l = 1.1 \times 10^6$, $Re_g = 9.0 \times 10^5$

165
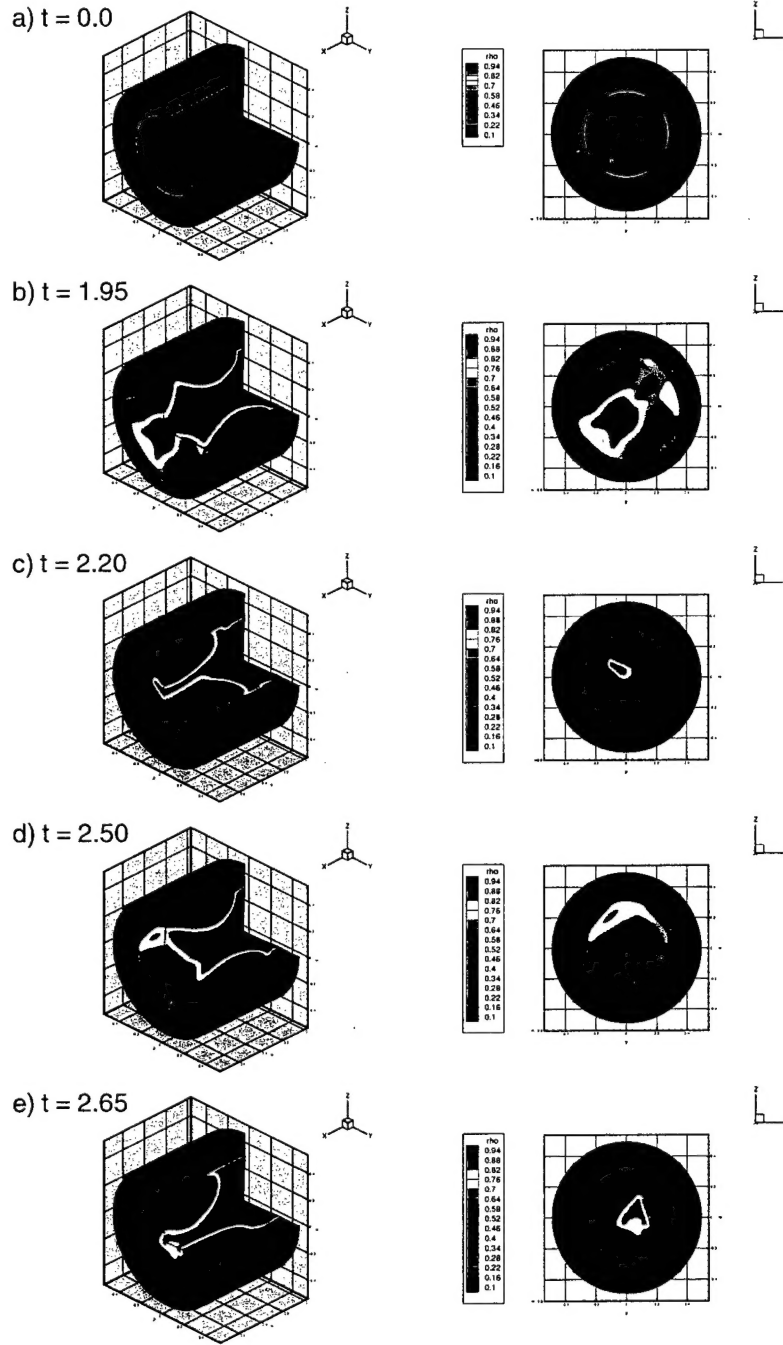
Figure 16: Density contours in initial development of Self-pulsation: $\epsilon = 0.04$, $U_g/U_l = 12$, $L/D = 0.75$, $Re_l = 6.6 \times 10^5$, $Re_g = 3.37 \times 10^6$
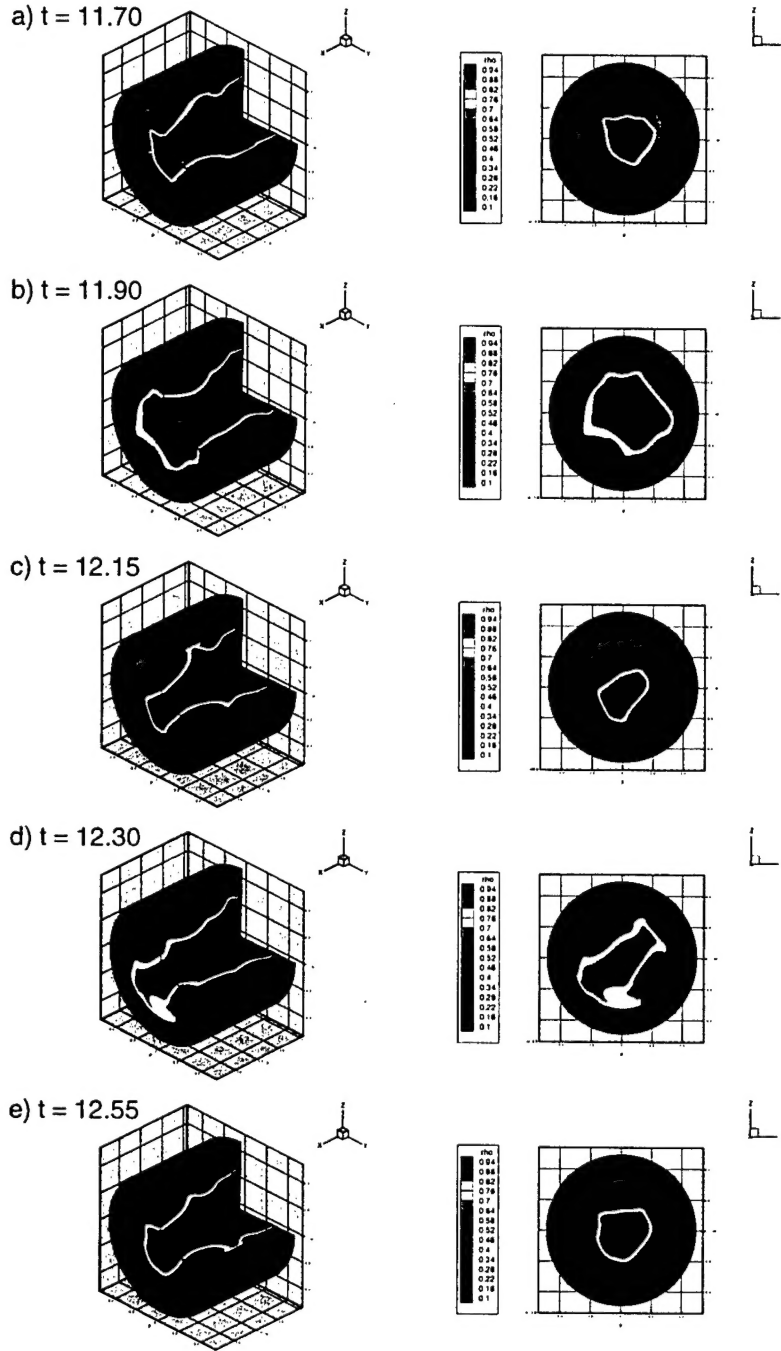
Figure 17: Density contours in small magnitude Self-pulsation mode: $\epsilon = 0.04$, $U_g/U_l = 12$, $L/D = 0.75$, $Re_l = 6.6 \times 10^5$, $Re_g = 3.37 \times 10^6$
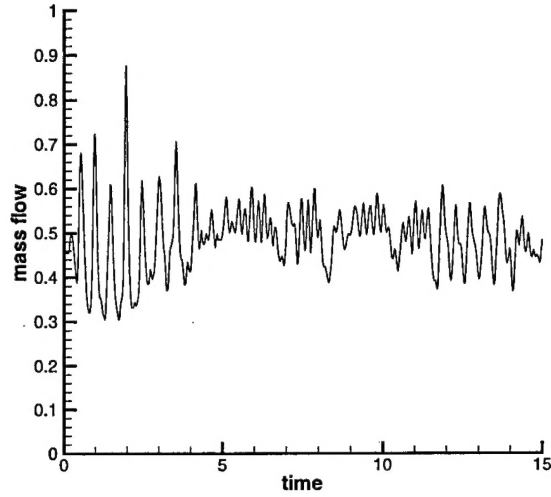
Figure 18: Time history of mass flow at exit plane: main burner geometry with preburner flow properties, $\epsilon = 0.04$, $U_g/U_l = 12$, $L/D = 0.75$, $Re_l = 6.6 \times 10^5$, $Re_g = 3.37 \times 10^6$
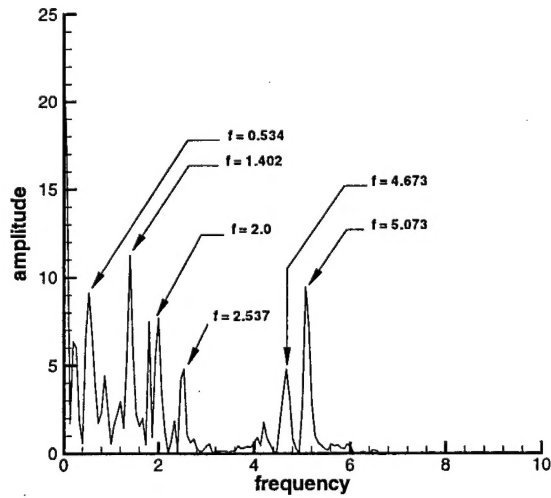

Figure 19: Spectral analysis of mass flow fluctuation: $\epsilon = 0.04$, $U_g/U_l = 12$, $L/D = 0.75$, $Re_l = 6.6 \times 10^5$, $Re_g = 3.37 \times 10^6$